UAS Contingency Management Autonomy with Experimentally Validated Models

by

Prashin Santosh Sharma

A dissertation submitted in partial fulfillment
of the requirements for the degree of
Doctor of Philosophy
(Robotics)
in The University of Michigan
2022

Doctoral Committee:

Professor Ella Atkins, Chair
Assistant Professor Jean-Baptiste Jeannin
Associate Professor Peter Seiler
Assistant Professor Zachary Sunberg
Professor Craig Woolsey

Prashin Santosh Sharma
prashinr@umich.edu
ORCID iD: 0000-0003-2828-4087

For my parents, wife and daughter

ACKNOWLEDGEMENTS

This dissertation was made possible by the support of a lot of people. Firstly, I would like to thank my advisor, Prof. Ella Atkins, for giving me the fantastic opportunity to conduct research on such an essential topic of contingency management for UAS. I truly appreciate the guidance and flexibility offered to me while pursuing the subject of my interest. Prof. Atkins is an immense source of knowledge and through our weekly meetings had an opportunity to learn a lot from her.

I want to thank my parents, Capt. Santosh Sharma, Zuliya Sharma, my wife Dr. Ritika Agrawal, and my daughter Rineisha Sharma. My parents taught me a lot of essential life principles such as discipline, persistence, hard work, dignity, and many more during my upbringing. These principles were fundamental to my success as a Ph.D. student. Also, thanks a lot for being so supportive throughout my education. To my dearest wife Dr. Agrawal, thanks a lot for taking this giant leap of faith by moving with me to the USA, motivating and encouraging me throughout my education. My wonderful daughter, thanks a lot for your smiles and warm hugs. They were very comforting during the difficult days of my research. I would also like to thank my in-laws Rajkumar and Mamta Agrawal, for helping us raise our daughter during her early years, allowing me to devote more time to research.

Thank you to my awesome friends and colleagues at the Autonomous Aerospace Systems (A2Sys) lab, Jeremy Castagno, Mia Stevens, Cosme Ochoa, Mathew Romano, Prince Kuevor, Akshay Mathur, Joseph Kim, Brian Yao, Paul Flanigen, and Mark Nail. I enjoyed all our discussions related to aerospace, robotics, and life.

Also, I would like to thank some of my collaborators with whom I have published papers and had an absolute pleasure working. They include Juan Paredes, Brian Ha, Manuel Lanchares, Dr. Peter Gaskell, Prof. Ilya Kolmanovsky, Dr. Javier González-Rocha, Prof. Peng Wei, Ben Kraske, and Zaki Laouar.

Lastly, I would also like to thank some staff members who were very helpful in conducting experiments and administrative matters. These include Christopher Chartier, Damen Provost, Denise Edmund, Kimberly Mann and Dan Newman.

TABLE OF CONTENTS

LIST OF FIGURES

Figure

LIST OF TABLES

Table

LIST OF ABBREVIATIONS

UAS Uncrewed Aircraft System

RUL Remaining Useful Life

EOD End of Discharge

BLDC Brushless Direct Current Motors

ECR Equivalent Circuit Resistance Battery Model

UTM UAS Traffic Management

ESC Electronic Speed Controller

RPM Rotations Per Minute

DOF Degrees of Freedom

PWM Pulse Width Modulation

SOC State of Charge

ECS Enhanced Self Correcting Battery Model

OCV Open Circuit Voltage

MDP Markov Decision Process

MC Monte Carlo

CMA Contingency Management Autonomy

SOH State of Health

ABSTRACT

Uncrewed Aerial Systems (UAS) are increasingly deployed for surveillance and transport applications. However, their safety and performance are significant concerns. This dissertation develops a **risk-aware autonomy architecture** backed by experimentally validated performance and degradation models necessary to maintain acceptable risk levels even when flying at low altitude in urban areas.

The first contribution is an **experimental model of aerodynamic performance for tractor and pusher hexacopter configurations**. This work was motivated by experimental analysis of a single propulsion unit with different propeller configurations for which a pusher configuration generated 20% more thrust than tractor configurations. Wind tunnel experiments yielded the insight that in static conditions, the pusher hexacopter has a higher lift-to-weight ratio than the tractor configuration because the pusher generates 15% more thrust than the tractor. However, in forward flight this higher lift-to-weight ratio is traded against a lower lift-to-drag ratio for the pusher design that has 25% more drag than the tractor design. We verified these results by conducting outdoor autonomous flight tests. These results further motivated an investigation of wind sensing sensitivity for a hexacopter in tractor and pusher configurations. Wind sensing experiments and analysis revealed that the pusher hexacopter configuration offers higher sensitivity to wind fluctuations than the tractor hexacopter.

The second contribution is a battery and motor reconfiguration scheme in a multi-battery pack to assure a UAS has sufficient stored energy to reach its destination. The proposed reconfiguration scheme is proactive by design, utilizing component failure

predictions from model-based prognostic methods. A model for the LiPo battery is experimentally determined using a novel low-cost testbed to collect charge/discharge data for battery model parameter identification. Fault modes of BLDC motors are studied, and a technique for motor fault prognosis is presented. Battery and motor degradation models are used for prognosis, providing End of Discharge and Remaining Useful Life estimates, respectively. Using abstractions of EOD value and other critical state features, **a novel battery reconfiguration MDP** is proposed for a series-parallel battery pack. The MDP policy optimally reconfigures the battery pack in flight. Case studies are presented to demonstrate benefits of the battery reconfiguration MDP.

The third contribution is a **MDP-based Contingency Management Autonomy (CMA) capability to generate mission-level directives that preserve safety when component reconfiguration alone is insufficient**. Although component reconfiguration prevents most sudden mission failures, there is no guarantee a degraded UAS can safely complete its planned flight. Optimal CMA policy effectiveness is evaluated on a high-fidelity simulator using experimentally validated models. Metrics such as mission failure rate are used to analyze CMA MDP performance over 900 Monte Carlo simulations. In poor battery health conditions, CMA MDP policy has a failure rate of 1.3% compared to a baseline policy's failure rate of 71%.

In summary, this thesis contributes to better understanding multicopter flight performance and to improving safety of small UAS flight. Safety is addressed using an abstract MDP decision-making approach due to vehicle and operational complexity. Component reconfiguration and contingency management will be instrumental in deploying autonomous UAS. This dissertation provides a baseline capability on which future component and systems performance and prognostics elements can be added.

CHAPTER I

Introduction

1.1 Motivation

Multicopters are a popular platform for emerging low-altitude Uncrewed Aircraft System (UAS) operations such as inspection, surveillance, and package delivery eg. Wing, Flytrex, Zipline. A variety of fixed wing, rotary wing and hybrid UAS configurations have been developed. To assure flight safety it is essential to understand UAS performance in nominal and off-nominal conditions. Fixed wing aircraft have been studied extensively with wind tunnel experiments and flight tests, but UAS performance characterization experiments with different rotor configurations have not been as carefully studied. This dissertation presents a suite of multicopter wind tunnel experiments to address this gap.

Urban UAS operation at low altitude can expose an overflown population to non-trivial risk due to uncertainty in actuator and battery performance, external disturbances, potential for lost link, and to-date a void in UAS community standards related to system redundancy or resilience. A survey conducted of 1500 UAS or "drone" companies [50] shows that UAS have a relatively high failure rate of 10^{-3} per flight hour. Multicopter batteries and motor failures were the most frequent contributing factors to UAS accidents because of limited energy and thrust margins, respectively.

A relatively high UAS component failure rate can be addressed by adding redun-

dant systems. However, UAS thrust and cost limits discourage the triple redundancy architectures required in commercial transport aviation. Although current UAS autopilots can build and accurately follow nominal flight plans they are not resilient to most system failures and harsh environmental conditions, e.g., precipitation, strong wind gusts or shear. Automated emergency landing planning and contingency management are required to improve UAS operational safety by making real-time flight planning as well as guidance, navigation, and control (GNC) decisions. Such contingency management autonomy will enable an UAS to avoid collision and land at a safe unpopulated site rather than descending uncontrolled and/or unpowered (e.g., with a parachute) into whatever lies below the UAS flight path.

A key to safe contingency management is establishing context-appropriate optimization metrics that ensure the UAS remains within its potentially degraded safe operating envelope, flies well-clear of terrain, buildings, and other aircraft, and minimizes overflight risk to people and property. Prognostics methods provide a set of tools for predicting component failures. They can also serve as a valuable source of information and optimization metrics, e.g., the remaining useful life of a component, to assure a contingency action is planned and executed before total component or system failure is likely. These methods are broadly classified as model-based and data-driven methods. Although physics-based models typically offer better explainability than data-driven methods, experimental validation of each physics-based model is critical.

This dissertation designs and evaluates contingency management autonomy relying on model-based health prognostic updates for UAS motors and battery pack(s). The health of these components is predicted for the near future, and these data are used in contingency plans prepared to safely react. Closing the health management loop onboard in real-time can appreciably reduce the likelihood of single or cascading failures leading to a crash.

1.2 Problem Statement

This dissertation develops contingency management autonomy with experimentally validated component models to address the following UAS challenges:

1. *What is the aerodynamic performance of a multicopter, and how does this performance vary as a function of propeller/motor configuration? In particular, how does a small hexacopter offering motor redundancy perform in hover and forward flight?*

   Efforts to study the aerodynamic performance of multicopters have been undertaken [26] to understand their off-nominal behavior and performance under different wind conditions [30]. However, experimental investigation of performance under different rotor orientations has not previously been examined. Accurate aerodynamic and propulsion models are essential for accurate simulation-based studies of prognostics and contingency management.

2. *How can safety-critical UAS components be reconfigured based on associated health indicators and prognosis information to safely continue a flight through landing? In particular, this dissertation investigates reconfiguration of UAS operation with multi-battery energy storage and redundant propulsion systems.*

   Previous research has proposed methods for reconfiguration of a multiple battery pack system based on End Of Discharge (EOD) [53] and State Of Charge (SOC) [68]. In [32] the authors propose an algorithm to optimally charge electric vehicles. Hidden Markov Models (HMMs) are obtained by fitting data collected from stochastic usage patterns for a single vehicle. Dynamic programming is used to determine optimal charge policies. However, none of these papers account for battery health, duration of battery operation or cell voltage in reconfiguring the battery pack. Prognosis of brushless DC motors popular in UAS platforms requires estimating Remaining Useful Life (RUL) [80]. This disser-

tation relies on RUL as a primary metric for propulsion system reconfiguration and contingency management.

3. *What is the best possible contingency action or plan a UAS can execute following component degradation event(s) to assure component availability through a safe [nearby] UAS landing?*

   System-level prognosis information has been used to determine maintenance schedules for UAS [20]. Prognosis-informed contingency management has also been studied in the context of mission management ([70],[64]). We believe this thesis is first to propose a contingency management system formulated as a Markov Decision Process (MDP) utilizing UAS prognosis information from experimentally validated component models to feed into reconfiguration and urgent landing planning algorithms.

1.3 Research Approach and Dissertation Outline

A suite of experiments was first designed and conducted to provide validated aerodynamic, propulsion, and battery models for subsequent model-based prognostics and contingency management research. Battery prognosis estimates End Of Discharge (End of Discharge (EOD)), and propulsion module prognosis estimates Remaining Useful Life (Remaining Useful Life (RUL)). EOD and RUL are used to reconfigure redundant battery and propulsion systems, respectively, as needed. Contingency Management Autonomy (CMA) monitors progress through the executing flight plan along with prognosis and reconfiguration states to recommend actions that preserve safety of the UAS in off-nominal scenarios. CMA actions are simulated in a virtual environment based on experimentally validated aerodynamic and propulsion models for a hexacopter UAS.

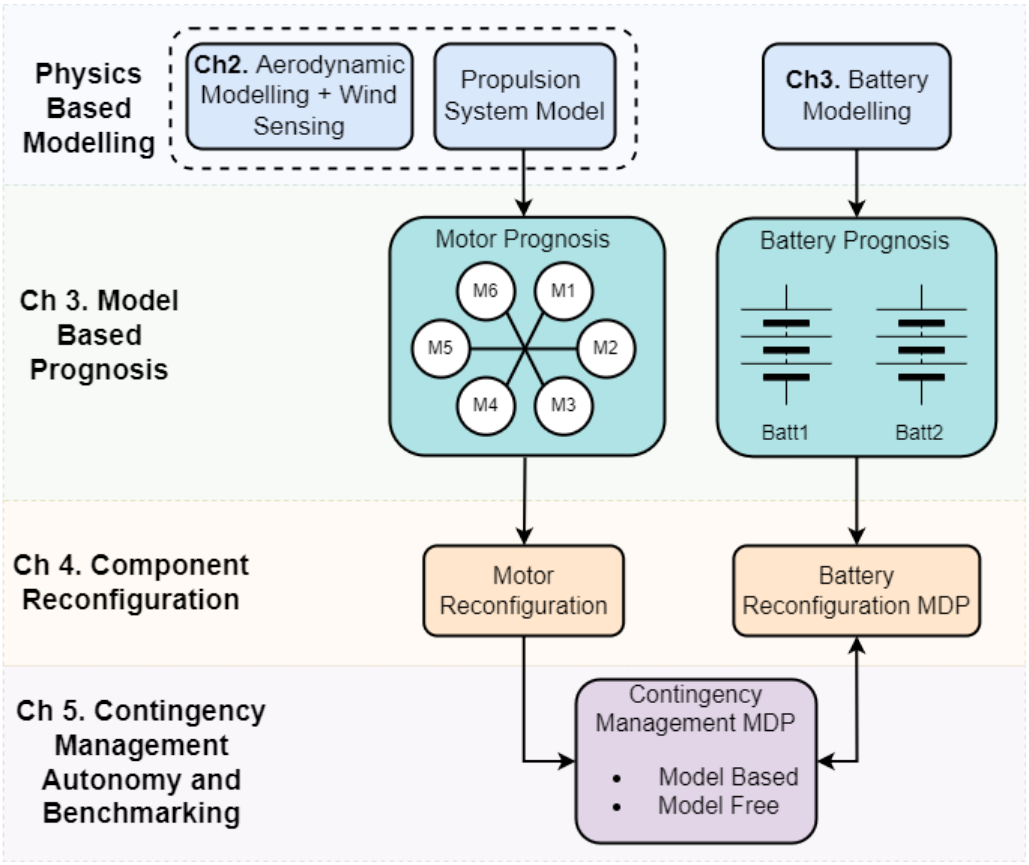

Figure 1.1: Contingency Management Architecture and Dissertation Outline

The contingency management pipeline investigated in this dissertation is shown in Figure 1.1. Functionality is summarized as follows:

- Aerodynamic performance characterization of hexacopters having different rotor configurations (Ch. II).
- Model-based prognosis of brushless direct current (Brushless Direct Current Motors (BLDC)) motors and battery pack to determine their RUL and EOD models, respectively (Ch. III).
- Reconfiguration of components based on their health indicators and prognosis information (Ch. IV).
- Contingency action selection based on health indicators of UAS components. This action is obtained from model-based and model-free reinforcement learn-

ing MDP formulations. Benchmarking of the two approaches against baseline contingency management approaches. (Ch. V).

Ch. II Aerodynamic Performance Characterization

Understanding vehicle performance is essential to ensure that flight envelope limits are always respected during flight. This chapter presents an experimental analysis of small multicopter motor and propeller performance through tests with a dynamometer. The data obtained from dynamometer experiments are used to characterize motor power, current requirements and generated thrust. Several propellers were tested in puller/tractor (traditional) and pusher (inverted) configurations. The pusher configuration is most efficient, with similar results reported in [72]. This result led to further aerodynamic performance exploration for tractor and pusher propulsion unit configurations in a fully-assembled hexacopter. A series of wind tunnel and outdoor autonomous flight tests are presented to characterize hexacopter forces over a family of forward airspeeds and incidence angles. A case study was conducted to determine open-loop wind sensing sensitivity for both hexacopter configurations. In this case study the pusher hexacopter exhibited higher sensitivity to resolve wind fluctuations than did the tractor configuration.

Ch. III Model Based Prognosis

Prognosis of Lithium Polymer (LiPo) batteries has been previously studied ([58], [27], [60], [18]) and typically focuses on estimating LiPo battery cell or pack End of Discharge (EOD) time. This chapter first describes the experimental setup developed to support UAS battery pack data collection. Experimental data is utilized to identify Equivalent Circuit Resistance (Equivalent Circuit Resistance Battery Model (ECR)) battery model parameters. Independently collected data are also used for ECR model validation. Identified parameters are varied to reflect battery health. Utilizing the battery model, model-based prognosis is performed to determine EOD. Propagation of the ECR model enables computation of EOD as the total time to reach a threshold

voltage.

Ch. IV Battery Reconfiguration

Prognostics methods provide tools for predicting failure scenarios and sending key health updates to assure an UAS can safely reach its destination. This chapter presents a battery management Markov Decision Process (MDP) that utilizes an experimentally-derived UAS LiPo battery model to reconfigure an onboard multiple battery energy storage system. This work assumes the multicopter UAS carries multiple battery packs because a single hardwired LiPo pack cannot offer backup should a failure (e.g., internal short, failed cell) occur.

Ch. V Contingency Management

The contingency management functional module combines information from component health and reconfiguration with mission objectives to define appropriate contingency action(s) for the UAS in off-nominal scenarios. This chapter provides an UAS contingency management solution formulated as a Markov Decision Process (MDP). Two approaches are proposed in this thesis to obtain and compare optimal policies. The first defines a model-based expert system MDP formulation solved with value iteration. The second uses a model-free Q-learning specification that relies on Monte Carlo simulations to learn an appropriate policy.

1.4 Contributions and Innovations

This thesis makes the following contributions:

- An experimentally-validated UAS battery model captured in a Markov Decision Process. Case studies examining battery MDP performance over various health and mission length scenarios.
- A multi-element contingency management solution for UAS that recommends or autonomously executes safety preserving actions during off-nominal scenarios.

Innovations of the thesis are as follows:

- The first aerodynamic comparison of tractor and pusher hexacopter performance through a series of wind tunnel experiments and autonomous outdoor flight tests.
- Specification and evaluation of a prognostics-informed MDP for battery management in UAS with multiple battery packs.
- The first MDP-based UAS contingency management solution incorporating component prognosis information in decision-making.

1.5 Products

- Prashin Sharma, Benjamin Kraske, Joseph Kim, Zakaria Laouar, Ella Atkins, and Zachary Sunberg,“ Investigation of Risk-Aware MDP and POMDP Contingency Management Autonomy for UAS”, 2022 (In Preparation).
- Javier Gonzalez-Rocha, Prashin Sharma, Ella Atkins and Craig Woolsey, “A Study of the Wind Sensing Performance of Pusher and Puller Hexacopter Small Unmanned Aircraft”, *Journal of Aircraft*, 2021 (submitted).
- Joseph Kim, Prashin Sharma, Ella Atkins, Natasha Neogi, Evan Dill and Steve Young, “Assured Contingency Landing Management for Advanced Air Mobility”, *40th Digital Avionics Systems Conference (DASC)*,IEEE/AIAA, 2021. https://doi.org/10.1109/DASC52595.2021.9594498
- Juan Paredes, Prashin Sharma, Brian Ha, Manuel Lanchares, Ella Atkins and Ilya Kolmanovsky, “Development, Implementation, and Experimental Outdoor Evaluation of Quadcopter Controllers for Computationally Limited Embedded Systems”, *Annual Reviews in Control*, Volume 53, 2021. Pages 372-389, https://doi.org/10.1016/j.arcontrol.2021.06.001

- Prashin Sharma and Ella Atkins, "Prognostics Informed Battery Reconfiguration in a Multi-Battery Small UAS Energy System", *International Conference on UAS (ICUAS)*, IEEE, 2021. https://doi.org/10.1109/ICUAS51884.2021.9476773

- Prashin Sharma and Ella Atkins, "Prognostics Based Decision Making for Safe Autonomous Flight", Doctoral Symposium, Prognostics and Health Management (PHM) Conference, 2020.

- Prashin Sharma and Cosme A. Ochoa, and Ella Atkins, "Sensor Constrained Flight Envelope for Urban Air Mobility", *SciTech Forum*, AIAA, 2019. https://doi.org/10.2514/6.2019-0949

- Prashin Sharma and Ella Atkins, "Experimental Investigation of Tractor and Pusher Hexacopter Performance", *Journal of Aircraft*,Volume 56, No.5, AIAA, 2019. Pages 1920-1934, https://doi.org/10.2514/1.C035319

- Prashin Sharma and Ella Atkins, "Multicopter Aerodynamics: Characterizing Thrust on a Hexacopter", *Aeronautical Engineering*, JoVE Science Education Database, Cambridge, MA, 2019. https://www.jove.com/v/10469/multicopter-aerodynamics-characterizing-thrust-on-a-hexacopter

- Prashin Sharma and Ella Atkins, "An Experimental Investigation of Tractor and Pusher Hexacopter Performance", *Atmospheric Flight Mechanics Conference*, Aviation Conference, AIAA, 2018. https://doi.org/10.2514/6.2018-2983

CHAPTER II

Experimental Aerodynamic Modelling of Hexacopter

2.1 Introduction

Multicopters have broad application for surveillance and package delivery as well as hobby. A variety of quadcopter, hexacopter, and octocopter designs have emerged, but the performance of small multicopters is not well-characterized in the literature. This chapter presents an experimental analysis of small multicopter propulsion unit performance and assembled hexacopter performance in two configurations: a standard tractor configuration in which propellers are mounted above the motors, and a less common pusher configuration in which propellers are mounted below the motors, "pushing" them up. This investigation was motivated by results from initial dynamometer experiments indicating that the rare pusher configuration generates more thrust than the tractor configuration.

A hexacopter was selected for this study despite the popularity and simplicity of the quadcopter due to its resilience to motor (propulsion unit) failure [16]. Selection of high-reliability components and redundancy are key ingredients to safe flight, particularly over populated regions. In [4] the authors discuss optimal selection of multicopter parts such as motors, blades, batteries, and electronic speed controllers.

Similar research has also been reported in [12], which discusses proper selection of a propeller system to address mission requirements. While redundancy and relability are key ingredients of safe flight, understanding vehicle performance is also essential to assure flight envelope limits are respected and to select the most efficient design.

This chapter presents an experimental analysis of small multicopter motor and propeller performance through tests with a dynamometer. The data obtained from dynamometer experiments is used for characterization of motor power, current requirements and generated thrust. Several propellers were tested in pusher and puller configurations. The pusher configuration was found to be more efficient, with similar results reported in [72]. This result led us to further exploring the aerodynamic performance of tractor and pusher configuration propulsion unit configurations in fully-assembled multicopters. For tests, we selected a modular small hexacopter frame with arms that could easily be mounted to the central body in tractor (traditional) or pusher (inverted arm mounting) configurations. A series of wind tunnel outdoor autonomous flight tests are presented to characterize hexacopter forces over a variety of airspeeds and incidence angles. The hexacopter in wind tunnel was driven by a power converter to assure consistent power and voltage levels throughout all tests. While commercially-available quadrotors can be purchased with tractor (puller) and pusher configurations as shown in Figure 2.1, to the best of our knowledge no publication has previously compared the performance of the two configurations experimentally.

This chapter is organized as follows. A literature review in Section 2.2 first summarizes aerodynamic performance and control systems for multicopter vehicles. The hexacopter system model is presented in Section 2.3. Section 2.4 describes both dynamometer, wind tunnel experimental apparatus, hexacopter designs and description of trajectories used for autonomous flight test. Experimental results are presented in Section 2.5, including a description of the curve-fit model obtained from these experiments. The discussion related to results is presented in Section 2.6. Motivated

(a) GhostDrone 2.0 by Ehang, pusher configuration quadrotor

(b) Phantom by DJI, tractor configuration quadrotor

Figure 2.1: Commercially available quadrotors

by the experimental results on aerodynamic performance of the tractor and pusher hexacopter, a case study to understand their wind sensing sensitivity is presented in 2.7. Lastly, the summary and future work are presented in Section 2.8.

2.2 Literature Review

Multicopter dynamics and control has been studied in detail. They are inherently under-actuated, however by providing adequate tilt angle to the rotors results in full controllability of the vehicle. In [23] the author proposes a control allocation algorithm exploiting the vehicle's capability to generate thrust and moments which were previously limited due to classical control allocation methods. Ref [31] addresses issues faced by quadrotors in flight regimes beyond hover by exploring forces and moments due to aerodynamic effects experienced by a quadrotor flying at high forward speed. In [37] the author discusses the design of a non-flat multicopter configuration. Reviewing literature on control methods for multicopter provided an insight into the importance of modelling the system.

Static tests to evaluate the performance of a multicopter propulsion system have

also been conducted. In [21], the authors studied thrust and power consumption from propellers of commercially available multicopter aerial vehicles. Tests were performed for individual propellers in tractor and pusher configuration, with the aim of building a database. Ref. [10] uses momentum and blade element theory to develop models of aerodynamic forces, including thrust, horizontal side forces, and torque and power for different quadrotor propellers. Models are developed beyond hovering steady state flight to account for vortex states in climbing flight.

Multicopter vehicle aerodynamic analysis results are reported in [26] with focus on modelling and simulation of off-nominal behaviors in commercially-available quadrotors. A series of wind tunnel tests were conducted to create a preliminary high fidelity model of a commercially available quadrotor for risk assessment and safety analysis. Ref. [30] presents a multicopter wind tunnel study to determine flight performance under different wind conditions for creation of a database for NASA's UAS Traffic Management (UAS Traffic Management (UTM)) program.

The design of multicopters has been studied extensively in [77]. Emphasis in [77] is on distributed, modular and heterogenous multicopter flows compared to traditional configurations in which rotors assume an evenly-spaced pattern. Rotor separation in symmetrical-pattern hexacopters was also explored for hover performance. Increasing rotor separation improved the hover performance, but it also resulted in increased vehicle weight, yielding a tradeoff. Ref. [76] presents a computational study of the interaction of quadcopter flows with similar results.

While tractor configurations are more common, the influence of pusher propeller configurations has been studied in a fixed wing Micro Aerial Vehicle (MAV), e.g., [14]. From the presented computational analysis, when the pusher propeller is ON, lift coefficient, drag coefficient and pitching moment coefficient increase by 2-5 % and decrease of lift to drag ratio by 1-2 %, compared to cases when the propeller is OFF. In [5] it was also concluded that fixed wing UAS has higher lift to drag ratio when

propellers are mounted in a tractor configuration. CFD analysis for overmount (tractor) and undermount (pusher) rotor configurations for quadcopters is performed in [75]. Results show that the undermount configuration generates 1% less thrust compared to traditional configuration with overmount rotors. Aerodynamic interactions between forward and rear motors in forward flight, results in decreased efficiency of the rear motors. However, drag properties of the overmount and undermount were not discussed in their paper. To the best of our knowledge, this paper presents the first experimental analysis of aerodynamic performance for tractor versus pusher configuration propellers on a multicopter platform.

2.3 System Modelling

This section presents multicopter dynamics models relevant to this work with focus on the multicopter electrical propulsion system. Each propulsion unit includes a motor, an electronic speed controller (Electronic Speed Controller (ESC)), and a propeller. All multicopter motors are connected to a single battery or regulated power supply. We first present a lumped parameter model as described in [57],[41] for aerodynamic forces acting on a single rotor. Using this model, we fit a curve to the observed data to identify numerical parameters. We then describe usage of this lumped parameter model to define hexacopter control inputs and forces acting on the integrated multicopter platform.

The aerodynamic forces generated by multicopter blades can be understood from momentum theory yielding simple relationships between thrust (T), torque (τ), power (P), and rotor speed (ω). These relationships are typically based on a hover assumption yielding a static thrust model. The static free air model for thrust, torque and power equations are as follows :

$$T = C_T \omega^2 \tag{2.1}$$

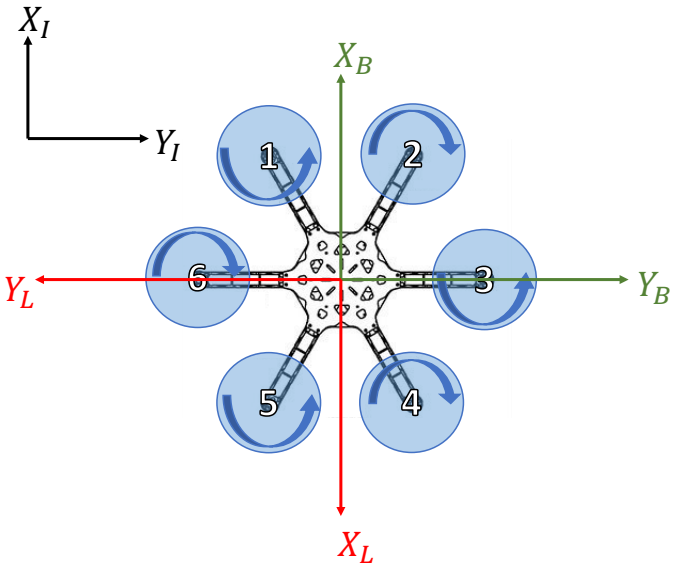

Figure 2.2: Illustration of body and world hexacopter frame as seen from the top view

$$\tau = C_Q \omega^2 \tag{2.2}$$

$$P = C_P \omega^3 \tag{2.3}$$

To specify the dynamics of the system, three coordinate frames are defined: inertial frame denoted by $\{ X_I, Y_I, Z_I \}$, body frame denoted by $\{ X_B, Y_B, Z_B \}$ and load cell frame denoted by $\{ X_L, Y_L, Z_L \}$, all shown in Figure 2.2. We define roll angle ϕ about X_B, pitch angle θ about Y_B and yaw angle ψ about Z_B.

The rotors are numbered from 1-6 and are located at a distance L from the hexacopter center of gravity. The hexacopter's total motor thrust magnitude T and torque magnitude τ_i about each body axis are related to six motor commands as described by the following equations [39]:

$$\begin{pmatrix} T \\ \tau_x \\ \tau_y \\ \tau_z \end{pmatrix} = \begin{pmatrix} C_T & C_T & C_T & C_T & C_T & C_T \\ \frac{LC_T}{2} & \frac{-LC_T}{2} & -LC_T & \frac{-LC_T}{2} & \frac{LC_T}{2} & LC_T \\ \frac{\sqrt{3}lC_T}{2} & \frac{\sqrt{3}lC_T}{2} & 0 & \frac{-\sqrt{3}LC_T}{2} & \frac{-\sqrt{3}lC_T}{2} & 0 \\ C_Q & -C_Q & C_Q & -C_Q & C_Q & -C_Q \end{pmatrix} \begin{pmatrix} \omega_1^2 \\ \omega_2^2 \\ \omega_3^2 \\ \omega_4^2 \\ \omega_5^2 \\ \omega_6^2 \end{pmatrix} \tag{2.4}$$

Let C_x,C_y and C_z represent hexacopter drag coefficients, m the mass of the hexacopter, and g acceleration due to gravity. Then, Newton's equations of motion for the hexacopter can be defined as

$$m\ddot{r} = R_B^W \begin{pmatrix} 0 \\ 0 \\ -T \end{pmatrix} + \begin{pmatrix} 0 \\ 0 \\ mg \end{pmatrix} + \begin{pmatrix} C_x & 0 & 0 \\ 0 & C_y & 0 \\ 0 & 0 & C_z \end{pmatrix} \dot{r} \tag{2.5}$$

where rotation matrix R_B^W is defined by Z-X-Y Euler angle rotation and is given as follows,

$$R_B^W = \begin{pmatrix} C\psi C\theta - S\phi S\psi S\theta & -C\phi S\psi & C\psi S\theta + C\theta S\phi S\psi \\ C\theta S\psi + C\psi S\phi S\theta & C\phi C\psi & S\psi S\theta - C\psi C\theta S\phi \\ -C\phi S\theta & S\phi & C\phi C\theta \end{pmatrix} \tag{2.6}$$

The attitude equations of motion for the hexacopter are defined as follows, where p is angular velocity about the x-axis, q is angular velocity about the y axis, and r is angular velocity about the z-axis,

$$I\begin{pmatrix}\dot{p}\\ \dot{q}\\ \dot{r}\end{pmatrix} = \begin{pmatrix}\frac{L}{2} & \frac{-L}{2} & -L & \frac{-L}{2} & \frac{L}{2} & L\\ \frac{\sqrt{3}L}{2} & \frac{\sqrt{3}L}{2} & 0 & \frac{-\sqrt{3}L}{2} & \frac{-\sqrt{3}L}{2} & 0\\ \gamma & -\gamma & \gamma & -\gamma & \gamma & -\gamma\end{pmatrix}\begin{pmatrix}T_1\\ T_2\\ T_3\\ T_4\\ T_5\\ T_6\end{pmatrix} - \begin{pmatrix}p\\ q\\ r\end{pmatrix} \times I\begin{pmatrix}p\\ q\\ r\end{pmatrix} \tag{2.7}$$

where $\gamma = \frac{C_Q}{C_T}$, γ is the ratio of moment coefficient to thrust coefficient.

The relation between body and world frame angular velocity is given by,

$$\begin{pmatrix}\dot{\phi}\\ \dot{\theta}\\ \dot{\psi}\end{pmatrix} = \begin{pmatrix}cos(\theta) & 0 & sin(\theta)\\ sin(\theta)tan(\phi) & 1 & -cos(\theta)tan(\phi)\\ -\frac{sin(\theta)}{cos(\phi}) & 0 & -\frac{cos(\theta)}{cos(\phi)}\end{pmatrix}\begin{pmatrix}p\\ q\\ r\end{pmatrix} \tag{2.8}$$

To specify hexacopter performance, mechanical power (P_{mech}), electrical power (P_{elec}) and overall efficiency η are defined in terms of system voltage V and motor current I as follows:

$$P_{mech} = \tau\omega \tag{2.9}$$

$$P_{elec} = VI \tag{2.10}$$

$$\eta = \frac{P_{mech}}{P_{elec}} \tag{2.11}$$

2.4 Experimental Method

To obtain an aerodynamic model of the hexacopter, we first determine the forces acting on it which includes lift and drag of the bare airframe, and thrust generated by individual motors. For this purpose, isolated propulsion units were tested in pusher and tractor configurations on a dynamometer with static flow conditions. Tests were conducted over different throttle commands and propeller choices to determine thrust coefficient, power requirement, motor Rotations Per Minute (RPM), and voltage relationships. To investigate the interaction of the rotors with the airframe in pusher versus tractor configurations, a hexacopter was mounted on a test stand equipped with load cell, and data was collected in the University of Michigan's 5'x7' wind tunnel at different free stream flow speeds, motor thrust, and hexacopter angle of attack (pitch angle) conditions. Lift and drag aerodynamic data from the load cell were acquired over all tested conditions. The wind tunnel also supported flow visualization around the vehicle using vaporised diesel. To provide comparison and validation of wind tunnel tests findings, a series of autonomous flight tests were conducted outdoors. Below, we describe in detail the setup and methods for conducting the experiments.

2.4.1 Dynamometer Tests

A single propulsion module was mounted on an off-the-shelf dynamometer including brushless DC motor (BLDC), electronic speed controller (ESC), propeller and battery. Mutlistar Elite 2204 and 2300Kv motors, AfroESC 20 amp ESC, and Turnigy 3s 11.1V, 30-40C 2200mah batteries were used for the test on the RC Benchmark Dynamometer Stand as shown in Figure 2.3. Two and three-blade propellers recommended by the motor manufacturer were tested in puller and pusher configurations. During these experiments the throttle command was varied from 1100 μs to 1900 μs. Thrust, torque, power consumption and electrical RPM values were

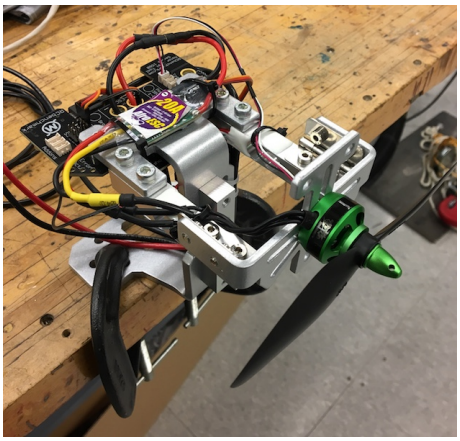

Figure 2.3: Motor setup on Dynamometer stand

(a) Pusher Design.

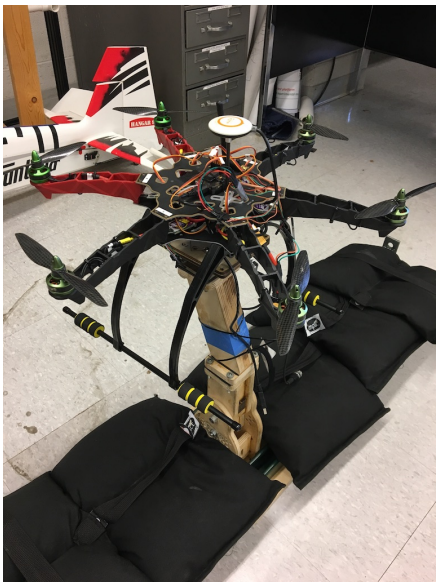

(b) Tractor Design.

Figure 2.4: Hexacopter Static Thrust Test Setup

measured.

2.4.2 Hexacopter Platform

A commercially-available modular hexacopter airframe was selected for these experiments. The center plate is made of glass fiber while the arms are down-step style glass-filled nylon arms for high strength and durability. The overall frame diameter is 450mm with other dimensions as shown in Figure 2.5.

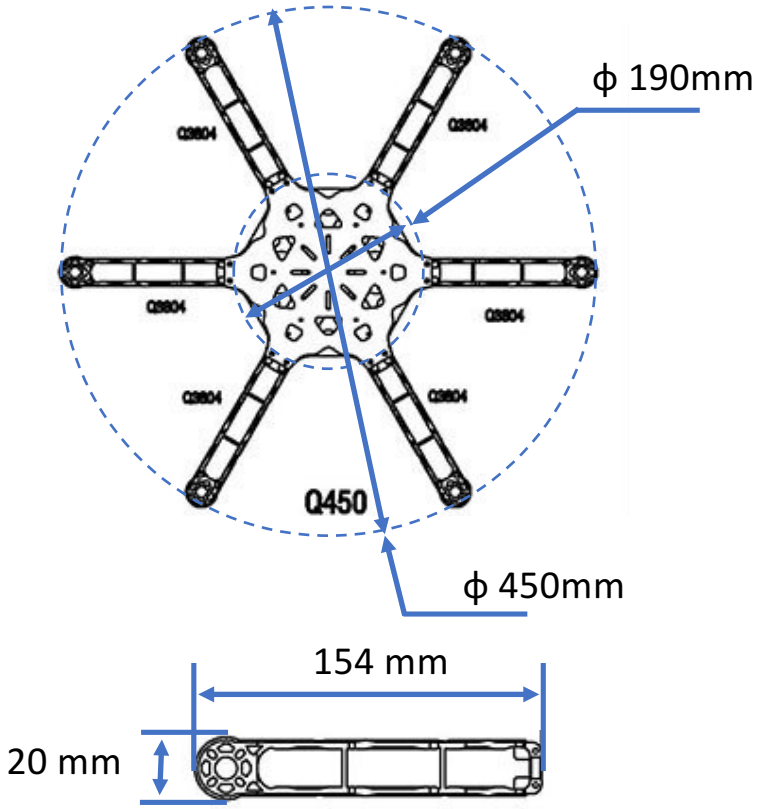

Figure 2.5: Model for motor RPM based on throttle command and battery voltage

The frame is outfitted with six Multistar Elite 2204 2300Kv motors affixed to a 6040 carbon fiber propeller [1] chosen for flight testing based on dynamometer test results. The airframe was outfitted with landing gear to include landing gear in aerodynamic force analysis. The hexacopter was controlled with a CC3D Revolution (Revo) 10Degrees of Freedom (DOF) flight controller capable of stabilizing multicopters. Revo runs an open source LibrePilot Software suite to control multirotor vehicles, but open-loop commands were issued for our aerodynamic performance experiments to assure consistent motor command values. Identical components were used for both the pusher and tractor configuration hexacopters as shown in Figure 2.4 to enable direct comparison between datasets. Turnigy 3s 30-40C 2200mah batteries would be used for flight tests, however, while testing in the wind tunnel, a MeanWell RSP 12VDC 1600 Watt power supply was used to eliminate the need for battery

charging and swapping.An Attopilot voltage and current sensor was used to measure the overall current draw of the hexacopter. The vehicle was assembled such that it could be used either for wind tunnel and outdoor flight testing. The hexacopter plus battery weighs approximately 1kg.

2.4.3 Hexacopter Test Stand with Load Cell

A load cell-equipped test stand was used to determine forces acting on the hexacopter in static and dynamic conditions. The hexacopter was mounted on the test stand as shown in Fig. 2.6; the test stand would be reconfigured to vary vehicle pitch angle from -30 to +30 degrees; note that pitch angle is equal to angle of attack in the wind tunnel. Based on hexacopter maximum thrust calculations, the ATI sensor Mini 45 sensor was selected and connected to a Diamond Systems Athena ATHM-800 256 ALP data acquisition computer running the QNX operating system. Data from the load cell was recorded at 1KHz. Experiments were conducted at airspeeds ranging from 0 mph to 20 mph at 5 mph increments. Equal throttle commands were given to all motors ranging from 1300μs to 1700μs with a 200μs increment. The pitch angle was also varied from -30 to 30 degrees with 10 degree increments. These parameters were selected based on experimental apparatus constraints and also match expected conditions when flying in an open outdoor environment.

2.4.4 Autonomous Flight

In order to validate the results of wind tunnel and dynamometer experiments, autonomous flight tests of both hexacopters were conducted in Michigan's M-Air outdoor netted facility using a Qualisys motion capture system. For the hexcaopters to fly with motion capture they were refitted with BeagleBone Blue(BBBL), [3] an embedded computer running RC Pilot [67] flight controller. Small motion capture reflective targets were also added to the vehicle.

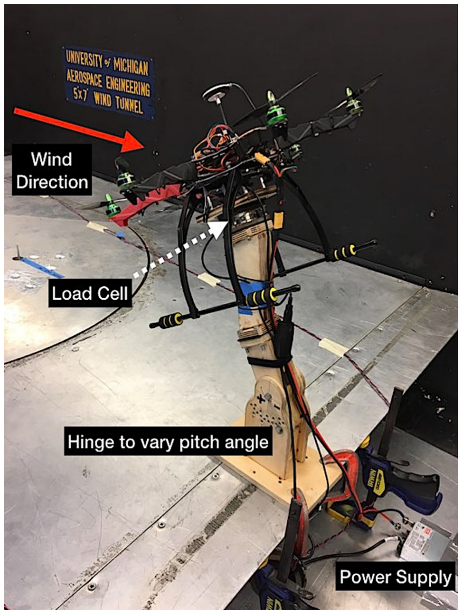

Figure 2.6: Test Stand in the wind tunnel

Because motor thrust coefficient were not determined for appreciable winds, in order to compare the performance of the two vehicles we decided to compare the energy consumption of the two vehicles for different phases of flight. ACS712 [2] current sensors were mounted to read current draw from each motor, and data was recorded using an Arduino Uno microcontroller. The BBBL is then interfaced with Uno via USB to log current data from each motor along with flight telemetry data. The full instrument and embedded computer stack on the hexacopter can be seen in Figure 2.7. The control law for autonomous flight was developed by linearizing the plant dynamics of the vehicle described in Section 2.3 and using it to determine the control inputs, similar to the approach undertaken in [43].

For autonomous flight, two flight profiles were tested:

- Climb-Hover-Descent - The goal of these test is to complement the static load cell tests. A cubic spline profile [42] for climb and descent was provided to the hexacopters.

- Circular steady flight trajectory tracking- The goal of these test cases is to

complement the results obtained from wind tunnel experiments. As the netted facility has limited length for such high velocities, circular trajectory of large radius was selected with continuous heading change for the hexcopters so that tangential velocity remains constant. A tangential velocity of $2.2m/s$ was selected, close to the wind speed selected in wind tunnel test matrix.

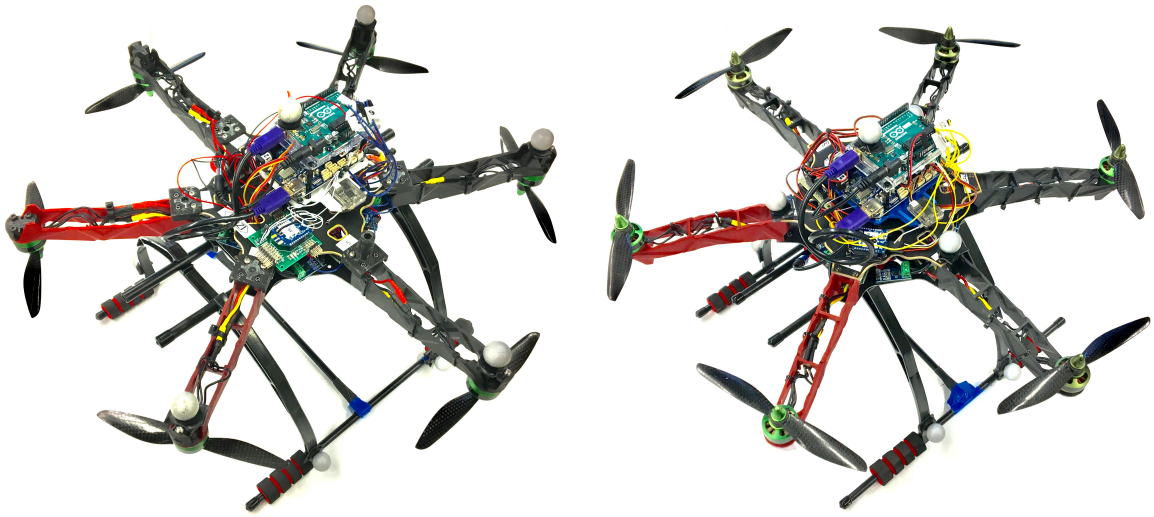

(a) Pusher Design. (b) Tractor Design.

Figure 2.7: Hexacopter setup for autonomous flight using motion capture

2.5 Experimental Results

This section presents results obtained from the experiments described above. First we present results from dynamometer experiments to characterize static thrust and torque parameters. Next, we summarize the propulsion system model and provide an experimental validation of this model. Finally, we provide results of static, wind tunnel and outdoor flight tests results for both pusher and tractor configuration hexacopters.

2.5.1 Thrust Coefficients

Three types of propellers were tested on the dynamometer. Propellers were selected based on motor manufacturer recommendation. Propellers used for the experiments are 6040 x 2 blade, 5030 x 2 blade, and 5030 x 3 blade. Note that a 6040 propeller has a 6 inch diameter and moves 4 inches forward in a single revolution. The throttle commands given to the controller on the dynamometer were varied from 1100μs to 1900μs Pulse Width Modulation (PWM) (pulse width modulation). Dynamometer data including thrust, torque, voltage, and current were recorded at 45Hz. The measured thrust and overall efficiency shown in (2.11), are plotted in Figures 2.8 and 2.9, respectively. The 5030 x 3 blade propeller induced large vibrations and "squealing" in the propulsion unit at high RPM, so hexacopter tests were restricted to the 2-blade propellers. As shown, the pusher configuration for all three propellers was more efficient than the tractor propeller configuration. Since the 6040 propeller generated a higher thrust to weight ratio for the hexacopter than the other two propellers, the 6040 propeller was selected for all hexacopter testing.

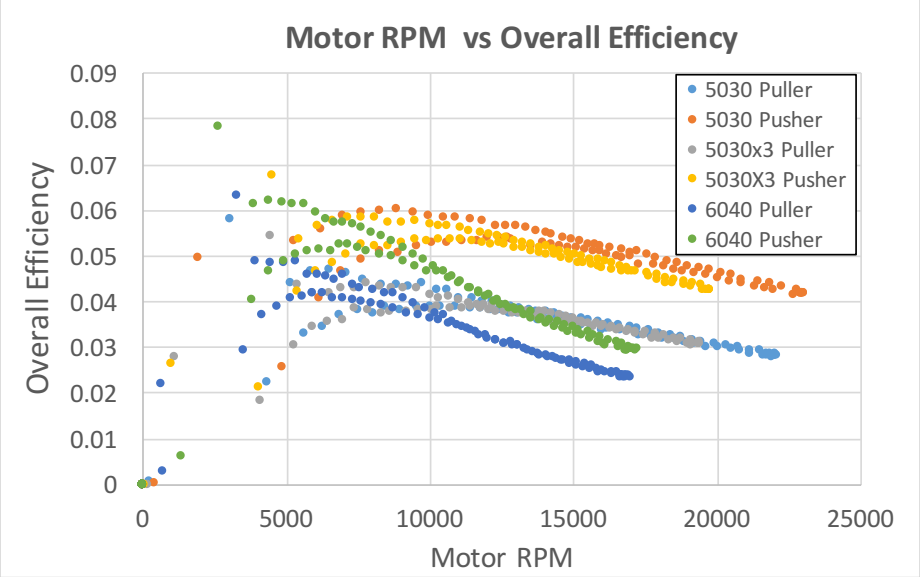

Figure 2.8: Plot for efficiency of motor with increase in RPM

Thrust and torque coefficients are defined in equations (2.1) and (2.2), respectively

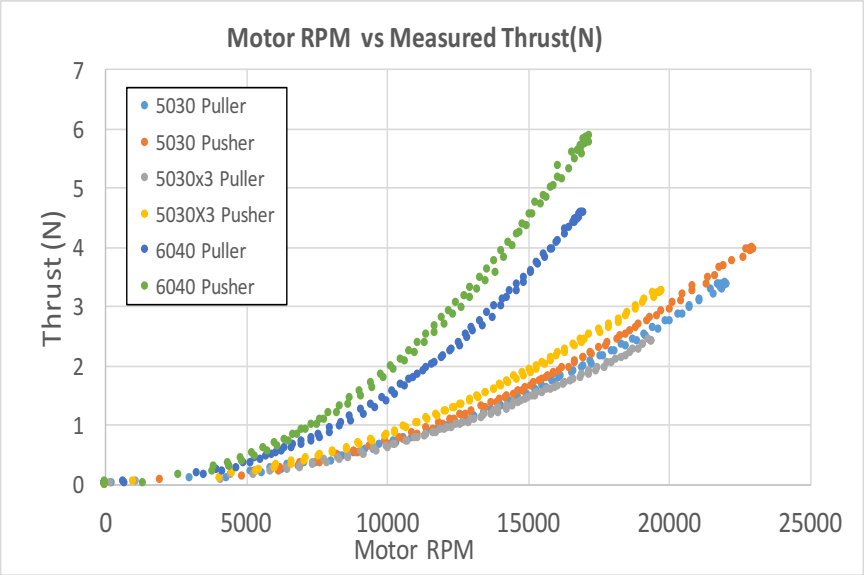

Figure 2.9: Plot for thrust generated by motor in static conditions

were determined by regression of dynamometer data and are presented in Table 2.1.

Table 2.1: 6040 Propeller Static Thrust and Moment Coefficients

Configuration	C_T $(\frac{N}{RPM^2})$	R^2 **error for** C_T	C_Q $(\frac{Nm}{RPM^2})$	R^2 **error for** C_Q
Tractor	1.5652e-08	0.9968	2.0862e-10	0.9849
Pusher	1.9693e-08	0.9975	2.1374e-10	0.9903

2.5.2 Motor RPM Estimation

Once mounted on the hexacopter, motor RPM's could no longer be directly measured with the chosen low-cost lightweight ESCs. We therefore developed a model to estimate motor RPM for the hexacopter. Data was collected from the dynamometer by sending throttle commands to the dynamometer controller varying from 1100μs to 1900μs PWM until the battery dipped below a minimum threshold. Measured parameters including motor electrical RPM, throttle command, battery voltage and current where then analyzed. A polynomial surface was fitted to the data using a robust Least Absolute Residuals (LAR) method since the collected data had few out-

liers / anomalies. A cubic polynomial relationship was chosen for throttle (PWM) command (δ_t), and a quadratic was chosen for Electrical Power P_{elec}. The resulting fit, shown in Figure 2.10 had an R^2 value of 0.9985 and is given by:

$$\begin{aligned} RPM_{est} &= p_{00} + p_{10} * \delta_t + p_{01} * P_{elec} + p_{20} * \delta_t^2 + p_{11} * \delta_t * P_{elec} + p_{02} * P_{elec}^2 + \\ &\quad p_{30} * \delta_t^3 + p_{21} * \delta_t^2 * P_{elec} + p_{12} * \delta_t * P_{elec}^2 \\ p_{00} &= 1.239e+04, p_{10} = -803.8, p_{01} = 4125, p_{20} = 979.3, p_{11} = -2757 \\ p_{02} &= 334.4, p_{30} = 450, p_{21} = -17.38, p_{12} = 69.46 \end{aligned} \tag{2.12}$$

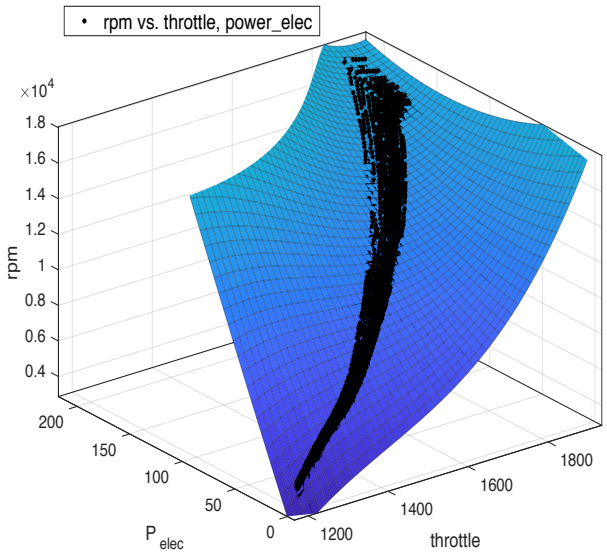

Figure 2.10: Model for motor RPM based on throttle command and battery voltage

where δ_t is normalized by mean 1550 μs and standard deviation 201.9 μs and where P_{elec} is normalized by mean 71.11 W and standard deviation 55.75 W. To validate the fitted model, another dataset was collected. As shown in Figure 2.11 measured RPM values are within 95% confidence bounds of the model. We also calculated thrust using Equation (2.1) and the estimated RPM obtained from Equation (2.12). It was observed that the relative error with this approach was less than 10%, except at lower throttle inputs is insufficient to lift the hexacopter, as shown in Figure

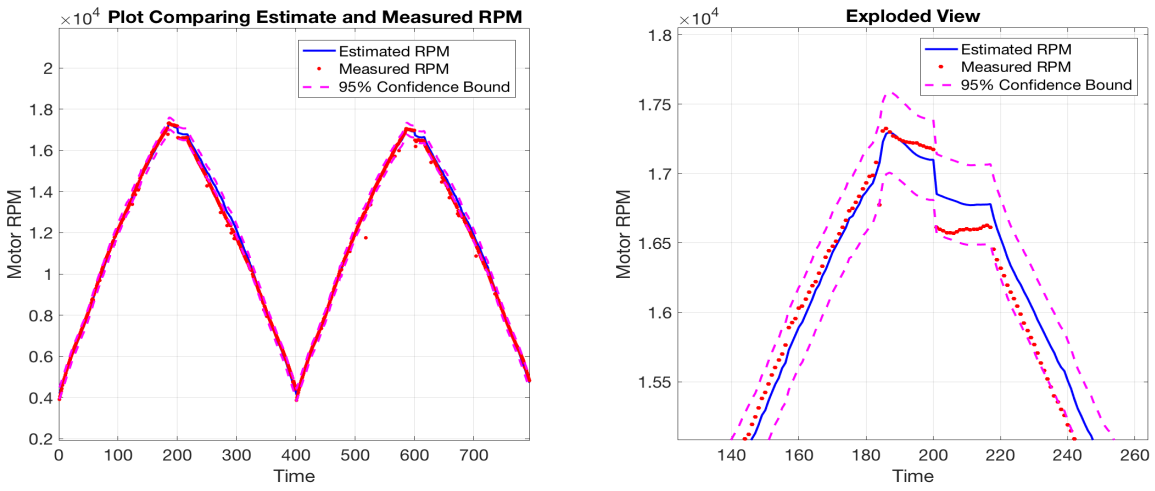

Figure 2.11: Validation of the RPM Estimation model

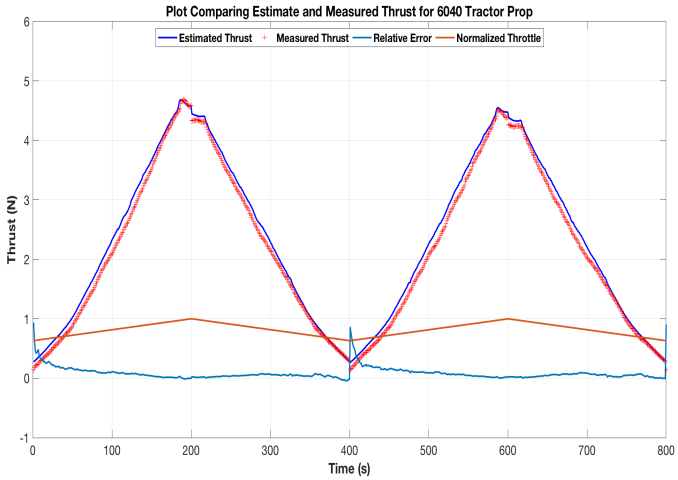

Figure 2.12: Comparison of estimated and measured thrust

2.12.

2.5.3 Hexacopter Aerodynamic Forces

2.5.3.1 Static test

Static tests were conducted in a lab with the two hexacopters mounted on the Load Cell Test Stand as shown in Figure 2.4. The hexcaopters were given 1500μs and 1900μs throttle commands. The hexacopters were mounted with thrusters level representing a 0° pitch angle. Table 2.2 shows the total thrust as measured from the

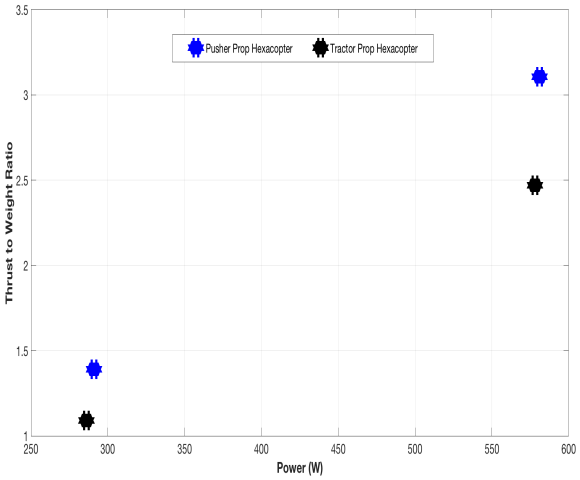

Figure 2.13: Thrust to weight ratio comparison for push and tractor hexacopter configurations

load cell and the estimated total thrust per Equations (2.1) and (2.12), respectively. The primary result is that the pusher hexacopter produced 15% more total thrust than the tractor hexacopter. Given similar power input, the pusher has a higher thrust to weight ratio than the tractor hexacopter as shown in Figure 2.13 representing static hovering flight. As shown above, the error in RPM estimate is relatively high for lower throttle commands. The error in total estimated thrust is also higher for lower throttle commands compared to higher throttle commands.

Table 2.2: Static Thrust comparison for different throttle values applied to hexacopters

	Thrust (N)	**Est Thrust (N)**	**Power (W)**
Throttle	δ_t= 1500μs		
Tractor	15	10.76	286
Pusher	15.56	13.64	291
Throttle	δ_t = 1900μs		
Tractor	26.85	24.22	578
Pusher	31	30.42	581

2.5.3.2 Dynamic Test: Wind Tunnel

To measure aerodynamic forces with free stream flow, the two hexacopters were mounted in the wind tunnel on the test stand described in the previous section. Load cell data was measured for each experiment listed in Table 2.3 with coordinate frame sign conventions based on the load cell frame shown in Figure 2.2. For every change in pitch angle, the load cell was first tared with no free stream flow so that only the lift and drag produced by the hexacopters are recorded when motors are off. Note that the bare airframe aerodynamic lift and drag were obtained by setting throttle (motor) commands to zero for each free stream flow speed. Hexacopter throttle command was limited to 1700μs due to appreciable vibrations in the load cell stand at high wind tunnel speeds. Wind tunnel speeds were measured with multiple pitot tube readings.

Table 2.3: Full Airframe Test Matrix

Hex Config	**Wind Speed ($\frac{m}{s}$)**	**Pitch Angle ($^\circ$)**	**Yaw Angle ($^\circ$)**	δ_t **(μs)**
Tractor	2.2	-30 to 30	0	0 to 1700
	4.5	-30 to 30	0	0 to 1700
	6.7	-30 to 30	0	0 to 1700
	8.9	-30 to 30	0	0 to 1700
Pusher	2.2	-30 to 30	0	0 to 1700
	4.5	-30 to 30	0	0 to 1700
	6.7	-30 to 30	0	0 to 1700
	8.9	-30 to 30	0	0 to 1700

Lift and drag forces were measured by load cell for both pusher and tractor hexacopters. The force data for different throttle commands (δ_t) and wind speeds 5m/s and 8.47 m/s are plotted in Figures 2.14 - 2.19. The wind speeds shown in the plots differ somewhat from the test matrix because the wind tunnel used for experiments has low resolution in setting wind speed, so exact values could not be reached. Lift and drag trends for the tractor hexacopter are similar to those obtained in [59]. It can be inferred from our plots that with an increase in δ_t there is a corresponding increase

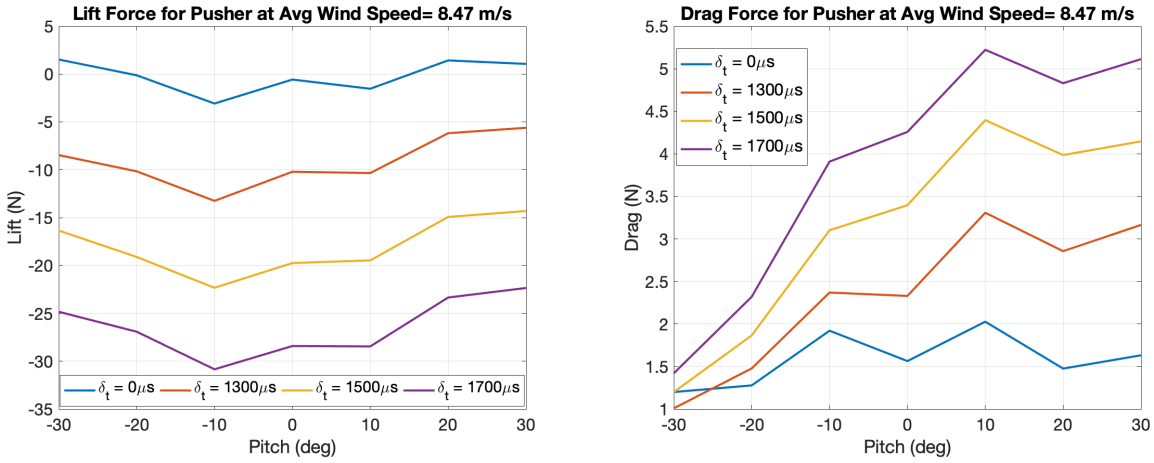

Figure 2.14: Lift and drag forces for the pusher hexacopter at average wind speed 8.47m/s

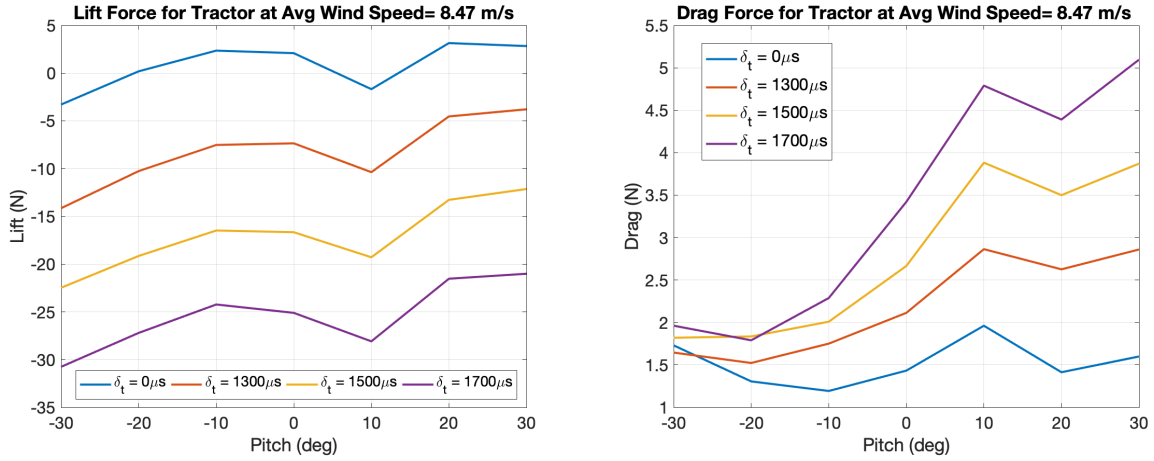

Figure 2.15: Lift and drag forces for the tractor hexacopter at average wind speed 8.47m/s

in lift force at different pitch angles. The drag force varies with throttle command, wind speed and pitch angle.A positive pitch angle induces hexacopter braking so drag increases significantly with increase in throttle command for this configuration. Conversely, at negative pitch the throttle command has less effect on hexacopter drag. The lift to drag ratios for the two hexacopters are plotted in Figures 2.16 and 2.19. From the plots it can be inferred that the tractor configuration exhibits higher lift to drag ratio at different pitch angles. A direct comparison is shown in Figure 2.20.

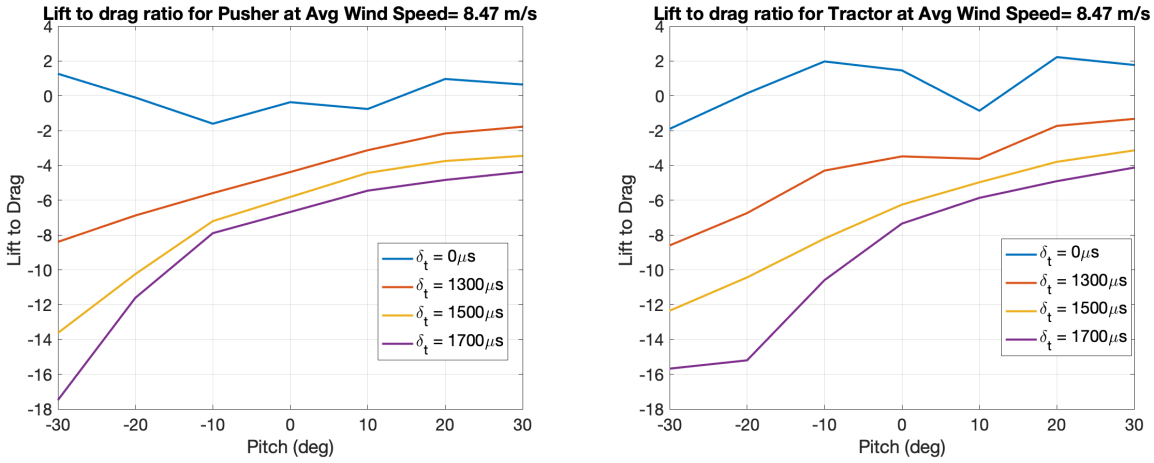

Figure 2.16: Lift to drag ratio comparison for average wind speed 8.47m/s

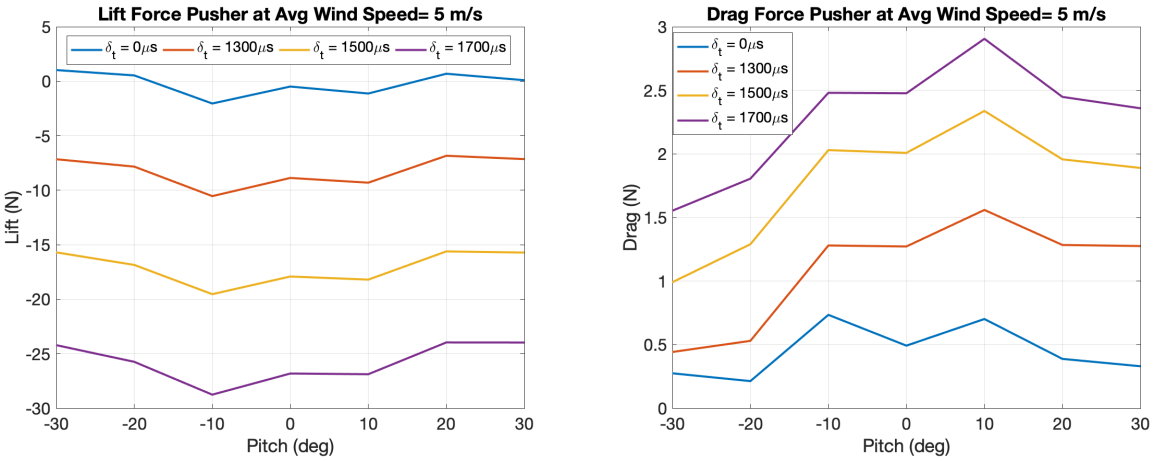

Figure 2.17: Lift and drag forces for the pusher hexacopter at average wind speed 5m/s

2.5.4 Flight Test

To provide further analysis of tractor versus pusher performance, we performed a series of outdoor free flight tests in the University of Michigan's M-Air netted facility. For this test series, we utilized a Qualisys motion capture system to provide position and attitude data, and collected data for the two specific autonomous flight sequences described below with the Beaglebone Blue (BBBL) embedded computer running an augmented version of the RC Pilot open-source autopilot software.

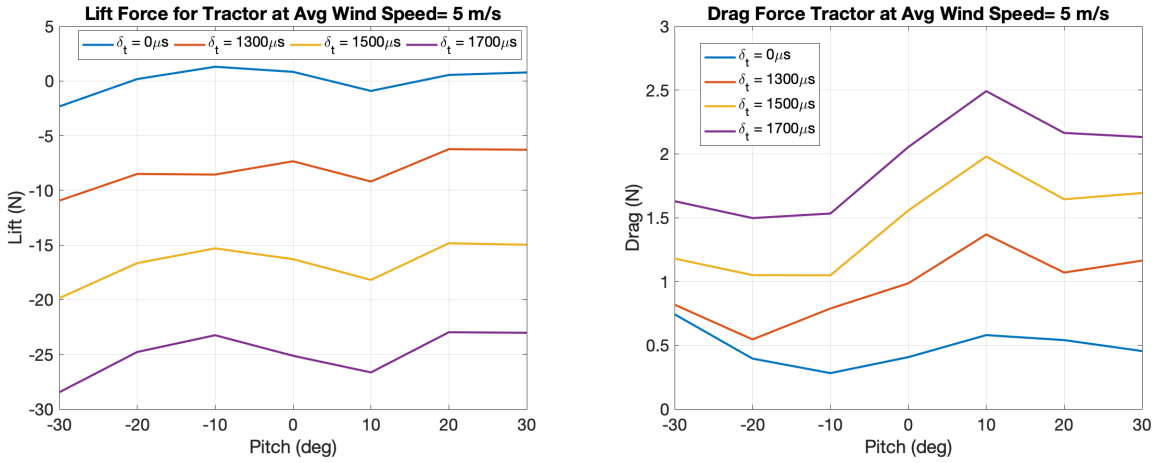

Figure 2.18: Lift and drag forces for the tractor hexacopter at average wind speed 5m/s

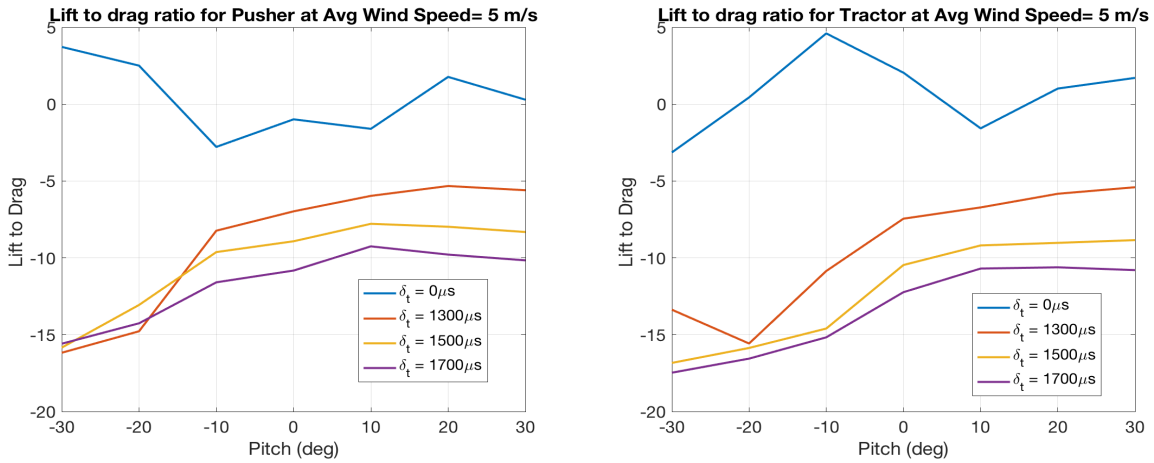

Figure 2.19: Lift to drag ratio comparison for average wind speed 5m/s

2.5.4.1 Climb-Hover-Descent

For this experiment, the hexacopters were commanded to climb vertically to a specified height above the ground, hover for a specified time, and then execute a descent to landing. Both hexacopters followed the same climb, hover, descent profiles. This profile was executed multiple times for both hexacopters. The reference trajectory given to both hexacopters is shown in Figure 2.22. The vertical position starts with an offset from zero because the centroid of the hexacopter begins above the ground plane. Winds of $1 - 2m/s$, 180° relative to True North, were observed as

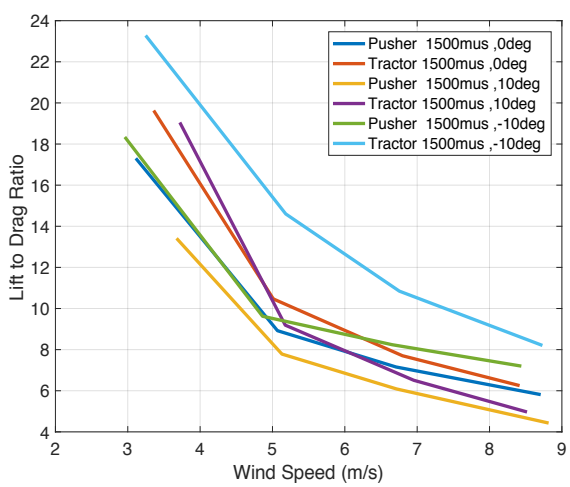

(a) Lift to drag ratio for δ_t=1500μs

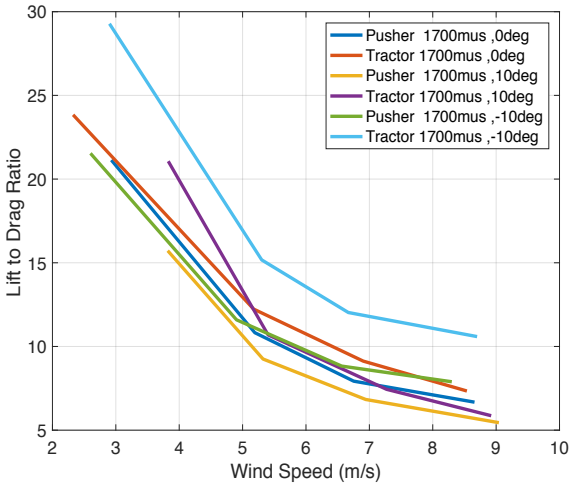

(b) Lift to drag ratio for δ_t=1700μs

Figure 2.20: Lift to drag ratio variation with wind speed

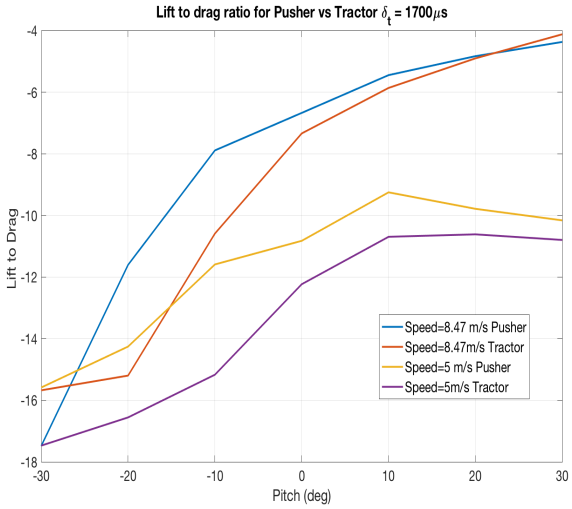

Figure 2.21: Lift to Drag ratio comparison at constant throttle

a result of which position tracking bias can be seen in the figure. Position was held was within a 0.5m radius circle as shown in Figure 2.23 for one of the runs despite winds and a simple proportional-derivative control law. Because altitude hold was accurate and drift was not dominant, we were able to compare the performance of both hexacopters.

Electrical current data is shown in Figure 2.24. A negative spike in battery voltage occurs when autonomous mode is first turned ON, resulting in all motors receiving

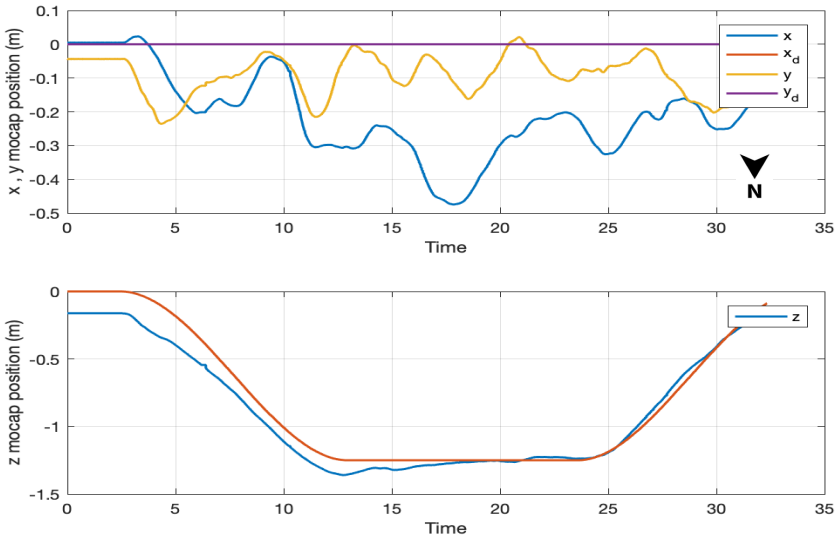

Figure 2.22: Commanded climb and descent profile for pusher hexcopter.

large thrust commands simultaneously. After the hexacopters stabilize, current also stabilizes and the hexacopters then follow a smooth climb/descent profile. Power consumption for the hexacopters is plotted against time in Figure 2.25. Energy data for the required phases of flight are obtained by taking integral of the area under the Power vs Time graph. It can be seen from the figure that for all the phases of flight the pusher hexacopter requires less energy than the tractor hexacopter. A direct comparison of energy of the two configurations over multiple position hold flight tests is shown in Figure 2.26.

2.5.4.2 Circular Steady Flight Trajectory Tracking

For a second set of experiments, each hexacopter was commanded to follow a circular flight path of radius $4m$. The full flight plan first commanded a climb, then commanded three complete turns with $4m$ turn radius and forward flight speed of $2.2m/s$. Each flight concluded with a short hover followed by an automatic descent to landing. This reference command sequence is shown in Figure 2.27. While tracking the circular trajectory shown in Figure 2.28, each hexacopter continually adjusted

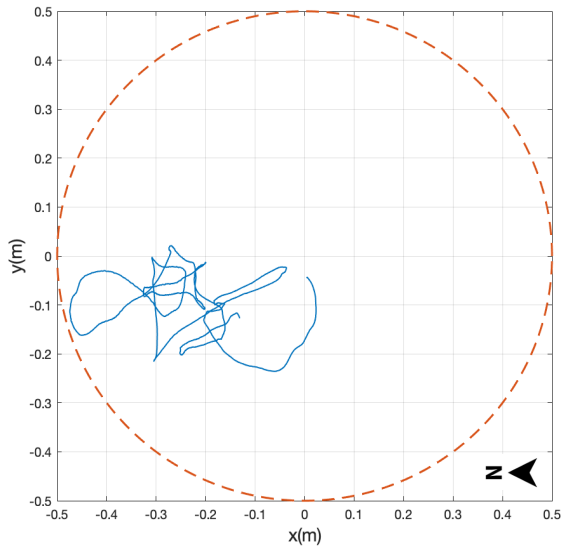

Figure 2.23: This plot illustrates position hold is within the max bound of $1m$ diameter circle.

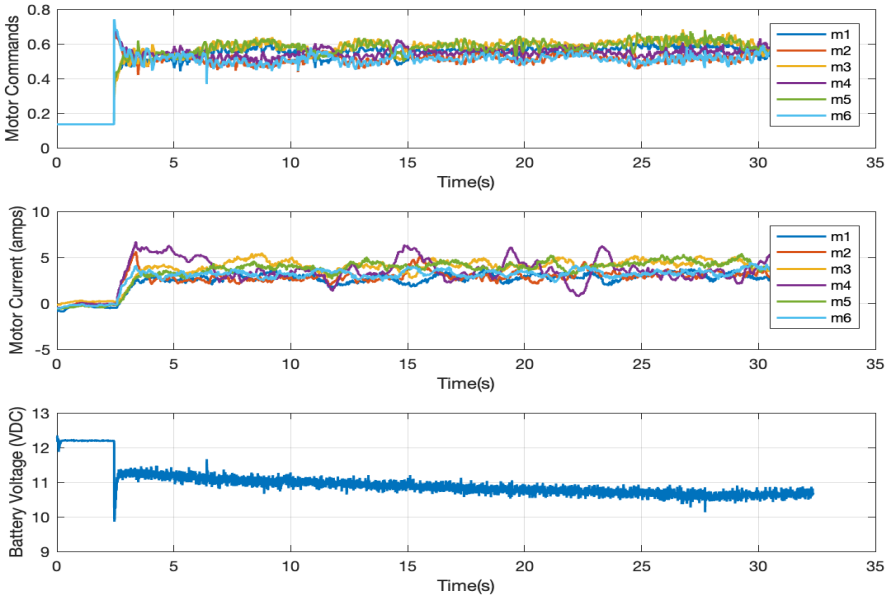

Figure 2.24: This plot provides details about the motor commands, current drawn and battery voltage of the hexacopter during one of the climb-hover-descent routine.

its heading angle to maintain the reference tangential velocity and turn radius as shown in Figure 2.29. During the experiments average winds of $1.1m/s$,187° relative to North were observed. Note that since only a proportional-derivative controller

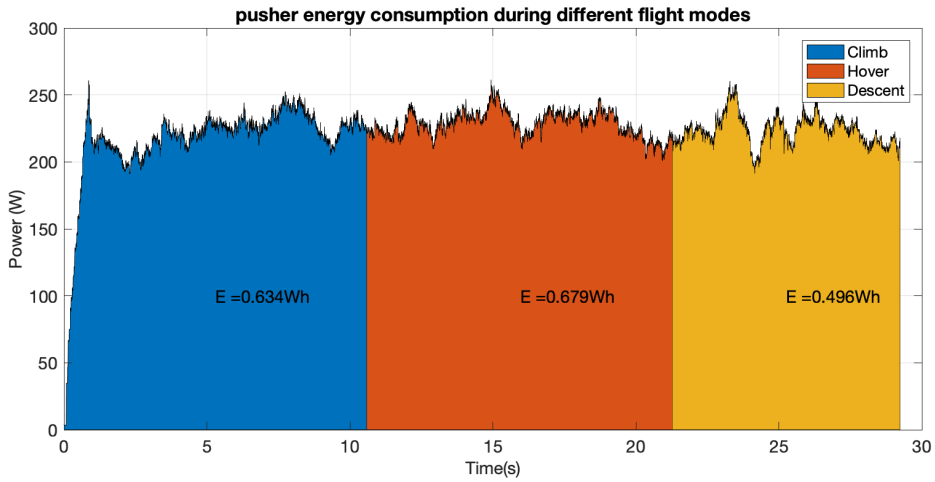

(a)

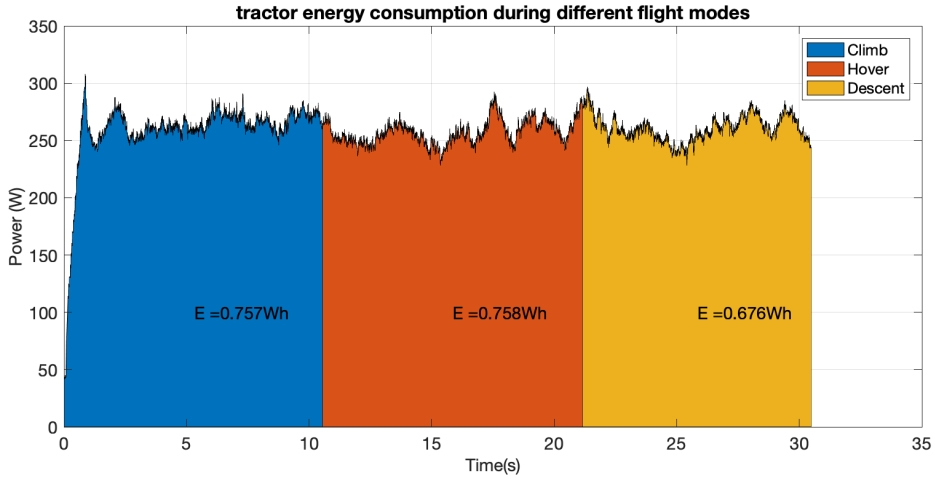

(b)

Figure 2.25: Plots illustrating power vs time and energy of the two hexacopters for different phases of flight climb-hover-descent (a) pusher hexacopter (b) tractor hexacopter.

was used, there is an uncorrected bias in the tracked position. The velocity of the hexacopters was estimated using a Linear Kalman Filter, which fused motion capture and onboard accelerometer data. Velocity magnitude (airspeed) is plotted in Figure 2.30. We acknowledge the trajectory tracking error is nontrivial. However, the focus of this paper is on hexacopter thruster performance and overall energy use. For performance comparison, the near-constant portion of the desired velocity profile was selected from multiple turns and flight sequences conducted for both hexacopters.

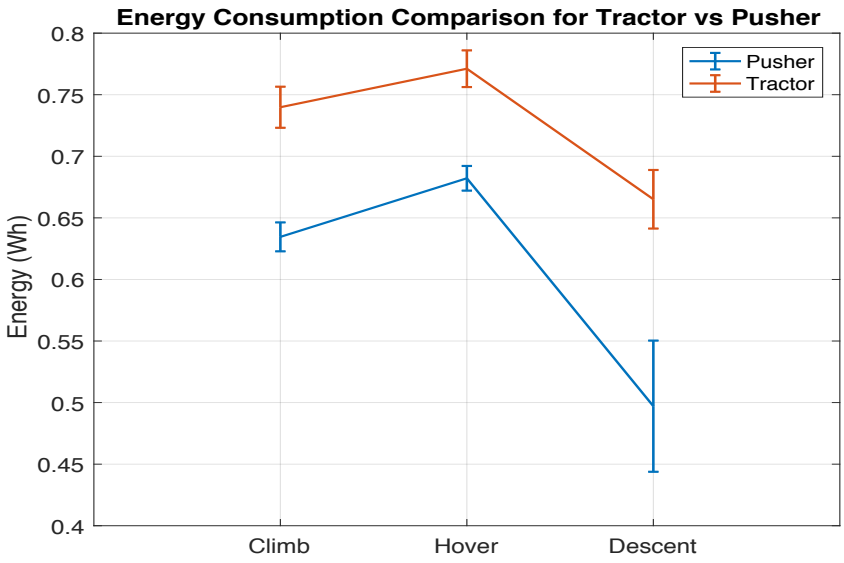

Figure 2.26: This plot provides a direct comparison of energy requirements by tractor and pusher configuration for the different phases of climb-hover-descent flight test.

Figure 2.27: Tractor hexacopter tracking a circular trajectory with tangential velocity $2.2m/s$.

Energy consumption data for the two hexacopters over the constant (flat) segments of each velocity profile are shown in Figure 2.31.

2.6 Discussion

2.6.1 Propulsion System model

In our experiments static (hover) thrust and torque coefficients based only on rotor speed were used to estimate thrust over all test conditions. Our simple model

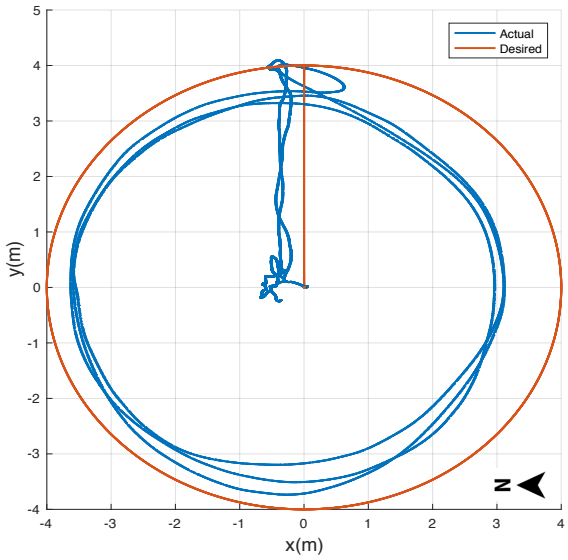

Figure 2.28: Actual and desired positions of the tractor hexacopter while tracking a circle with tangential velocity $2.2m/s$.

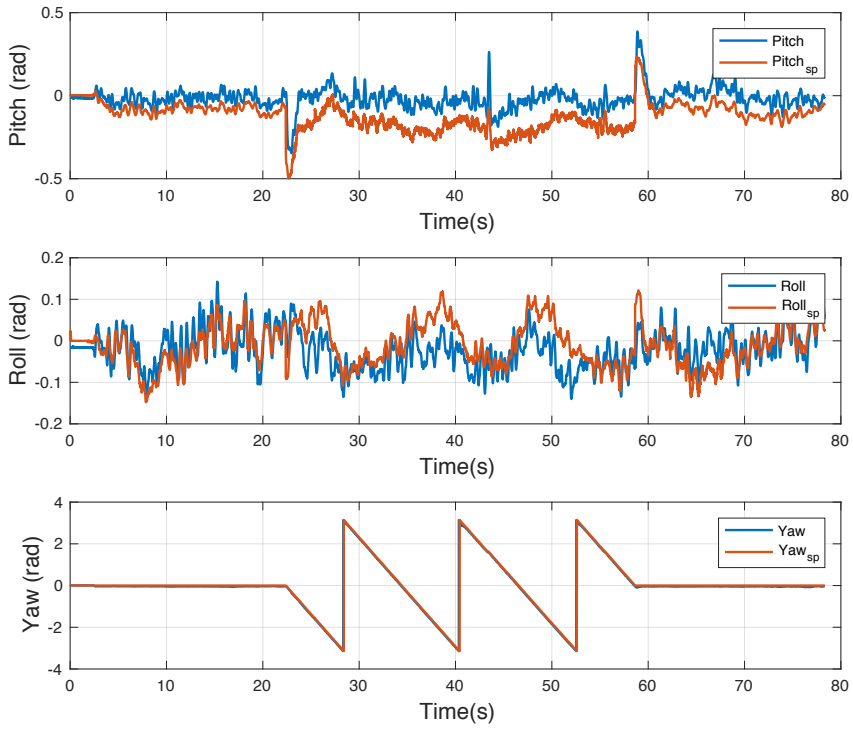

Figure 2.29: Actual and desired roll, pitch and yaw of the tractor hexacopter. Note that the heading angle is measured from $+\pi$ to $-\pi$ radians.

also assumed flow through the rotor is one dimensional, quasi-steady, incompressible, inviscid, and behaves as an ideal fluid. The radius of the plane perpendicular to

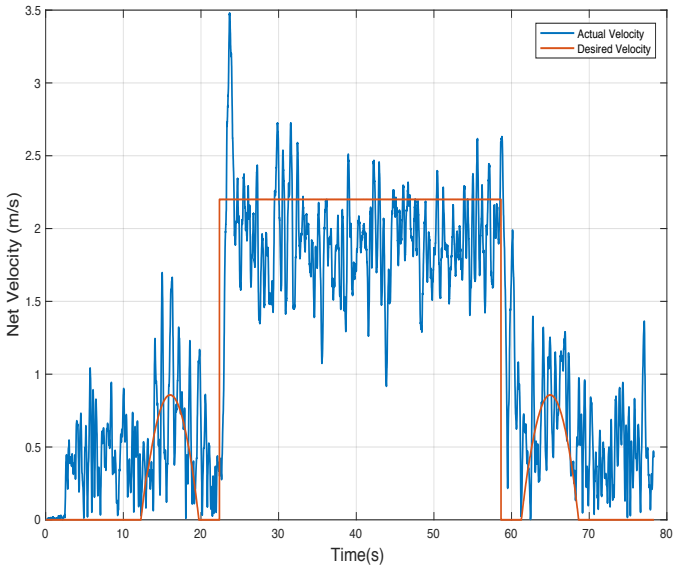

Figure 2.30: Actual and desired desired net velocity of the tractor hexacopter while traversing a circle.

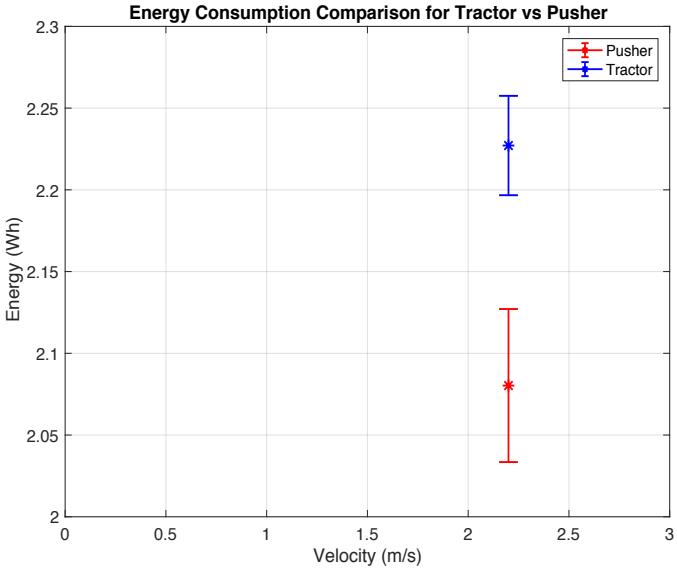

Figure 2.31: Tractor and pusher hexacopter energy requirements while traversing a circle with tangential velocity $2.2m/s$.

the control volume at the rotor disc is assumed equal to the rotor radius. These assumptions simplify our computations but can be relaxed in future work.

Table 2.2 shows that the average relative error in thrust estimates for appreciable throttle commands was approximately 5%. However, this error was as high as 20%

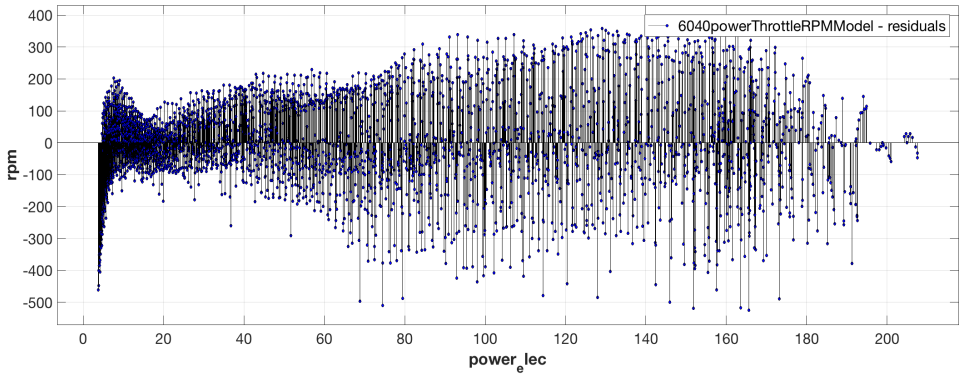

Figure 2.32: Residual plot for power vs rpm

for low throttle commands. This error is likely due to poor estimates motor rpm at low throttle commands and explains trends observed in residual plot Figure 2.32. As shown, there is a strong correlation (non-zero mean) in data errors at low power ($< 20W$) and low throttle ($< 1250\mu$s). Similarly, for high power ($> 180W$) and high throttle ($> 1850\mu$s) non-zero mean in data residuals is also observed. Methods to deal with this data correlation will be investigated in future work.

Note that another error source not modeled in this work is flow disturbance due to rotor-rotor interaction on the hexacopter that cannot be captured with a simple lumped parameter model for propulsion system.

2.6.2 Hexacopter Force and Energy Consumption Comparison

As observed in experimental results, in static conditions the pusher hexacopter generates 15% more thrust than the tractor hexacopter. In outdoor climb-hover-descent flight testing the tractor required 20% more energy than the pusher. This can be explained by the tractor hexacopter's downstream flow experiencing more obstruction from the mounting arm. Since the downstream flow in the pusher hexacopter is more free from obstruction, more thrust is generated.

Similarly, from analysis of forces in non-zero free stream flow conditions, it was observed that the pusher hexacopter generated higher thrust along with higher drag at

low speeds, thus having a lower lift to drag ratio compared to the tractor hexacopter. The lift to drag ratio was also compared for a given speed and different pitch angle as shown in Figure 2.21. For forward flight i.e. negative pitch angle, there is appreciable difference in lift to drag ratio for the two configurations. However this difference reduces with positive pitch angle or during braking. To understand the flow of air, vaporised diesel was circulated inside the wind tunnel for flow visualisation as shown in Figure 2.33. A clear contrast of the slipstream of the two motor configurations can be observed.

Figure 2.31 provides free flight energy data. At the relatively slow $2.2m/s$ flight speed, the tractor requires 7% more energy than the pusher. This figure also illustrates the reduction in tractor efficiency shown in the wind tunnel. Note that we have not been able to collect data at higher speeds in the constrained netted facility. Per wind tunnel results, we anticipate pusher drag increasing more quickly than tractor drag.

2.7 Case Study : Wind Sensing

Ref. [29] is a case study that compares the performance of puller and pusher multirotors inferring time-varying wind velocity fluctuations from vehicle motion in hovering flight. For this analysis, linear models approximating the closed-loop airframe dynamics of pusher and puller multirotors were characterized from system identification experiments.

The identified linear models were then used to synthesize a state observer for puller and pusher configurations. To validate wind estimation results based on vehicle motion, field experiments were performed in which the multirotors were stationed in hover above the ground at the center of a sensor array consisting of four sonic anemometers arranged in a tetrahedron configuration as shown in Figure 2.34. Results from validation experiments show that puller and pusher hexacopters have compa-

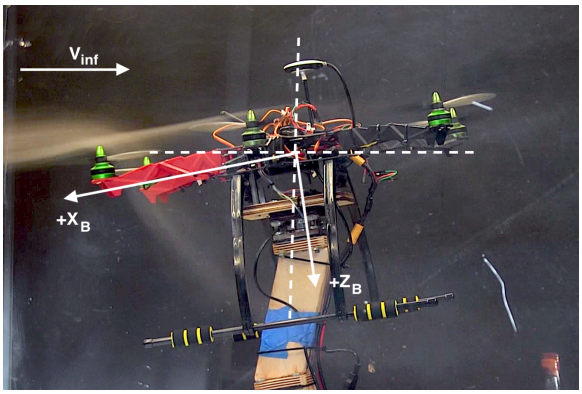

(a) -10 deg pitch, tractor configuration

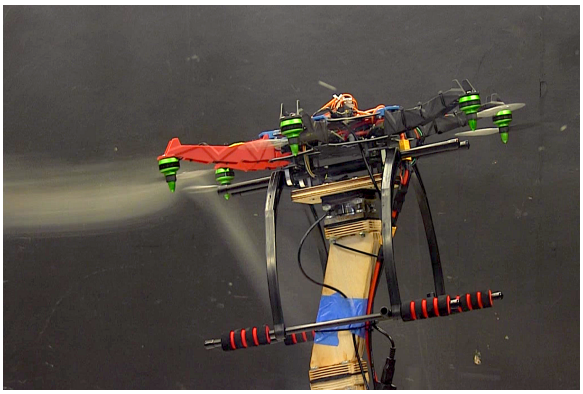

(b) -10 deg pitch, pusher configuration

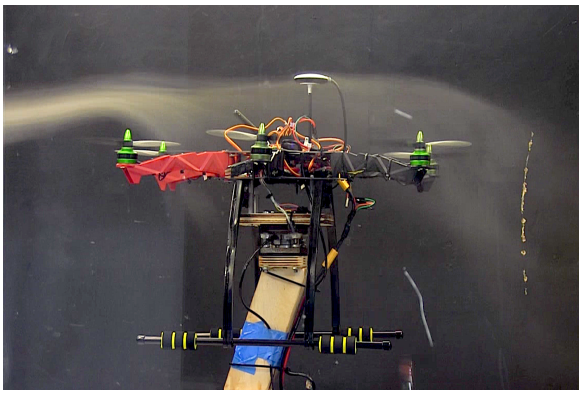

(c) 0 deg pitch, tractor configuration

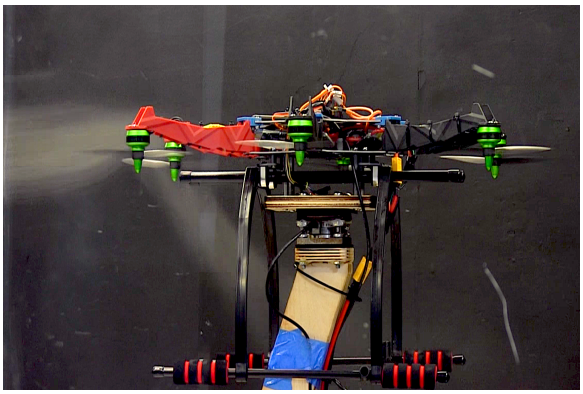

(d) 0 deg pitch, pusher configuration

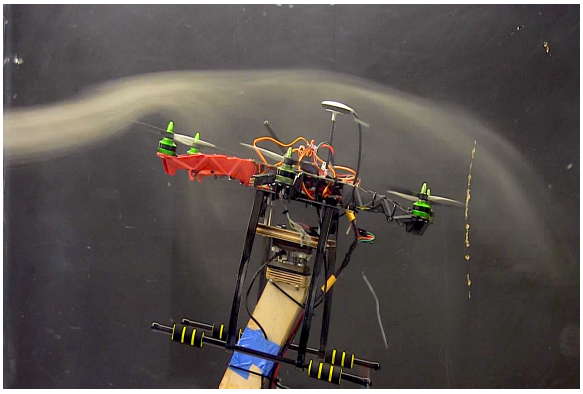

(e) 10 deg pitch, tractor configuration

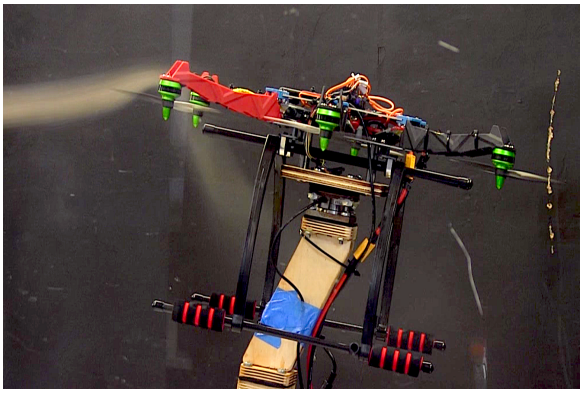

(f) 10 deg pitch, pusher configuration

Figure 2.33: Wind tunnel flow visualization for the tractor and pusher hexacopter configurations

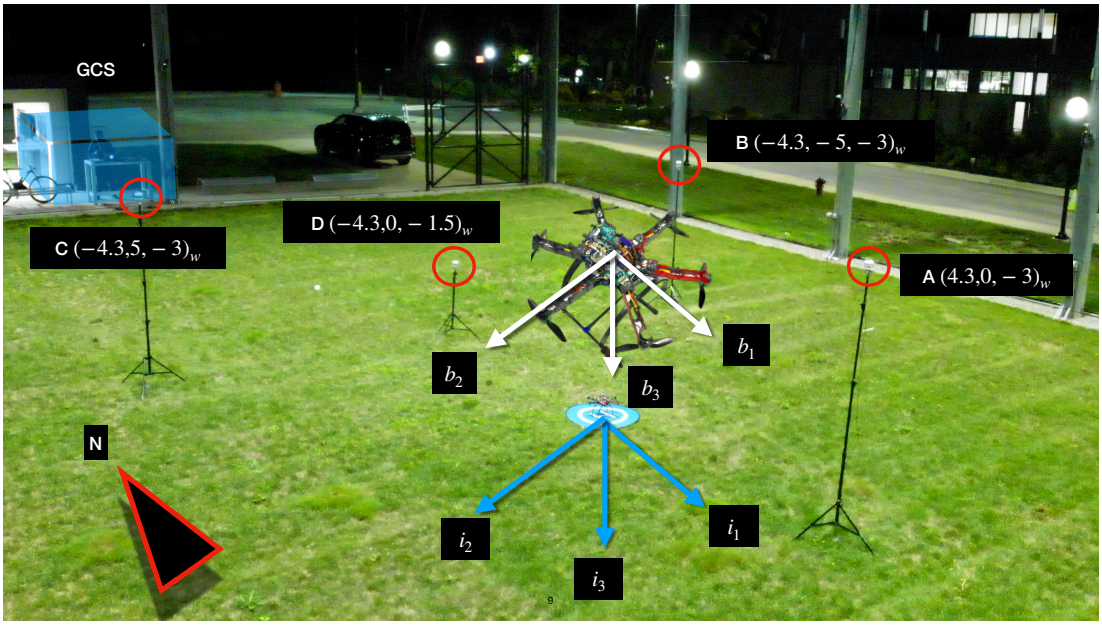

Figure 2.34: Placement of wind sensors and hexacopter hover position for outdoor wind sensing experiments. All coordinates are in meters with respect to the inertial (ground) frame shown in blue.

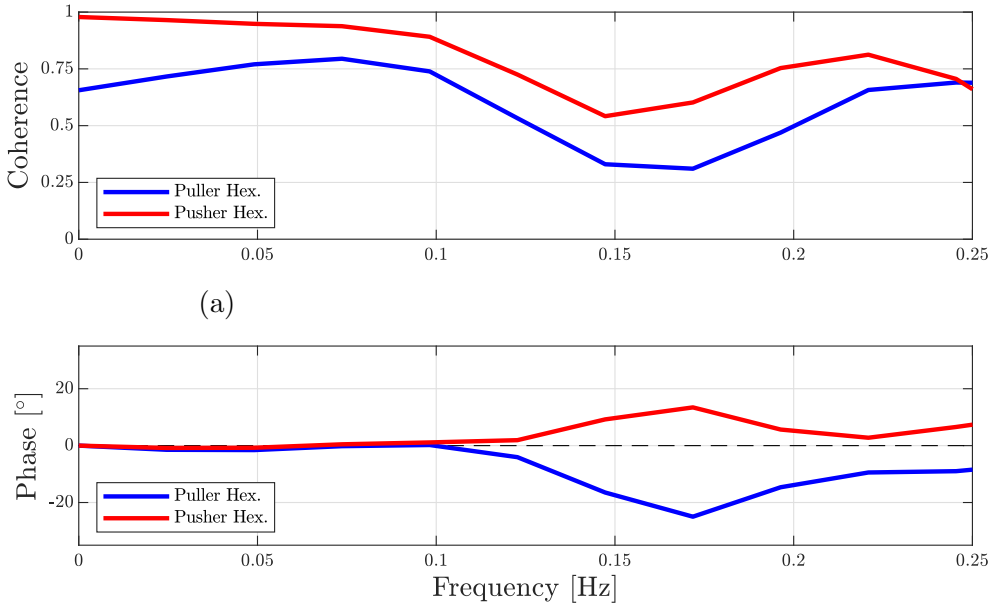

Figure 2.35: Coherence and phase lag estimates of tractor and pusher hexacopter wind estimates.

rable performance measuring wind velocity, but the pusher hexacopter platform was found to resolve time-varying wind fluctuations more accurately based on frequency-

domain analysis of coherence and phase lag as inferred from Figure 2.35. The ease with which model-based estimation can be implemented for puller and pusher aircraft's, further support the use of multirotors to infer wind velocity variations in the lower atmosphere.

2.8 Summary and Future Work

This chapter has developed an experimental model of a multicopter propulsion unit with different propellers as well as pusher and puller configurations. We used this model to estimate thrust generated for pusher and tractor hexacopter designs. Based on measured thrust values, we determined that in static conditions the pusher hexacopter has a higher lift to weight ratio. However, in forward flight conditions this higher lift to weight ratio is traded against a lower lift to drag ratio for the pusher design as seen from wind tunnel experiments. The drag introduced by the load cell stand could be nontrivial though the load cell was mounted near the hexacopter body. The drag data from the wind tunnel experiments for various pitch angles and wind velocity is stored in a look up table. This drag look up table is used for simulations in the following chapters.

Autonomous climb-hover-descent and steady circular flight tests were also conducted to provide a comparison to wind tunnel experiments. A clear design trade-off was seen in wind tunnel test results with confirmation of trends during flight tests. A pusher design is more efficient for hovering and slow flight missions such as local-area surveillance and inspection, while a tractor design is more efficient for missions requiring appreciable transit such as package delivery.

Results from an outdoor wind measurement case study were also presented. The case study demonstrated the pusher hexacopter configuration offers higher sensitivity to wind fluctuations than the puller hexacopter. Hence, the pusher configuration is preferred in applications that require higher sensitivity to wind fluctuations.

For future work, dynamic thrust and torque models might be improved with wind tunnel based dynamometer experiments. More propulsion data will enable better curve fits to estimate motor RPM and power use at very low and high throttle settings. Trajectory tracking experiments with a state-space controller at higher forward flight speeds would further enhance comparisons with wind tunnel results. Results and conclusions presented in this chapter related to the performance tractor and pusher hexacopter are solely based on experimental analysis. An investigation into the theoretical underpinnings of these results could help generalize them to different multicopters with pusher/tractor configurations.

CHAPTER III

Model Based Prognosis of UAS Components

3.1 Introduction

Batteries and propulsion system modules are identified as safety-critical UAS components with the highest likelihood of failure. Prognostics methods provide tools for predicting failure scenarios and sending key health updates to ensure a UAS can safely reach its destination. This thesis focuses on model-based prognostics methods that utilize either standard physics-derived models or fault propagation models to predict failure conditions. As UAS battery is a component of interest and Lithium-polymer batteries are a common choice, a model for standard lithium-polymer (Lipo) multicopter batteries is derived experimentally. A novel low-cost test bed was developed to collect the experimental data for battery model parameter identification. Also, as the propulsion system is the second UAS component of interest for prognosis, various fault modes of BLDC motors are studied, and a technique used for motor fault prognosis is discussed.

This chapter starts with the literature review of existing prognosis methods, presented in Section 3.2. A description of battery model, its parameter identification technique, data collection test-bed description, various battery degradation conditions and EOD calculation are discussed in Section 3.3. The motor fault prognosis model is described in Section 3.4. Finally, we present a summary and future work in

Section 3.5.

3.2 Literature Review

Prognosis algorithms are critical for UAS safety assurance. In [38], the author presents a methodology for health management in an electric UAS. The probability of subsystems failure is quantified by combining failure mode, effects, and critical analysis using a qualitative Bayesian approach. A distributed diagnosis algorithm detects and diagnoses a failed power train subsystem and instantiates a prognoser to determine remaining useful life (RUL) of the faulty system. A model-based prognosis algorithm is proposed in [58] to determine remaining flight time for an electric UAS. The authors use an Extended Kalman Filter (EKF) to estimate lithium polymer battery state of charge (State of Charge (SOC)). A polynomial function is used to estimate SOC until the low voltage threshold is reached to determine flight endurance, assuming no sudden variation in SOC. In [25], the authors use an Unscented Kalman Filter (UKF) to determine battery SOC. Assuming the remaining flight plan was known, the UKF was used to simulate the flight plan energy demand into the future until an critical SOC threshold was reached. These approaches have applied model-based methods for prognostics. In [47] the authors use a data-driven strategy to determine RUL and predict battery end of discharge (EOD) time dynamically. Machine learning algorithms such as Gradient Boost Trees (GBT), Bayesian Neural Network and Non-Homogeneous Hidden Semi Markov Model (NHHSMM) have been proposed. Ref. [47] recommends NHHSMM and GBT over Bayesian Neural Networks due to potential model constraint violations and difficulty closing the distance between upper and lower RUL estimate bounds with the neural network approach.

3.3 Battery Prognosis

3.3.1 Enhanced Self-Correcting Battery Model

The Lipo battery can be modelled as a voltage source (Open Circuit Voltage) that has a resistance and one or more sub-circuits of resistance and capacitor in parallel with hysteresis as shown in Figure 3.1. This model is referred to as the Enhanced Self-Correcting System (Enhanced Self Correcting Battery Model (ECS)) Model.

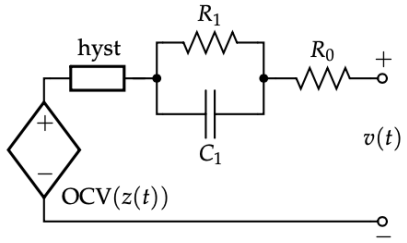

Figure 3.1: ECS model of a Lipo Battery.

The discrete state space ECS model formulation [51] using multiple parallel resistor-capacitor pair current can be written as:

$$i_r[k+1] = \underbrace{\begin{bmatrix} F_1 & 0 & \cdots \\ 0 & F_2 & \\ \vdots & & \ddots \end{bmatrix}}_{A_{RC}} i_r[k] + \underbrace{\begin{bmatrix} (1-F_1) \\ (1-F_2) \\ \vdots \end{bmatrix}}_{B_{RC}} i[k] \tag{3.1}$$

where i_r is the current through the sub-circuit of the parallel resistor-capacitor and $F_j = exp(\frac{-\Delta t}{R_j C_j})$. Let $A_H[k] = exp(-|\frac{\eta[k] i[k] \gamma \Delta t}{Q}|)$. The state-space equation for the ECS model is given by:

$$\begin{bmatrix} z[k+1] \\ i_r[k+1] \\ h[k+1] \end{bmatrix} = \begin{bmatrix} 1 & 0 & 0 \\ 0 & A_{RC} & 0 \\ 0 & 0 & A_H[k] \end{bmatrix} \begin{bmatrix} z[k] \\ i_r[k] \\ h[k] \end{bmatrix} + \begin{bmatrix} \frac{-\eta[k]\Delta t}{Q} & 0 \\ B_{RC} & 0 \\ 0 & (A_H[k]-1) \end{bmatrix} \begin{bmatrix} i[k] \\ sgn(i[k]) \end{bmatrix} \tag{3.2}$$

where η = charge efficiency, $i[k]$ = current through the circuit, γ = a positive constant, Q = total charge capacity (ampere-secs),$z[k]$ = State of Charge (SOC), and $h[k]$ = dynamic hysteresis. The battery voltage output equation is given by:

$$v[k] = OCV(z[k]) + M_0 s[k] + Mh[k] + \sum_j R_j i_{R_j}[k] - R_0 i[k] \tag{3.3}$$

where, $OCV(z[k])$ = Open Circuit Voltage as function of time, M, M_0 = Constants, $s[k]$ =Instantaneous hysteresis.

3.3.1.1 Battery Model Parameter Identification

To use the ECS model defined by equations (3.1), (3.2) and (3.3) parameters including the Open Circuit Voltage (OCV) vs SOC relation, γ, η, Q,R_j,R_0 must be identified. The experimental setup to determine these parameters is described in this section. For all experiments, a 3s standard UAS Lipo battery was used.

The Lipo battery parameter identification experimental setup is shown in Figure 3.2. An Arduino UNO was used for data collection. Each of the cell voltages was measured by 16-bit ADC converters [1] connected to analog optoisolators [2]. A load of 4Ω was attached across the battery terminal to draw a maximum current of $3Amp$ (1C).

[1] https://www.adafruit.com/product/1085
[2] https://www.digikey.com/en/products/detail/dfrobot/DFR0504/7682221

Output current was sensed with a low-cost current sensor [3] during the discharged cycle. A relay was also added in series with the resistance to turn the resistive load on and off. For the battery charge cycle, a standard Lipo charger, a Venom Pro Duo 80W [4] battery balance-charger product, was used.

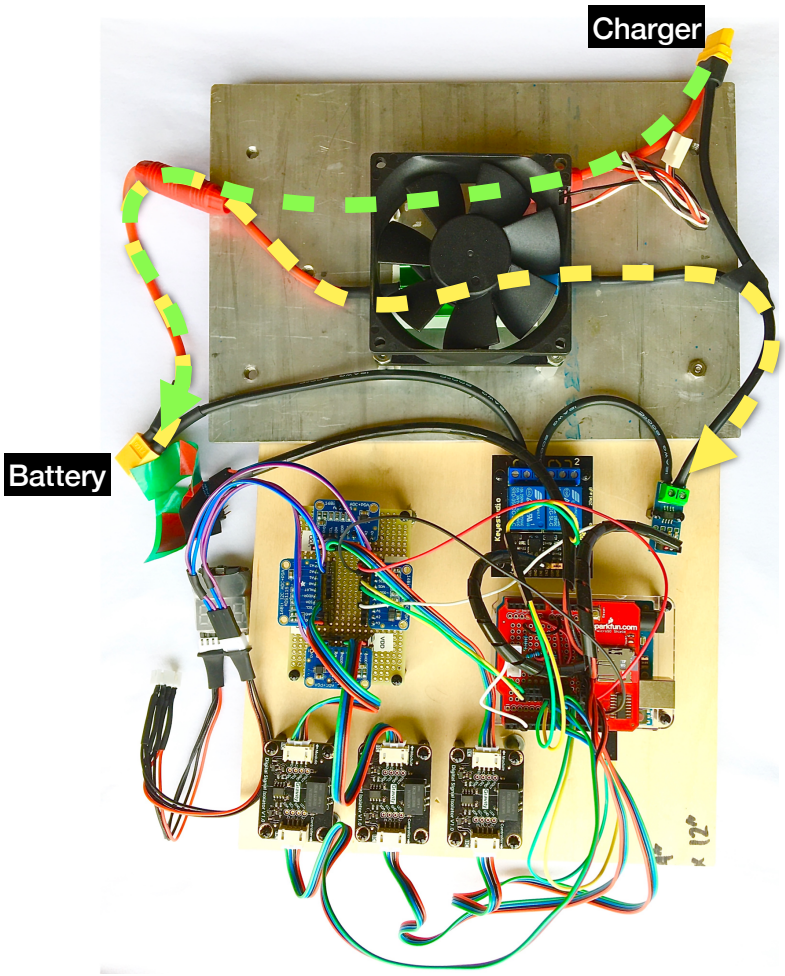

Figure 3.2: Experimental setup to measure voltage and current during charge/discharges cycle of a 3S Lipo battery.

For this experiment, voltage and current measurements over the full charge and discharge cycles of the Lipo battery were collected over time. The battery was discharged to 3.3VDC per cell per the manufacturer's recommendation and charged using

[3] https://www.sparkfun.com/datasheets/BreakoutBoards/0712.pdf

[4] https://www.venompower.com/venom-pro-duo-80w-x2-dual-ac-dc-7a-lipo-lihv-nimh-rc-battery-balance-charger-0685

the Venom balance-charger. A sample time history of collected data is shown in Figure 3.3. Because the low-cost battery cells have some manufacturing variability, not

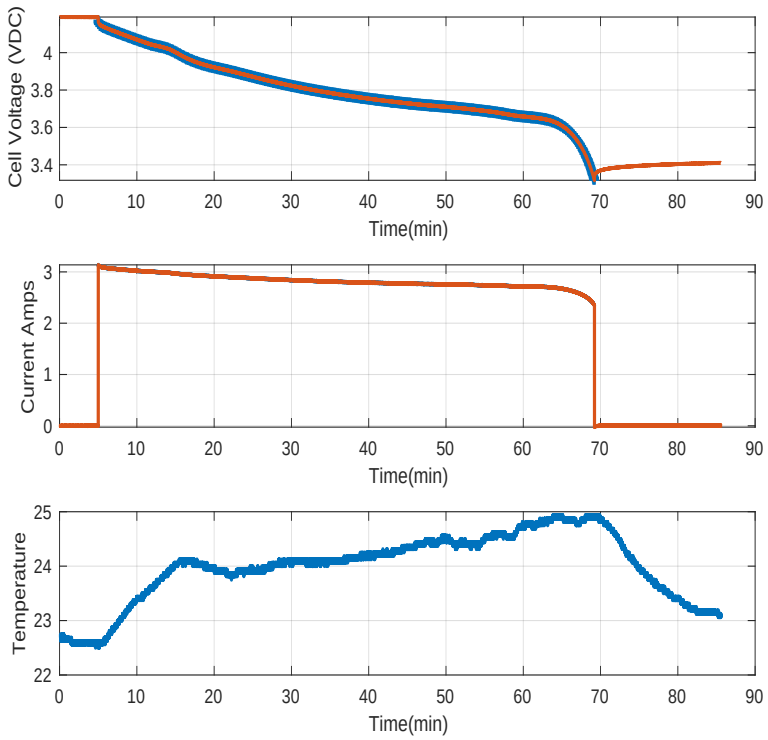

Figure 3.3: Time series plot of single cell battery voltage, current and surface temperature($^{\circ}C$) sensed during a 1C discharge of a 3s battery pack. The blue highlighted segment in the first two plots is used for further analysis.

all cells reached the set critical voltage limit at the same time; the cells typically differ by a few mV. Data was collected at a single room temperature with battery surface temperature variation $\pm 2^{\circ}C$. The setup can be placed in a temperature-controlled environment to obtain a relationship between parameters and temperature, but this was beyond the scope of our experiments. Our simple setup does not replace manufacturer battery testing systems but does provide an economical option for battery parameter identification and model validation.

The detailed procedure we applied for parameter identification can be found in [51]. The relation between SOC and charge/discharge voltage for each of the cells can be identified, as shown in Figure 3.4. After obtaining the charge/discharge relation

to SOC we can obtain the OCV relation to SOC. Similar to the approach taken in [62], OCV was obtained by taking an average of the charge and discharge curve.

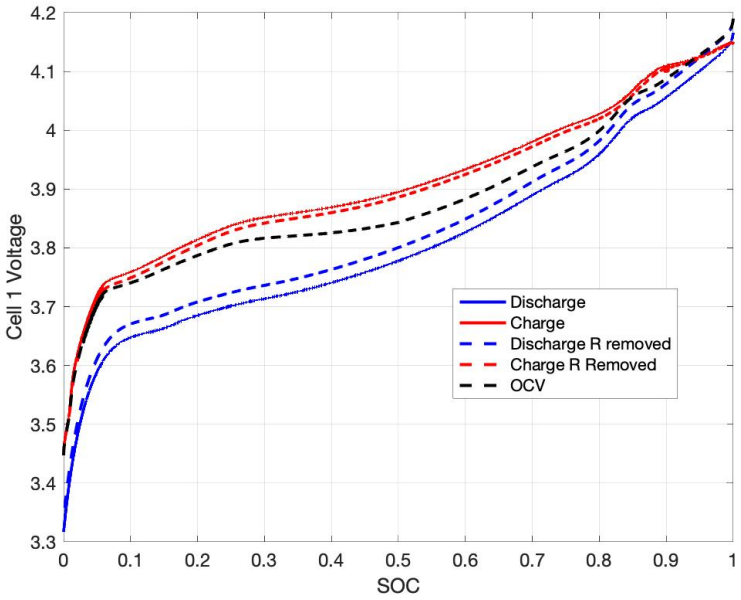

Figure 3.4: Battery voltage variation with State of Charge (SOC) during the charge/discharge cycle for a single cell.

The identified parameters are tabulated in Table 3.1. Additional data was collected to validate the identified model. Battery cell response to a pulsed discharge is shown in Figure 3.5. Error was observed on the order of mV, which we deemed acceptable for our simulations.

For simulations the current draw through each branch of the parallel battery pack is shown in Figure 4.1 and is determined by the following equations:

$$V_k = \frac{\sum_{j=1}^{N_P} \frac{V_{OCV,k}^j}{R_0^j} - i_k}{\sum_{j=1}^{N_P} \frac{1}{R_0^j}} \tag{3.4}$$

$$i_k^j = \frac{V_{OCV,k}^j - V_k}{R_0^j} \tag{3.5}$$

$$V_{OCV,k}^j = V_{OCV,k}^{j,1} + V_{OCV,k}^{j,2} + V_{OCV,k}^{j,3} \tag{3.6}$$

$$R_0^j = R_0^{j,1} + R_0^{j,2} + R_0^{j,3} \tag{3.7}$$

Table 3.1: Identified parameters for a 3s Lipo battery.

Parameter	$\boldsymbol{Cell_1}$	$\boldsymbol{Cell_2}$	$\boldsymbol{Cell_3}$
$R_0\ (m\Omega)$	6	5.5	5.5
$R_1\ (m\Omega)$	9.9	8.8	8.7
$C_1\ (kF)$	51.5	52.5	60.5
$Q\ (Ah)$	3.0271	3.0271	3.0271
γ	300	200	300
$M(10^{-3})$	17.8	31.2	18.4
$M_0(10^{-3})$	5.1	5.3	5.2
η_{Charge}	0.973	0.973	0.973
$\eta_{Discharge}$	1	1	1

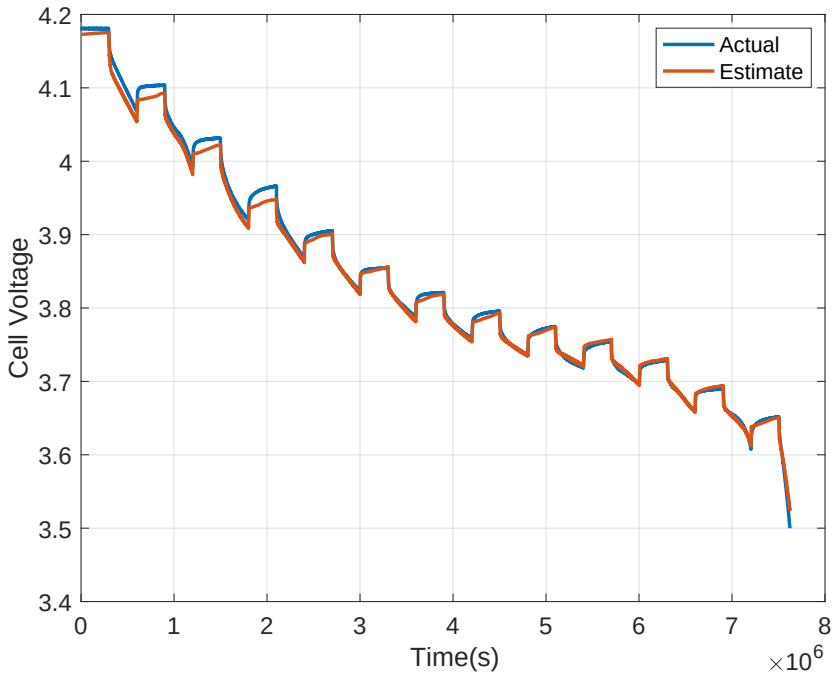

Figure 3.5: Time series plot comparing model estimate and actual cell voltage during pulsed discharge.

where V_k = bus voltage, N_p = number of cells in parallel, and j = branch.

3.3.1.2 Battery Degradation Model

Degradation effects on Lipo battery parameters experiencing different aging mechanisms in lithium-ion cathode material are described in [74]. Battery aging results in

power fade, capacity fade, and other degradation effects. Temperature effects on parameters in the ECS cell model are presented in [52] and are manifested as increased internal resistance. Service limits for UAS batteries are defined in [7] as a pack that has lost 20% of its rated capacity. Battery degradation models aim to determine which parameters and range of values to vary during simulation to estimate degraded battery performance. Degraded battery parameters are provided in Table 3.2. This list of parameters is not exhaustive but provides a useful baseline. Our simulations assume degradation/fault information will be available for our MDP since existing Battery Management Systems can flag faults [73].

Table 3.2: Battery degraded health parameter values.

Type	**Description**
Capacity Fade	$0.8 \times Q$
Power Fade	$2 \times R_0$
Temperature effect	$R_{0L} : 1.5 \times R_0$,if $T < 50F$

3.3.2 Motor Current Draw Model

This section described the model used to determine the current draw from UAS brushless DC motors (BLDC). Given our hexacopter case studies, rotors are numbered from 1-6 and are located at a distance L from the UAS center of gravity. A hexacopter's total motor thrust magnitude T and torque magnitude τ_i about each body axis are related to six motor speeds as described by the following equations [54]:

$$\begin{pmatrix} \omega_1^2 \\ \omega_2^2 \\ \omega_3^2 \\ \omega_4^2 \\ \omega_5^2 \\ \omega_6^2 \end{pmatrix} = \begin{pmatrix} C_T & C_T & C_T & C_T & C_T & C_T \\ \frac{LC_T}{2} & \frac{-LC_T}{2} & -LC_T & \frac{-LC_T}{2} & \frac{LC_T}{2} & LC_T \\ \frac{-\sqrt{3}lC_T}{2} & \frac{-\sqrt{3}lC_T}{2} & 0 & \frac{\sqrt{3}LC_T}{2} & \frac{\sqrt{3}lC_T}{2} & 0 \\ C_Q & -C_Q & C_Q & -C_Q & C_Q & -C_Q \end{pmatrix}^{\dagger} \begin{pmatrix} T \\ \tau_x \\ \tau_y \\ \tau_z \end{pmatrix}$$

where ω_i = motor angular speed, L = arm length (m), C_T = thrust coefficient, C_Q = torque coefficient, $\dagger$ = pseudoinverse. A dynamometer[5] was used to collect data for full throttle cycle of a BLDC reference motor. Least-squares curve fitting was performed to determine the current drawn by a motor for a given angular speed in our hexacopter experiments. Figure 3.6 shows the curve fit equation.

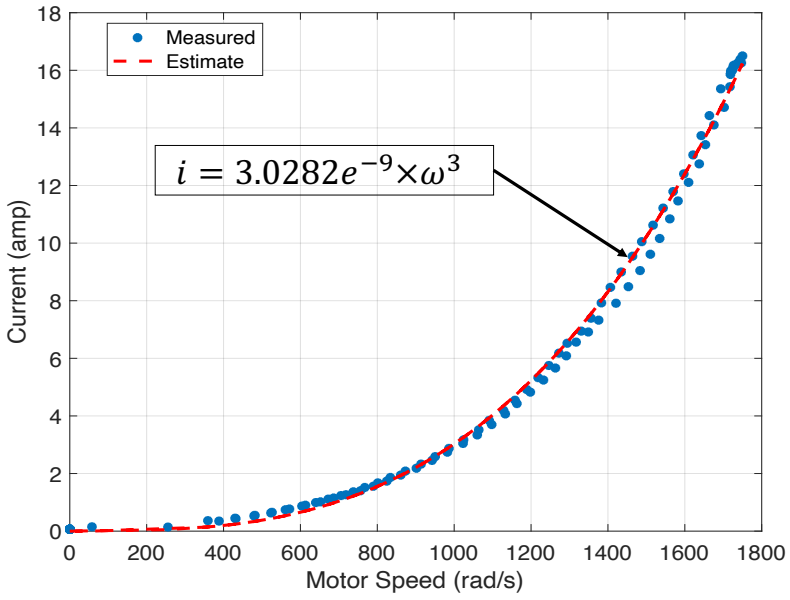

Figure 3.6: Motor current as a function of motor speed.

[5]https://www.rcbenchmark.com/pages/series-1580-thrust-stand-dynamometer

3.3.2.1 End Of Discharge Calculation

EOD of a cell is calculated using the ESC model of battery, which is propagated until it reaches the threshold voltage of $3.3VDC$ with a constant current input. Then the EOD of battery pack is determined as the minimum cell EOD in the pack.

3.4 Motor Prognosis

BLDC motors on UAS undergo a broad spectrum of operating conditions with variations in temperature, vibrations, dynamic loading, etc. As a result faults in BLDC motors can occur in rotor/field, stator/armature, inverter, or mechanical components connected to it [17]. The faults can be broadly classified as the following:

- Armature Faults
- Permanent Magnetic Faults
- Mechanical Faults

Among all the types of faults, bearing-related failure is one of the top contributing factors. Bearings are a critical component of a BLDC motor as bearing failure renders the motor inoperative. There exist various failure modes of bearings [6] and techniques to detect these faults [61], [78],[81]. Once the fault is detected, its prognosis can provide valuable information about the Remaining Useful Life(RUL) of the bearing, which also motor RUL.

In this research we have chosen to investigate the prognosis of a spalling fault: surface or sub-surface fatigue causing fractures in the running surfaces. If unchecked, the growth of a spalling fault can eventually lead to motor jamming. This fault was selected as spalling of the races and rolling elements is the most common cause of

[6] https://www.iso.org/standard/59619.html

bearing failures [56]. It is assumed there exists a capability to detect the incipient fault in the following section.

3.4.1 Remaining Useful Life

The spalling fault when detected the RUL of motor is calculated based on method presented in [80]. Briefly the spall growth is performed by utilizing the Paris Law and is described by the following equation:

$$\begin{aligned} D(t+\Delta t) &= D(t) + \Delta C_D (D(t))^n \\ C_D &= C_D + \omega_{C_D} \\ n &= n + \omega_n \end{aligned} \tag{3.8}$$

where D = defect area, C_D, n = are model parameters and based on operating conditions, ω_{C_D}, ω_n =zero mean random noise.

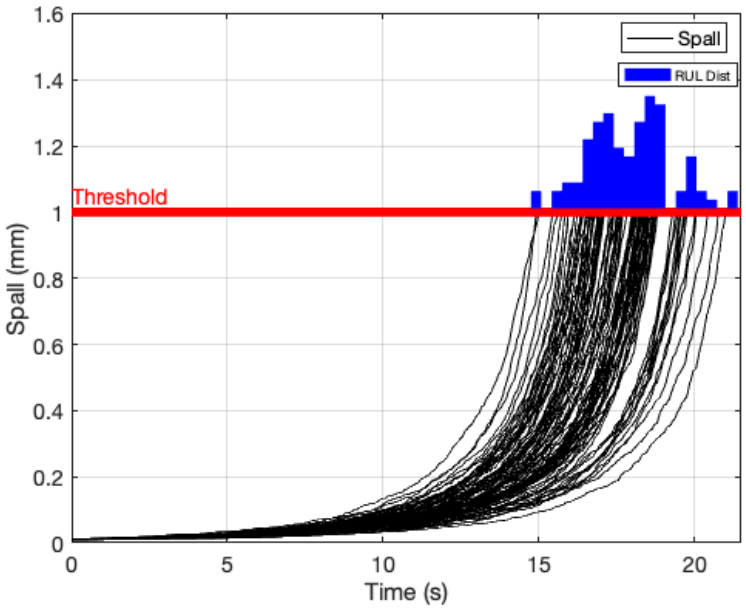

Figure 3.7: Spall propagation

In [80] , C_D, n are parameters determined by online adaption. This thesis always assumes the initial defect area as $0.01mm^2$. The parameters C_D, n are assigned initial

values as recommended in [80] and are $C_D = 0.2, n = 1$. Then the RUL is predicted by propagating 100 particles following 3.8 until a threshold of $1mm^2$ defect area is reached as shown in Figure 3.7. Mean RUL value is then computed. The parameter values and initial spall size is selected so that propagation of the particles in the simulation is tractable on parallel loops. For implementation on an actual system the initial fault size and computation time would be based on the results of the incipient fault detected.

3.5 Summary and Future Work

This chapter describes experimentally determined UAS battery and motor models to be used in subsequent health and contingency management simulations for hexacopter flight. The identified battery model is for single ambient temperature only. However, since the LiPo battery chemistry changes with change ambient temperature values, their resulting performance is also different. Hence, models of battery at different operating temperature can be determined using the same method.

In the following chapters we discuss integration of these validated models in the high-fidelity simulator used for evaluating the autonomous decision-making for component reconfiguration and safe contingency planning/management.

CHAPTER IV

Component Reconfiguration

4.1 Introduction

Battery failures often cause UAS failure. Ref. [40] recommends battery failures be mitigated by employing batteries in parallel. However, series-parallel battery pack capacity fade and high impedance typically cause imbalance resulting in permanent battery pack degradation [44]. This chapter described the development of a novel battery reconfiguration Markov Decision Process (MDP) for a series-parallel battery pack shown in Figure 4.1. The novelty of the proposed method is the utilization of multiple health and system indicators for optimal battery switching. Existing battery reconfiguration techniques only utilize EOD values.

The battery reconfiguration MDP architecture is shown in Figure 4.2. The MDP framework based reconfiguration concept was first proposed in the context of a mission planning hierarchical MDP (hMDP) in [55]. As shown in the Figure 4.2, the battery reconfiguration MDP has inputs as remaining flight time, expected motor current draw, State of Health (SOH), each battery's EOD values and outputs an optimal battery switching action. Accurate models of battery cell and pack charge and discharge dynamics, mission execution including expected motor current draw and remaining flight time, and battery health must be developed. The MDP action and state-space must be decomposed to the extent possible to minimize computational

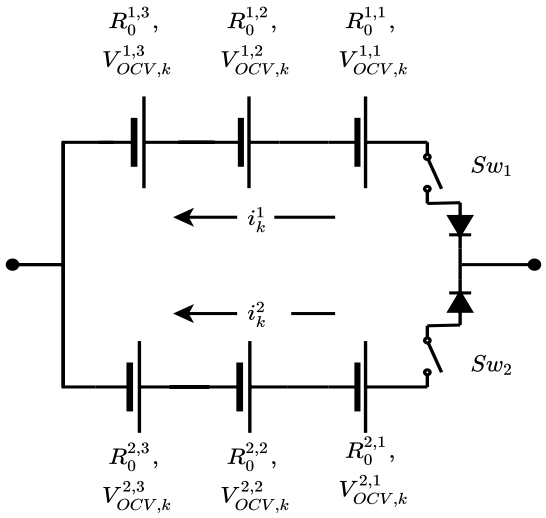

Figure 4.1: The UAS series-parallel battery pack system.

overhead and facilitate explainability. Rewards must reflect user and mission preferences, and state transition probabilities must be obtained from realistic Monte Carlo simulations.

Also, as in this thesis, UAS motor failures are considered. A novel for motor reconfiguration is presented. This method reconfigures the hexacopter to a quadcopter configuration to prevent instability in the system due to motor failure. Further, analysis is carried out to determine the roll and pitch authority of the hexacopter after motor reconfiguration.

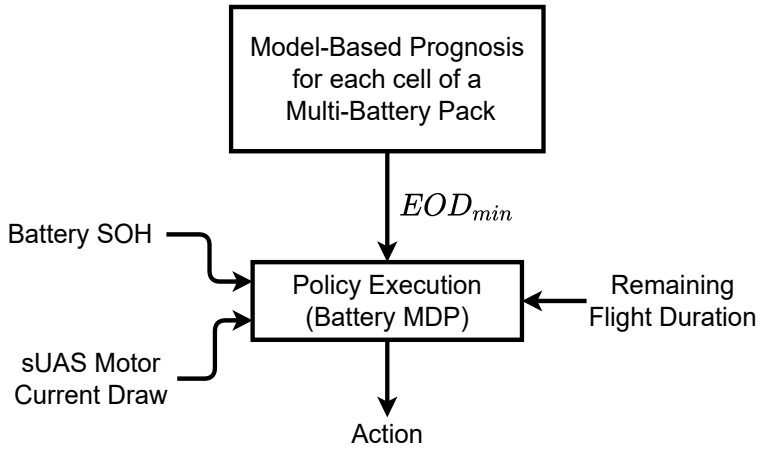

Figure 4.2: Battery reconfiguration MDP inputs.

This chapter is organized as follows. A literature review of existing methods is presented in Section 4.2. The description of battery reconfiguration MDP and its evaluation is presented in Section 4.3. Section 4.4 provides details of the proposed motor reconfiguration scheme and roll and pitch authority analysis. Finally, the summary and future work are presented in 4.5.

4.2 Literature Review

Ref. [53] utilizes prognostics outputs in battery reconfiguration using a constraint satisfaction algorithm. A survey of battery reconfiguration techniques is presented in [15]. In [33], the authors present a novel method for in-flight battery swap. A primary battery is consistently carried onboard a long-endurance host drone, and a smaller drone carrying a secondary battery sporadically attaches to the primary or host drone. Once docked, the host drone switches from primary to secondary battery, and once the secondary battery depletes, the smaller "recharging" drone undocks from the host drone.

In [32] the authors proposes an algorithm to optimally charge electric vehicles. Hidden Markov Models (HMMs) are obtained from fitting data collected from stochastic usage patterns for a single vehicle. Dynamic programming is used to determine optimal charge policies. There is no mention of battery health in this work. Life-cycle assessment for Lipo batteries using a Markov Decision Process (MDP) is proposed in [66]. Optimal policies obtained from solving the MDP act as a condition-based decision-maker to either recycle, inspect, or reuse a battery.

Our proposed method's innovations relative to state-of-the-art are in the specification and evaluation of a prognostics-informed MDP for battery management in multi-battery UAS.

4.3 Battery Pack Reconfiguration

4.3.1 Battery MDP Model Formulation

Battery reconfiguration is modelled as a stationary infinite-horizon Markov Decision Process (MDP) [45] with the assumption that the system is fully observable. An MDP is defined by tuple $\langle T, S, A_s, p(.|s,a), r(s,a)\rangle$, where T is decision epoch, S is the finite set of system states, A_s is allowable actions for states $s \in S$, $p(.|s,a)$ is state transition probability tensor and $r(s,a)$ is the reward for executing action $a \in A_s$ in state $s \in S$. The MDP computes actions that maximize expected value for each state based on the Bellman equation. Classic algorithms such as Value Iteration or Policy Iteration can be used to determine optimal MDP policy $\pi^\star$.

Table 4.1: Battery MDP state definition.

States,i=$\{1,2\}$	**Criteria**
B_iS_1	EOD > RFD $+t_{sf}$
B_iS_2	RFD > EOD > RFD$+t_{sf}$
B_iS_3	EOD < RFD
B_iC_0	Cell Voltage $\geq$ Critical Voltage Value(3.4VDC)
B_iC_1	Cell Voltage < Critical Voltage Value
B_iSw	Battery Switch Position ie. ON or OFF
$I_{(H,L)}$, Total Motor Current Draw	$I_H : I > 0.2I_{max}$, $I_L : I < 0.2I_{max}$
Terminal State	
$FAILURE$	when Cell voltage $\leq$ 3.3VDC and is unusable

where, EOD = End of Discharge (time), RFD = Remaining Flight Duration (time), t_{sf} = Safety Margin (time), $I_{max} = 105$ amps, I = motor current draw.

4.3.1.1 MDP State Definition

Battery MDP states describing cell voltage, mission success status, and battery switch positions are defined per Table 4.1 as state vector with the complete set of indices in the subscripts $S = [I_{H,L}, B_1Sw,\ B_1S_{1,2,3},\ B_1C_{0,1},\ B_2Sw, B_2S_{1,2,3},\ B_2C_{0,1}]$ and a singleton $FAILURE$ state. $B_iS_{1,2,3}$ is dependent on an inequality relation of

EOD and RFD. When the battery is in $B_iS_{1,2}$ there is sufficient energy to complete the mission. However, when the battery reaches B_iS_3 the battery will deplete before the mission ends. The element $B_iC_{0,1}$ indicates cell voltage and informs the decision-maker to take appropriate action so that the battery voltage does not reach a disabling limit. B_iSw provides information on which battery of a series-parallel battery pack is in use. The elements of battery MDP state are computed from the minimum (worst-case) value of any cell in each series battery pack. The I_{max} value is determined from the maximum permissible battery current draw per manufacturer data. The special state $FAILURE$ occurs when cell voltage dips below the lowest Lipo voltage limit, i.e. $3.3VDC$. In low voltage conditions, electronic speed controllers (ESC) used to drive BLDC motors will shut down resulting in a loss of thrust and subsequent UAS uncontrolled descent. The combinations of these state elements results in total

Battery health state is captured in the discrete MDP state values listed in Table 4.2. Because we do not model battery health transition dynamics in this work we assume conditions are known or accurately measured and remain constant over each flight simulation.

Table 4.2: Battery health state values.

Condition,i-(1,2)	**Criteria**
B_iF_1	Healthy battery
B_iF_2	Medium health battery
B_iF_3	Unhealthy battery
T,Temperature	$T_H : T > 50F$, $T_L : T < 50F$

where, Medium health battery = either power or capacity fade in at least one cell, Unhealthy Battery = has power and capacity fade in at least one cells, T = ambient temperature.

The states are abstracted to aggregate important decision regions for battery reconfiguration. This state space abstraction results in $|S| = |B_iS_{1-3}| \times |B_iC_{0,1}| \times |B_iSw| \times |I_{H,L}| + |F| = 9 \times 4 \times 4 \times 2 + 1 = 289$ states.

4.3.1.2 Battery MDP Action Definitions

Battery MDP actions are defined in Table 4.3 for the series-parallel battery pack shown in Figure 4.1. These actions are chosen to allow using either one of the batteries or both, based on their health conditions, available energy capacity, and other state-space considerations. Some assumptions for these actions include the switches are single pole single throw, no reverse current flow between the batteries when both the switches are ON due to diodes, no leakage current from the diode and switches have deterministic operation i.e. the switches will turn ON/OFF with 100% reliability when commanded to do so.

Table 4.3: Battery management MDP action definitions.

Actions	**Description**
$UseBatt_1$	Sw_1 is ON , Sw_2 is OFF
$UseBatt_2$	Sw_1 is OFF , Sw_2 is ON
$UseBoth$	Sw_1 is ON , Sw_2 is ON

4.3.1.3 Reward Function

The reward function is designed to reward utilization of battery/batteries to complete the mission. The reward assigned to each MDP state/action pair is defined by the following equations:

$$R(s, UseBatt_1) = w_1 R_{B_1 S_*} + w_2 R_{B_1 C_*} - w_3 R_{B_2 Sw} \tag{4.1}$$

$$\tag{4.2}$$

$$R(s, UseBoth) = w_1 \frac{\sum_{i=1}^{2} R_{B_i S_*}}{2} + w_2 \frac{\sum_{i=1}^{2} R_{B_i C_*}}{2} - w_3 \left[\frac{\sum_{i=1}^{2} R_{B_i Sw}}{2} - 1 \right] \tag{4.3}$$

$$\tag{4.4}$$

$$R_{B_iS_*} = \begin{cases} 0 & \text{For all conditions with } B_iS_1 \\ [-5,-10] & \text{Based on relative conditions of} \\ & \text{the two battery packs in } B_iS_2 \\ [-20,-25] & \text{Based on relative conditions of} \\ & \text{the two battery packs in } B_iS_3 \end{cases} \tag{4.5}$$

$$R_{B_iC_*} = \begin{cases} 0 & \text{For } C_* = C_0 \\ -10 & \text{For } C_* = C_1 \end{cases} \tag{4.6}$$

$$R_{B_iSw} = \begin{cases} 1 & \text{For } B_iSw = ON \\ 0 & \text{For } B_iSw = OFF \end{cases} \tag{4.7}$$

$$R(Failure) = -30 \tag{4.8}$$

$$w_1 + w_2 + w_3 = 1 \tag{4.9}$$

where $i = [1, 2]$. Reward $R(s, UseBatt_2)$ is computed analogously to Eqn. 4.2 depicting $R(s, UseBatt_1)$. Reward component $R_{B_iS_\star}$ penalizes states with lower EOD value and poor health relative to the other battery. $R_{B_1C_\star}$ penalizes states with low voltage value, while R_{B_1Sw} penalizes a switch position action that cycles the batteries (unnecessarily). The $FAILURE$ state is assigned the highest penalty. The different reward components are weighted with user-specified w_i.

4.3.2 State Transition Model from Monte Carlo Simulation

Monte Carlo (MC) simulations are used to determine the battery MDP state transition probabilities. The list of parameters varied for MC simulations is presented in Table 4.4. These parameters were randomly chosen at the start of each simulation

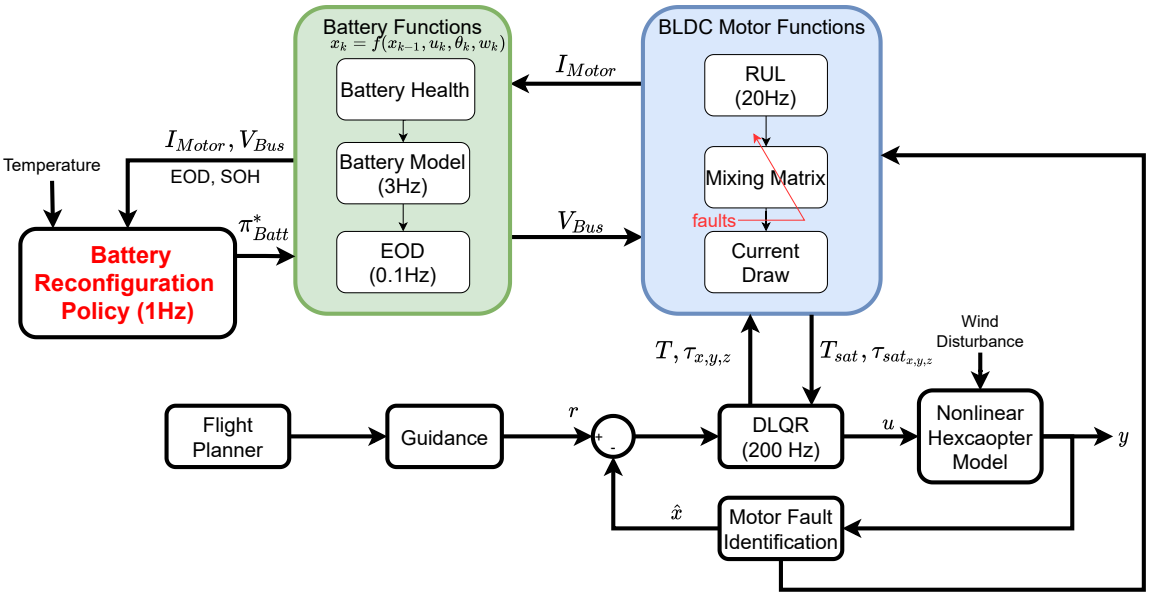

Figure 4.3: Monte Carlo simulation system diagram.

and held constant throughout each simulated flight except for wind gust magnitude. The range of parameters was defined to cover a wide variety of UAS operating conditions and its load demand from the battery pack. For each mission the UAS carries standard equipment including the modeled series-parallel battery pack. The ranges for initial cell voltages and hexacopter velocities are based on past flight tests [54] conducted with a hexacopter. The batteries are expected to be fully charged at the start of each flight.

Data flow through MC simulations is shown in Figure 4.3. The first step is randomly assigning MC parameters from the prescribed ranges and generating a representative flight plan for a package drop mission. For trajectory tracking, a Discrete Linear Quadratic Regulator (DLQR) state feedback controller is implemented with 200Hz update rate. Closed-loop control forces and torques are fed into the motor model to determine current, scaling by battery bus voltage, and any motor thrust saturation condition. Motor current draw is considered the dominant source for battery voltage drop. Hotel load i.e., current draw from an onboard computer, communication system, and sensors, is considered relatively small. Current drawn is used to

Table 4.4: Parameters varied for Monte Carlo simulations.

Parameter	**Range**
Action	$UseBatt_1, UseBatt_2, UseBoth$
Safety Margin, t_{sf}	[5,10]
Initial Cell Voltage, $B_{i,VDC}$	[4.05,4.12]VDC
Hexacopter Velocity, Vel_{hex}	[1,9]m/s
Wind Speed, w	[1,3]m/s
Wind Direction, θ	[0,π]rad
$WindGust^{\ddagger}$	[Low Light, Low Moderate, Medium Light, Medium Moderate]
Cell Health, B_iF_*	$[F_1, F_2, F_3]$

‡ = Dryden wind model[11]

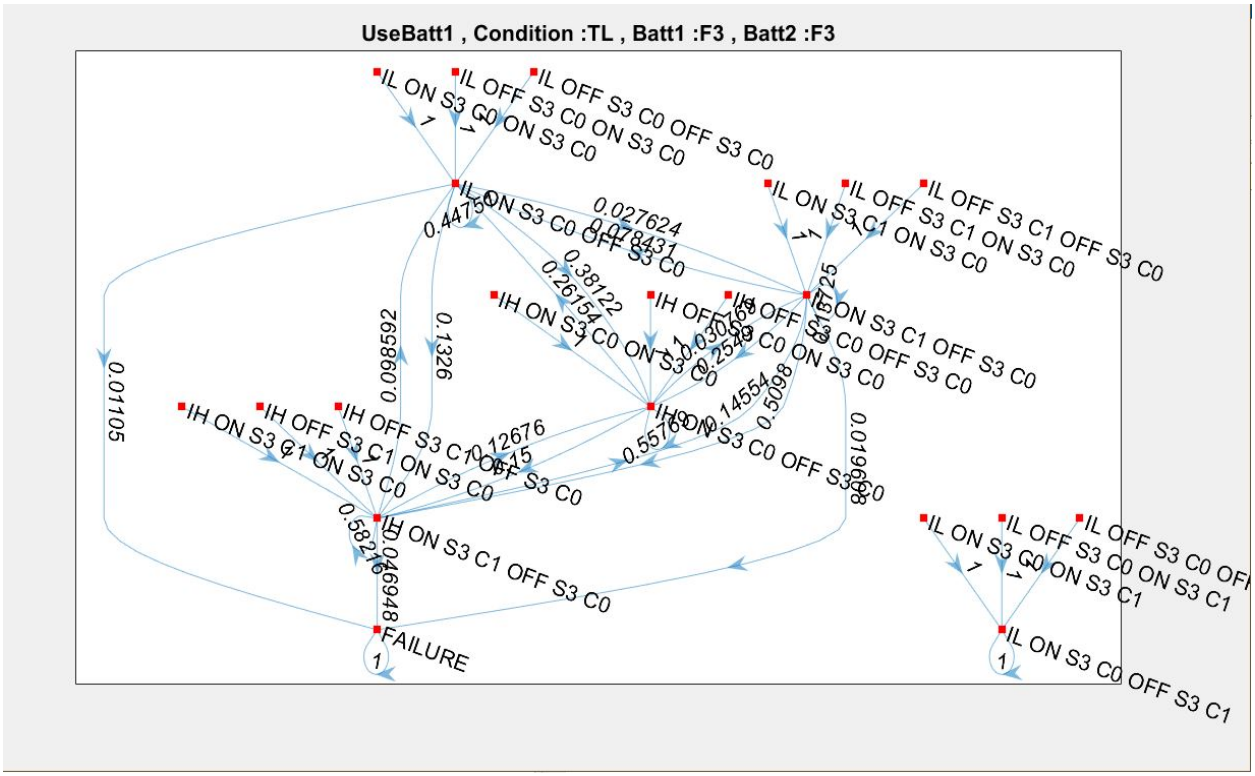

Figure 4.4: Excerpt of the 289 state directed graph showing battery MDP state transitions for action $UseBatt_1$ with both batteries having poor health conditions $B_{1,2}F_3$ and operating in low ambient temperature T_L. Left sub-graph states all lead to an absorbing failure state. The right sub-graph shows an example absorbing state in this simulation series. Nodes with color coded labels such as ILOFFS3C0OFFS3C0 describe states associated with $Batt_1$ and $Batt_2$.

determine battery EOD time. The same system diagram is used to determine state transition probabilities and simulate MDP policy execution in this work. The battery MDP policy executor responsible for battery management actions runs at 1Hz.

5000 MC simulations were conducted to determine MDP state transition probabilities equally split between each of the three MDP actions. As the parameters chosen from the Table 4.4 were assumed constant during each simulated flight, some state transition probabilities were not accurately captured in the given MDP state space, resulting in more self-looping states than would actually be encountered. Ideally, for MC simulations to capture the dynamics of the abstract state space, parameters should be time varying in every flight simulation. Since battery degradation dynamics and associate time varying temperature effects were not modelled, the battery health and the temperature were held constant. The large number of simulations did provide reasonable coverage of the MDP state-space.

An excerpt of the state transition probability table obtained from MC simulations is shown in Figure 4.4 as a directed graph. Nodes in the graph are color coded with labels such as ILOFFS3C0OFFS3C0 to describe states associated with $Batt_1$ and $Batt_2$. The illustrated graph excerpt assumes both battery packs are unhealthy (B_iF_3) and the ambient temperature is low. As a result, all initial states have feature $B_{1,2}S_3$ (abbreviated as $S3$ in the figure) indicating insufficient battery energy, i.e. $EOD < RFD$. Since, none of the MC parameters are varied in flight, dynamics from $B_iS_{1,2}$ states to B_iS_3 state elements are not observed. Two directed sub-graphs are seen in the figure. The states in the left sub-graph lead to a self-absorbing failure state, and the right sub-graph consists of states that do not transition to failure. This disconnect between the states is attributed to the absence of MC parameter dynamics and the potential for the limited number of MC simulations to not capturing state transitions with low probabilities. This transition diagram example was chosen to illustrate failure dynamics critical to capture and mitigate with the MDP described

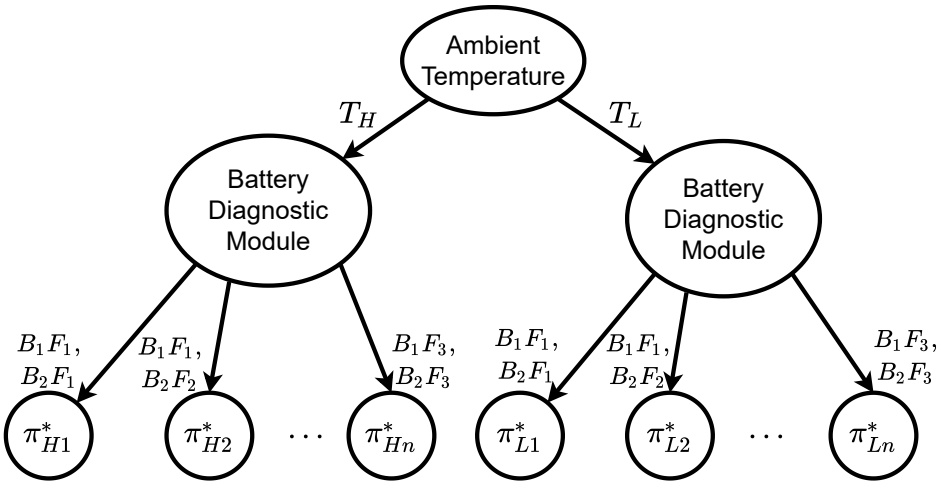

Figure 4.5: MDP decision tree to match policy π^* with current battery health conditions.

in Chapter 5. We assume each commanded battery switching action works with $p = 1$. Further, we assume a battery switch occurs instantaneously and there is no intermediate change in any other MDP state features, i.e. temperature, current, health, or battery state. Hence, it can be seen that when the $UseBatt_1$ action is taken the batteries from the initial state with both $Sw_1 = ON, Sw_2 = ON$ or $Sw_1 = OFF, Sw_2 = ON$ transition with probability 1 to $Sw_1 = ON, Sw_2 = OFF$, e.g., the topmost state ILONS3C0ONS3C0 transitions to ILONS3C0OFFS3C0 with $p = 1$.

4.3.2.1 Policy Evaluation and Implementation

Each optimal policy $\pi^\star$ for the MDP was determined using Value Iteration with a discount factor $\gamma = 0.95$. Value iteration was chosen due to the small state space and action space size. The policies are calculated offline and were stored in a lookup table for different health conditions and ambient temperatures. In simulation the policies are selected traversing the appropriate tree branch shown in Figure 4.5 based on the available ambient temperature and health information.

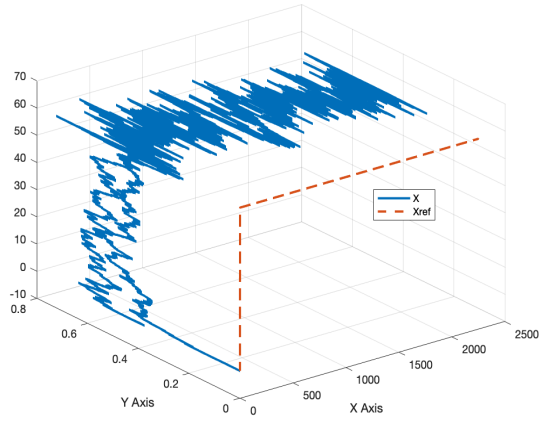

Figure 4.6: 3-D flight trajectory of hexacopter simulation.

4.3.3 Results

A series of case studies was performed to determine the performance of series-parallel battery pack usage with the MDP policy benchmarked against a fixed battery usage rule. Case studies are summarized in Table 4.5.

Table 4.5: UAS battery case study summary.

No.	Flight Time(sec)	**Action**	**Battery Health**
1	EOD_{Batt_1}	$UseBoth$	$B_1F_{1,2,3},\ B_2F_{1,2,3}$
2	EOD_{Batt_1}	$\pi^\star$	$B_1F_{1,2,3},\ B_2F_{1,2,3}$
3	$EOD_{BothBatt}$	$UseBoth$	$B_1F_{1,2,3},\ B_2F_{1,2,3}$
4	$EOD_{BothBatt}$	$\pi^\star$	$B_1F_{1,2,3},\ B_2F_{1,2,3}$

In studies 1 and 2, battery pack EOD time is twice the flight time, so all mission simulations were successful. 3D trajectory tracking of the simulated hexacopter is shown in Figure 4.6. The hexacopter climbs to a known altitude, translates to its destination, hovers for a specified time to simulate package drop, then returns to the start location. Since no integrator term was added to the controller, there is an offset between reference and actual trajectory. The controller could have been tuned to provide better performance; however, noise is an important and practical element of the simulations. Force, torque and motor current time responses are plotted in Figure

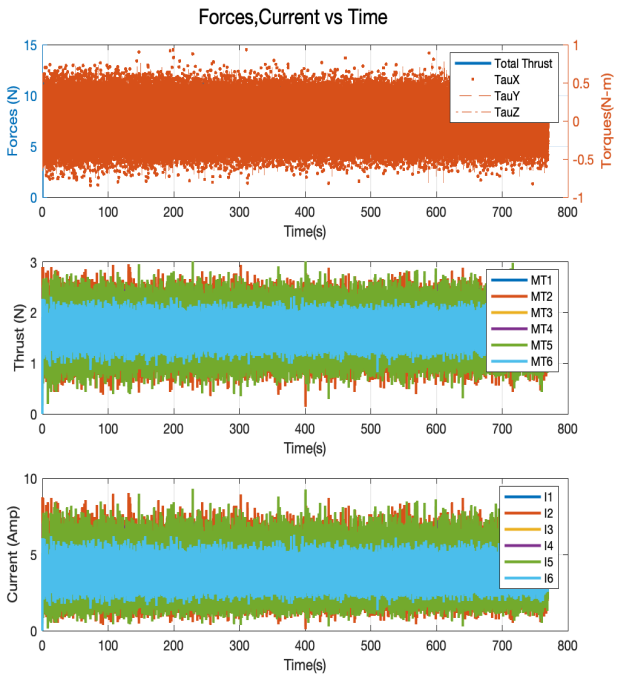

Figure 4.7: Time series plots of forces, motor thrust and current draw during a hexacopter trajectory tracking simulation.

4.7. White noise is introduced into the system so data appears noisy to emulate non-ideal real world conditions.

In case study 3, three scenarios were considered based on battery health: $(B_1F_1, B_2F_2), (B_1F_1, B_2F_3), (B_1F_3, B_2F_3)$. Results from scenario one i.e. (B_1F_1, B_2F_2) are presented in Figure 4.8. Battery current consumed is plotted in Figure 4.8a. A slight difference in current drawn from the two battery branches exists until $100sec$ into the flight due to an initial difference in internal resistance. Once there is an unequal voltage drop, the current draw equalizes. The EOD for both the batteries is shown in Figure 4.8b.The thick black line defines remaining flight time, and the vertical dashed-dotted line represents end of mission. Since both the batteries are healthy, the mission is completed successfully.

Results from scenario two i.e.(B_1F_1, B_2F_3) of case study 3 are plotted in Figure 4.9. Due to difference in health of the parallel batteries there is a significant difference in current drawn from the battery branches as seen in Figure 4.9a. Current draw in

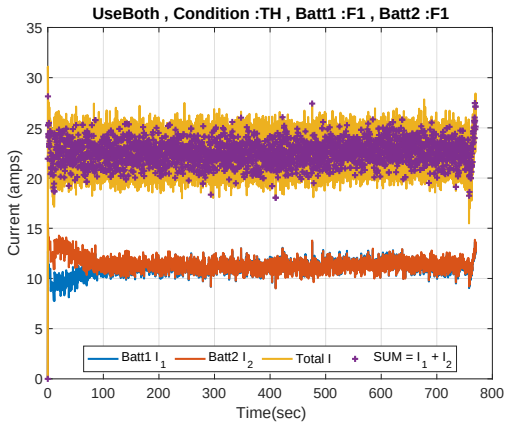

(a) Total current and current passing through each branch of a series-parallel battery pack.

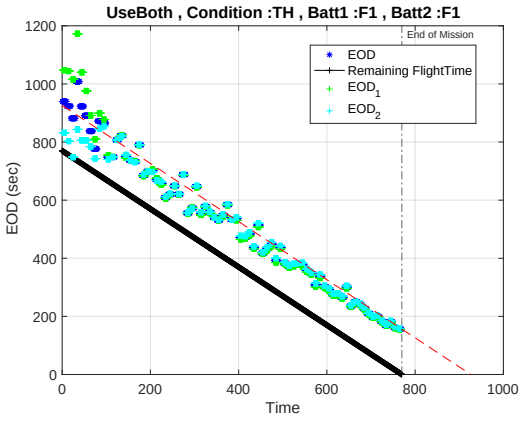

(b) EOD variation.

Figure 4.8: Simulated battery data for Case Study 3 Scenario 1 where all cells of $Batt_1$ and $Batt_2$ are healthy (F_1).

parallel cells is modeled per [28]. Individual battery pack variations are shown in Figure 4.9b. Inspection of EODs at $\sim 810sec$ shows that the UAS fails to complete the mission due to imbalance in branch currents. Even though $Batt_1$ is healthy, its EOD_1 value is always below the Remaining Flight Time line. In such scenarios mission success cannot be guaranteed.

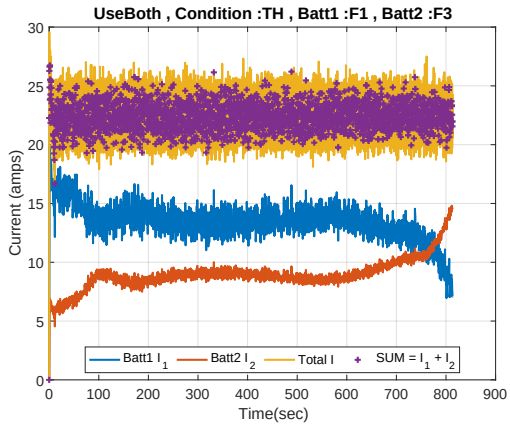

(a) Total current and current passing through each branch of a series-parallel battery pack.

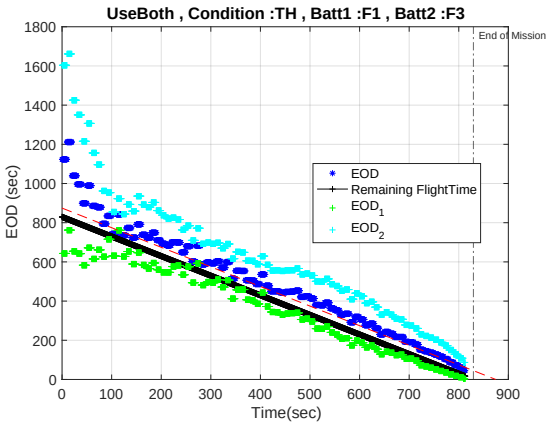

(b) EOD variation.

Figure 4.9: Simulated battery data for Case 3 Scenario 2 where all cells of $Batt_1$ are healthy but cells of $Batt_2$ encounter both capacity and power fade (i.e. F_3).

In scenario three i.e. i.e.(B_1F_3, B_2F_3) of case study 3, both of the batteries are

in poor health due to aging. The current drawn through each branch is thus about the same as shown in Figure 4.10a. However, since both batteries have capacity fade, the EOD value for both batteries is below the remaining flight time line throughout the mission, which implies the mission will fail. Such a situation highlights the importance of a higher-level planner that redefines the mission or executes an appropriate contingency plan when insufficient battery energy remains to safely continue the original flight plan.

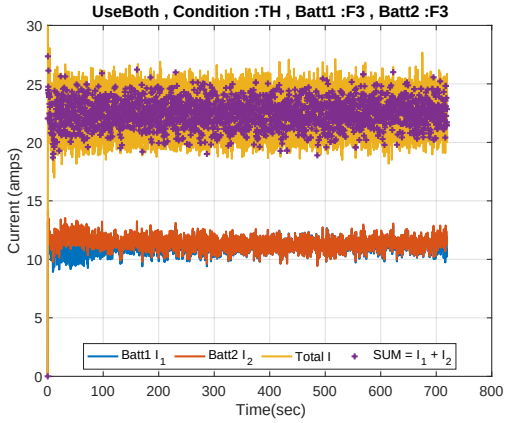

(a) Total current and current passing through each branch of the series-parallel battery pack.

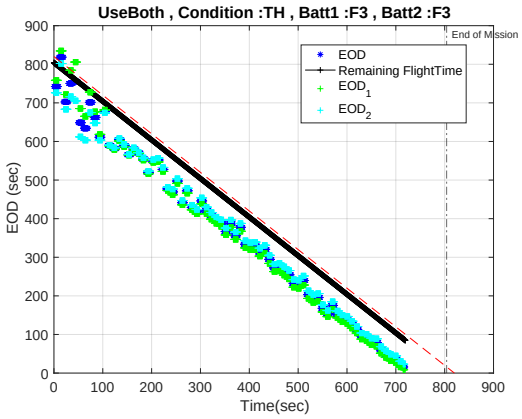

(b) EOD variation.

Figure 4.10: Simulated battery data for Case Study 3 Scenario 3 where all cells of $Batt_1$ and all cells of $Batt_2$ experience both capacity and power fade (i.e. F_3).

For case study 4, results from scenario (B_1F_2, B_2F_1) are plotted in Figure 4.11. The MDP policy switches with $UseBoth \rightarrow UseBatt_2$ occurs at $\sim 20sec$ and not to $UseBatt_1$ due to its poor health. Preference in this case is given to utilizing a single battery instead of both batteries when both are in the B_iS_1 state. With this formulation, repeated battery switching can occur. The UAS is still able to complete the mission as shown in Figure 4.11b. A similar scenario can be set up with a single action of $UseBoth$. An observed benefit of battery reconfiguration is that an unused battery can rest for subsequent use as needed.

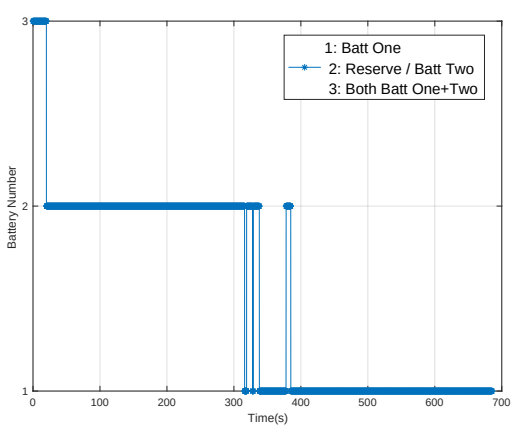

(a) MDP Policy battery switching actions for the series-parallel battery configuration.

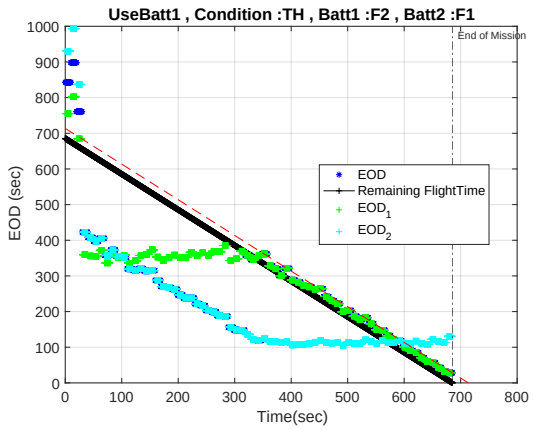

(b) EOD Variation.

Figure 4.11: Analysis of simulated trajectory tracking data for Case Study 4, Scenario 1 where $Batt_1$ has one cell with capacity fade and $Batt_2$ is healthy.

4.4 Hexacopter Motor Reconfiguration

The hexacopter configuration of multicopters offers redundancy in propulsion system. If they have a rotor failure the hexacopter can be reconfigured as a quadcopter and prevent destabilization due to loss of thrust. In this section we describe the technique used to reconfigure the control allocation matrix of the hexacopter while accounting for a single motor failure and preventing destabilization. The max motor thrust values and coefficients are from the validated motor model presented in Chapter II.

4.4.1 Motor Reconfiguration Scheme

The hexacopter rotors are numbered from 1-6 and are located at a distance L from the hexacopter center of gravity as shown in 4.12a. The hexacopter's total motor thrust magnitude T and torque magnitude τ_i about each body axis are related

to six motor commands as described by the following equation :

$$\begin{pmatrix} T \\ \tau_x \\ \tau_y \\ \tau_z \end{pmatrix} = M \times \begin{pmatrix} T_1 \\ T_2 \\ T_3 \\ T_3 \\ T_4 \\ T_5 \end{pmatrix} \tag{4.10}$$

where T_i = individual motor thrust, M = Mixing matrix. Pseudo inverse of the mixing matrix is referred to as the control allocation matrix, $M^{\dagger}$. For nominal scenarios where all the motors are operating the M_{nom} is defined as follows:

$$M_{nom} = \begin{pmatrix} 1 & 1 & 1 & 1 & 1 & 1 \\ \frac{-L}{2} & -L & \frac{-L}{2} & \frac{L}{2} & L & \frac{L}{2} \\ \frac{\sqrt{3}L}{2} & 0 & \frac{-\sqrt{3}L}{2} & \frac{-\sqrt{3}L}{2} & 0 & \frac{\sqrt{3}L}{2} \\ -\gamma & \gamma & -\gamma & \gamma & -\gamma & \gamma \end{pmatrix} \tag{4.11}$$

where $\gamma = C_Q/C_T$, C_Q = Torque coefficient and C_T = Thrust Coefficient.
If there is a motor failure the controller sets the diametrically opposite rotor to produce zero thrust. For e.g. if motor 1 is failed , motor 4 is also commanded to produce zero thrust , as shown in Figure 4.12c. Due to thrust limitations of motors, as a consequence there is poor pitching and yaw control authority to stabilize the hexacopter in event of motor failure. In such a scenario reconfiguration of the control allocation matrix is necessary and is achieved by rotating the body frame along the $Z - axis$. With this reconfiguration the hexacopter acts as quadcopter. The rotation of body axis for different motor failures scenarios are shown in Figure 4.12.

If motor 2 or 5 fails the M_{nom} mixing matrix is used, because both 2 or 5 are situated along the $Y - axis$ of the body frame. Failure of any other motors require

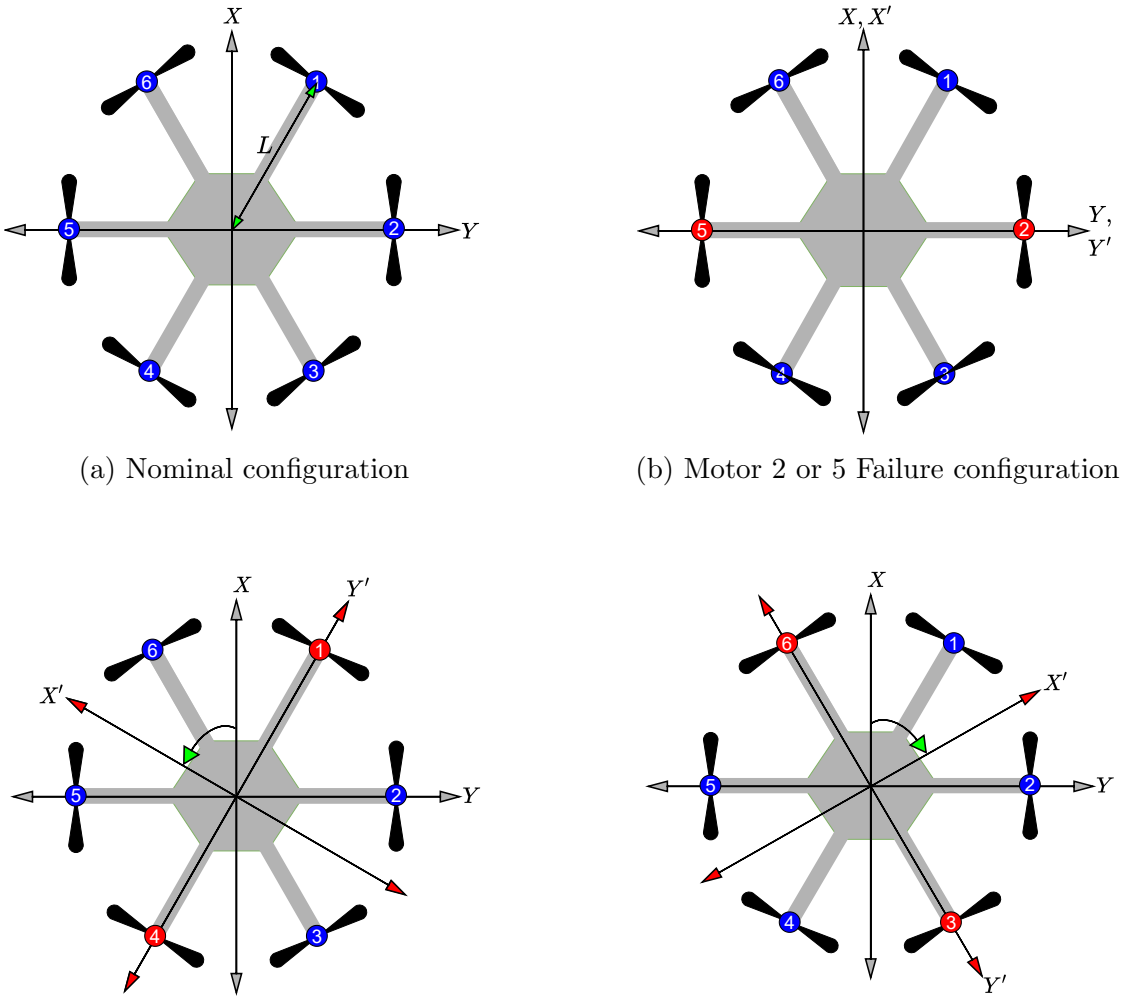

(a) Nominal configuration

(b) Motor 2 or 5 Failure configuration

(c) Motor 1 or 4 Failure configuration

(d) Motor 3 or 6 failure configuration

Figure 4.12: Hexacopter motor orientation and different reconfiguration solutions given motor failure

rotation of the body frame to represent the hexacopter as a quadcopter.

When motor 1 or 4 fails the body frame is rotated counterclockwise by 60° about the $Z-axis$ as shown in Figure 4.12c and the new frame is shown by the X', Y' axis pair. The mixing matrix is modified as the following:

$$M_{2,5} = \begin{pmatrix} 1 & 1 & 1 & 1 & 1 & 1 \\ -L & \frac{-L}{2} & \frac{L}{2} & L & \frac{L}{2} & \frac{-L}{2} \\ 0 & \frac{-\sqrt{3}L}{2} & \frac{-\sqrt{3}L}{2} & 0 & \frac{\sqrt{3}L}{2} & \frac{\sqrt{3}L}{2} \\ -\gamma & \gamma & -\gamma & \gamma & -\gamma & \gamma \end{pmatrix} \tag{4.12}$$

When motor 3 or 6 fails the body frame is rotated clockwise by 60° about the $Z - axis$ as shown in Figure 4.12d and the new frame is shown by X', Y' axis. The mixing matrix is modified as the following:

$$M_{3,6} = \begin{pmatrix} 1 & 1 & 1 & 1 & 1 & 1 \\ \frac{L}{2} & \frac{-L}{2} & -L & \frac{-L}{2} & \frac{L}{2} & L \\ \frac{\sqrt{3}L}{2} & \frac{\sqrt{3}L}{2} & 0 & \frac{-\sqrt{3}L}{2} & \frac{-\sqrt{3}L}{2} & 0 \\ -\gamma & \gamma & -\gamma & \gamma & -\gamma & \gamma \end{pmatrix} \tag{4.13}$$

4.4.2 Control Authority

Along with appropriate motor reconfiguration implementation based on motor fault detected it is also critical to determine the control authority along the lateral and longitudinal axis of the hexacopter. The control authority of the hexacopter is determined in terms of maximum roll and pitch angles it can tilt while maintaining altitude. This section describes the details of determining hexacopter control authority and can be generalized to any other multicopter configuration.

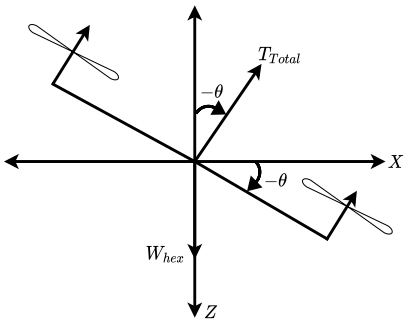

Figure 4.13: Longitudinal motion diagram

Considering the combined roll and pitch tilt of the multicopter, as can be seen from 4.13 the vertical component of total thrust can be resolved as $T_{Total_Z} = T_{Total} \cos\theta \cos\phi$. In order maintain constant altitude this vertical thrust component has to balance the weight of the hexacopter. In nominal scenarios when there is no motor failure the

T_{Total_Z} variation for different pitch and roll angles are shown in Figure 4.14. The green plan shown in the figure represents the weight of the hexacopter. There is no intersection between the two surfaces when there is no rotor failure and the multicopter can tilt to its maximum roll and pitch angles while maintaining stability along the $z - axis$.

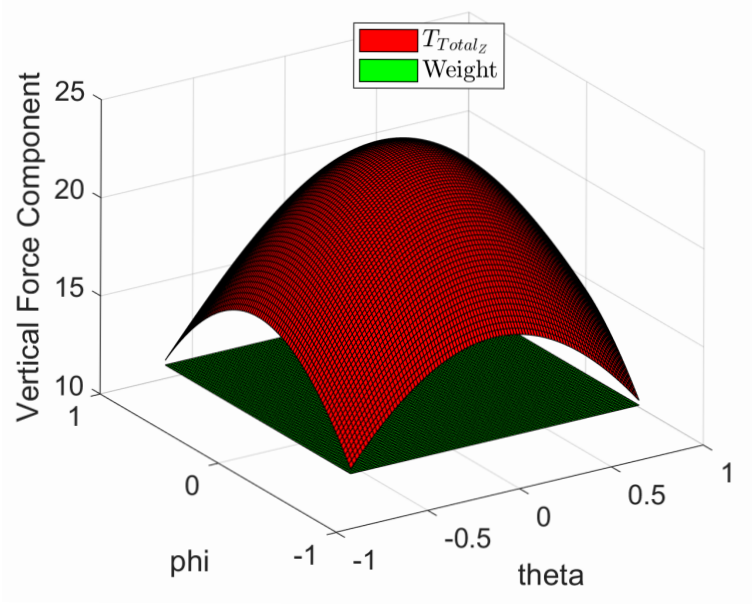

Figure 4.14: Total thrust variation with no rotor failures and total $T_{Total} = 24N$

In scenarios when there is one motor failure and with application of motor reconfiguration scheme i.e. switching a hexacopter to quadrotor configuration, it can be seen that there is intersection between the T_{Total_Z} and weight plane, as shown in Figure 4.15. From the intersection we can determine the maximum pitch and roll angles of the multicopter that can support vertical stability, shown in Figure 4.15b denoted by blue dotted line. We simplify the the max roll and pitch limits by assuming largest square in the circle.

To visualize how the maximum roll and pitch angles shrink due to reduced T_{Total_Z}, Figure 4.16 shows a scenario where there are three motor failures. As a result, Figure 4.16b shows that the dimensions of the maximum square inscribed in the circular intersection decreases substantially.

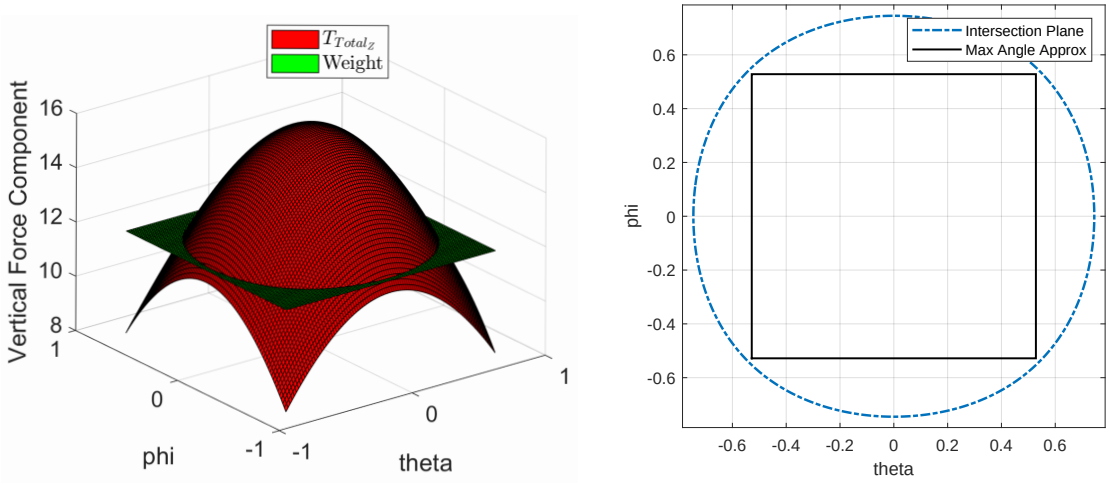

(a) Vertical component of thrust (b) 2D Cross-section

Figure 4.15: Total thrust variation with two rotor failures and total $T_{Total} = 16N$

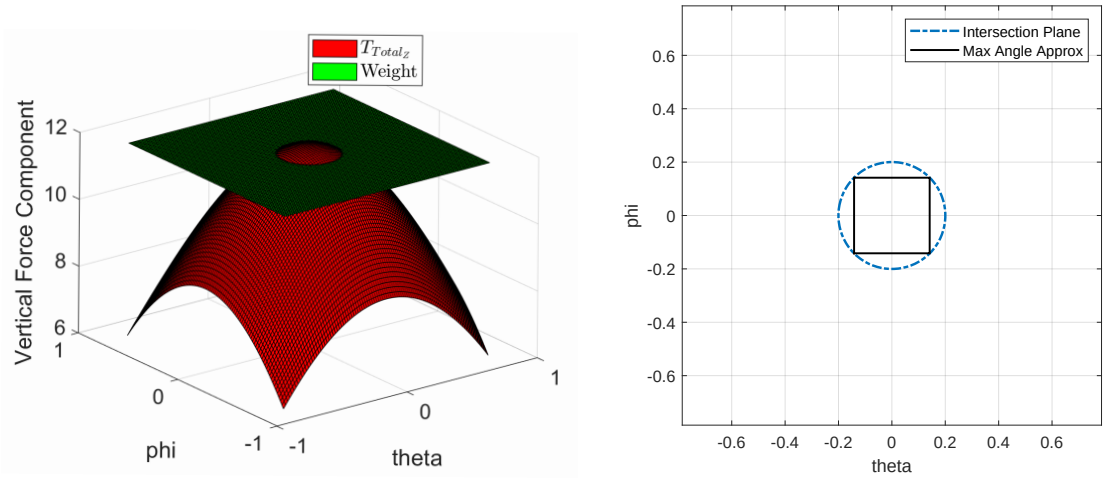

(a) Vertical component of total thrust (b) 2D Cross-section

Figure 4.16: Total thrust variation with two rotor failures and total $T_{Total} = 12N$

4.5 Summary and Future Work

This chapter has presented an approach to UAS battery management and motor reconfiguration. With our state-space abstraction for battery reconfiguration, MDP reward tuning required substantial effort to achieve desirable behavior. Our proposed battery reconfiguration MDP provides benefits in terms of optimal battery switching. As seen from baseline case studies, if both batteries have unexpectedly poor health,

the original flight plan can still be impossible. Therefore battery prognostics results must be shared with a flight planner capable of updating the flight plan in real-time to assure the UAS lands before battery energy is fully expended. In future work it will be important to model battery degradation and associated time varying temperature effects in each MC simulation. This will support accurate capture of MDP state transitions from MC simulations. However, we expect the MDP optimal policies to look similar, as the reward function was tuned to obtain the desired switching behaviour. Tuning of the optimal policies utilizing an updated state transition matrix is not expected to generate a substantially different MDP contingency management policy (see Chapter V).

Along with battery reconfiguration, motor reconfiguration is critical to keeping the UAS airborne. A technique to perform motor reconfiguration in a hexacopter to accommodate a single rotor failure is proposed. Maximum allowable pitch and roll angles to maintain vertical stability is also presented. Based on the position of the jammed motor, appropriate control allocation is determined, transforming the hexacopter to a quadcopter configuration. One limitation of the proposed technique is that it can only handle single rotor failure. Future work could investigate the accommodation of multiple rotor failures. This motor reconfiguration technique is utilized in simulations presented in the following chapter.

CHAPTER V

Contingency Management

5.1 Introduction

The previous chapters developed the multicopter dynamics, battery, and motor models. Optimal component reconfiguration was performed in Chapter IV to mitigate risk to the UAS as components degrade or fail. While component reconfiguration prevents sudden failure, there is no guarantee that the UAS with degraded/failed components can safely complete its planned flight. This chapter focuses on developing a novel MDP-based contingency management decision module and its evaluation to assure safety through in-flight re-planning as needed. Computed policies assure that under UAS component degradation or failure scenarios, appropriate actions are taken to prevent a crash.

The proposed contingency manager recommends safety-preserving actions for the UAS utilizing the abstracted information related to flight status, remaining flight plan, and component health indicator. To limit the scope of work, endogenous events considered in this chapter are battery degradation and motor fault status. However, for certification of the contingency manager, a detailed analysis of the comprehensive suite of exogenous and endogenous events would have to be considered. Endogenous events include failure analysis as cited in Ref. [49, 19] include lost communication links, degradation of navigation system due to sensor failure and many more. Simi-

(a) Top-down view of an example package delivery mission in Manhattan. The flight path is shown as a blue line, and nearby contingency landing sites (e.g., building rooftop, playground, parking lots, etc.) are shown as red stars. Potential landing site contours are shown in green.

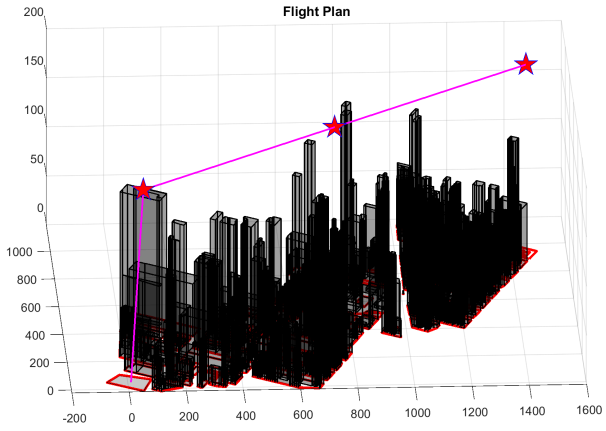

(b) Visualization of the 3-D environment in Manhattan for a preflight contingency database. The nominal flight path is shown in a magenta line. Red stars indicate the checkpoints, where pre-planned emergency landing solutions are generated.

larly exogenous events include severe weather, bird strike, traffic conflict and many more.

The effectiveness of the contingency manager is assessed in a simulation of a multicopter operating in an urban environment. The simulation environment was constructed using post-processed OpenStreetMaps (OSM) building data from [35, 48]. This map data builds 3-D building structures in Southern Manhattan with relevant information (i.e., building height, category, coordinates). Once the start and destination of the UAS flight are determined, the algorithm generates a region of interest, and potential landing sites within this region are identified. These landing sites are represented as coordinates of the centroid of the buildings. Our contingency manager is simulated on this emergency landing site map using a hexacopter that experiences a sudden in-flight fault. Figure 5.1a shows a top-down view of an example package delivery mission in Southern Manhattan with offline landing sites highlighted in green lines and red stars. Figure 5.1b shows a 3-D preflight contingency database, as well as a nominal flight trajectory for a package delivery mission in our simulation.

A literature review of existing contingency management techniques is described in Section 5.2. The development of contingency management using the MDP framework is presented in Section 5.3; this includes the state space definition, action definition, state transition probabilities, reward function, the optimal policy and its sensitivity analysis. A brief discussion on the offline model-free method for contingency management is also covered in Section 5.3. The simulation environment developed for the evaluation of the contingency manager is detailed in Section 5.4. Various case studies and results from Monte Carlo simulations to assess the efficacy of contingency management is discussed. Section 5.5. Finally, Section 5.6 summarizes the chapter and provides future work for the proposed contingency manager.

To the best of our knowledge, a comprehensive study of evaluating MDP's effectiveness in contingency management settings within a high fidelity simulator has not been conducted. This work aims to bridge this gap.

5.2 Literature Review

Prognostics information alone is not helpful unless used in an active system for preventative maintenance or contingency management. Ref. [24] proposes the Prognostics-based Decision Making (PDM) architecture consisting of four main elements: a diagnoser (DX), decision maker (DM), vehicle simulation (VS) and the vehicle itself. The prognostics problem is formulated as a constraint satisfaction problem (CSP) and solved using backtracking search and particle filtering. In this framework, mission waypoints are defined a priori; waypoints are assumed reachable even in the presence of faults. A similar prognostics architecture is proposed in [9] and implemented on an unmanned ground vehicle.

In [63] the authors propose a mission planning strategy for UAS multicopters that incorporates battery State of Charge (SoC) and State of Health (SoH) to generate updated mission plans. The planning problem is formulated as an optimization

problem to minimize total energy consumed by the multicopter, subject to nonlinear constraints defined by UAS dynamics, brushless motor dynamics and battery dynamics. References [70] and [71] present an Automated Contingency Planner enhanced by prognostic information. Online optimization determines a minimum cost reconfiguration for the system and components. A receding horizon planner is utilized in [79] to incorporate the constraints determined from prognostics information.

Systematic auto-mitigation strategies assured contingency landing management (ACLM) in the case of rotor failures is developed in [36] . The paper presents ACLM logic flow and mathematical derivations needed to guarantee assurance efficacy (AE). Case studies highlight cost metric based contingency landing site selection using offline and online flight planners. This chapter is distinctive and innovative in its computation of UAS contingency management using a Markov Decision Process (MDP) formulation that incorporates flight plan and health information in decisions.

5.3 Contingency Management MDP

Contingency Management Autonomy (CMA) is modeled as a Markov Decision Process (MDP). Briefly, a MDP is defined by the 4-tuple $\langle S, A, p(s'|s,a), r(s,a)\rangle$, where S is the finite set of system states, A is a finite set of actions, $p(s'|s,a)$ is state transition probability tensor and $r(s,a)$ is the reward for executing action a in state s. These models can be broadly classified as model-free and model-based. In model-based methods data is available to define all the elements of the MDP tuple and in model-free the state transition probabilities are unknown.

An MDP requires definition of state variables and their discrete value sets, identifying actions, generating transition probabilities, and defining the reward function. Once the MDP tuple is defined, methods such as Value Iteration or Policy Iteration can be used to determine optimal MDP policy $\pi^\star$ for model-based methods. Algorithms such as Q-learning and SARSA can be used to determine the optimal policy

for model-free MDPs. This section describes the model-based MDP formulation and its supporting functions.

5.3.1 Approximate Footprint Calculation

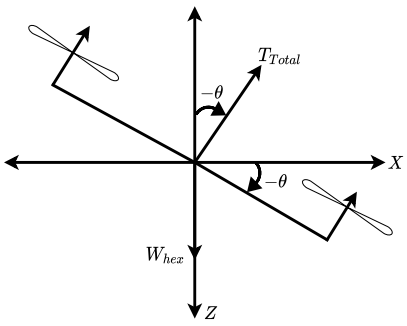

Figure 5.2: 1-D motion diagram

An approximate footprint defines the region on the ground that can be reached by an aircraft given its current position, velocity, and performance capabilities [8, 22]. Approximate footprint for the multicopter is calculated provided the End of Discharge (EOD) time of the Lipo batteries. All the points that lie within the footprint constitute set of reachable states by the multicopter for the given EOD constraints. To calculate the approximate footprint, longitudinal level flight for a multirotor is considered as shown in Figure 5.2. The equations of motion are defined as follows:

$$\begin{aligned} m\ddot{x} &= u - d_x\dot{x} \\ T_{Total}\cos\theta &= W_{hex}mg \\ where,\ \ u &= -T_{Total}\sin\theta \end{aligned} \tag{5.1}$$

The state space form of Eq. (5.1), with position $x_1 = x$ and velocity $x_2 = \dot{x}_1$ is as

follows:

$$\begin{aligned}\dot{x}_1 &= x_2 \\ \dot{x}_2 &= \frac{1}{m}u - \frac{d_x}{m}x_2\end{aligned} \tag{5.2}$$

The aim then is to determine the maximum distance the drone can travel in longitudinal level flight with minimum energy consumption. Hence, an optimal control problem with minimum control effort input as the cost functional is defined as follows:

$$J = \frac{1}{2}\int_{t_0}^{t_f} u^2 \, dt \tag{5.3}$$

where $t_0 = 0$, $t_f = EOD(s)$.

Pontryagin's Minimum Principle (PMP) is used to determine optimal control input u^* [46]. Given longitudinal level flight dynamics, using PMP an analytical solution can be determined in milliseconds.

The Hamiltonian for the optimal control problem is defined as follows:

$$H = \frac{1}{2}u^2 + [\lambda_1 \ \lambda_2] \begin{bmatrix} x_2 \\ \frac{1}{m}u - \frac{d_x}{m}x_2 \end{bmatrix} \tag{5.4}$$

The solution for optimal states (x_1^*,x_2^*), co-states (λ_1^*, λ_2^*) and controls (u^*) is given by the following equations:

$$x_1^*(t) = -\frac{C_1}{d_x^2}t + \frac{C_2}{2d_x^2}\exp\left(\frac{d_x}{m}t\right) - \frac{C_3}{d_x}m\exp\left(\frac{-d_x}{m}t\right) + C_4 \tag{5.5}$$

$$x_2^*(t) = -\frac{C_1}{d_x^2} + \frac{C_2}{2d_x m}\exp\left(\frac{d_x}{m}t\right) - C_3\exp\left(\frac{-d_x}{m}t\right) \tag{5.6}$$

$$u^*(t) = -\frac{C_1}{d_x} + \frac{C_2}{m}\exp\left(\frac{d_x}{m}t\right) \tag{5.7}$$

$$\lambda_1^*(t) = C_1 \tag{5.8}$$

$$\lambda_2^*(t) = \frac{mC_1}{d_x} - C_2\exp\left(\frac{d_x}{m}t\right) \tag{5.9}$$

To determine the maximum distance covered by the hexacopter in longitudinal and lateral directions, we formulate the problem as a fixed final time and free final state problem to determine the constants C_1, C_2, C_3, C_4. The following boundary conditions are used for determining maximum distance travelled forward:

$$x_1(t_0) = x_0,\ x_2(t_0) = v_{init},\ x_2(t_f) = v_{init},\ \lambda_2(t_f) = 0 \tag{5.10}$$

For determining maximum distance travelled backward with initial velocity v_{init} forward the following boundary conditions are used:

$$x_1(t_0) = x_0,\ x_2(t_0) = v_{init},\ x_2(t_f) = -v_{init},\ \lambda_2(t_f) = 0 \tag{5.11}$$

The initial and final velocities are kept the same to reflect approximately constant current consumption, resulting in EOD value holding true when the final position is calculated. With the available conditions the system of linear equations is solved to obtain the C_i values. Considerations similar to the longitudinal direction are made for the lateral direction except $x_1(t_0) = 0, x_2(t_0) = 0$.

In the implementation, *exp* is replaced by an n order MacLauren Series expansion of the exponential. For the current implementation $n = 5$.

Once the optimal control ($u^*(t)$) available with us for steady level flight, T and θ

values are calculated by rearranging terms in (5.1) and using (5.7) as shown :

$$\theta_{opt}(t) = atan^{-1}\left(\frac{u^*(t)}{mg}\right) \tag{5.12}$$

$$T_{opt}(t) = \frac{mg}{cos(\theta_{opt}(t))} \tag{5.13}$$

Algorithm 1: Footprint Approximation Function

Input: v_{init},EOD,T_{Avail}, $\theta_{min/max}$
Output: $\mathcal{F}_{Lim}$
// EOD = `Battery End of Discharge (s)`
// T_{Avail} = `Available Maximum Total Thrust (N)`
// $\theta_{min/max}$ = `Min/Maximum pitching or rolling angle`
// $\mathcal{F}_{Lim}$ = `Foot print limits`
1 Assign the boundary conditions as per eqn (5.10),(5.11)
2 Calculate C_i values along the longitudinal and lateral direction
3 Determine u^*_{fwd},u^*_{bkwd} using eqn (5.7)
4 Determine [$\theta_{opt-fwd}$, $T_{opt-fwd}$] and [$\theta_{opt-bkwd}$, $T_{opt-bkwd}$] using eqn (5.13),(5.12)
5 Bound the [θ_{opt} , T_{opt}] with [$\theta_{min/max}$, T_{Avail}]
6 Determine u_{bound} using eqn (5.1) and bounded values of θ_{bound},T_{bound}
7 Simulate system given by eqn (5.2) until EOD using u_{bound}
8 Determine footprint limits based on the position at end of simulation

The footprint is calculated in the multirotor frame. For determining the boundary of the footprint, analysis similar to longitudinal level flight, is conducted for lateral level flight. The limits for the longitudinal and lateral flights are as shown in Figure 5.3. Then algorithm (1) is used to determine if the emergency landing site reachable. An example of the footprint cone for initial velocity of $9m/s$ and EOD varying from $1sec$ to $50sec$ is shown in Figure 5.4.

5.3.2 Model-Based CMA

The purpose of CMA is to generate risk-aware safety-preserving actions for the UAS while considering any observed degradation in the multi-battery pack and motors. CMA is modelled as a stationary infinite-horizon Markov Decision Process. The optimal CMA policy $\pi^\star$ is obtained using value iteration. This section describes the

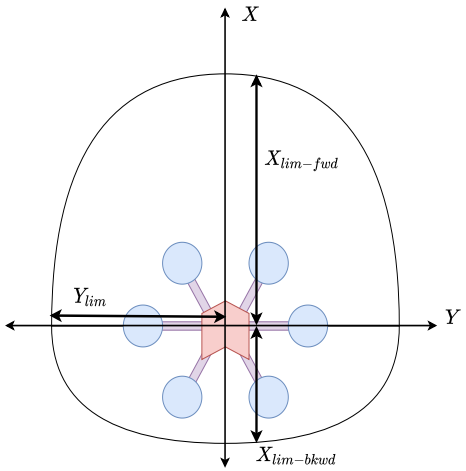

Figure 5.3: Footprint of a multicopter

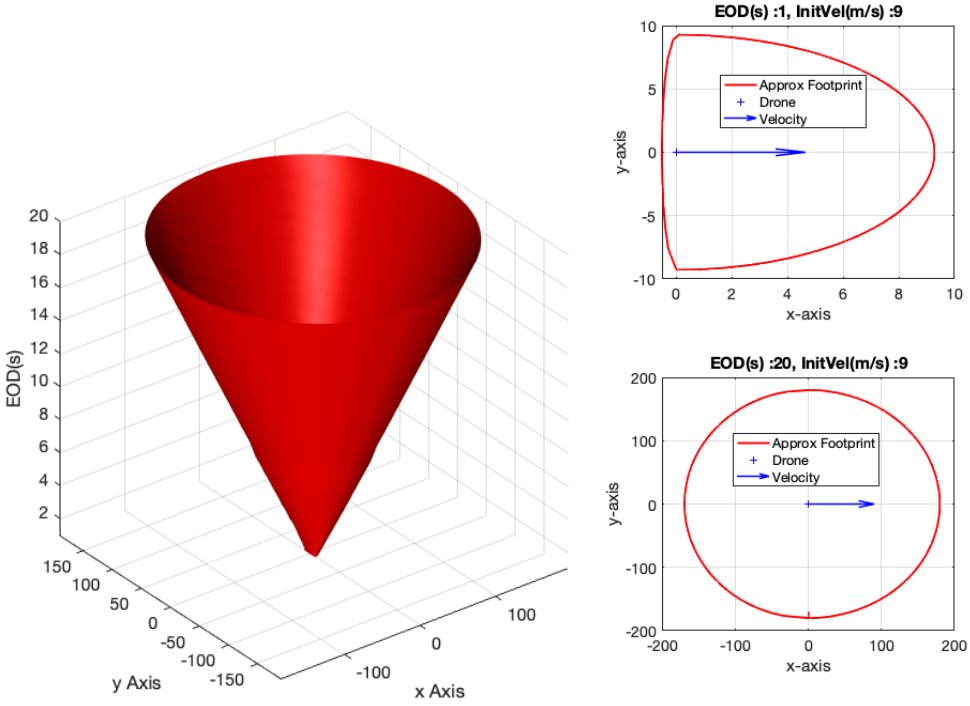

Figure 5.4: (Left) Variation in footprint of a multicopter for different EOD values, and initial velocity of $9m/s$ along the positive x-axis, (Top Right) Footprint for EOD value of $1sec$, (Bottom Right) Footprint for EOD value of $20sec$.

CMA MDP model formulation.

5.3.2.1 State Definition

The CMA MDP is designed to prevent UAS crash by executing emergency landing options as needed. Thus the MDP state space is modeled to include information related to motor and battery health, available battery energy and remaining useful life of motors. The CMA MDP state-space is defined as $S = S_E \cup S_S$, $S_E = \{C, T, FL, E\}$ and $S_S = \{S = (FS, MH, MM, BH, RM) | FS \in \{N, ELASAP, ELPract\}, MH \in \{NF, SF, JF\}, MM \in \{MM0, MM1\}, BH \in \{G, M, P\}, RM \in \{RM0, RM1\}\}$ and the action space is defined as $A = \{NOOP, Terminate, LandASAP, LandPract\}$.

A detailed description of CMA MDP state S is as follows:

- Flight Status (FS)

  Due to the Markov assumption, the current state must contain relevant system status information. The FS state feature has three possible values: N: Nominal flight, $ELASAP$: Executing emergency landing ASAP (as soon as possible), $ELPract$: Executing emergency landing when practical. If $FS = ELPract$ the action space reduces to $A_s = \{NoOp, Terminate, LandASAP\}$. if $FS = ELASAP$ the action space reduces to $A_s = \{NoOp, Terminate\}$. All actions are available with $FS = N$. The action availability based on FS has been manually coded in the MDP.

- Motor Health (MH)

  This feature assumes the following values $MH = \{NF : No - Fault, SF : SpallingFault, JF : JamFault\}$ defined for a single motor. The motor health values are assigned based on its degraded condition and progression to failure. Motor health degradation is limited to spalling degradation, a critical failure condition in motor bearings. However, various motor degradation events exist as discussed in Chapter III and the motor health definition can be extended to include multiple degradation modes. The spalling fault occurs in any one of the

UAS motors with a probability [1] of 4.75×10^{-5} [34] and is assumed to be fully observable by the system. Once a spalling fault is observed, it is assumed not to occur in the remaining motors. But in practice, spalling could occur in multiple motors simultaneously. Observation of spalling sets the MH value to SF and the spalled area is propagated until it exceeds a threshold value, eventually leading the motor to seize operation. The fault diagnosis module described in Section 5.4 detects the motor jamming, and motor health MH is set to JF status. Jam fault considered in this research is due to spall propagation only. Hence no fault cannot directly transition to jam fault.

- *Motor Margin (MM)*

  Motor Margin is defined for a single motor only, by the following formula:

$$MM = 1 - \sum_{i=1}^{n_f} w_i \frac{t_{FlightTime}}{t_{RUL_i}} \tag{5.14}$$

  where $t_{FlightTime}$ = Flight time (sec), t_{RUL} = Remaining Useful Life of the motor (sec), n_f = different types of motor faults, $\sum_{i=1}^{n_f} w_i = 1$. In this research, spalling fault in a single motor is considered, hence $n_f = 1$. When a spalling fault in the motor is detected, t_{RUL} is calculated using Paris' Law as described in Chapter III. In nominal motor health conditions, $t_{RUL} \geq 10 \times t_{FlightTime}$, because in practise the propulsion systems would be designed to have a high safety margin under nominal conditions. MDP discrete state feature MM is assigned two logical values for a single motor: $MM0 : MM < 0$ and $MM1 : 0 \leq MM < 1$. This discretization is shown by the red plane in Figure 5.5. $MM < 0$ indicates that either a single motor has seized (failed) or $t_{RUL} < t_{FlightTime}$, i.e. a single motor under consideration will not be able to provide thrust for the total remaining flight duration. Range $0 \leq MM < 1$ signifies that a motor is

[1] The spalling fault for six motors would be $6 \times (4.75 \times 10^{-5})$, but since we are only considering spalling in a single motor the 6 multiplier is not used for our analyses.

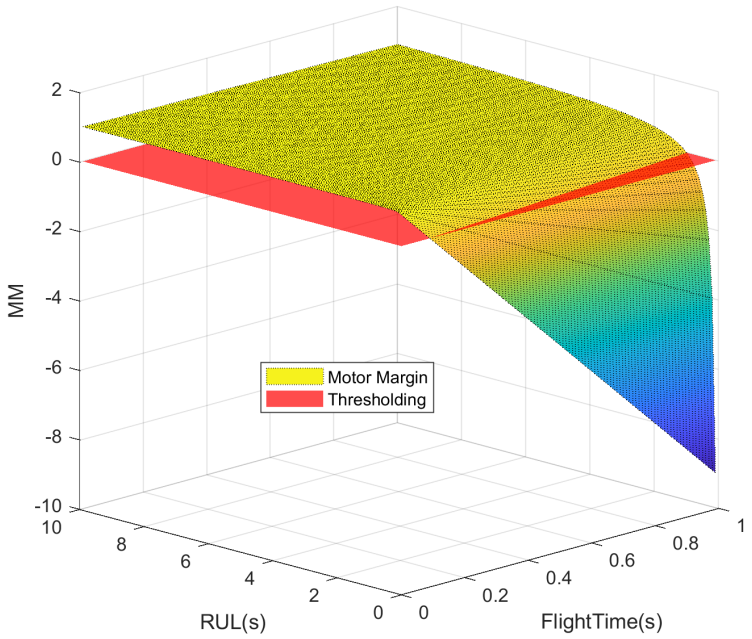

Figure 5.5: Motor Margin threshold

either in nominal health or undergoing a spalling fault but expected to provide thrust for the remaining flight duration. For consideration of multiple types of motor faults or multiple motor failures at once, further investigation would be required for discretization MM.

- *Battery Health (BH)* is a composite battery pack health state abstracted to three possible health conditions: $Good$, $Medium$ and $Poor$. Nominally $BH = Good$. Details of the series parallel battery pack used in this research can be found in Chapter IV, however, there is no switching between the batteries. If a cell/cells in the battery pack experience either power fade or capacity fade but not both the health is set as $BH = Medium$. If a cell/cells in the battery pack experience both power and capacity fade the battery health is set to $BH = Poor$. Also battery degradation is a relatively slow process compared to the short flight plan duration, we assume as a simplification in this work that BH remains constant during a single flight. Details of the battery health description are provided in Section 4.3.1.1.

- *Reachability Margin (RM)* is defined by:

$$RM = 1 - \frac{t_{FlightTime}}{t_{EOD}} \tag{5.15}$$

where t_{EOD} = End of discharge time for a series-parallel battery pack with both the batteries being used and is calculated as described in Section 3.3.2.1. $t_{FlightTime}$ is the time the UAS takes to complete the executing flight plan. When an emergency landing is being executed $t_{FlightTime}$ is then based on minimum time obstacle free trajectory to the emergency landing sites. RM is discretized as $RM0 : RM < 0$ and $RM1 : 0 \leq RM < 1$. $RM0$ indicates the battery pack does not have sufficient energy to complete the executing flight plan. $RM1$ indicates the battery pack has sufficient energy to complete the flight plan.

- *Complete(C)* assumes value $False(0)$ while the mission is in progress and $True(1)$ when the UAS completes its nominal or emergency flight plan. All $s \in S$ with $C = 1$ transition to E (end), an absorbing state.

- *Terminated (T)* assumes value $False(0)$ until the flight termination action is executed at which time it becomes $True(1)$. All $s \in S$ with $T = 1$ transition to E (end), an absorbing state.

- *Failure (FL)* assumes value $False(0)$ unless its value is set to $True(1)$ indicating the mission has failed due to controller instability (measured by trajectory tracking error) or insufficient battery energy ($RM < 0$). Other system failures are not considered in this work but would be necessary to model and manage with CMA in fully-implemented autonomous system. All $s \in S$ with $FL = 1$ transition to E (end), an absorbing state.

- *End (E)* is the absorbing final or end state.

The states are abstracted to aggregate important decision regions for contingency

management. This state space abstraction results in $|S_E| = 4$, $|S_S| = |FS| \times |MH| \times |MM| \times |BH| \times |RM| = 3 \times 3 \times 2 \times 3 \times 2 = 108$, totalling to $|S| = 112$ states.

5.3.2.2 Action Definition

The CMA action space is designed to respond to component degradation scenarios considered in this thesis, while preserving the safety of UAS and avoiding a crash. The set of actions available to CMA are $A = \{NOOP, Terminate, LandASAP, LandPract\}$ defined as follows:

- *NoOp: No Operation:* With this action, the UAS continues executing the current flight plan with no change.
- *Terminate:* This action indicates termination of the flight plan to prevent a crash due to failure. The terminate action on an actual UAS could be implemented as deployment of a parachute and cutting motor power. This action immediately renders the UAS inoperable.

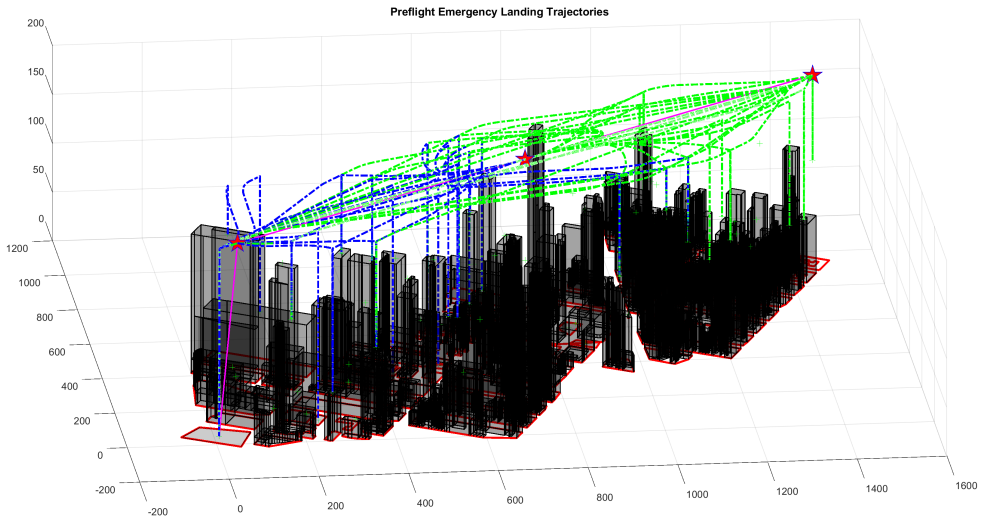

Figure 5.6: Pre-planned emergency landing flight plans from checkpoints shown as stars in the 3-D Manhattan environment. The magenta line is the nominal flight plan. The trajectories to emergency landing sites from checkpoints are shown in blue when the hexacopter is flying towards the destination and in green lines are when the hexacopter is on the return journey.

- *LandPract:* When this action is executed, the UAS utilizes pre-calculated trajectories to reachable emergency landing sites from checkpoints located along the nominal flight plan. These checkpoints are currently shown as ★ in Figure 5.6. In this thesis checkpoints are selected to equally divide flight plan length. For more informed selection of these checkpoints the readers are referred to [36]. Based on current UAS location and its proximity to a checkpoint in the nominal flight plan, an emergency landing site from the list of pre-planned emergency landing trajectories with the maximum RM is selected. An example pre-flight calculated emergency landing flight trajectories for a flight plan is shown in Figure 5.6. This action is computationally efficient because it uses table lookup from a flight plan database generated offline.

- *LandASAP:* When this action is executed, the UAS determines a list of available emergency landing sites within its approximate footprint. The approximate footprint is calculated as described above and as shown in Figure 5.4 with given initial velocity and constrained by battery End of Discharge (EOD) time. $LandASAP$ then plans a minimum time trajectory to reachable emergency landing sites and selects the solution with maximum RM. This step is computationally time consuming and slower process compared to $LandPract$ because of optimization required to find an obstacle free minimum time trajectory over all the available emergency landing sites

5.3.2.3 State Transition Probabilities

CMA MDP state transitions are modeled with the dynamic decision networks (DDNs) shown in Figure 5.8 and their associated state transition probabilities shown in Tables 5.1-5.7 assuming a $1Hz$ update rate. To simplify notation, each transient or absorbing state is labeled with a single feature (C for mission complete, FL for failure, T for flight terminate, E for end). Any other state at time t is defined by

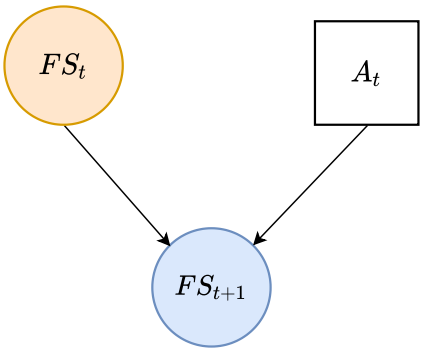

(a) Flight Status

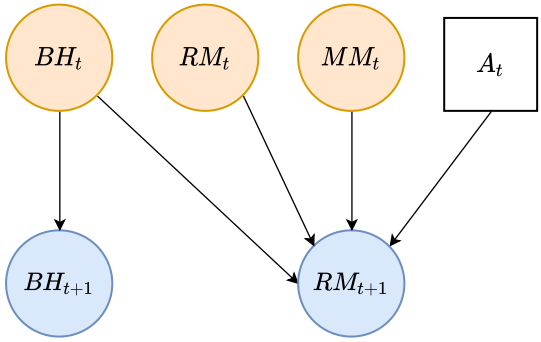

(b) Battery Health and Reachability Margin

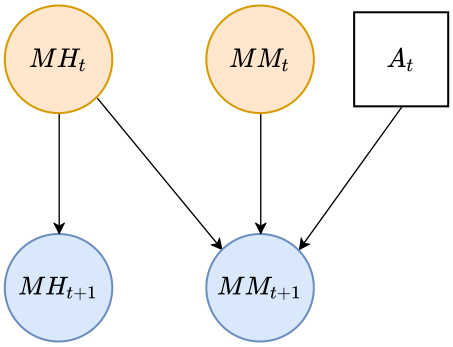

(c) Motor Health and Motor Margin

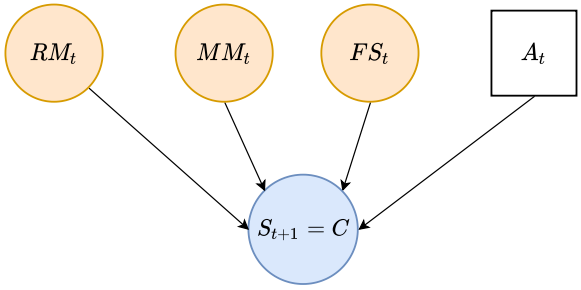

(d) Completion state

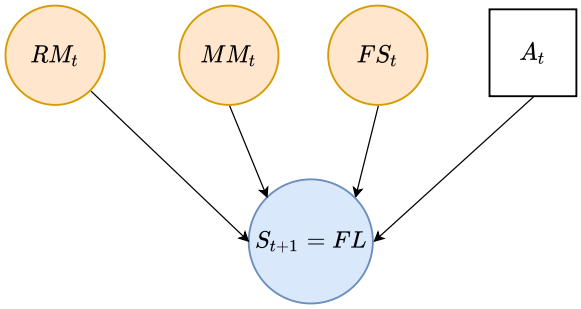

(e) Failure State

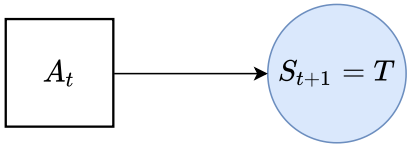

(f) Termination State

Figure 5.7: Dynamic Decision Networks (DDN) capturing dependencies for MDP state feature transitions.

feature set $S_t = \{FS, MH, MM, BH, RM\}_t$. This approach to defining the state transition probabilities rather than manually defining each element of the table exploits conditional independence and improves explainability. The state transitions for full MDP states at time t and $t+1$ are shown in Figure 5.7 and the complete transition probability tables calculated from the DDN's are added in the Appendix

A.1.

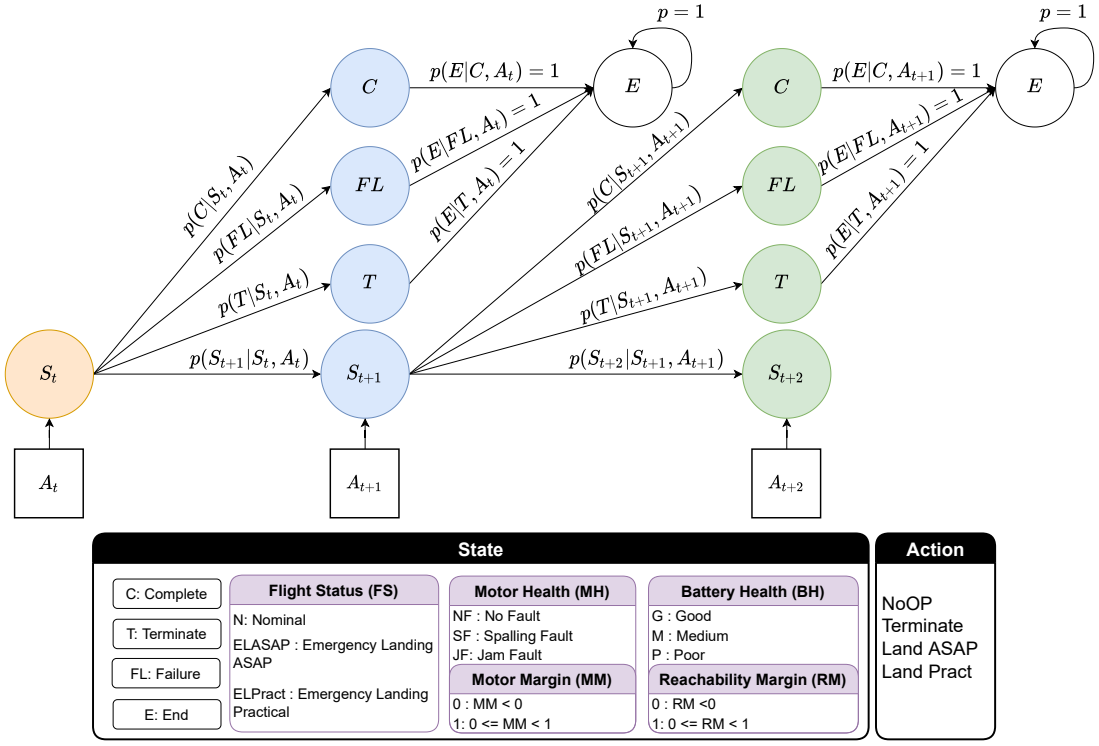

Figure 5.8: State transition graph for the CMA MDP. $C : Complete$, $FL : Failure$, $T : Terminate$ represent terminal / absorbing states, $A_t : Action$

Table 5.1: State Transition Probabilities for FS_{t+1}

		$P(FS_{t+1}\|FS_t, A_t)$			
FS_{t+1}	FS_t	$A_t = NoOp$	$LandASAP$	$LandPract$	$Terminate$
N	N	1	0	0	0
ELASAP	N	0	1	0	0
ELPRACT	N	0	0	1	0
N	ELASAP	0	0	0	0
ELASAP	ELASAP	1	0	0	0
ELPRACT	ELASAP	0	0	0	0
N	ELPRACT	0	0	0	0
ELASAP	ELPRACT	0	1	0	0
ELPRACT	ELPRACT	1	0	0	0

Flight status (FS) as previously described abstractly captures relevant system status information. As shown in Figure 5.7a FS_{t+1} depends only on the flight status

from previous time step FS_t and action A_t executed at time t. State transition probabilities for FS are shown in Table 5.1.

Table 5.2: State Transition Probabilities for BH_{t+1}

BH_{t+1}	BH_t	$P(BH_{t+1}\|BH_t)$
G	G	1
M	G	0
P	G	0
G	M	0
M	M	1
P	M	0
G	P	0
M	P	0
P	P	1

Battery health BH is randomly selected at the start of the simulation as the battery degradation process occurs over an extended duration compared to small UAS flight time. Hence, it is assumed that battery health does not change during flight. The state transition probabilities for BH are shown in Table 5.2. Reachability Margin RM per equation 5.15 contains the t_{EOD} value which is affected by the battery's health and motor margin. RM also contains $t_{FlightTime}$ in its equation which changes per action(A_t) selection. To track changes in reachability margin, RM_t is added to the dynamic decision network. The complete network for RM is shown in Figure 5.7b. State transition values for RM are presented in Table 5.3. State transition probabilities are defined in this manner because if the UAS is in $RM0$, it will remain in $RM0$ unless it performs an emergency landing. Conversely, $RM1$ can transition to $RM0$ with a low probability in flight, which could be attributed to a high wind gust or motor failure. If an emergency landing action is selected, which likely shortens the flight plan, then only $RM0$ can transition to $RM1$. Further, the $LandASAP$ action has a slightly higher probability of transitioning $RM0 -> RM1$ because it generates a trajectory from the current position and not from the checkpoint, thus it has lower $t_{FlightTime}$.

Table 5.3: State Transition Probabilities for RM_{t+1}

$P(RM_{t+1}\|RM_t, BH_t, MM_t, A_t)$							
RM_{t+1}	RM_t	BH_t	MM_t	$A_t = NoOp$	*LandASAP*	*LandPract*	*Terminate*
RM0	RM0	G	MM0	1	0.003	0.0025	0
RM1	RM0	G	MM0	0	0.997	0.9975	0
RM0	RM0	M	MM0	1	0.004	0.0045	0
RM1	RM0	M	MM0	0	0.996	0.9955	0
RM0	RM0	P	MM0	1	0.005	0.0055	0
RM1	RM0	P	MM0	0	0.995	0.9945	0
RM0	RM1	G	MM0	0.005	0.0003	0.00035	0
RM1	RM1	G	MM0	0.995	0.9997	0.99965	0
RM0	RM1	M	MM0	0.01	0.0004	0.00045	0
RM1	RM1	M	MM0	0.99	0.9996	0.99955	0
RM0	RM1	P	MM0	0.05	0.005	0.0055	0
RM1	RM1	P	MM0	0.95	0.9995	0.9945	0
RM0	RM0	G	MM1	1	0.0035	0.004	0
RM1	RM0	G	MM1	0	0.9975	0.996	0
RM0	RM0	M	MM1	1	0.0045	0.005	0
RM1	RM0	M	MM1	0	0.9965	0.995	0
RM0	RM0	P	MM1	1	0.0055	0.006	0
RM1	RM0	P	MM1	0	0.9955	0.994	0
RM0	RM1	G	MM1	5e-05	5e-06	5.5e-06	0
RM1	RM1	G	MM1	0.99995	0.99999	0.99999	0
RM0	RM1	M	MM1	0.0005	5e-05	5.5e-05	0
RM1	RM1	M	MM1	0.9995	0.99995	0.99994	0
RM0	RM1	P	MM1	0.005	0.0004	0.00045	0
RM1	RM1	P	MM1	0.995	0.9996	0.99955	0

Table 5.4: State Transition Probabilities for MH_{t+1}

MH_{t+1}	MH_t	$P(MH_{t+1}\|MH_t)$
NF	NF	0.99995
SF	NF	4.75e-05
JF	NF	0
NF	SF	0
SF	SF	0.99719
JF	SF	0.002809
NF	JF	0
SF	JF	0
JF	JF	1

Table 5.5: State Transition Probabilities for MM_{t+1}

			$P(MM_{t+1}\|MM_t, MH_t, A_t)$			
MM_{t+1}	MM_t	MM_t	$A_t = NoOp$	$LandASAP$	$LandPract$	$Terminate$
MM0	MM0	NF	0	0	0	0
MM1	MM0	NF	1	1	1	0
MM0	MM0	SF	0.995	0.9	0.89	0
MM1	MM0	SF	0.005	0.1	0.11	0
MM0	MM0	JF	1	1	1	0
MM1	MM0	JF	0	0	0	0
MM0	MM1	NF	0	0	0	0
MM1	MM1	NF	1	1	1	0
MM0	MM1	SF	0.002809	0.002	0.0025	0
MM1	MM1	SF	0.99719	0.998	0.9975	0
MM0	MM1	JF	1	1	1	0
MM1	MM1	JF	0	0	0	0

In this research, motor health transitions are dependent on previous time step health as shown in Figure 5.7c. Environmental factors such as temperature, dust, etc. also play an important role in a motor's performance degradation and should be considered in future work. Since motor health is indicated as no-fault NF, spalling fault SF or jam fault JF; any of these faults can occur in flight due to dynamic loading conditions. The transition probability values for MH are presented in Table 5.4. The transition from $NF- > SF$ is obtained from [34]. The probability value for $SF- > JF$ transition was obtained by 1000 simulations of the motor prognosis algorithm presented in Section 3.4.

DDN for motor margin (MM_{t+1}) is shown in Figure 5.7c. MM is defined in equation 5.14 and based on t_{RUL} and $t_{FlightTime}$ values. t_{RUL} is influenced by motor health MH_t and flight duration $t_{FlightTime}$ which depend on action choice, i.e., if an emergency landing is executed flight duration will reduce compared to nominal flight duration. Hence MM_{t+1} depends on action (A_t), motor margin (MM_t) and motor health (MH_t). The transition probability values for MM are shown in Table 5.5. The probability values were estimated similar to RM.

Table 5.6: State Transition Probabilities for C_{t+1}

				$P(C_{t+1}\|FS_t, RM_t, MM_t, A_t)$			
C_{t+1}	FS_t	RM_t	MM_t	$A_t = NoOp$	$LandASAP$	$LandPract$	$Terminate$
C	N	RM0	MM0	0	0	0	0
C	N	RM0	MM1	0	0	0	0
C	N	RM1	MM0	0.08	0.0095	0.009	0
C	N	RM1	MM1	0.1	0.01	0.015	0
C	ELASAP	RM0	MM0	0	0	0	0
C	ELASAP	RM0	MM1	0	0	0	0
C	ELASAP	RM1	MM0	0.095	0	0	0
C	ELASAP	RM1	MM1	0.2	0	0	0
C	ELPRACT	RM0	MM0	0	0	0	0
C	ELPRACT	RM0	MM1	0	0	0	0
C	ELPRACT	RM1	MM0	0.09	0.0095	0	0
C	ELPRACT	RM1	MM1	0.15	0.01	0	0

Table 5.7: State Transition Probabilities for FL_{t+1}

				$P(FL_{t+1}\|FS_t, RM_t, MM_t, A_t)$			
FL_{t+1}	FS_t	RM_t	MM_t	$A_t = NoOp$	$LandASAP$	$LandPract$	$Terminate$
FL	N	RM0	MM0	1	0.0002	0.0002	0
FL	N	RM0	MM1	1	0.0001	0.0003	0
FL	N	RM1	MM0	0.01	0	0	0
FL	N	RM1	MM1	0.001	0	0	0
FL	ELASAP	RM0	MM0	1	0	0	0
FL	ELASAP	RM0	MM1	1	0	0	0
FL	ELASAP	RM1	MM0	0.009	0	0	0
FL	ELASAP	RM1	MM1	0.0001	0	0	0
FL	ELPRACT	RM0	MM0	1	1	0	0
FL	ELPRACT	RM0	MM1	1	1	0	0
FL	ELPRACT	RM1	MM0	0.0095	0.00085	0	0
FL	ELPRACT	RM1	MM1	0.0005	0.00075	0	0

States $S_{t+1} = \{C, FL\}$ depend on RM_t, MM_t, FS_t and A_t as shown in Figures 5.7e and 5.7d. This dependence is based on the ability of the UAS to either complete or fail its existing flight plan inferred from the reachability margin and remaining useful life of the motors. Consider a scenario of a UAS executing an emergency landing. If $RM_t = 0$ there is a high risk of failure. Conversely, if $RM_t = 1$ the probability of

reaching the completion state is high. The transition probability values for C and FL are shown in Tables 5.6 and 5.7, respectively. These transition probability values are estimated based on reaching completion or failure in one time-step versus the remaining flight plan. Lastly, the termination state (T) is reached deterministically when action $A_t = Terminate$ is executed as shown in Figure 5.7f.

Overall state transition probability values are calculated from the DDNs as shown in the following steps. Define $S'_{t+1}, S'_t = (\ S_{t+1}, S_t \neq \{C, T, FL\})$ and $A'_t = (A_t \neq Terminate)$. The state transition probability equation can be written for four cases as follows:

- Suppose $S_{t+1}, S_t \neq \{C, T, FL\}$. Then

$$\begin{aligned} &P(S'_{t+1}|S'_t, A'_t) = P(FS_{t+1}|FS_t, A'_t)P(MH_{t+1}|MH_t)\times \\ &P(MM_{t+1}|MM_t, MH_t, A'_t)P(BH_{t+1}|BH_t)P(RM_{t+1}|RM_t, BH_t, MM_t, A'_t) \\ &P(S'_{t+1}|S'_t, A_t = Terminate) = 0 \end{aligned} \tag{5.16}$$

- Suppose $S_{t+1} \neq \{C, T, FL\}$, $S_t = \{C, T, FL\}$. Then
  Since all the terminal states $\{C, T, FL\}$ are absorbing states, no transitions occur out of them, and can be written as :

$$P(S'_{t+1}|S_t = \{C, T, FL\}, A_t) = 0 \tag{5.17}$$

- Suppose $S_{t+1} = \{C, T, FL\}$, $S_t \neq \{C, T, FL\}$. Then

$$\begin{aligned} P(C|S'_t, A'_t) &= P(C|FS_t, MM_t, RM_t, A'_t) \\ P(FL|S'_t, A'_t) &= P(FL|FS_t, MM_t, RM_t, A'_t) \\ P(T|S'_t, A_t = Terminate) &= 1 \end{aligned} \tag{5.18}$$

- Suppose $S_{t+1}, S_t = \{C, T, FL, E\}$. As the end states are absorbing state they are defined as follows:

$$\begin{aligned} P(E|C, T, FL, A_t) &= 1 \\ P(E|E, A_t) &= 1 \end{aligned} \tag{5.19}$$

The MDP state transition probabilities are represented in a tabular format for each actions. Each row is normalized to ensure it sums to one. The complete transition probability tables calculated from the DDN's are added in the Appendix A.1. Note that the DDN probability values defined here serve as initial values; in practice these values would be refined further from a large database of flight test data.

5.3.2.4 Reward Function

The MDP reward function incentivizes actions that prevent UAS failure in degraded conditions or rewards continuation of the current flight plan if possible with acceptable risk. The reward function is formulated as follows:

$$R(S, A) = R(S) + R(A) \tag{5.20}$$

$$R(S) = \begin{cases} w_E(S) f_E(S), & S \in S_E \\ w_S^T f_S(S), & S \in S_S \end{cases}, \; R(A) = w_A(A) f_A(A) \tag{5.21}$$

$$w_E(S) + w_S + w_A(A) = 1 \tag{5.22}$$

$$f_E(S) = \begin{cases} 1, & S = C \\ -0.1, & S = T \\ -1, & S = FL \\ 0, & S = E \end{cases}, \; f_A(A) = \begin{cases} 1, & A = NoOp \\ -1, & A = Terminate \\ -0.5, & A = LandASAP \\ 0.5, & A = LandPract \end{cases} \tag{5.23}$$

$$f_S(S) = [f_{S_{FS}}(FS), f_{S_{MH}}(MH), f_{S_{MM}}(MM), f_{S_{BH}}(BH), f_{S_{RM}}(RM)]' \tag{5.24}$$

$$f_{S_{FS}}(FS) = \begin{cases} 1, & FS = Nominal \\ -1, & FS = \{ELPract, ELASAP\} \end{cases}, f_{S_{MH}} = \begin{cases} 1, & MH = NF \\ 0, & MH = SF \\ -1, & MH = JF \end{cases} \tag{5.25}$$

$$f_{S_{MM}}(MM) = \begin{cases} 1, & MM = MM1 \\ -1, & MM = MM0 \end{cases}, f_{S_{BH}} = \begin{cases} 1, & BH = G \\ 0, & BH = M \\ -1, & BH = P \end{cases} \tag{5.26}$$

$$f_{S_RM}(RM) = \begin{cases} 1, & RM = RM1 \\ -1, & RM = RM0 \end{cases} \tag{5.27}$$

The values for MDP states were chosen to favor completion of the nominal mission without interruption. However, if there is any occurrence of an off-nominal scenario such as degraded battery or motor failure, these states are penalized to encourage safe nearby landing. Similarly, values for action were chosen to continue the mission without interruption when possible and to prefer emergency landing actions over

flight termination. The difference in values assigned for $LandASAP$ and $LandPract$ action is because of the higher computation cost of executing $LandASAP$ compared to $LandPract$. Weights w_E, w_S and w_A were selected based on a sensitivity analysis described below.

5.3.2.5 Optimal Policy

Given the computational complexity of value iteration ($\mathcal{O}(|S|^2|A|)$) and modest size of our state and action space, iterative algorithms can easily find an optimal policy within tractable time. CMA MDP optimal policy π^* is calculated offline using value iteration with a decision epoch of $1Hz$. The reward function weights are tuned based on the observed optimal action in quadrants of the Figure 5.9 to obtain a desirable behavior set. The process of tuning the weights could be defined in a context similar to inverse reinforcement learning [6], where the agent infers it reward function given its policy or observed behavior. Similarly, in this research the agent's role is played by the human/engineer who tunes the reward function to obtain a desired behaviour of the MDP policy. The quadrant categorization shown is based on RM and MM values starting with green as Quadrant I and moving counter-clockwise for the numbering convention.

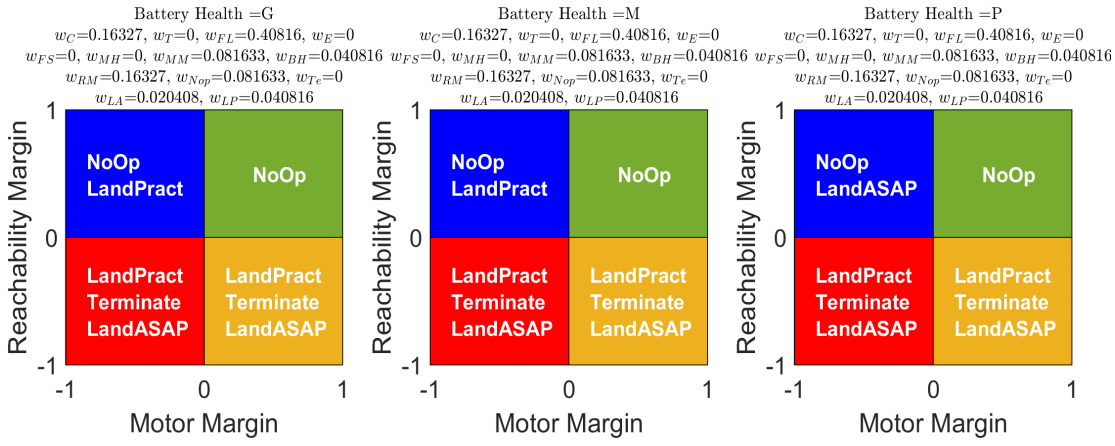

Figure 5.9: Reward sensitivity analysis, where the color of quadrant signifies: ■ : Safe region, ■ : Hazardous region, ■ : Critical region, ■ : Hyper Critical region,

Quad I is classified as *Safe* with $RM \geq 0$,$MM \geq 0$. $RM \geq 0$ indicates the UAS will have sufficient battery energy for the rest of the flight plan. $MM \geq 0$ indicates all motors will be operational for the rest of the flight plan. Therefore, in this region, the UAS is highly likely to complete its flight plan. An optimal action in this region expects to continue the current flight plan.

Quad II is classified as *Hazardous* with $RM \geq 0$,$MM < 0$. $RM \geq 0$ indicates the UAS will have sufficient battery energy for the rest of the flight plan. $MM < 0$ implies either one motor has failed or will be failing soon and not survive the rest of the flight plan. Therefore, the UAS is less likely to complete its flight plan due to a greater risk of system failure or instability. The expected optimal action in this region would be to either continue the current flight plan or execute an emergency landing. Quad III is the *Hyper-Critical* region with $RM < 0$ and $MM < 0$. $RM < 0$ indicates the UAS has insufficient battery energy to complete the flight plan. $MM < 0$ implies either one motor has failed or will be failing soon and not survive the rest of the flight plan. The UAS is likely to fail or crash due to insufficient battery energy and loss of single motor thrust. In this region expected behavior of an optimal action would be either to perform an emergency landing or flight termination to prevent a loss-of-control crash that likely imparts significant kinetic energy.

Lastly, Quad IV is the *Critical* region with $RM < 0$,$MM \geq 0$. $RM < 0$ indicates the UAS has insufficient battery energy to complete the flight plan. $MM \geq 0$ indicates all motors will be operational for the rest of the flight plan. The UAS is likely to fail due to insufficient battery energy to complete the flight plan. In this region, the UAS will likely not be able to complete its original mission but might safely execute an emergency landing. Hence, the expected behavior of the optimal action would be to perform an emergency landing or terminate to prevent a crash

Behaviour of the optimal policy and its sensitivity for different values of weights w_E,w_S and w_A were examined. Final values of weights selected are shown below and

their desired behaviour is shown in Figure 5.9:

$$w_E(S) = \begin{cases} 0.163, & S = C \\ 0.408, & S = FL \\ 0, & S = \{T, E\} \end{cases}, w_A(A) = \begin{cases} 0.082, & A = NoOp \\ 0, & A = Terminate \\ 0.02, & A = LandASAP \\ 0.041, & A = LandPract \end{cases} \tag{5.28}$$

$$w_S = [0,\ 0,\ 0.082,\ 0.041,\ 0.163]' \tag{5.29}$$

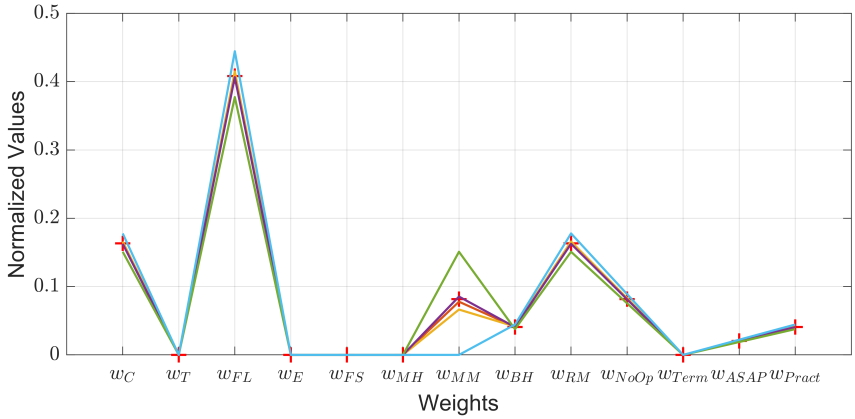

Figure 5.10: Normalized values of different weights

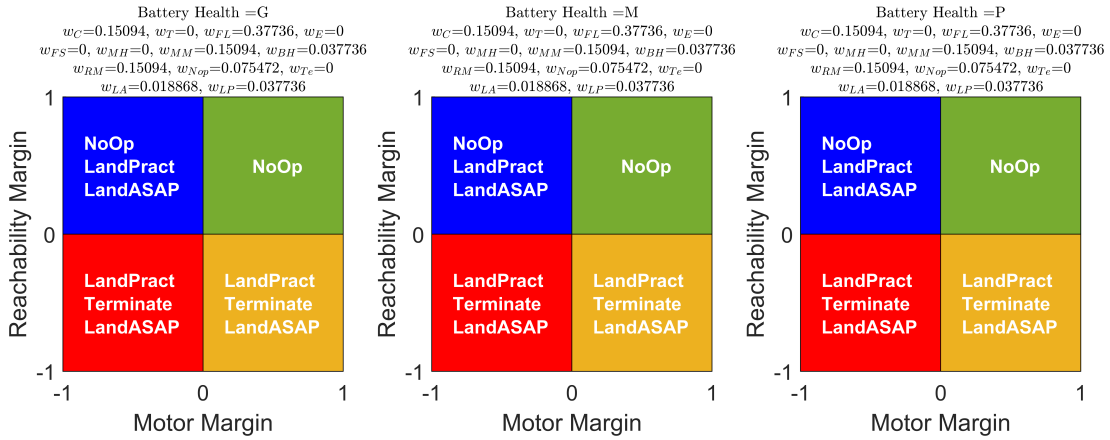

Figure 5.11: Reward sensitivity analysis, where the color of quadrant signify ■ : Safe region, ■ : Hazardous region, ■ : Critical region, ■ : Hyper Critical region,

Since weights are normalized by their sum, the sensitivity of optimal policy ex-

pected behaviour with respect to variation in weight values in equation 5.11 is also investigated. Figure 5.10 shows the variation in weights while changing the value of only a single weight w_{MM} as an example. There exists a coupling effect because the weights are normalized by their sum. The red cross in Figure 5.10 is representative of weights used in Figure 5.9 as is the final policy used in simulations.

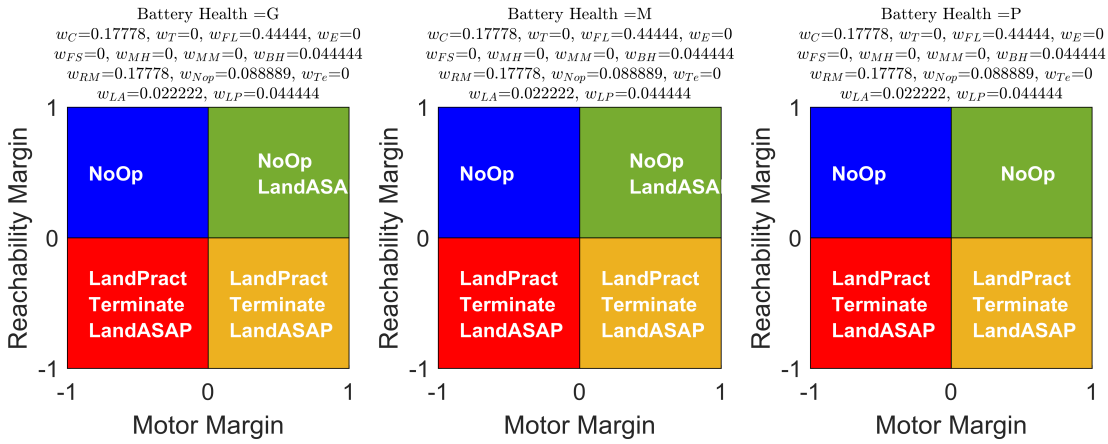

Figure 5.12: Reward sensitivity analysis, where ■ : Safe region, ■ : Hazardous region, ■ : Critical region, ■ : Hyper Critical region,

The policy behaviour represented by the green line of weights in Figure 5.10 is shown in Figure 5.11. By setting w_{MM} to a higher value, $LandASAP$ is also included in Quad II for Good and Medium battery health conditions thus being conservative. Similarly, the policy behaviour represented by the light blue line in Figure 5.10 is shown in Figure 5.12. With w_{MM} set to zero, no consideration of emergency landing is made in Quad II. However, $LandASAP$ is recommended in Quad I displaying very conservative behaviour. We can conclude the reward function terms are not conditionally independent so changing one weight can also change other behaviors.

As snippet of the full MDP policy is shown in Figure 5.13, with the recommended optimal action $LandPract$ from state $S_t = \{N, NF, MM0, G, RM0\}$. Both $MM < 0$ and $RM < 0$ indicate that the UAS is in critical condition. The LiPo batteries have insufficient energy to complete the nominal flight plan, and one motor has either ceased operation or its t_{RUL} is inadequate to complete the flight plan. Hence, the

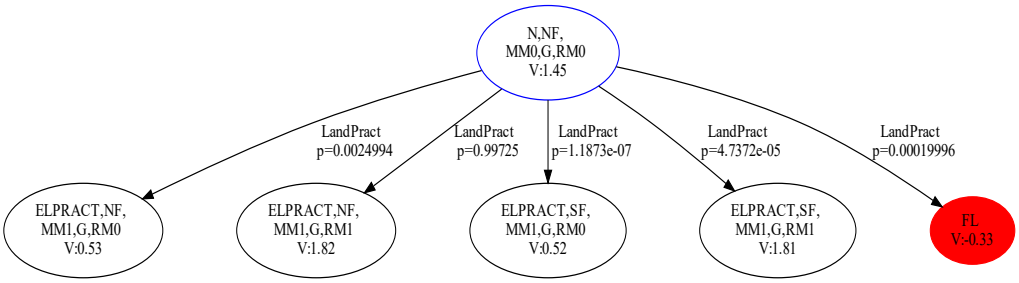

Figure 5.13: Optimal action that is executed from S_t ={N, NF, $MM0$, G, $RM0$}

best action for the UAS is to execute $LandPract$, as the battery health is good. With the selection of this action, an emergency landing flight plan from the database of a much shorter duration than the nominal flight plan is chosen.

5.3.3 Model-Free CMA

This thesis briefly explores a model-free CMA formulation. For the model-free method a slightly different formulation of state space was utilized. The Flight Status (FS) is considered as the flight completion status of the UAS in the flight plan and is discretized into four bins [$0 \leq FS < 25, 25 \leq FS < 50, 50 \leq FS < 75, 75 \leq FS \leq 75$]. Similarly the Reachability Margin (RM) is discretized into four bins [$0 \leq RM < 25, 25 \leq RM < 50, 50 \leq RM < 75, 75 \leq RM \leq 75$]. Q-learning from [69] is used to determine the optimal policy for the model-free CMA.

Q-learning was conducted on 10000 episodes in the high fidelity simulator. The parameters for Q-learning were set to following values: step size $\alpha = 0.8$, discount factor $\gamma = 0.9$ and epsilon greedy parameter $\epsilon = 0.01$. All the episodes started from a single initial location. The training was conducted for a single flight plan. Figure 5.14 shows the average sum of reward over the number of episodes. It can be seen that after 1000 episodes the average sum of rewards settles so there is no more learning. Upon further investigation it was observed that only a few initial states of the MDP were explored. From the results it is inferred that because of aggregation of states in the defined MDP, exploration is not motivated while learning. Further discretization

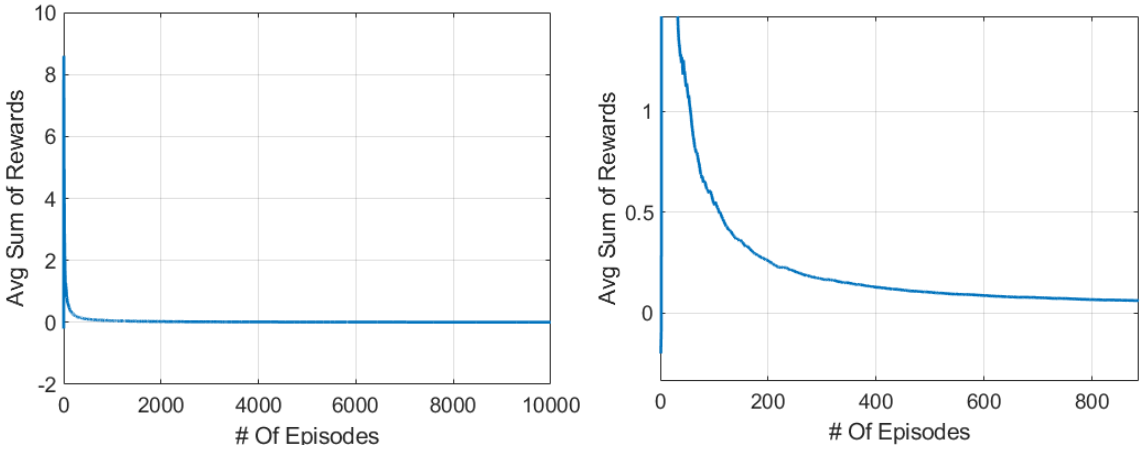

Figure 5.14: Average reward over different episodes, (b) is expanded view of (a)

of the state space is required to enable exploration and modifying the reward function appropriately. No further work toward a model-free CMA MDP is pursued in this thesis.

5.4 Simulations

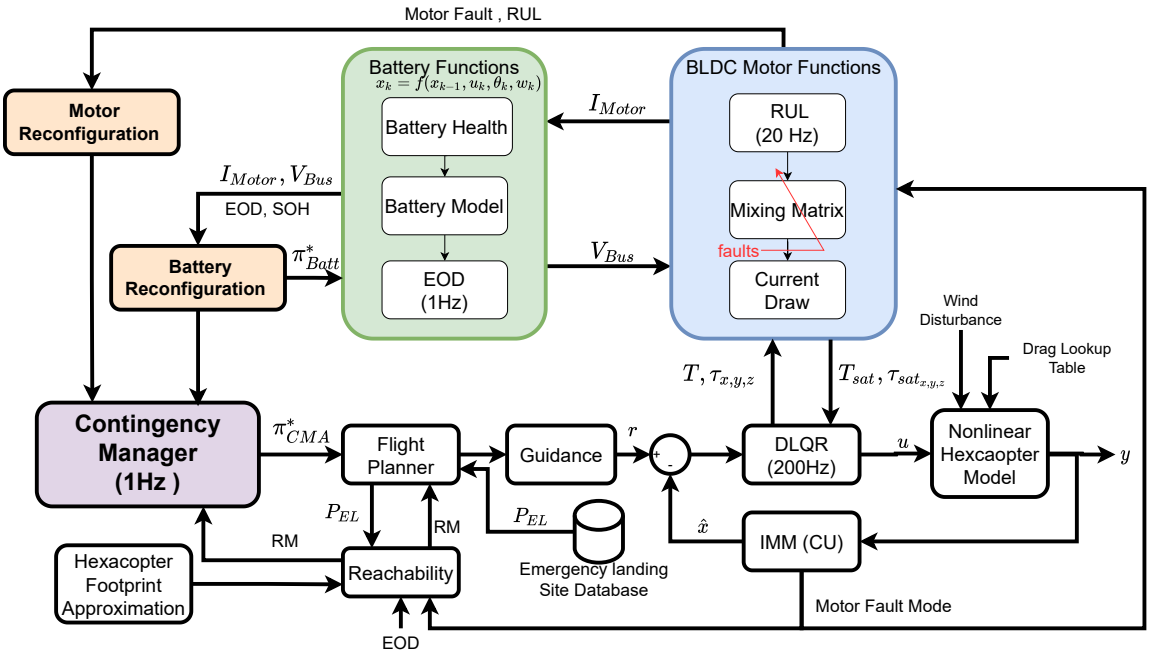

Figure 5.15: System diagram for simulating MDP policies

Before CMA is deployed on a UAS, rigorous testing of CMA is required in a simulated environment. The simulation environment is written in Matlab from scratch to enable utilization of all the experimentally validated models of hexacopter i.e., Lipo battery model and propulsion system model described in Chapter IV, the drag data converted into look-up tables obtained from wind tunnel experiments described in Chapter II .The power source of hexacopter is two $3s$ battery packs in parallel. This UAS configuration was chosen as it offers redundancy in the propulsion and power source.

Figure 5.15 shows the high fidelity simulation control loop developed by us in Matlab for this thesis. The simulation starts from the Flight Planner providing a package delivery flight trajectory to the guidance module of the UAS. This flight trajectory generated uses a trapezoidal velocity profile with limits on velocity and accelerations. These limits are obtained from previous experiments with the actual hexacopter hardware. Along with the trajectory, the flight planner also receives information about the emergency landing sites from the Emergency Landing Site Database, the contingency action from Contingency Manager (developed offline), and the Reachability module. Based on the appropriate policy action recommended by the Contingency Manage, the flight planner provides a new flight plan to the hexacopter's Guidance-Navigation-Control (GNC) module.

The battery function block contains sub-modules which consist of equivalent circuit resistance model of LiPo battery, battery health identification module, and End of Discharge calculator. The motor function module consists of sub-modules to determine the motor's remaining useful life (RUL), reconfiguration of hexacopter mixing matrix, motor thrust saturation, and motor current draw based on thrust requirements.

The rotor fault is diagnosed using a custom Interacting Multiple Model (IMM) [65] filter developed by the University of Colorado. The IMM is capable of delivering

sufficient accuracy while remaining computationally tractable. The employed IMM maintains a probability distribution over seven regimes or modes that the hexacopter operates in. The first mode corresponds to nominal dynamics, while the remaining six modes correspond to dynamics under a failed rotor (six for a hexacopter). In the MDP setting, full observability over rotor health is assumed and thus the maximum a posteriori (MAP) estimate is used to determine the hexacopter mode.

The system modules are simulated at different rates to mirror actual flight hardware. The GNC module operates as $200Hz$. Battery end of discharge (EOD) calculations are updated at $1Hz$, as EOD variation is not changed instantaneously. The Contingency Manager runs at $1Hz$. The current Matlab simulations have a series-parallel battery pack without switching between the batteries, using both; hence the Battery Reconfiguration is assumed to operate at the same rate as the GNC module. To implement the different operating rates of the modules in Matlab, the program structure consists of an outer GNC while loop which runs at 200 Hz i.e. with $\Delta t = 0.005sec$ time step increments until the flight plan is terminated or finished. Within this while loop, the function modules shown in 5.15 are written sequentially and checks are made at each time step to see if a particular module needs execution. All the modules are executed at the first step, and checks are performed for the following time steps. Consider an example of the Contingency Manager running at $1Hz$ or every $1sec$. At $t = 0$, it is executed, then at $t = 1sec$ or 200 timesteps of the while loop, the Contingency Manager is again executed, and the process continues. Figure 5.16 shows the implementation of π^*. During each epoch, $NoOp$ action is executed in the code to prevent repeated execution of the same action from the decision epoch.

The simulation's probability of a spalling fault occurrence is set to $P(SF|NF) = 0.5$. Note that this probability is higher than that used to find the optimal MDP policy per Table 5.4. Simulation results thus represent a higher frequency of fault occurrence than expected under normal circumstances. This higher sampling rate is

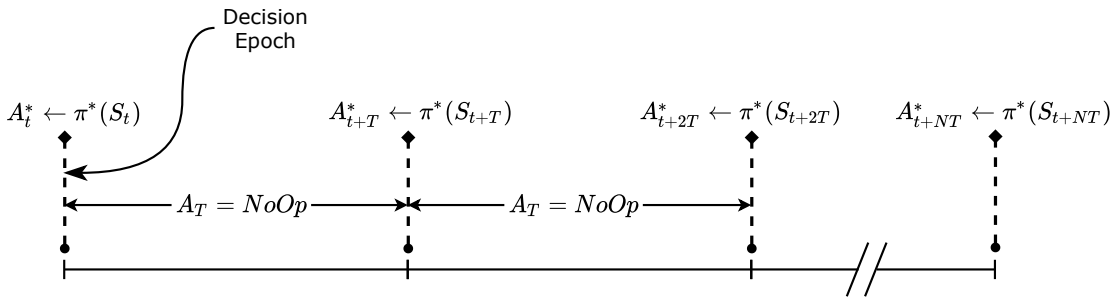

Figure 5.16: Implementation of optimal policy in simulation where $T = 1Hz$

used to reduce the number of simulations necessary to evaluate the performance of the policy. Lastly, Failure in the simulation occurs when the UAS is unstable or the available battery voltage is below the preset threshold voltage.

5.5 Results

A total of 930 Monte Carlo simulations were conducted with an equal split using the CMA MDP optimal policy and a simple baseline policy of *NoOp*. Parameters varied in these simulations include different flight plans and associated safety margin, wind speed, direction, gust category, individual battery health, ambient temperature, time of motor failure during flight and location of motor failure on the hexacopter. Figure 5.17 shows an example histogram of wind speed and direction used over the MC simulations. From the MC simulations, two scenarios are presented to highlight the benefit of CMA.

5.5.1 Scenario I : Execution of *LandPract*

In Scenario I UAS LiPo batteries are in the medium health condition and experiences an in-flight single motor failure. Plots from Scenario I are shown in Figure **??** - 5.24. The hexacopter is provided with a package delivery flight trajecoty by the Fight Planner shown in solid lines in Figure 5.18.

The hexacopter experiences a spalling fault in motor No.3 at $175sec$. This fault

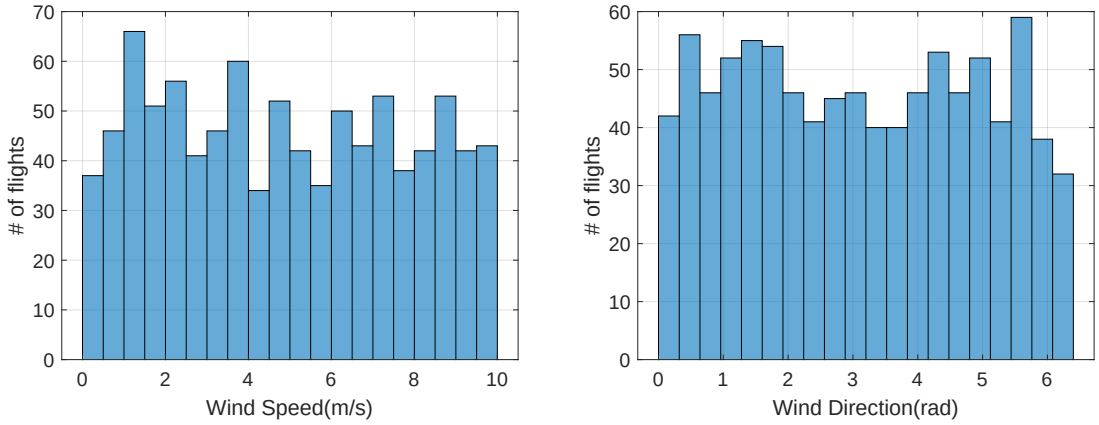

(a) (b)

Figure 5.17: Wind speed and direction distribution for MC simulations

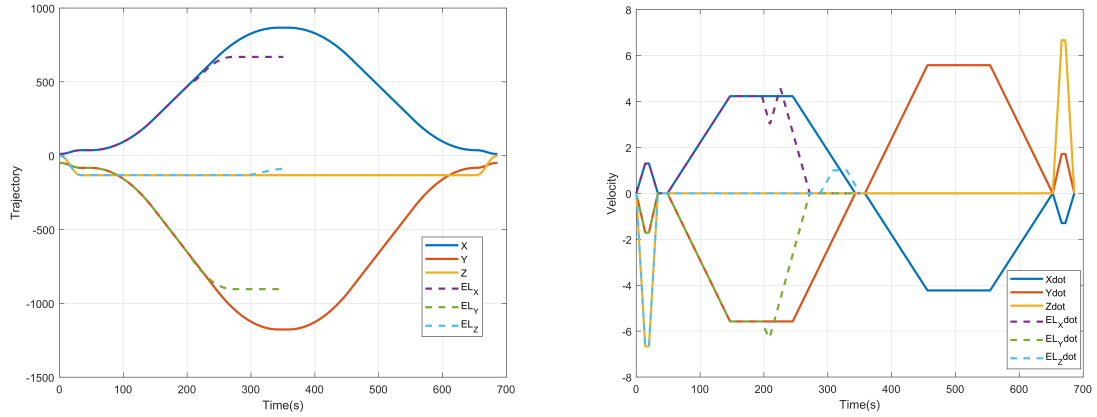

(a) (b)

Figure 5.18: Figure showing the Original flight plan in solid lines and the executed flight plan in dotted line for Scenario I

is detected and triggers the prognosis algorithm to calculate t_{RUL} for motor No.3. The CMA recommends no action at this time-step. Due to continued operation, motor No. 3 eventually jams at $192sec$, and the IMM detects and isolates the jam fault. This detection of jam fault by IMM sets the fault flag to true; shown as a step function in Figure 5.19 and the hexacopter then reconfigures to an appropriate quad-copter configuration. However, the remaining four motors still have to generate the same thrust as the six motors to maintain level flight. This causes the remaining four

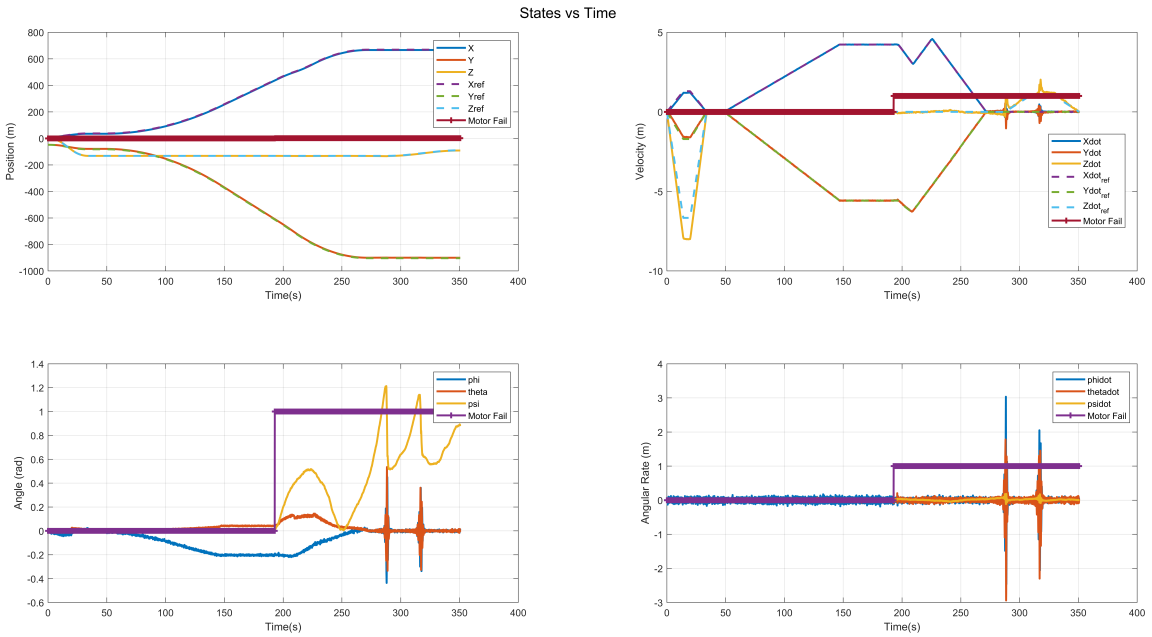

Figure 5.19: Time series plot of hexacopter states for Scenario I. The step function shown in the plots is indicative of when the motor fault flag is raised by fault identification module.

operational motors to produce higher thrust (middle plot Figure 5.20) than nominal operations, increasing current draw as shown in the bottom plot of Figure 5.20. This high current demand causes the battery voltage to drop show in Figure 5.21. Consequently, the EOD values also drop drastically below the black line shown in Figure 5.22, indicating battery energy is insufficient to complete the flight plan and will lead to a crash. The CMA recommends *LandPract* action as seen in Figure 5.23. On execution of *LandPract* trajectories defined offline available in onboard database, are scanned through to determine an emergency landing site with a minimum reachability margin. After selecting the feasible emergency landing site and the Flight Planner feeds the new flight trajectory (dashed line in Figure 5.19), which is shorter than the original flight plan (seen as a sudden drop in the black line in Figure 5.22) got hexacopters GNC module. The hexacopter performs a successful emergency landing with the new flight plan shown in Figure 5.24. As the hexacopter was closer to the middle checkpoint, an emergency landing site in proximity of middle checkpoint is

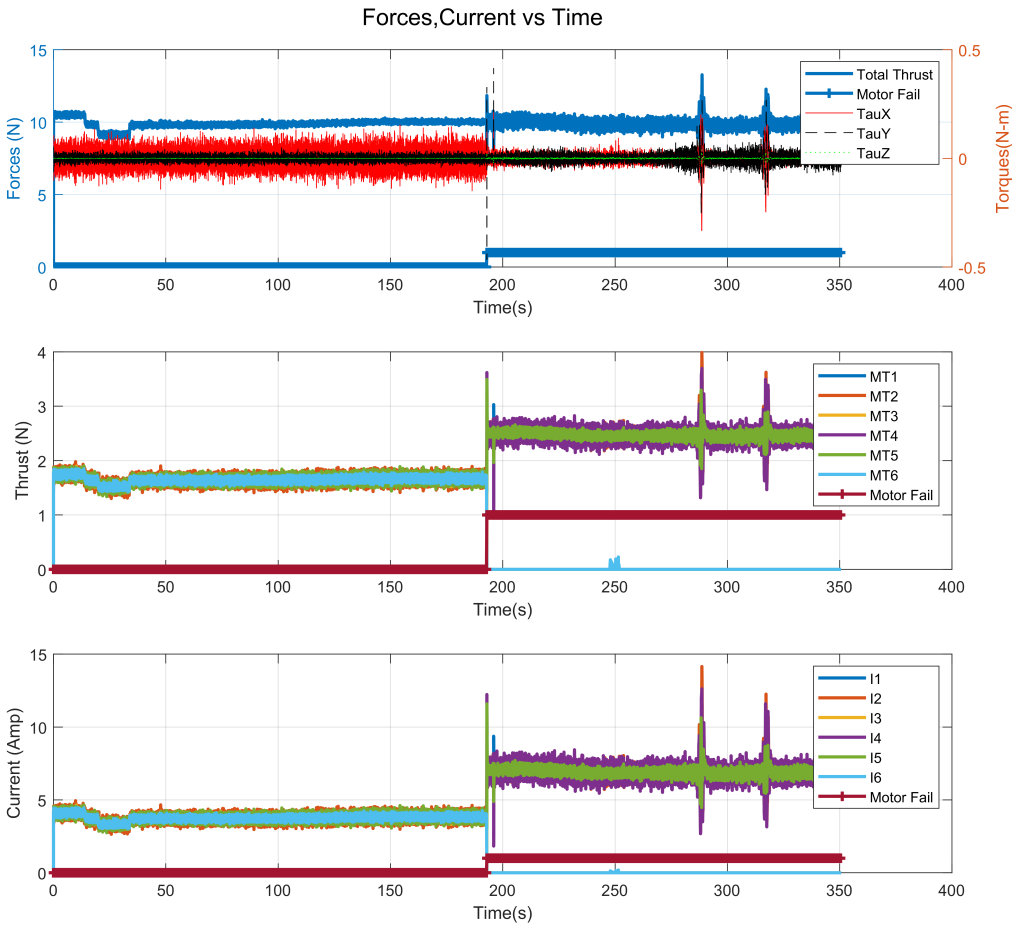

Figure 5.20: Time series plot of hexacopter forces and torques for Scenario I

selected. Thus, with contingency management MDP, the system prevented the crash due to insufficient energy and landed safely.

5.5.2 Scenario II : Execution of *LandASAP*

Similar to Scenario I in Scenario II during the package delivery mission by hexacopter, the LiPo batteries are identified to be in medium health condition and an in-flight motor failure is experienced.

At $525sec$ a spalling fault is detected for a motor of the hexacopter, triggering execution of *LandPract* action by the CMA as shown in Figure 5.26. In this particular scenario, the *LandPract* action leads to selecting an emergency landing site from the database closer to the first checkpoint as the hexacopter is closer to the home

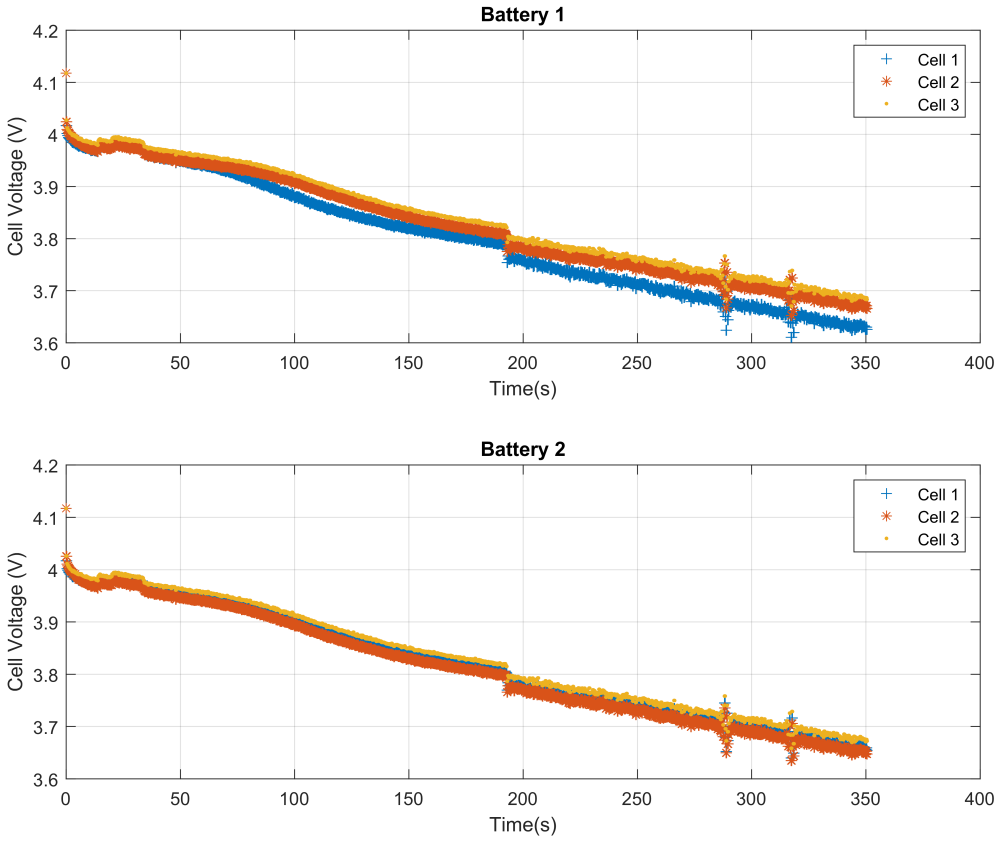

Figure 5.21: Time series plot of Cell voltages in the battery pack for Scenario I

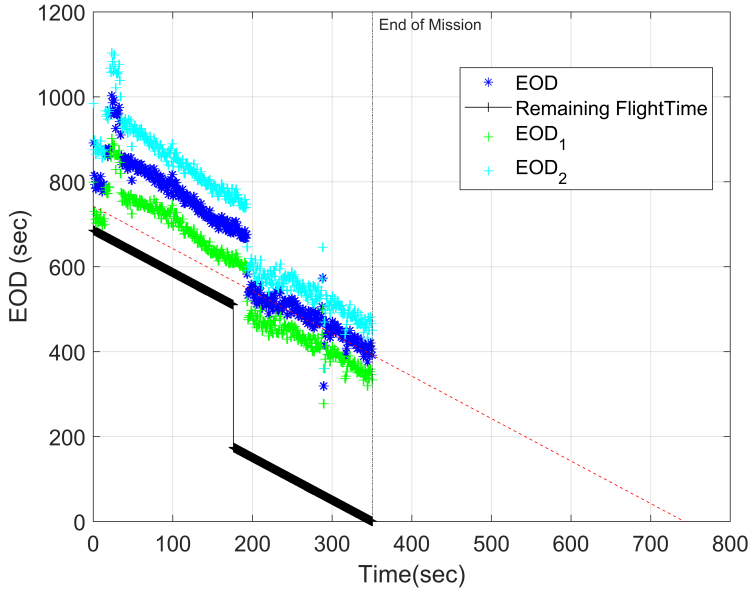

Figure 5.22: End of Discharge (EOD) plot for hexacopter battery pack for Scenario I

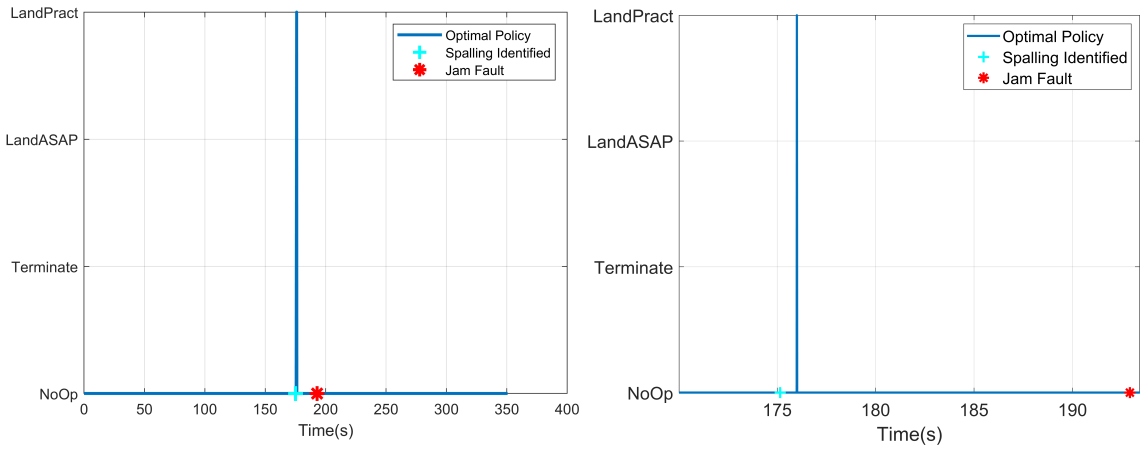

(a) Full flight plan time duration (b) Close up

Figure 5.23: Optimal actions recommended by CMA MDP to hexacopter for Scenario I

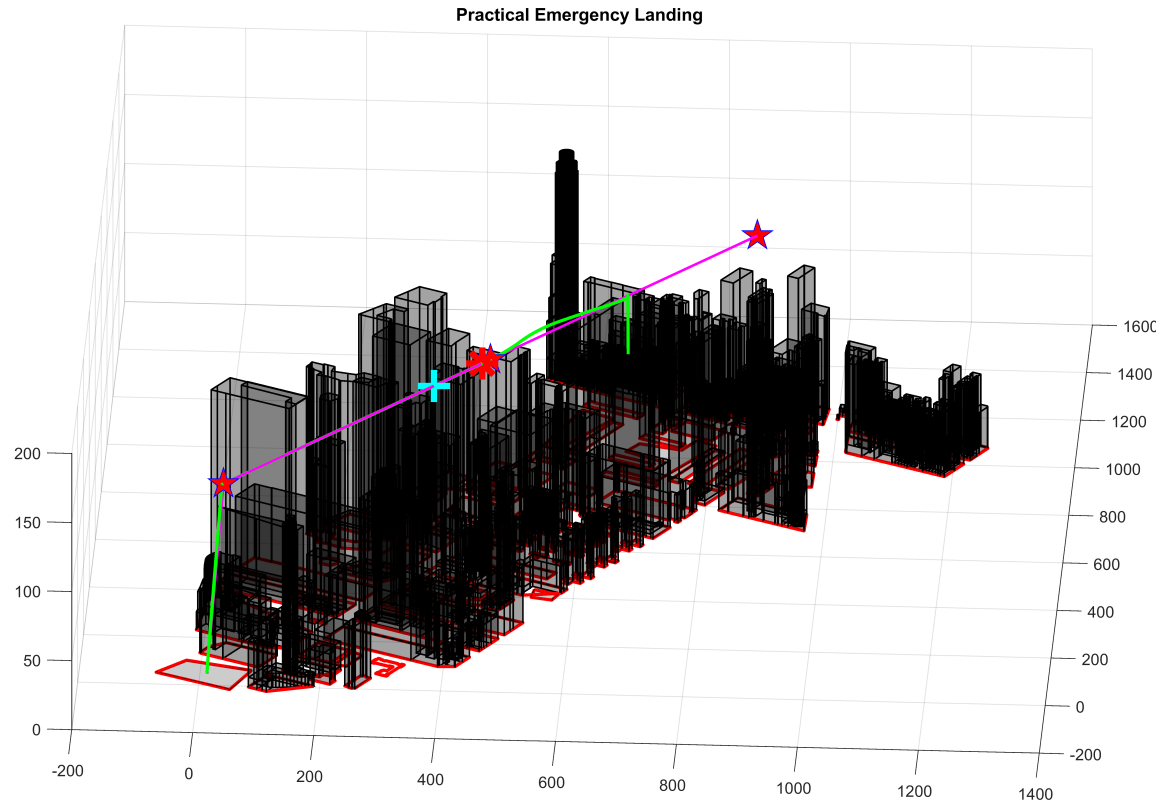

Figure 5.24: 3D plot showing execution of emergency landing in simulation where Actual Flight Plan, Nominal Flight Plan,★- Checkpoints, for Scenario I

location. In contrast to the previous scenario where the flight time decreases on selection of *LandPract*, there is an increase in flight time due to the emergency

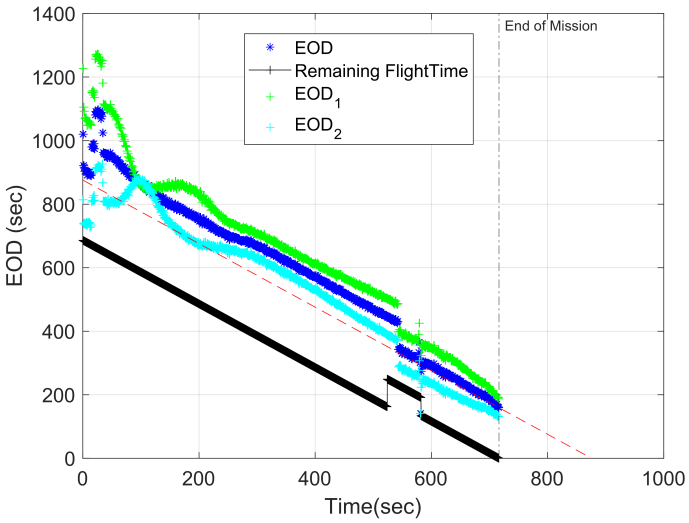

Figure 5.25: End of Discharge (EOD) plot for hexacopter battery pack for Scenario II

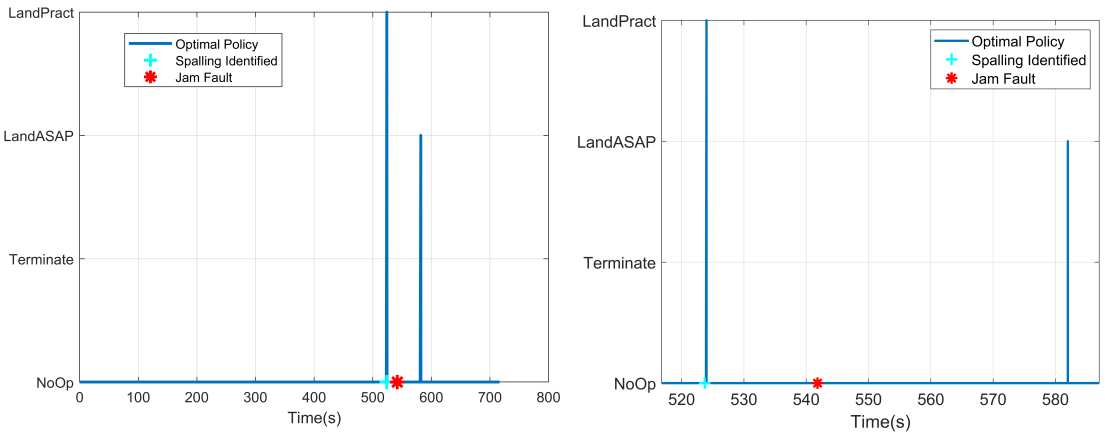

(a) Full flight plan time duration (b) Close up

Figure 5.26: Optimal actions recommended by CMA MDP to hexacopter for Scenario II

landing site selection. As a result, once a jam fault occurs in the spalled motor at 542*sec*, it results in increase of current consumption due to hexacopter reconfiguring to quadcopter and there is an increase in force demand from the quadrotor as shown in Figure 5.27. As a result, the EOD drastically drops as seen in Figure 5.25. In this faulted state, the hexacopter experiences a disturbance leading to higher current demanded by the motors while stabilizing, causes the battery voltage to drop suddenly

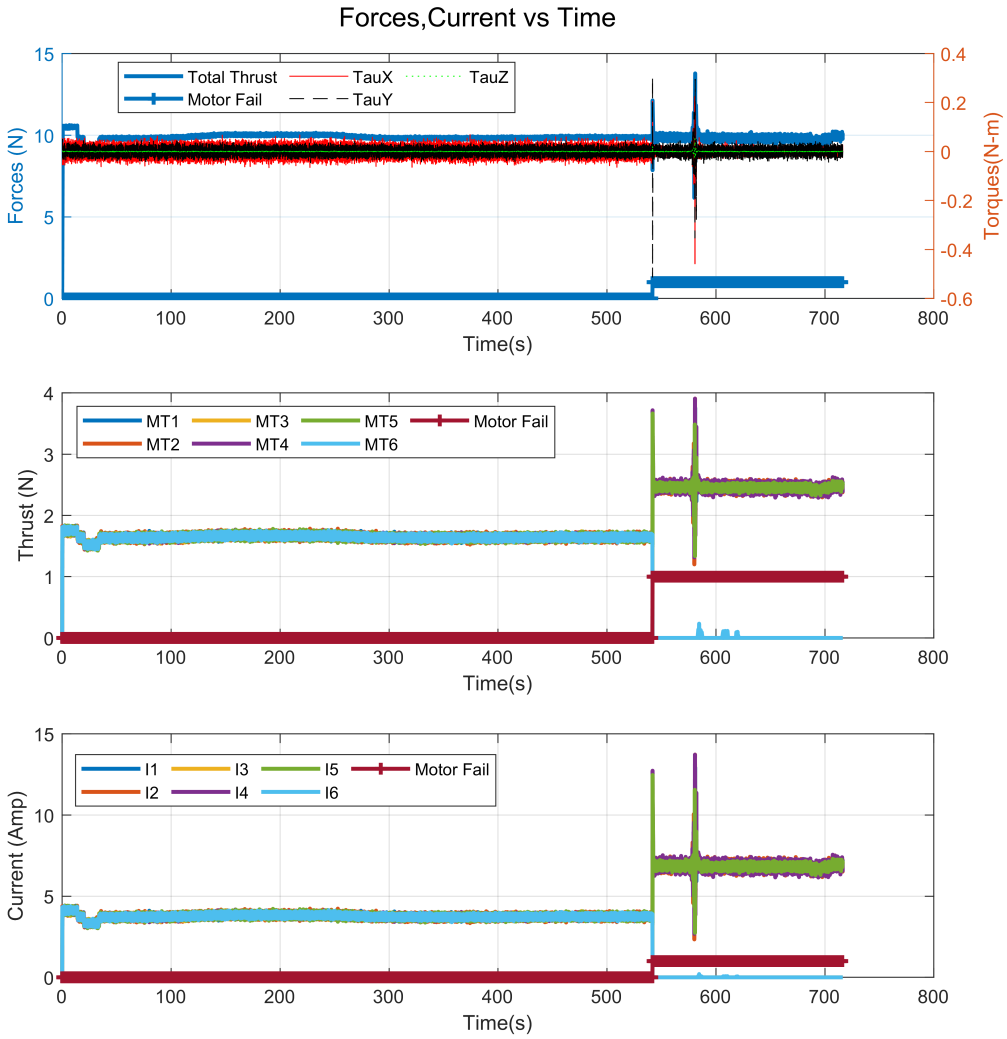

Figure 5.27: Time series plot of hexacopter forces and torques for Scenario II

and results in lower battery EOD values. This lower battery EOD value indicates insufficient battery energy for the flight plan. At this timestep *LandASAP* action is recommended by CMA as shown in Figure 5.26. Upon execution of *LandASAP* action, minimum time trajectories to emergency landing sites within the approximate footprint of UAS are calculated online, shown in Figure 5.28. The final execution of the emergency landing site is shown in Figure 5.29.

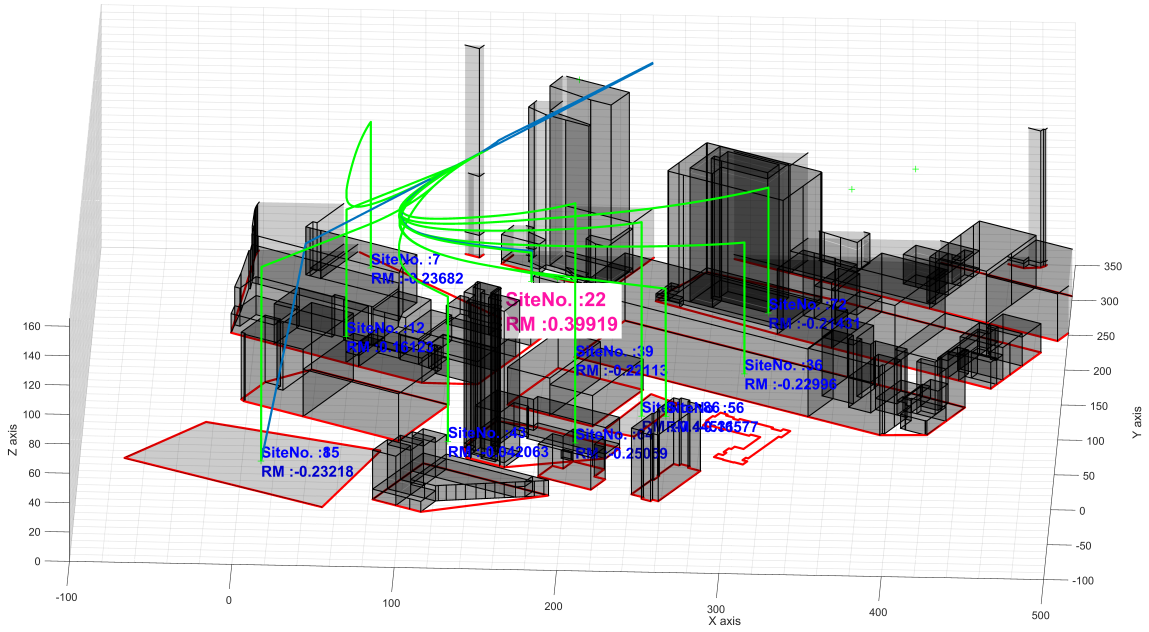

Figure 5.28: Emergency landing trajectories calculated when *LandASAP* action is executed in Scenario II

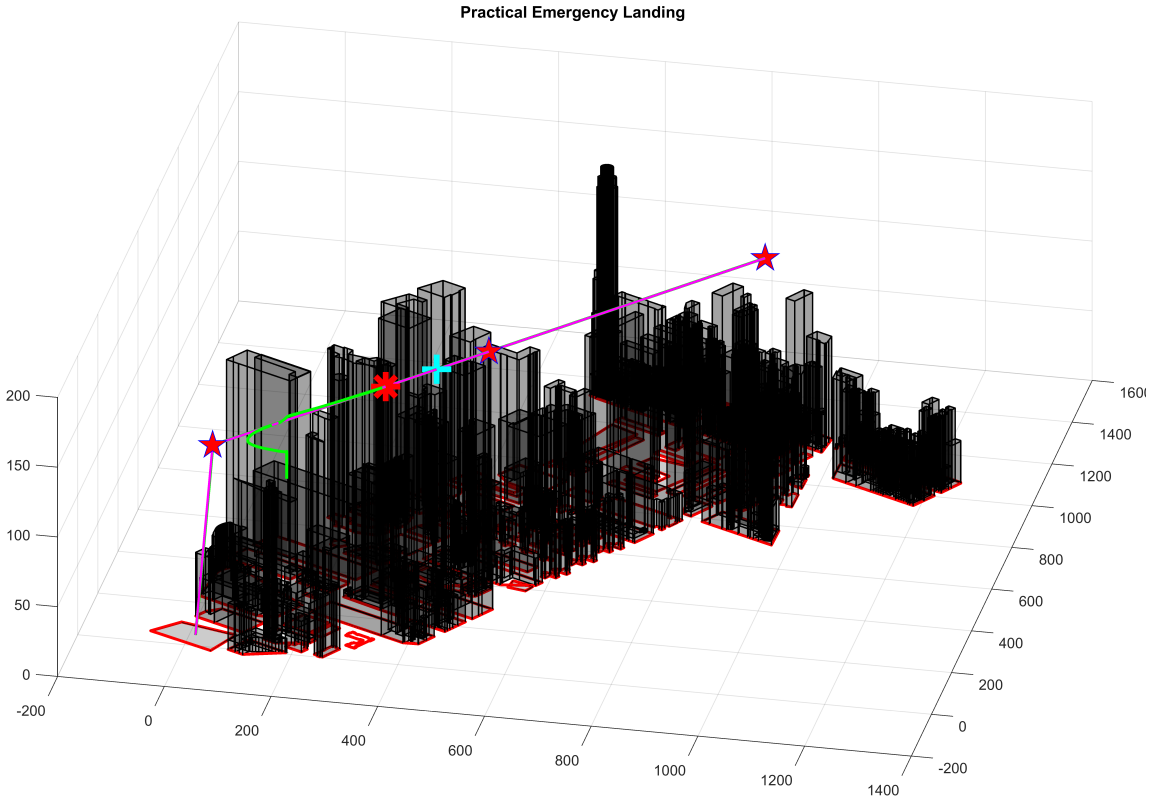

Figure 5.29: 3D plot showing execution of emergency landing in simulation where Actual Flight Plan, Nominal Flight Plan,★- Checkpoints, for Scenario II

5.5.3 Monte Carlo Simulations

The overall performance of the CMA is compared to a Baseline policy of *NoOp* action performing Monte Carlo Simulations varying mission profiles, wind speed and direction, battery health, motor failure location on the hexacopter and time of motor failure. Different metrics used for comparing their performance include Failure Rate, Average Reward and Min Instantaneous Reward over different battery health conditions.

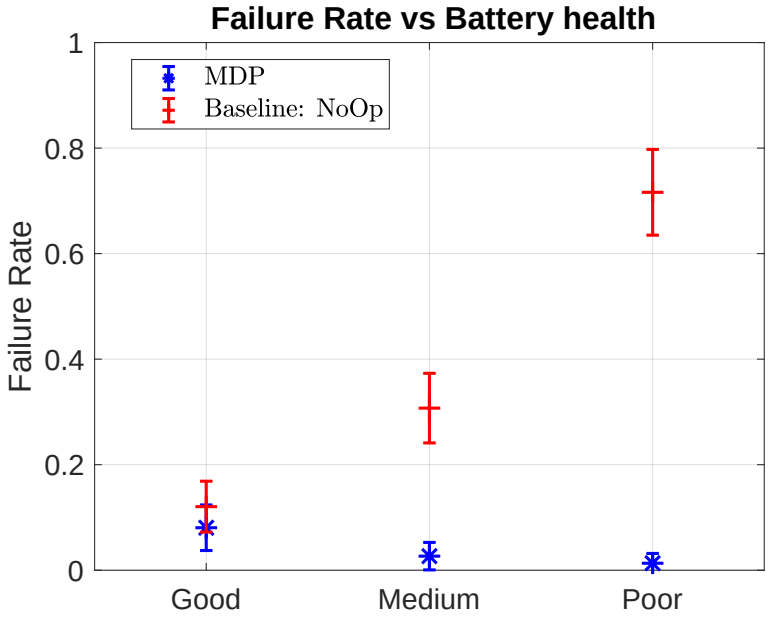

Figure 5.30: Failure rate and its standard error of mean for various battery health conditions

The failure rates over different hexacopter battery health conditions of CMA MDP and Baseline policies is shown in Figure 5.30. It can be seen that CMA MDP has a comparatively lower failure rate than the Baseline policy. Notably, the CMA offers improved safety in medium and poor health conditions compared to the Baseline policy. The lower hexacopter mission failure rate is due to executing emergency landing by CMA when components are in critical health conditions.

Following the failure rate of UAS, original flight plan completion rate was also

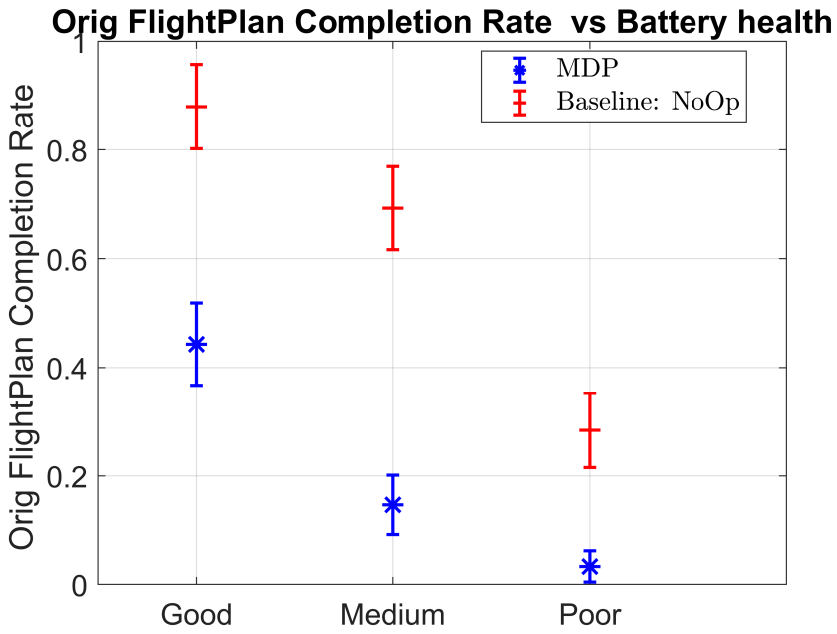

Figure 5.31: Original Flight Plan completion rate and its standard error of mean for various battery health conditions

investigated to determine the performance of the MDP as shown in Figure 5.31. The MDP is cautious compared to the Baseline Policy. In good battery health conditions, the Baseline Policy of $NoOp$ has a higher completion rate of the original flight plan. This is because the CMA MDP executes emergency landing in scenarios where $MM < 0$, i.e. a single motor is about to fail or has already failed and $RM > 0$, i.e. it has sufficient energy to complete the flight plan. Similarly, the overcautious nature of CMA MDP leading to the execution of emergency landing can also be observed for medium and poor battery health conditions.

Upon analyzing the flight logs for poor battery pack health conditions, it was observed that for scenarios where the $RM < 0$, i.e. hexacopter does not have sufficient battery energy to complete the flight plan at the start of the mission, the CMA MDP recommends emergency landing action for the hexacopter which translates into not taking off. As a result, it has a very low failure rate and a low original flight plan completion rate.

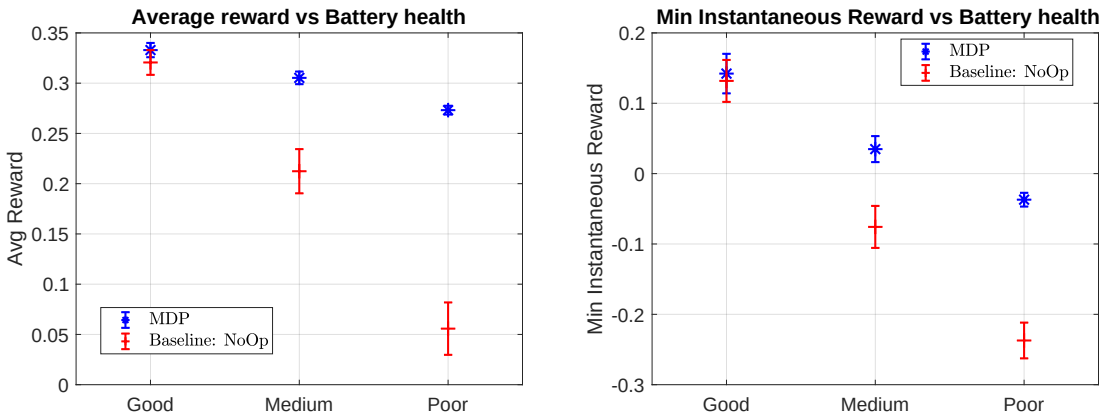

(a) (b)

Figure 5.32: Different reward metrics and their standard error of mean plots showing performance comparison of CMA MDP with Baseline *NoOp* policy

Apart from the failure rate, the average reward and minimum instantaneous reward at each time step, shown in Figure 5.32, is also investigated to get a deeper understanding of the performance of CMA. In both the metrics, CMA MDP offers better performance which is correlated to the higher safety rate in the previous plot. CMA has higher average reward values as it performs emergency landings when the critical health of a component is detected without crashing and receiving a higher reward than crashing. Whereas, Baseline policy shows a decreasing trend and has lower average reward values than CMA because of its higher number of crashes which results in negative penalties.

5.6 Summary and Future Work

In this chapter, we have proposed a risk-aware Contingency Management Autonomy (CMA) built using Markov Decision Processes as a framework to generalize a manually specified contingency policy. The CMA MDP is designed with helper functions which are embedded in the abstracted state space and actions. The helper functions defined provide the flexibility to determine optimal paths outside of the MDP framework, rather than requiring the MDP to determine the optimal path.

This results in reduced MDP state space complexity.

The effectiveness of the CMA optimal policy for contingency management is evaluated on a high-fidelity simulator over various component degradation scenarios, wind conditions, ambient temperature and flight plans. Different metrics such as failure rate, average reward per time step and minimum instantaneous reward are used to analyze and compare the performance of the CMA MDP and Baseline Policy of $NoOp$. We conclude that implementing CMA MDP to modify the mission-level directives has increased the safety of UAS by preventing catastrophic crashes.

During our extensive testing, it was identified that there was some discrepancy in the state transition model of the MDP and the high-fidelity simulator. In future work, we aim to refine the state transition model to accurately reflect the simulator's transition probabilities. Adaptive techniques [13] to estimate the system model and adjust the system control policy online could also be investigated to overcome the discrepancy in state transition modelling. Lastly, the success of CMA is currently evaluated in simulations only; to validate our results, the next step would be to conduct hardware experiments.

In this thesis we have investigated component degradation in only two components. In reality there there are multiple failure modes of the UAS. These failure modes can be handled with the following future possible augmentation in the proposed MDP framework:

- Addition of elements to the state vector of the existing MDP to accommodate for the different failure modalities. With this implementation the state space size would increase and the MDP would have a larger state probability transition table. The benefit of this implementation is that it captures the inter-dependencies between various failure modes. However, the challenge in this implementation is in accurately defining the state transition probabilities for each of the elements in the table. Also as the state space size increases the

complexity in the simple value iteration algorithm also increases as $O(S^2A)$.

- The second approach is to design multiple MDPs, each handling different failure modes of the UAS and each MDP having an associated criticality value based on resulting failure of the UAS. Conditional independence is assumed between the different failure modes. The resulting optimal action from the set of individual optimal actions from each MDP can be selected on the basis of its criticality. The benefit of this approach is that each of the MDP are smaller in size, relatively easier to define, and simpler to optimize. The challenge in this implementation is that the interaction between the different failure modes is not captured due to conditional independence assumptions as opposed to the previous approach where dependence/ interaction between different failure modes is considered.

Also motivated by the potential for noise on indicators of fault and failure, partial observability of the MDP state space is being investigated in our ongoing collaboration with the University of Colorado [65]. The performance of various optimal policies will be analyzed over varying observabilities in the high-fidelity simulator.

CHAPTER VI

Conclusion and Future Work

6.1 Conclusion

Safety is a crucial enabler for widespread adoption of UAS. It is a multifaceted problem that involves automated flight and contingency management, resiliency in air traffic management, robust system design, heterogeneous vehicle operations, weather tolerant airspace operations and many more. In this thesis, we have addressed the contingency management autonomy for the UAS. Our approach to CMA development utilized experimentally validated models for multicopter components and aerodynamic models.

We started with experimental modeling of a multicopter propulsion unit with different propellers and configurations, namely pusher and puller configurations. A difference in performance was observed for the pusher and puller configuration, which motivated further investigation of aerodynamic model of the full hexacopter built with different motor configurations. The investigation was conducted by a series of wind tunnel experiments and autonomous outdoor flight tests. A clear design trade-off was seen in wind tunnel test results, confirming trends during flight tests. A pusher design is more efficient for hovering and slow flight missions such as local-area surveillance and inspection. In contrast, a tractor design is more efficient for missions requiring appreciable transit, such as package delivery.

Following the aerodynamic and propulsion system modeling, its power plant is the next vital component to be modeled for UAS. Typically the power plant for UAS consists of LiPo battery. We built and tested a novel economic equipment to gather data from the LiPo battery. This data is used to determine LiPo battery's Equivalent Circuit Resistance Model.

Having identified UAS component models, we wanted to investigate adding redundant components to increase systems safety. Since hexacopter configuration was chosen, the system already had a redundant propulsion system. An additional battery pack was added to make the power plant doubly redundant. However, the addition of redundant components does not necessarily make the system safe. Hence, we developed a battery and motor reconfiguration solution that utilizes their prognosis information.

The component reconfiguration scheme focuses on safety-critical battery and propulsion system modules and prevents system failure by optimally reconfiguring them when necessary. However, reconfiguration alone may be insufficient without changing/modifying mission objectives. The proposed CMA MDP makes emergency landing decisions based on the health of its components. Various case studies and the efficacy of the CMA MDP has been presented.

6.2 Future Work

In this thesis, we have presented an approach for automated contingency management to preserve the safety of the UAS. A lot of time and effort was dedicated to determining the system models and experimentally validating them. However, the systems models can be further improved by conducting additional experiments, including improvement of our dynamic thrust and torque models with wind tunnel dynamometer experiments, lateral drag models for UAS with wind tunnel experiments, and modelling battery at different ambient temperatures.

Currently, the battery reconfiguration scheme and CMA utilize the MDP framework and are tuned for specific performance separately. There could be scenarios where their performance might conflict with each other or be sub-optimal overall. Hence, further investigation of architecture presented in Chapter I Figure 1.1 with hierarchical MDP methods are required to determine optimal policy accounting for both the battery reconfiguration and CMA.

Other possible directions for investigating the proposed MDP schemes would be refining the state transition model so that it accurately reflects the transition probabilities of the simulator, varying the state aggregation of MDP models and looking at the performance of MDP solutions including policy approximation techniques. Also for contingency management actions there is a cyberphysical tradeoff between $LandASAP$ and $LandPract$. $LandASAP$ requires more real-time computation but is "more optimal" for the specific real-time situation. $LandPract$ can lookup a plan immediately but may not be as optimal for the particular real-time scenario. This tradeoff should be explored in future work.

Lastly, the performance assessment of both the battery reconfiguration scheme and CMA is performed in simulations only. Field experimentation of CMA and battery reconfiguration are of critical importance for future work of this thesis to determine their feasibility.

APPENDIX

APPENDIX A

A.1 State Transition Probability Tables

Table A.1: State Transition Probabilities for $A_t = NoOp$

S_t	S_{t+1}	**P**
N,NF,MM0,G,RM0	N,NF,MM1,G,RM0	0.49998
N,NF,MM0,G,RM0	N,SF,MM1,G,RM0	2.375e-05
N,NF,MM0,G,RM0	FL	0.5
N,NF,MM0,G,RM1	N,NF,MM1,G,RM0	0.0045869
N,NF,MM0,G,RM1	N,NF,MM1,G,RM1	0.9128
N,NF,MM0,G,RM1	N,SF,MM1,G,RM0	2.1789e-07
N,NF,MM0,G,RM1	N,SF,MM1,G,RM1	4.336e-05
N,NF,MM0,G,RM1	C	0.073394
N,NF,MM0,G,RM1	FL	0.0091743
N,NF,MM0,M,RM0	N,NF,MM1,M,RM0	0.49998
N,NF,MM0,M,RM0	N,SF,MM1,M,RM0	2.375e-05

Continued on next page

Table A.1 – continued from previous page

S_t	S_{t+1}	**P**
N,NF,MM0,M,RM0	FL	0.5
N,NF,MM0,M,RM1	N,NF,MM1,M,RM0	0.0091739
N,NF,MM0,M,RM1	N,NF,MM1,M,RM1	0.90821
N,NF,MM0,M,RM1	N,SF,MM1,M,RM0	4.3578e-07
N,NF,MM0,M,RM1	N,SF,MM1,M,RM1	4.3142e-05
N,NF,MM0,M,RM1	C	0.073394
N,NF,MM0,M,RM1	FL	0.0091743
N,NF,MM0,P,RM0	N,NF,MM1,P,RM0	0.49998
N,NF,MM0,P,RM0	N,SF,MM1,P,RM0	2.375e-05
N,NF,MM0,P,RM0	FL	0.5
N,NF,MM0,P,RM1	N,NF,MM1,P,RM0	0.045869
N,NF,MM0,P,RM1	N,NF,MM1,P,RM1	0.87152
N,NF,MM0,P,RM1	N,SF,MM1,P,RM0	2.1789e-06
N,NF,MM0,P,RM1	N,SF,MM1,P,RM1	4.1399e-05
N,NF,MM0,P,RM1	C	0.073394
N,NF,MM0,P,RM1	FL	0.0091743
N,NF,MM1,G,RM0	N,NF,MM1,G,RM0	0.49998
N,NF,MM1,G,RM0	N,SF,MM1,G,RM0	2.375e-05
N,NF,MM1,G,RM0	FL	0.5
N,NF,MM1,G,RM1	N,NF,MM1,G,RM0	4.5411e-05
N,NF,MM1,G,RM1	N,NF,MM1,G,RM1	0.90818
N,NF,MM1,G,RM1	N,SF,MM1,G,RM0	2.1571e-09
N,NF,MM1,G,RM1	N,SF,MM1,G,RM1	4.314e-05
N,NF,MM1,G,RM1	C	0.090827

Continued on next page

Table A.1 – continued from previous page

S_t	S_{t+1}	**P**
N,NF,MM1,G,RM1	FL	0.00090827
N,NF,MM1,M,RM0	N,NF,MM1,M,RM0	0.49998
N,NF,MM1,M,RM0	N,SF,MM1,M,RM0	2.375e-05
N,NF,MM1,M,RM0	FL	0.5
N,NF,MM1,M,RM1	N,NF,MM1,M,RM0	0.00045411
N,NF,MM1,M,RM1	N,NF,MM1,M,RM1	0.90777
N,NF,MM1,M,RM1	N,SF,MM1,M,RM0	2.1571e-08
N,NF,MM1,M,RM1	N,SF,MM1,M,RM1	4.3121e-05
N,NF,MM1,M,RM1	C	0.090827
N,NF,MM1,M,RM1	FL	0.00090827
N,NF,MM1,P,RM0	N,NF,MM1,P,RM0	0.49998
N,NF,MM1,P,RM0	N,SF,MM1,P,RM0	2.375e-05
N,NF,MM1,P,RM0	FL	0.5
N,NF,MM1,P,RM1	N,NF,MM1,P,RM0	0.0045411
N,NF,MM1,P,RM1	N,NF,MM1,P,RM1	0.90368
N,NF,MM1,P,RM1	N,SF,MM1,P,RM0	2.1571e-07
N,NF,MM1,P,RM1	N,SF,MM1,P,RM1	4.2927e-05
N,NF,MM1,P,RM1	C	0.090827
N,NF,MM1,P,RM1	FL	0.00090827
N,SF,MM0,G,RM0	N,SF,MM0,G,RM0	0.4961
N,SF,MM0,G,RM0	N,SF,MM1,G,RM0	0.002493
N,SF,MM0,G,RM0	N,JF,MM0,G,RM0	0.0013975
N,SF,MM0,G,RM0	N,JF,MM1,G,RM0	7.0225e-06
N,SF,MM0,G,RM0	FL	0.5

Continued on next page

Table A.1 – continued from previous page

S_t	S_{t+1}	**P**
N,SF,MM0,G,RM1	N,SF,MM0,G,RM0	0.0045514
N,SF,MM0,G,RM1	N,SF,MM0,G,RM1	0.90573
N,SF,MM0,G,RM1	N,SF,MM1,G,RM0	2.2871e-05
N,SF,MM0,G,RM1	N,SF,MM1,G,RM1	0.0045514
N,SF,MM0,G,RM1	N,JF,MM0,G,RM0	1.2821e-05
N,SF,MM0,G,RM1	N,JF,MM0,G,RM1	0.0025514
N,SF,MM0,G,RM1	N,JF,MM1,G,RM0	6.4427e-08
N,SF,MM0,G,RM1	N,JF,MM1,G,RM1	1.2821e-05
N,SF,MM0,G,RM1	C	0.073394
N,SF,MM0,G,RM1	FL	0.0091743
N,SF,MM0,M,RM0	N,SF,MM0,M,RM0	0.4961
N,SF,MM0,M,RM0	N,SF,MM1,M,RM0	0.002493
N,SF,MM0,M,RM0	N,JF,MM0,M,RM0	0.0013975
N,SF,MM0,M,RM0	N,JF,MM1,M,RM0	7.0225e-06
N,SF,MM0,M,RM0	FL	0.5
N,SF,MM0,M,RM1	N,SF,MM0,M,RM0	0.0091028
N,SF,MM0,M,RM1	N,SF,MM0,M,RM1	0.90118
N,SF,MM0,M,RM1	N,SF,MM1,M,RM0	4.5743e-05
N,SF,MM0,M,RM1	N,SF,MM1,M,RM1	0.0045285
N,SF,MM0,M,RM1	N,JF,MM0,M,RM0	2.5642e-05
N,SF,MM0,M,RM1	N,JF,MM0,M,RM1	0.0025385
N,SF,MM0,M,RM1	N,JF,MM1,M,RM0	1.2885e-07
N,SF,MM0,M,RM1	N,JF,MM1,M,RM1	1.2756e-05
N,SF,MM0,M,RM1	C	0.073394

Continued on next page

Table A.1 – continued from previous page

S_t	S_{t+1}	**P**
N,SF,MM0,M,RM1	FL	0.0091743
N,SF,MM0,P,RM0	N,SF,MM0,P,RM0	0.4961
N,SF,MM0,P,RM0	N,SF,MM1,P,RM0	0.002493
N,SF,MM0,P,RM0	N,JF,MM0,P,RM0	0.0013975
N,SF,MM0,P,RM0	N,JF,MM1,P,RM0	7.0225e-06
N,SF,MM0,P,RM0	FL	0.5
N,SF,MM0,P,RM1	N,SF,MM0,P,RM0	0.045514
N,SF,MM0,P,RM1	N,SF,MM0,P,RM1	0.86477
N,SF,MM0,P,RM1	N,SF,MM1,P,RM0	0.00022871
N,SF,MM0,P,RM1	N,SF,MM1,P,RM1	0.0043456
N,SF,MM0,P,RM1	N,JF,MM0,P,RM0	0.00012821
N,SF,MM0,P,RM1	N,JF,MM0,P,RM1	0.002436
N,SF,MM0,P,RM1	N,JF,MM1,P,RM0	6.4427e-07
N,SF,MM0,P,RM1	N,JF,MM1,P,RM1	1.2241e-05
N,SF,MM0,P,RM1	C	0.073394
N,SF,MM0,P,RM1	FL	0.0091743
N,SF,MM1,G,RM0	N,SF,MM0,G,RM0	0.0014006
N,SF,MM1,G,RM0	N,SF,MM1,G,RM0	0.49719
N,SF,MM1,G,RM0	N,JF,MM0,G,RM0	3.9452e-06
N,SF,MM1,G,RM0	N,JF,MM1,G,RM0	0.0014006
N,SF,MM1,G,RM0	FL	0.5
N,SF,MM1,G,RM1	N,SF,MM0,G,RM0	1.2721e-07
N,SF,MM1,G,RM1	N,SF,MM0,G,RM1	0.002544
N,SF,MM1,G,RM1	N,SF,MM1,G,RM0	4.5158e-05

Continued on next page

Table A.1 – continued from previous page

S_t	S_{t+1}	**P**
N,SF,MM1,G,RM1	N,SF,MM1,G,RM1	0.90312
N,SF,MM1,G,RM1	N,JF,MM0,G,RM0	3.5833e-10
N,SF,MM1,G,RM1	N,JF,MM0,G,RM1	7.1663e-06
N,SF,MM1,G,RM1	N,JF,MM1,G,RM0	1.2721e-07
N,SF,MM1,G,RM1	N,JF,MM1,G,RM1	0.002544
N,SF,MM1,G,RM1	C	0.090827
N,SF,MM1,G,RM1	FL	0.00090827
N,SF,MM1,M,RM0	N,SF,MM0,M,RM0	0.0014006
N,SF,MM1,M,RM0	N,SF,MM1,M,RM0	0.49719
N,SF,MM1,M,RM0	N,JF,MM0,M,RM0	3.9452e-06
N,SF,MM1,M,RM0	N,JF,MM1,M,RM0	0.0014006
N,SF,MM1,M,RM0	FL	0.5
N,SF,MM1,M,RM1	N,SF,MM0,M,RM0	1.2721e-06
N,SF,MM1,M,RM1	N,SF,MM0,M,RM1	0.0025429
N,SF,MM1,M,RM1	N,SF,MM1,M,RM0	0.00045158
N,SF,MM1,M,RM1	N,SF,MM1,M,RM1	0.90272
N,SF,MM1,M,RM1	N,JF,MM0,M,RM0	3.5833e-09
N,SF,MM1,M,RM1	N,JF,MM0,M,RM1	7.1631e-06
N,SF,MM1,M,RM1	N,JF,MM1,M,RM0	1.2721e-06
N,SF,MM1,M,RM1	N,JF,MM1,M,RM1	0.0025429
N,SF,MM1,M,RM1	C	0.090827
N,SF,MM1,M,RM1	FL	0.00090827
N,SF,MM1,P,RM0	N,SF,MM0,P,RM0	0.0014006
N,SF,MM1,P,RM0	N,SF,MM1,P,RM0	0.49719

Continued on next page

Table A.1 – continued from previous page

S_t	S_{t+1}	**P**
N,SF,MM1,P,RM0	N,JF,MM0,P,RM0	3.9452e-06
N,SF,MM1,P,RM0	N,JF,MM1,P,RM0	0.0014006
N,SF,MM1,P,RM0	FL	0.5
N,SF,MM1,P,RM1	N,SF,MM0,P,RM0	1.2721e-05
N,SF,MM1,P,RM1	N,SF,MM0,P,RM1	0.0025314
N,SF,MM1,P,RM1	N,SF,MM1,P,RM0	0.0045158
N,SF,MM1,P,RM1	N,SF,MM1,P,RM1	0.89865
N,SF,MM1,P,RM1	N,JF,MM0,P,RM0	3.5833e-08
N,SF,MM1,P,RM1	N,JF,MM0,P,RM1	7.1308e-06
N,SF,MM1,P,RM1	N,JF,MM1,P,RM0	1.2721e-05
N,SF,MM1,P,RM1	N,JF,MM1,P,RM1	0.0025314
N,SF,MM1,P,RM1	C	0.090827
N,SF,MM1,P,RM1	FL	0.00090827
N,JF,MM0,G,RM0	N,JF,MM0,G,RM0	0.5
N,JF,MM0,G,RM0	FL	0.5
N,JF,MM0,G,RM1	N,JF,MM0,G,RM0	0.0045872
N,JF,MM0,G,RM1	N,JF,MM0,G,RM1	0.91284
N,JF,MM0,G,RM1	C	0.073394
N,JF,MM0,G,RM1	FL	0.0091743
N,JF,MM0,M,RM0	N,JF,MM0,M,RM0	0.5
N,JF,MM0,M,RM0	FL	0.5
N,JF,MM0,M,RM1	N,JF,MM0,M,RM0	0.0091743
N,JF,MM0,M,RM1	N,JF,MM0,M,RM1	0.90826
N,JF,MM0,M,RM1	C	0.073394

Continued on next page

Table A.1 – continued from previous page

S_t	S_{t+1}	**P**
N,JF,MM0,M,RM1	FL	0.0091743
N,JF,MM0,P,RM0	N,JF,MM0,P,RM0	0.5
N,JF,MM0,P,RM0	FL	0.5
N,JF,MM0,P,RM1	N,JF,MM0,P,RM0	0.045872
N,JF,MM0,P,RM1	N,JF,MM0,P,RM1	0.87156
N,JF,MM0,P,RM1	C	0.073394
N,JF,MM0,P,RM1	FL	0.0091743
N,JF,MM1,G,RM0	N,JF,MM0,G,RM0	0.5
N,JF,MM1,G,RM0	FL	0.5
N,JF,MM1,G,RM1	N,JF,MM0,G,RM0	4.5413e-05
N,JF,MM1,G,RM1	N,JF,MM0,G,RM1	0.90822
N,JF,MM1,G,RM1	C	0.090827
N,JF,MM1,G,RM1	FL	0.00090827
N,JF,MM1,M,RM0	N,JF,MM0,M,RM0	0.5
N,JF,MM1,M,RM0	FL	0.5
N,JF,MM1,M,RM1	N,JF,MM0,M,RM0	0.00045413
N,JF,MM1,M,RM1	N,JF,MM0,M,RM1	0.90781
N,JF,MM1,M,RM1	C	0.090827
N,JF,MM1,M,RM1	FL	0.00090827
N,JF,MM1,P,RM0	N,JF,MM0,P,RM0	0.5
N,JF,MM1,P,RM0	FL	0.5
N,JF,MM1,P,RM1	N,JF,MM0,P,RM0	0.0045413
N,JF,MM1,P,RM1	N,JF,MM0,P,RM1	0.90372
N,JF,MM1,P,RM1	C	0.090827

Continued on next page

Table A.1 – continued from previous page

S_t	S_{t+1}	**P**
N,JF,MM1,P,RM1	FL	0.00090827
ELASAP,NF,MM0,G,RM0	ELASAP,NF,MM1,G,RM0	0.49998
ELASAP,NF,MM0,G,RM0	ELASAP,SF,MM1,G,RM0	2.375e-05
ELASAP,NF,MM0,G,RM0	FL	0.5
ELASAP,NF,MM0,G,RM1	ELASAP,NF,MM1,G,RM0	0.0045288
ELASAP,NF,MM0,G,RM1	ELASAP,NF,MM1,G,RM1	0.90123
ELASAP,NF,MM0,G,RM1	ELASAP,SF,MM1,G,RM0	2.1513e-07
ELASAP,NF,MM0,G,RM1	ELASAP,SF,MM1,G,RM1	4.281e-05
ELASAP,NF,MM0,G,RM1	C	0.086051
ELASAP,NF,MM0,G,RM1	FL	0.0081522
ELASAP,NF,MM0,M,RM0	ELASAP,NF,MM1,M,RM0	0.49998
ELASAP,NF,MM0,M,RM0	ELASAP,SF,MM1,M,RM0	2.375e-05
ELASAP,NF,MM0,M,RM0	FL	0.5
ELASAP,NF,MM0,M,RM1	ELASAP,NF,MM1,M,RM0	0.0090575
ELASAP,NF,MM0,M,RM1	ELASAP,NF,MM1,M,RM1	0.8967
ELASAP,NF,MM0,M,RM1	ELASAP,SF,MM1,M,RM0	4.3025e-07
ELASAP,NF,MM0,M,RM1	ELASAP,SF,MM1,M,RM1	4.2595e-05
ELASAP,NF,MM0,M,RM1	C	0.086051
ELASAP,NF,MM0,M,RM1	FL	0.0081522
ELASAP,NF,MM0,P,RM0	ELASAP,NF,MM1,P,RM0	0.49998
ELASAP,NF,MM0,P,RM0	ELASAP,SF,MM1,P,RM0	2.375e-05
ELASAP,NF,MM0,P,RM0	FL	0.5
ELASAP,NF,MM0,P,RM1	ELASAP,NF,MM1,P,RM0	0.045288
ELASAP,NF,MM0,P,RM1	ELASAP,NF,MM1,P,RM1	0.86047

Continued on next page

Table A.1 – continued from previous page

S_t	S_{t+1}	**P**
ELASAP,NF,MM0,P,RM1	ELASAP,SF,MM1,P,RM0	2.1513e-06
ELASAP,NF,MM0,P,RM1	ELASAP,SF,MM1,P,RM1	4.0874e-05
ELASAP,NF,MM0,P,RM1	C	0.086051
ELASAP,NF,MM0,P,RM1	FL	0.0081522
ELASAP,NF,MM1,G,RM0	ELASAP,NF,MM1,G,RM0	0.49998
ELASAP,NF,MM1,G,RM0	ELASAP,SF,MM1,G,RM0	2.375e-05
ELASAP,NF,MM1,G,RM0	FL	0.5
ELASAP,NF,MM1,G,RM1	ELASAP,NF,MM1,G,RM0	4.1661e-05
ELASAP,NF,MM1,G,RM1	ELASAP,NF,MM1,G,RM1	0.83318
ELASAP,NF,MM1,G,RM1	ELASAP,SF,MM1,G,RM0	1.979e-09
ELASAP,NF,MM1,G,RM1	ELASAP,SF,MM1,G,RM1	3.9578e-05
ELASAP,NF,MM1,G,RM1	C	0.16665
ELASAP,NF,MM1,G,RM1	FL	8.3326e-05
ELASAP,NF,MM1,M,RM0	ELASAP,NF,MM1,M,RM0	0.49998
ELASAP,NF,MM1,M,RM0	ELASAP,SF,MM1,M,RM0	2.375e-05
ELASAP,NF,MM1,M,RM0	FL	0.5
ELASAP,NF,MM1,M,RM1	ELASAP,NF,MM1,M,RM0	0.00041661
ELASAP,NF,MM1,M,RM1	ELASAP,NF,MM1,M,RM1	0.83281
ELASAP,NF,MM1,M,RM1	ELASAP,SF,MM1,M,RM0	1.979e-08
ELASAP,NF,MM1,M,RM1	ELASAP,SF,MM1,M,RM1	3.956e-05
ELASAP,NF,MM1,M,RM1	C	0.16665
ELASAP,NF,MM1,M,RM1	FL	8.3326e-05
ELASAP,NF,MM1,P,RM0	ELASAP,NF,MM1,P,RM0	0.49998
ELASAP,NF,MM1,P,RM0	ELASAP,SF,MM1,P,RM0	2.375e-05

Continued on next page

Table A.1 – continued from previous page

S_t	S_{t+1}	**P**
ELASAP,NF,MM1,P,RM0	FL	0.5
ELASAP,NF,MM1,P,RM1	ELASAP,NF,MM1,P,RM0	0.0041661
ELASAP,NF,MM1,P,RM1	ELASAP,NF,MM1,P,RM1	0.82906
ELASAP,NF,MM1,P,RM1	ELASAP,SF,MM1,P,RM0	1.979e-07
ELASAP,NF,MM1,P,RM1	ELASAP,SF,MM1,P,RM1	3.9382e-05
ELASAP,NF,MM1,P,RM1	C	0.16665
ELASAP,NF,MM1,P,RM1	FL	8.3326e-05
ELASAP,SF,MM0,G,RM0	ELASAP,SF,MM0,G,RM0	0.4961
ELASAP,SF,MM0,G,RM0	ELASAP,SF,MM1,G,RM0	0.002493
ELASAP,SF,MM0,G,RM0	ELASAP,JF,MM0,G,RM0	0.0013975
ELASAP,SF,MM0,G,RM0	ELASAP,JF,MM1,G,RM0	7.0225e-06
ELASAP,SF,MM0,G,RM0	FL	0.5
ELASAP,SF,MM0,G,RM1	ELASAP,SF,MM0,G,RM0	0.0044937
ELASAP,SF,MM0,G,RM1	ELASAP,SF,MM0,G,RM1	0.89424
ELASAP,SF,MM0,G,RM1	ELASAP,SF,MM1,G,RM0	2.2581e-05
ELASAP,SF,MM0,G,RM1	ELASAP,SF,MM1,G,RM1	0.0044937
ELASAP,SF,MM0,G,RM1	ELASAP,JF,MM0,G,RM0	1.2658e-05
ELASAP,SF,MM0,G,RM1	ELASAP,JF,MM0,G,RM1	0.002519
ELASAP,SF,MM0,G,RM1	ELASAP,JF,MM1,G,RM0	6.361e-08
ELASAP,SF,MM0,G,RM1	ELASAP,JF,MM1,G,RM1	1.2658e-05
ELASAP,SF,MM0,G,RM1	C	0.086051
ELASAP,SF,MM0,G,RM1	FL	0.0081522
ELASAP,SF,MM0,M,RM0	ELASAP,SF,MM0,M,RM0	0.4961
ELASAP,SF,MM0,M,RM0	ELASAP,SF,MM1,M,RM0	0.002493

Continued on next page

Table A.1 – continued from previous page

S_t	S_{t+1}	**P**
ELASAP,SF,MM0,M,RM0	ELASAP,JF,MM0,M,RM0	0.0013975
ELASAP,SF,MM0,M,RM0	ELASAP,JF,MM1,M,RM0	7.0225e-06
ELASAP,SF,MM0,M,RM0	FL	0.5
ELASAP,SF,MM0,M,RM1	ELASAP,SF,MM0,M,RM0	0.0089874
ELASAP,SF,MM0,M,RM1	ELASAP,SF,MM0,M,RM1	0.88975
ELASAP,SF,MM0,M,RM1	ELASAP,SF,MM1,M,RM0	4.5163e-05
ELASAP,SF,MM0,M,RM1	ELASAP,SF,MM1,M,RM1	0.0044711
ELASAP,SF,MM0,M,RM1	ELASAP,JF,MM0,M,RM0	2.5317e-05
ELASAP,SF,MM0,M,RM1	ELASAP,JF,MM0,M,RM1	0.0025063
ELASAP,SF,MM0,M,RM1	ELASAP,JF,MM1,M,RM0	1.2722e-07
ELASAP,SF,MM0,M,RM1	ELASAP,JF,MM1,M,RM1	1.2595e-05
ELASAP,SF,MM0,M,RM1	C	0.086051
ELASAP,SF,MM0,M,RM1	FL	0.0081522
ELASAP,SF,MM0,P,RM0	ELASAP,SF,MM0,P,RM0	0.4961
ELASAP,SF,MM0,P,RM0	ELASAP,SF,MM1,P,RM0	0.002493
ELASAP,SF,MM0,P,RM0	ELASAP,JF,MM0,P,RM0	0.0013975
ELASAP,SF,MM0,P,RM0	ELASAP,JF,MM1,P,RM0	7.0225e-06
ELASAP,SF,MM0,P,RM0	FL	0.5
ELASAP,SF,MM0,P,RM1	ELASAP,SF,MM0,P,RM0	0.044937
ELASAP,SF,MM0,P,RM1	ELASAP,SF,MM0,P,RM1	0.8538
ELASAP,SF,MM0,P,RM1	ELASAP,SF,MM1,P,RM0	0.00022581
ELASAP,SF,MM0,P,RM1	ELASAP,SF,MM1,P,RM1	0.0042905
ELASAP,SF,MM0,P,RM1	ELASAP,JF,MM0,P,RM0	0.00012658
ELASAP,SF,MM0,P,RM1	ELASAP,JF,MM0,P,RM1	0.0024051

Continued on next page

Table A.1 – continued from previous page

S_t	S_{t+1}	**P**
ELASAP,SF,MM0,P,RM1	ELASAP,JF,MM1,P,RM0	6.361e-07
ELASAP,SF,MM0,P,RM1	ELASAP,JF,MM1,P,RM1	1.2086e-05
ELASAP,SF,MM0,P,RM1	C	0.086051
ELASAP,SF,MM0,P,RM1	FL	0.0081522
ELASAP,SF,MM1,G,RM0	ELASAP,SF,MM0,G,RM0	0.0014006
ELASAP,SF,MM1,G,RM0	ELASAP,SF,MM1,G,RM0	0.49719
ELASAP,SF,MM1,G,RM0	ELASAP,JF,MM0,G,RM0	3.9452e-06
ELASAP,SF,MM1,G,RM0	ELASAP,JF,MM1,G,RM0	0.0014006
ELASAP,SF,MM1,G,RM0	FL	0.5
ELASAP,SF,MM1,G,RM1	ELASAP,SF,MM0,G,RM0	1.167e-07
ELASAP,SF,MM1,G,RM1	ELASAP,SF,MM0,G,RM1	0.0023339
ELASAP,SF,MM1,G,RM1	ELASAP,SF,MM1,G,RM0	4.1429e-05
ELASAP,SF,MM1,G,RM1	ELASAP,SF,MM1,G,RM1	0.82855
ELASAP,SF,MM1,G,RM1	ELASAP,JF,MM0,G,RM0	3.2874e-10
ELASAP,SF,MM1,G,RM1	ELASAP,JF,MM0,G,RM1	6.5745e-06
ELASAP,SF,MM1,G,RM1	ELASAP,JF,MM1,G,RM0	1.167e-07
ELASAP,SF,MM1,G,RM1	ELASAP,JF,MM1,G,RM1	0.0023339
ELASAP,SF,MM1,G,RM1	C	0.16665
ELASAP,SF,MM1,G,RM1	FL	8.3326e-05
ELASAP,SF,MM1,M,RM0	ELASAP,SF,MM0,M,RM0	0.0014006
ELASAP,SF,MM1,M,RM0	ELASAP,SF,MM1,M,RM0	0.49719
ELASAP,SF,MM1,M,RM0	ELASAP,JF,MM0,M,RM0	3.9452e-06
ELASAP,SF,MM1,M,RM0	ELASAP,JF,MM1,M,RM0	0.0014006
ELASAP,SF,MM1,M,RM0	FL	0.5

Continued on next page

Table A.1 – continued from previous page

S_t	S_{t+1}	**P**
ELASAP,SF,MM1,M,RM1	ELASAP,SF,MM0,M,RM0	1.167e-06
ELASAP,SF,MM1,M,RM1	ELASAP,SF,MM0,M,RM1	0.0023329
ELASAP,SF,MM1,M,RM1	ELASAP,SF,MM1,M,RM0	0.00041429
ELASAP,SF,MM1,M,RM1	ELASAP,SF,MM1,M,RM1	0.82817
ELASAP,SF,MM1,M,RM1	ELASAP,JF,MM0,M,RM0	3.2874e-09
ELASAP,SF,MM1,M,RM1	ELASAP,JF,MM0,M,RM1	6.5716e-06
ELASAP,SF,MM1,M,RM1	ELASAP,JF,MM1,M,RM0	1.167e-06
ELASAP,SF,MM1,M,RM1	ELASAP,JF,MM1,M,RM1	0.0023329
ELASAP,SF,MM1,M,RM1	C	0.16665
ELASAP,SF,MM1,M,RM1	FL	8.3326e-05
ELASAP,SF,MM1,P,RM0	ELASAP,SF,MM0,P,RM0	0.0014006
ELASAP,SF,MM1,P,RM0	ELASAP,SF,MM1,P,RM0	0.49719
ELASAP,SF,MM1,P,RM0	ELASAP,JF,MM0,P,RM0	3.9452e-06
ELASAP,SF,MM1,P,RM0	ELASAP,JF,MM1,P,RM0	0.0014006
ELASAP,SF,MM1,P,RM0	FL	0.5
ELASAP,SF,MM1,P,RM1	ELASAP,SF,MM0,P,RM0	1.167e-05
ELASAP,SF,MM1,P,RM1	ELASAP,SF,MM0,P,RM1	0.0023224
ELASAP,SF,MM1,P,RM1	ELASAP,SF,MM1,P,RM0	0.0041429
ELASAP,SF,MM1,P,RM1	ELASAP,SF,MM1,P,RM1	0.82445
ELASAP,SF,MM1,P,RM1	ELASAP,JF,MM0,P,RM0	3.2874e-08
ELASAP,SF,MM1,P,RM1	ELASAP,JF,MM0,P,RM1	6.542e-06
ELASAP,SF,MM1,P,RM1	ELASAP,JF,MM1,P,RM0	1.167e-05
ELASAP,SF,MM1,P,RM1	ELASAP,JF,MM1,P,RM1	0.0023224
ELASAP,SF,MM1,P,RM1	C	0.16665

Continued on next page

Table A.1 – continued from previous page

S_t	S_{t+1}	**P**
ELASAP,SF,MM1,P,RM1	FL	8.3326e-05
ELASAP,JF,MM0,G,RM0	ELASAP,JF,MM0,G,RM0	0.5
ELASAP,JF,MM0,G,RM0	FL	0.5
ELASAP,JF,MM0,G,RM1	ELASAP,JF,MM0,G,RM0	0.004529
ELASAP,JF,MM0,G,RM1	ELASAP,JF,MM0,G,RM1	0.90127
ELASAP,JF,MM0,G,RM1	C	0.086051
ELASAP,JF,MM0,G,RM1	FL	0.0081522
ELASAP,JF,MM0,M,RM0	ELASAP,JF,MM0,M,RM0	0.5
ELASAP,JF,MM0,M,RM0	FL	0.5
ELASAP,JF,MM0,M,RM1	ELASAP,JF,MM0,M,RM0	0.009058
ELASAP,JF,MM0,M,RM1	ELASAP,JF,MM0,M,RM1	0.89674
ELASAP,JF,MM0,M,RM1	C	0.086051
ELASAP,JF,MM0,M,RM1	FL	0.0081522
ELASAP,JF,MM0,P,RM0	ELASAP,JF,MM0,P,RM0	0.5
ELASAP,JF,MM0,P,RM0	FL	0.5
ELASAP,JF,MM0,P,RM1	ELASAP,JF,MM0,P,RM0	0.04529
ELASAP,JF,MM0,P,RM1	ELASAP,JF,MM0,P,RM1	0.86051
ELASAP,JF,MM0,P,RM1	C	0.086051
ELASAP,JF,MM0,P,RM1	FL	0.0081522
ELASAP,JF,MM1,G,RM0	ELASAP,JF,MM0,G,RM0	0.5
ELASAP,JF,MM1,G,RM0	FL	0.5
ELASAP,JF,MM1,G,RM1	ELASAP,JF,MM0,G,RM0	4.1663e-05
ELASAP,JF,MM1,G,RM1	ELASAP,JF,MM0,G,RM1	0.83322
ELASAP,JF,MM1,G,RM1	C	0.16665

Continued on next page

Table A.1 – continued from previous page

S_t	S_{t+1}	**P**
ELASAP,JF,MM1,G,RM1	FL	8.3326e-05
ELASAP,JF,MM1,M,RM0	ELASAP,JF,MM0,M,RM0	0.5
ELASAP,JF,MM1,M,RM0	FL	0.5
ELASAP,JF,MM1,M,RM1	ELASAP,JF,MM0,M,RM0	0.00041663
ELASAP,JF,MM1,M,RM1	ELASAP,JF,MM0,M,RM1	0.83285
ELASAP,JF,MM1,M,RM1	C	0.16665
ELASAP,JF,MM1,M,RM1	FL	8.3326e-05
ELASAP,JF,MM1,P,RM0	ELASAP,JF,MM0,P,RM0	0.5
ELASAP,JF,MM1,P,RM0	FL	0.5
ELASAP,JF,MM1,P,RM1	ELASAP,JF,MM0,P,RM0	0.0041663
ELASAP,JF,MM1,P,RM1	ELASAP,JF,MM0,P,RM1	0.8291
ELASAP,JF,MM1,P,RM1	C	0.16665
ELASAP,JF,MM1,P,RM1	FL	8.3326e-05
ELPRACT,NF,MM0,G,RM0	ELPRACT,NF,MM1,G,RM0	0.49998
ELPRACT,NF,MM0,G,RM0	ELPRACT,SF,MM1,G,RM0	2.375e-05
ELPRACT,NF,MM0,G,RM0	FL	0.5
ELPRACT,NF,MM0,G,RM1	ELPRACT,NF,MM1,G,RM0	0.0045473
ELPRACT,NF,MM0,G,RM1	ELPRACT,NF,MM1,G,RM1	0.90491
ELPRACT,NF,MM0,G,RM1	ELPRACT,SF,MM1,G,RM0	2.1601e-07
ELPRACT,NF,MM0,G,RM1	ELPRACT,SF,MM1,G,RM1	4.2985e-05
ELPRACT,NF,MM0,G,RM1	C	0.081855
ELPRACT,NF,MM0,G,RM1	FL	0.0086403
ELPRACT,NF,MM0,M,RM0	ELPRACT,NF,MM1,M,RM0	0.49998
ELPRACT,NF,MM0,M,RM0	ELPRACT,SF,MM1,M,RM0	2.375e-05

Continued on next page

Table A.1 – continued from previous page

S_t	S_{t+1}	**P**
ELPRACT,NF,MM0,M,RM0	FL	0.5
ELPRACT,NF,MM0,M,RM1	ELPRACT,NF,MM1,M,RM0	0.0090946
ELPRACT,NF,MM0,M,RM1	ELPRACT,NF,MM1,M,RM1	0.90037
ELPRACT,NF,MM0,M,RM1	ELPRACT,SF,MM1,M,RM0	4.3201e-07
ELPRACT,NF,MM0,M,RM1	ELPRACT,SF,MM1,M,RM1	4.2769e-05
ELPRACT,NF,MM0,M,RM1	C	0.081855
ELPRACT,NF,MM0,M,RM1	FL	0.0086403
ELPRACT,NF,MM0,P,RM0	ELPRACT,NF,MM1,P,RM0	0.49998
ELPRACT,NF,MM0,P,RM0	ELPRACT,SF,MM1,P,RM0	2.375e-05
ELPRACT,NF,MM0,P,RM0	FL	0.5
ELPRACT,NF,MM0,P,RM1	ELPRACT,NF,MM1,P,RM0	0.045473
ELPRACT,NF,MM0,P,RM1	ELPRACT,NF,MM1,P,RM1	0.86399
ELPRACT,NF,MM0,P,RM1	ELPRACT,SF,MM1,P,RM0	2.1601e-06
ELPRACT,NF,MM0,P,RM1	ELPRACT,SF,MM1,P,RM1	4.1041e-05
ELPRACT,NF,MM0,P,RM1	C	0.081855
ELPRACT,NF,MM0,P,RM1	FL	0.0086403
ELPRACT,NF,MM1,G,RM0	ELPRACT,NF,MM1,G,RM0	0.49998
ELPRACT,NF,MM1,G,RM0	ELPRACT,SF,MM1,G,RM0	2.375e-05
ELPRACT,NF,MM1,G,RM0	FL	0.5
ELPRACT,NF,MM1,G,RM1	ELPRACT,NF,MM1,G,RM0	4.3457e-05
ELPRACT,NF,MM1,G,RM1	ELPRACT,NF,MM1,G,RM1	0.8691
ELPRACT,NF,MM1,G,RM1	ELPRACT,SF,MM1,G,RM0	2.0643e-09
ELPRACT,NF,MM1,G,RM1	ELPRACT,SF,MM1,G,RM1	4.1284e-05
ELPRACT,NF,MM1,G,RM1	C	0.13038

Continued on next page

Table A.1 – continued from previous page

S_t	S_{t+1}	**P**
ELPRACT,NF,MM1,G,RM1	FL	0.00043459
ELPRACT,NF,MM1,M,RM0	ELPRACT,NF,MM1,M,RM0	0.49998
ELPRACT,NF,MM1,M,RM0	ELPRACT,SF,MM1,M,RM0	2.375e-05
ELPRACT,NF,MM1,M,RM0	FL	0.5
ELPRACT,NF,MM1,M,RM1	ELPRACT,NF,MM1,M,RM0	0.00043457
ELPRACT,NF,MM1,M,RM1	ELPRACT,NF,MM1,M,RM1	0.86871
ELPRACT,NF,MM1,M,RM1	ELPRACT,SF,MM1,M,RM0	2.0643e-08
ELPRACT,NF,MM1,M,RM1	ELPRACT,SF,MM1,M,RM1	4.1266e-05
ELPRACT,NF,MM1,M,RM1	C	0.13038
ELPRACT,NF,MM1,M,RM1	FL	0.00043459
ELPRACT,NF,MM1,P,RM0	ELPRACT,NF,MM1,P,RM0	0.49998
ELPRACT,NF,MM1,P,RM0	ELPRACT,SF,MM1,P,RM0	2.375e-05
ELPRACT,NF,MM1,P,RM0	FL	0.5
ELPRACT,NF,MM1,P,RM1	ELPRACT,NF,MM1,P,RM0	0.0043457
ELPRACT,NF,MM1,P,RM1	ELPRACT,NF,MM1,P,RM1	0.8648
ELPRACT,NF,MM1,P,RM1	ELPRACT,SF,MM1,P,RM0	2.0643e-07
ELPRACT,NF,MM1,P,RM1	ELPRACT,SF,MM1,P,RM1	4.108e-05
ELPRACT,NF,MM1,P,RM1	C	0.13038
ELPRACT,NF,MM1,P,RM1	FL	0.00043459
ELPRACT,SF,MM0,G,RM0	ELPRACT,SF,MM0,G,RM0	0.4961
ELPRACT,SF,MM0,G,RM0	ELPRACT,SF,MM1,G,RM0	0.002493
ELPRACT,SF,MM0,G,RM0	ELPRACT,JF,MM0,G,RM0	0.0013975
ELPRACT,SF,MM0,G,RM0	ELPRACT,JF,MM1,G,RM0	7.0225e-06
ELPRACT,SF,MM0,G,RM0	FL	0.5

Continued on next page

Table A.1 – continued from previous page

S_t	S_{t+1}	**P**
ELPRACT,SF,MM0,G,RM1	ELPRACT,SF,MM0,G,RM0	0.0045121
ELPRACT,SF,MM0,G,RM1	ELPRACT,SF,MM0,G,RM1	0.8979
ELPRACT,SF,MM0,G,RM1	ELPRACT,SF,MM1,G,RM0	2.2674e-05
ELPRACT,SF,MM0,G,RM1	ELPRACT,SF,MM1,G,RM1	0.0045121
ELPRACT,SF,MM0,G,RM1	ELPRACT,JF,MM0,G,RM0	1.271e-05
ELPRACT,SF,MM0,G,RM1	ELPRACT,JF,MM0,G,RM1	0.0025293
ELPRACT,SF,MM0,G,RM1	ELPRACT,JF,MM1,G,RM0	6.387e-08
ELPRACT,SF,MM0,G,RM1	ELPRACT,JF,MM1,G,RM1	1.271e-05
ELPRACT,SF,MM0,G,RM1	C	0.081855
ELPRACT,SF,MM0,G,RM1	FL	0.0086403
ELPRACT,SF,MM0,M,RM0	ELPRACT,SF,MM0,M,RM0	0.4961
ELPRACT,SF,MM0,M,RM0	ELPRACT,SF,MM1,M,RM0	0.002493
ELPRACT,SF,MM0,M,RM0	ELPRACT,JF,MM0,M,RM0	0.0013975
ELPRACT,SF,MM0,M,RM0	ELPRACT,JF,MM1,M,RM0	7.0225e-06
ELPRACT,SF,MM0,M,RM0	FL	0.5
ELPRACT,SF,MM0,M,RM1	ELPRACT,SF,MM0,M,RM0	0.0090241
ELPRACT,SF,MM0,M,RM1	ELPRACT,SF,MM0,M,RM1	0.89339
ELPRACT,SF,MM0,M,RM1	ELPRACT,SF,MM1,M,RM0	4.5347e-05
ELPRACT,SF,MM0,M,RM1	ELPRACT,SF,MM1,M,RM1	0.0044894
ELPRACT,SF,MM0,M,RM1	ELPRACT,JF,MM0,M,RM0	2.542e-05
ELPRACT,SF,MM0,M,RM1	ELPRACT,JF,MM0,M,RM1	0.0025166
ELPRACT,SF,MM0,M,RM1	ELPRACT,JF,MM1,M,RM0	1.2774e-07
ELPRACT,SF,MM0,M,RM1	ELPRACT,JF,MM1,M,RM1	1.2646e-05
ELPRACT,SF,MM0,M,RM1	C	0.081855

Continued on next page

Table A.1 – continued from previous page

S_t	S_{t+1}	**P**
ELPRACT,SF,MM0,M,RM1	FL	0.0086403
ELPRACT,SF,MM0,P,RM0	ELPRACT,SF,MM0,P,RM0	0.4961
ELPRACT,SF,MM0,P,RM0	ELPRACT,SF,MM1,P,RM0	0.002493
ELPRACT,SF,MM0,P,RM0	ELPRACT,JF,MM0,P,RM0	0.0013975
ELPRACT,SF,MM0,P,RM0	ELPRACT,JF,MM1,P,RM0	7.0225e-06
ELPRACT,SF,MM0,P,RM0	FL	0.5
ELPRACT,SF,MM0,P,RM1	ELPRACT,SF,MM0,P,RM0	0.045121
ELPRACT,SF,MM0,P,RM1	ELPRACT,SF,MM0,P,RM1	0.85729
ELPRACT,SF,MM0,P,RM1	ELPRACT,SF,MM1,P,RM0	0.00022674
ELPRACT,SF,MM0,P,RM1	ELPRACT,SF,MM1,P,RM1	0.004308
ELPRACT,SF,MM0,P,RM1	ELPRACT,JF,MM0,P,RM0	0.0001271
ELPRACT,SF,MM0,P,RM1	ELPRACT,JF,MM0,P,RM1	0.0024149
ELPRACT,SF,MM0,P,RM1	ELPRACT,JF,MM1,P,RM0	6.387e-07
ELPRACT,SF,MM0,P,RM1	ELPRACT,JF,MM1,P,RM1	1.2135e-05
ELPRACT,SF,MM0,P,RM1	C	0.081855
ELPRACT,SF,MM0,P,RM1	FL	0.0086403
ELPRACT,SF,MM1,G,RM0	ELPRACT,SF,MM0,G,RM0	0.0014006
ELPRACT,SF,MM1,G,RM0	ELPRACT,SF,MM1,G,RM0	0.49719
ELPRACT,SF,MM1,G,RM0	ELPRACT,JF,MM0,G,RM0	3.9452e-06
ELPRACT,SF,MM1,G,RM0	ELPRACT,JF,MM1,G,RM0	0.0014006
ELPRACT,SF,MM1,G,RM0	FL	0.5
ELPRACT,SF,MM1,G,RM1	ELPRACT,SF,MM0,G,RM0	1.2173e-07
ELPRACT,SF,MM1,G,RM1	ELPRACT,SF,MM0,G,RM1	0.0024346
ELPRACT,SF,MM1,G,RM1	ELPRACT,SF,MM1,G,RM0	4.3216e-05

Continued on next page

Table A.1 – continued from previous page

S_t	S_{t+1}	**P**
ELPRACT,SF,MM1,G,RM1	ELPRACT,SF,MM1,G,RM1	0.86427
ELPRACT,SF,MM1,G,RM1	ELPRACT,JF,MM0,G,RM0	3.4292e-10
ELPRACT,SF,MM1,G,RM1	ELPRACT,JF,MM0,G,RM1	6.858e-06
ELPRACT,SF,MM1,G,RM1	ELPRACT,JF,MM1,G,RM0	1.2173e-07
ELPRACT,SF,MM1,G,RM1	ELPRACT,JF,MM1,G,RM1	0.0024346
ELPRACT,SF,MM1,G,RM1	C	0.13038
ELPRACT,SF,MM1,G,RM1	FL	0.00043459
ELPRACT,SF,MM1,M,RM0	ELPRACT,SF,MM0,M,RM0	0.0014006
ELPRACT,SF,MM1,M,RM0	ELPRACT,SF,MM1,M,RM0	0.49719
ELPRACT,SF,MM1,M,RM0	ELPRACT,JF,MM0,M,RM0	3.9452e-06
ELPRACT,SF,MM1,M,RM0	ELPRACT,JF,MM1,M,RM0	0.0014006
ELPRACT,SF,MM1,M,RM0	FL	0.5
ELPRACT,SF,MM1,M,RM1	ELPRACT,SF,MM0,M,RM0	1.2173e-06
ELPRACT,SF,MM1,M,RM1	ELPRACT,SF,MM0,M,RM1	0.0024335
ELPRACT,SF,MM1,M,RM1	ELPRACT,SF,MM1,M,RM0	0.00043216
ELPRACT,SF,MM1,M,RM1	ELPRACT,SF,MM1,M,RM1	0.86388
ELPRACT,SF,MM1,M,RM1	ELPRACT,JF,MM0,M,RM0	3.4292e-09
ELPRACT,SF,MM1,M,RM1	ELPRACT,JF,MM0,M,RM1	6.8549e-06
ELPRACT,SF,MM1,M,RM1	ELPRACT,JF,MM1,M,RM0	1.2173e-06
ELPRACT,SF,MM1,M,RM1	ELPRACT,JF,MM1,M,RM1	0.0024335
ELPRACT,SF,MM1,M,RM1	C	0.13038
ELPRACT,SF,MM1,M,RM1	FL	0.00043459
ELPRACT,SF,MM1,P,RM0	ELPRACT,SF,MM0,P,RM0	0.0014006
ELPRACT,SF,MM1,P,RM0	ELPRACT,SF,MM1,P,RM0	0.49719

Continued on next page

Table A.1 – continued from previous page

S_t	S_{t+1}	**P**
ELPRACT,SF,MM1,P,RM0	ELPRACT,JF,MM0,P,RM0	3.9452e-06
ELPRACT,SF,MM1,P,RM0	ELPRACT,JF,MM1,P,RM0	0.0014006
ELPRACT,SF,MM1,P,RM0	FL	0.5
ELPRACT,SF,MM1,P,RM1	ELPRACT,SF,MM0,P,RM0	1.2173e-05
ELPRACT,SF,MM1,P,RM1	ELPRACT,SF,MM0,P,RM1	0.0024225
ELPRACT,SF,MM1,P,RM1	ELPRACT,SF,MM1,P,RM0	0.0043216
ELPRACT,SF,MM1,P,RM1	ELPRACT,SF,MM1,P,RM1	0.85999
ELPRACT,SF,MM1,P,RM1	ELPRACT,JF,MM0,P,RM0	3.4292e-08
ELPRACT,SF,MM1,P,RM1	ELPRACT,JF,MM0,P,RM1	6.824e-06
ELPRACT,SF,MM1,P,RM1	ELPRACT,JF,MM1,P,RM0	1.2173e-05
ELPRACT,SF,MM1,P,RM1	ELPRACT,JF,MM1,P,RM1	0.0024225
ELPRACT,SF,MM1,P,RM1	C	0.13038
ELPRACT,SF,MM1,P,RM1	FL	0.00043459
ELPRACT,JF,MM0,G,RM0	ELPRACT,JF,MM0,G,RM0	0.5
ELPRACT,JF,MM0,G,RM0	FL	0.5
ELPRACT,JF,MM0,G,RM1	ELPRACT,JF,MM0,G,RM0	0.0045475
ELPRACT,JF,MM0,G,RM1	ELPRACT,JF,MM0,G,RM1	0.90496
ELPRACT,JF,MM0,G,RM1	C	0.081855
ELPRACT,JF,MM0,G,RM1	FL	0.0086403
ELPRACT,JF,MM0,M,RM0	ELPRACT,JF,MM0,M,RM0	0.5
ELPRACT,JF,MM0,M,RM0	FL	0.5
ELPRACT,JF,MM0,M,RM1	ELPRACT,JF,MM0,M,RM0	0.009095
ELPRACT,JF,MM0,M,RM1	ELPRACT,JF,MM0,M,RM1	0.90041
ELPRACT,JF,MM0,M,RM1	C	0.081855

Continued on next page

Table A.1 – continued from previous page

S_t	S_{t+1}	**P**
ELPRACT,JF,MM0,M,RM1	FL	0.0086403
ELPRACT,JF,MM0,P,RM0	ELPRACT,JF,MM0,P,RM0	0.5
ELPRACT,JF,MM0,P,RM0	FL	0.5
ELPRACT,JF,MM0,P,RM1	ELPRACT,JF,MM0,P,RM0	0.045475
ELPRACT,JF,MM0,P,RM1	ELPRACT,JF,MM0,P,RM1	0.86403
ELPRACT,JF,MM0,P,RM1	C	0.081855
ELPRACT,JF,MM0,P,RM1	FL	0.0086403
ELPRACT,JF,MM1,G,RM0	ELPRACT,JF,MM0,G,RM0	0.5
ELPRACT,JF,MM1,G,RM0	FL	0.5
ELPRACT,JF,MM1,G,RM1	ELPRACT,JF,MM0,G,RM0	4.3459e-05
ELPRACT,JF,MM1,G,RM1	ELPRACT,JF,MM0,G,RM1	0.86914
ELPRACT,JF,MM1,G,RM1	C	0.13038
ELPRACT,JF,MM1,G,RM1	FL	0.00043459
ELPRACT,JF,MM1,M,RM0	ELPRACT,JF,MM0,M,RM0	0.5
ELPRACT,JF,MM1,M,RM0	FL	0.5
ELPRACT,JF,MM1,M,RM1	ELPRACT,JF,MM0,M,RM0	0.00043459
ELPRACT,JF,MM1,M,RM1	ELPRACT,JF,MM0,M,RM1	0.86875
ELPRACT,JF,MM1,M,RM1	C	0.13038
ELPRACT,JF,MM1,M,RM1	FL	0.00043459
ELPRACT,JF,MM1,P,RM0	ELPRACT,JF,MM0,P,RM0	0.5
ELPRACT,JF,MM1,P,RM0	FL	0.5
ELPRACT,JF,MM1,P,RM1	ELPRACT,JF,MM0,P,RM0	0.0043459
ELPRACT,JF,MM1,P,RM1	ELPRACT,JF,MM0,P,RM1	0.86484
ELPRACT,JF,MM1,P,RM1	C	0.13038

Continued on next page

Table A.1 – continued from previous page

S_t	S_{t+1}	**P**
ELPRACT,JF,MM1,P,RM1	FL	0.00043459
C	E	1
T	E	1
FL	E	1
E	E	1

Table A.2: State Transition Probabilities for $A_t = \textit{Terminate}$

S_t	S_{t+1}	**P**
N,NF,MM0,G,RM0	T	1
N,NF,MM0,G,RM1	T	1
N,NF,MM0,M,RM0	T	1
N,NF,MM0,M,RM1	T	1
N,NF,MM0,P,RM0	T	1
N,NF,MM0,P,RM1	T	1
N,NF,MM1,G,RM0	T	1
N,NF,MM1,G,RM1	T	1
N,NF,MM1,M,RM0	T	1
N,NF,MM1,M,RM1	T	1
N,NF,MM1,P,RM0	T	1
N,NF,MM1,P,RM1	T	1
N,SF,MM0,G,RM0	T	1
N,SF,MM0,G,RM1	T	1

Continued on next page

Table A.2 – continued from previous page

S_t	S_{t+1}	**P**
N,SF,MM0,M,RM0	T	1
N,SF,MM0,M,RM1	T	1
N,SF,MM0,P,RM0	T	1
N,SF,MM0,P,RM1	T	1
N,SF,MM1,G,RM0	T	1
N,SF,MM1,G,RM1	T	1
N,SF,MM1,M,RM0	T	1
N,SF,MM1,M,RM1	T	1
N,SF,MM1,P,RM0	T	1
N,SF,MM1,P,RM1	T	1
N,JF,MM0,G,RM0	T	1
N,JF,MM0,G,RM1	T	1
N,JF,MM0,M,RM0	T	1
N,JF,MM0,M,RM1	T	1
N,JF,MM0,P,RM0	T	1
N,JF,MM0,P,RM1	T	1
N,JF,MM1,G,RM0	T	1
N,JF,MM1,G,RM1	T	1
N,JF,MM1,M,RM0	T	1
N,JF,MM1,M,RM1	T	1
N,JF,MM1,P,RM0	T	1
N,JF,MM1,P,RM1	T	1
ELASAP,NF,MM0,G,RM0	T	1
ELASAP,NF,MM0,G,RM1	T	1

Continued on next page

Table A.2 – continued from previous page

S_t	S_{t+1}	**P**
ELASAP,NF,MM0,M,RM0	T	1
ELASAP,NF,MM0,M,RM1	T	1
ELASAP,NF,MM0,P,RM0	T	1
ELASAP,NF,MM0,P,RM1	T	1
ELASAP,NF,MM1,G,RM0	T	1
ELASAP,NF,MM1,G,RM1	T	1
ELASAP,NF,MM1,M,RM0	T	1
ELASAP,NF,MM1,M,RM1	T	1
ELASAP,NF,MM1,P,RM0	T	1
ELASAP,NF,MM1,P,RM1	T	1
ELASAP,SF,MM0,G,RM0	T	1
ELASAP,SF,MM0,G,RM1	T	1
ELASAP,SF,MM0,M,RM0	T	1
ELASAP,SF,MM0,M,RM1	T	1
ELASAP,SF,MM0,P,RM0	T	1
ELASAP,SF,MM0,P,RM1	T	1
ELASAP,SF,MM1,G,RM0	T	1
ELASAP,SF,MM1,G,RM1	T	1
ELASAP,SF,MM1,M,RM0	T	1
ELASAP,SF,MM1,M,RM1	T	1
ELASAP,SF,MM1,P,RM0	T	1
ELASAP,SF,MM1,P,RM1	T	1
ELASAP,JF,MM0,G,RM0	T	1
ELASAP,JF,MM0,G,RM1	T	1

Continued on next page

Table A.2 – continued from previous page

S_t	S_{t+1}	**P**
ELASAP,JF,MM0,M,RM0	T	1
ELASAP,JF,MM0,M,RM1	T	1
ELASAP,JF,MM0,P,RM0	T	1
ELASAP,JF,MM0,P,RM1	T	1
ELASAP,JF,MM1,G,RM0	T	1
ELASAP,JF,MM1,G,RM1	T	1
ELASAP,JF,MM1,M,RM0	T	1
ELASAP,JF,MM1,M,RM1	T	1
ELASAP,JF,MM1,P,RM0	T	1
ELASAP,JF,MM1,P,RM1	T	1
ELPRACT,NF,MM0,G,RM0	T	1
ELPRACT,NF,MM0,G,RM1	T	1
ELPRACT,NF,MM0,M,RM0	T	1
ELPRACT,NF,MM0,M,RM1	T	1
ELPRACT,NF,MM0,P,RM0	T	1
ELPRACT,NF,MM0,P,RM1	T	1
ELPRACT,NF,MM1,G,RM0	T	1
ELPRACT,NF,MM1,G,RM1	T	1
ELPRACT,NF,MM1,M,RM0	T	1
ELPRACT,NF,MM1,M,RM1	T	1
ELPRACT,NF,MM1,P,RM0	T	1
ELPRACT,NF,MM1,P,RM1	T	1
ELPRACT,SF,MM0,G,RM0	T	1
ELPRACT,SF,MM0,G,RM1	T	1

Continued on next page

Table A.2 – continued from previous page

S_t	S_{t+1}	**P**
ELPRACT,SF,MM0,M,RM0	T	1
ELPRACT,SF,MM0,M,RM1	T	1
ELPRACT,SF,MM0,P,RM0	T	1
ELPRACT,SF,MM0,P,RM1	T	1
ELPRACT,SF,MM1,G,RM0	T	1
ELPRACT,SF,MM1,G,RM1	T	1
ELPRACT,SF,MM1,M,RM0	T	1
ELPRACT,SF,MM1,M,RM1	T	1
ELPRACT,SF,MM1,P,RM0	T	1
ELPRACT,SF,MM1,P,RM1	T	1
ELPRACT,JF,MM0,G,RM0	T	1
ELPRACT,JF,MM0,G,RM1	T	1
ELPRACT,JF,MM0,M,RM0	T	1
ELPRACT,JF,MM0,M,RM1	T	1
ELPRACT,JF,MM0,P,RM0	T	1
ELPRACT,JF,MM0,P,RM1	T	1
ELPRACT,JF,MM1,G,RM0	T	1
ELPRACT,JF,MM1,G,RM1	T	1
ELPRACT,JF,MM1,M,RM0	T	1
ELPRACT,JF,MM1,M,RM1	T	1
ELPRACT,JF,MM1,P,RM0	T	1
ELPRACT,JF,MM1,P,RM1	T	1
C	E	1
T	E	1

Continued on next page

Table A.2 – continued from previous page

S_t	S_{t+1}	**P**
FL	E	1
E	E	1

Table A.3: State Transition Probabilities for $A_t = LandASAP$

S_t	S_{t+1}	**P**
N,NF,MM0,G,RM0	ELASAP,NF,MM1,G,RM0	0.0029993
N,NF,MM0,G,RM0	ELASAP,NF,MM1,G,RM1	0.99675
N,NF,MM0,G,RM0	ELASAP,SF,MM1,G,RM0	1.4247e-07
N,NF,MM0,G,RM0	ELASAP,SF,MM1,G,RM1	4.7348e-05
N,NF,MM0,G,RM0	FL	0.00019996
N,NF,MM0,G,RM1	ELASAP,NF,MM1,G,RM0	0.00029716
N,NF,MM0,G,RM1	ELASAP,NF,MM1,G,RM1	0.99025
N,NF,MM0,G,RM1	ELASAP,SF,MM1,G,RM0	1.4116e-08
N,NF,MM0,G,RM1	ELASAP,SF,MM1,G,RM1	4.7039e-05
N,NF,MM0,G,RM1	C	0.0094106
N,NF,MM0,M,RM0	ELASAP,NF,MM1,M,RM0	0.003999
N,NF,MM0,M,RM0	ELASAP,NF,MM1,M,RM1	0.99575
N,NF,MM0,M,RM0	ELASAP,SF,MM1,M,RM0	1.8996e-07
N,NF,MM0,M,RM0	ELASAP,SF,MM1,M,RM1	4.7301e-05
N,NF,MM0,M,RM0	FL	0.00019996
N,NF,MM0,M,RM1	ELASAP,NF,MM1,M,RM0	0.00039622
N,NF,MM0,M,RM1	ELASAP,NF,MM1,M,RM1	0.99015

Continued on next page

Table A.3 – continued from previous page

S_t	S_{t+1}	**P**
N,NF,MM0,M,RM1	ELASAP,SF,MM1,M,RM0	1.8821e-08
N,NF,MM0,M,RM1	ELASAP,SF,MM1,M,RM1	4.7034e-05
N,NF,MM0,M,RM1	C	0.0094106
N,NF,MM0,P,RM0	ELASAP,NF,MM1,P,RM0	0.0049988
N,NF,MM0,P,RM0	ELASAP,NF,MM1,P,RM1	0.99475
N,NF,MM0,P,RM0	ELASAP,SF,MM1,P,RM0	2.3745e-07
N,NF,MM0,P,RM0	ELASAP,SF,MM1,P,RM1	4.7253e-05
N,NF,MM0,P,RM0	FL	0.00019996
N,NF,MM0,P,RM1	ELASAP,NF,MM1,P,RM0	0.0049307
N,NF,MM0,P,RM1	ELASAP,NF,MM1,P,RM1	0.98565
N,NF,MM0,P,RM1	ELASAP,SF,MM1,P,RM0	2.3422e-07
N,NF,MM0,P,RM1	ELASAP,SF,MM1,P,RM1	4.6821e-05
N,NF,MM0,P,RM1	C	0.0093688
N,NF,MM1,G,RM0	ELASAP,NF,MM1,G,RM0	0.003496
N,NF,MM1,G,RM0	ELASAP,NF,MM1,G,RM1	0.99636
N,NF,MM1,G,RM0	ELASAP,SF,MM1,G,RM0	1.6607e-07
N,NF,MM1,G,RM0	ELASAP,SF,MM1,G,RM1	4.7329e-05
N,NF,MM1,G,RM0	FL	9.989e-05
N,NF,MM1,G,RM1	ELASAP,NF,MM1,G,RM0	4.9503e-06
N,NF,MM1,G,RM1	ELASAP,NF,MM1,G,RM1	0.99005
N,NF,MM1,G,RM1	ELASAP,SF,MM1,G,RM0	2.3515e-10
N,NF,MM1,G,RM1	ELASAP,SF,MM1,G,RM1	4.7029e-05
N,NF,MM1,G,RM1	C	0.009901
N,NF,MM1,M,RM0	ELASAP,NF,MM1,M,RM0	0.0044948

Continued on next page

Table A.3 – continued from previous page

S_t	S_{t+1}	**P**
N,NF,MM1,M,RM0	ELASAP,NF,MM1,M,RM1	0.99536
N,NF,MM1,M,RM0	ELASAP,SF,MM1,M,RM0	2.1352e-07
N,NF,MM1,M,RM0	ELASAP,SF,MM1,M,RM1	4.7282e-05
N,NF,MM1,M,RM0	FL	9.989e-05
N,NF,MM1,M,RM1	ELASAP,NF,MM1,M,RM0	4.9503e-05
N,NF,MM1,M,RM1	ELASAP,NF,MM1,M,RM1	0.99
N,NF,MM1,M,RM1	ELASAP,SF,MM1,M,RM0	2.3515e-09
N,NF,MM1,M,RM1	ELASAP,SF,MM1,M,RM1	4.7027e-05
N,NF,MM1,M,RM1	C	0.009901
N,NF,MM1,P,RM0	ELASAP,NF,MM1,P,RM0	0.0054937
N,NF,MM1,P,RM0	ELASAP,NF,MM1,P,RM1	0.99436
N,NF,MM1,P,RM0	ELASAP,SF,MM1,P,RM0	2.6096e-07
N,NF,MM1,P,RM0	ELASAP,SF,MM1,P,RM1	4.7234e-05
N,NF,MM1,P,RM0	FL	9.989e-05
N,NF,MM1,P,RM1	ELASAP,NF,MM1,P,RM0	0.00039602
N,NF,MM1,P,RM1	ELASAP,NF,MM1,P,RM1	0.98966
N,NF,MM1,P,RM1	ELASAP,SF,MM1,P,RM0	1.8812e-08
N,NF,MM1,P,RM1	ELASAP,SF,MM1,P,RM1	4.7011e-05
N,NF,MM1,P,RM1	C	0.009901
N,SF,MM0,G,RM0	ELASAP,SF,MM0,G,RM0	0.0026763
N,SF,MM0,G,RM0	ELASAP,SF,MM0,G,RM1	0.88942
N,SF,MM0,G,RM0	ELASAP,SF,MM1,G,RM0	0.00029737
N,SF,MM0,G,RM0	ELASAP,SF,MM1,G,RM1	0.098825
N,SF,MM0,G,RM0	ELASAP,JF,MM0,G,RM0	2.3169e-05

Continued on next page

Table A.3 – continued from previous page

S_t	S_{t+1}	**P**
N,SF,MM0,G,RM0	ELASAP,JF,MM0,G,RM1	0.0076999
N,SF,MM0,G,RM0	ELASAP,JF,MM1,G,RM0	2.5744e-06
N,SF,MM0,G,RM0	ELASAP,JF,MM1,G,RM1	0.00085555
N,SF,MM0,G,RM0	FL	0.00019996
N,SF,MM0,G,RM1	ELASAP,SF,MM0,G,RM0	0.00026516
N,SF,MM0,G,RM1	ELASAP,SF,MM0,G,RM1	0.88361
N,SF,MM0,G,RM1	ELASAP,SF,MM1,G,RM0	2.9463e-05
N,SF,MM0,G,RM1	ELASAP,SF,MM1,G,RM1	0.098179
N,SF,MM0,G,RM1	ELASAP,JF,MM0,G,RM0	2.2956e-06
N,SF,MM0,G,RM1	ELASAP,JF,MM0,G,RM1	0.0076497
N,SF,MM0,G,RM1	ELASAP,JF,MM1,G,RM0	2.5507e-07
N,SF,MM0,G,RM1	ELASAP,JF,MM1,G,RM1	0.00084996
N,SF,MM0,G,RM1	C	0.0094106
N,SF,MM0,M,RM0	ELASAP,SF,MM0,M,RM0	0.0035684
N,SF,MM0,M,RM0	ELASAP,SF,MM0,M,RM1	0.88853
N,SF,MM0,M,RM0	ELASAP,SF,MM1,M,RM0	0.00039649
N,SF,MM0,M,RM0	ELASAP,SF,MM1,M,RM1	0.098725
N,SF,MM0,M,RM0	ELASAP,JF,MM0,M,RM0	3.0892e-05
N,SF,MM0,M,RM0	ELASAP,JF,MM0,M,RM1	0.0076922
N,SF,MM0,M,RM0	ELASAP,JF,MM1,M,RM0	3.4325e-06
N,SF,MM0,M,RM0	ELASAP,JF,MM1,M,RM1	0.00085469
N,SF,MM0,M,RM0	FL	0.00019996
N,SF,MM0,M,RM1	ELASAP,SF,MM0,M,RM0	0.00035355
N,SF,MM0,M,RM1	ELASAP,SF,MM0,M,RM1	0.88352

Continued on next page

Table A.3 – continued from previous page

S_t	S_{t+1}	**P**
N,SF,MM0,M,RM1	ELASAP,SF,MM1,M,RM0	3.9283e-05
N,SF,MM0,M,RM1	ELASAP,SF,MM1,M,RM1	0.098169
N,SF,MM0,M,RM1	ELASAP,JF,MM0,M,RM0	3.0608e-06
N,SF,MM0,M,RM1	ELASAP,JF,MM0,M,RM1	0.0076489
N,SF,MM0,M,RM1	ELASAP,JF,MM1,M,RM0	3.4009e-07
N,SF,MM0,M,RM1	ELASAP,JF,MM1,M,RM1	0.00084988
N,SF,MM0,M,RM1	C	0.0094106
N,SF,MM0,P,RM0	ELASAP,SF,MM0,P,RM0	0.0044605
N,SF,MM0,P,RM0	ELASAP,SF,MM0,P,RM1	0.88764
N,SF,MM0,P,RM0	ELASAP,SF,MM1,P,RM0	0.00049561
N,SF,MM0,P,RM0	ELASAP,SF,MM1,P,RM1	0.098626
N,SF,MM0,P,RM0	ELASAP,JF,MM0,P,RM0	3.8616e-05
N,SF,MM0,P,RM0	ELASAP,JF,MM0,P,RM1	0.0076845
N,SF,MM0,P,RM0	ELASAP,JF,MM1,P,RM0	4.2906e-06
N,SF,MM0,P,RM0	ELASAP,JF,MM1,P,RM1	0.00085383
N,SF,MM0,P,RM0	FL	0.00019996
N,SF,MM0,P,RM1	ELASAP,SF,MM0,P,RM0	0.0043998
N,SF,MM0,P,RM1	ELASAP,SF,MM0,P,RM1	0.87952
N,SF,MM0,P,RM1	ELASAP,SF,MM1,P,RM0	0.00048886
N,SF,MM0,P,RM1	ELASAP,SF,MM1,P,RM1	0.097724
N,SF,MM0,P,RM1	ELASAP,JF,MM0,P,RM0	3.809e-05
N,SF,MM0,P,RM1	ELASAP,JF,MM0,P,RM1	0.0076142
N,SF,MM0,P,RM1	ELASAP,JF,MM1,P,RM0	4.2322e-06
N,SF,MM0,P,RM1	ELASAP,JF,MM1,P,RM1	0.00084602

Continued on next page

Table A.3 – continued from previous page

S_t	S_{t+1}	**P**
N,SF,MM0,P,RM1	C	0.0093688
N,SF,MM1,G,RM0	ELASAP,SF,MM0,G,RM0	6.9323e-06
N,SF,MM1,G,RM0	ELASAP,SF,MM0,G,RM1	0.0019757
N,SF,MM1,G,RM0	ELASAP,SF,MM1,G,RM0	0.0034592
N,SF,MM1,G,RM0	ELASAP,SF,MM1,G,RM1	0.98588
N,SF,MM1,G,RM0	ELASAP,JF,MM0,G,RM0	6.0015e-08
N,SF,MM1,G,RM0	ELASAP,JF,MM0,G,RM1	1.7104e-05
N,SF,MM1,G,RM0	ELASAP,JF,MM1,G,RM0	2.9947e-05
N,SF,MM1,G,RM0	ELASAP,JF,MM1,G,RM1	0.008535
N,SF,MM1,G,RM0	FL	9.989e-05
N,SF,MM1,G,RM1	ELASAP,SF,MM0,G,RM0	9.816e-09
N,SF,MM1,G,RM1	ELASAP,SF,MM0,G,RM1	0.0019632
N,SF,MM1,G,RM1	ELASAP,SF,MM1,G,RM0	4.8982e-06
N,SF,MM1,G,RM1	ELASAP,SF,MM1,G,RM1	0.97963
N,SF,MM1,G,RM1	ELASAP,JF,MM0,G,RM0	8.498e-11
N,SF,MM1,G,RM1	ELASAP,JF,MM0,G,RM1	1.6996e-05
N,SF,MM1,G,RM1	ELASAP,JF,MM1,G,RM0	4.2405e-08
N,SF,MM1,G,RM1	ELASAP,JF,MM1,G,RM1	0.0084809
N,SF,MM1,G,RM1	C	0.0099009
N,SF,MM1,M,RM0	ELASAP,SF,MM0,M,RM0	8.9129e-06
N,SF,MM1,M,RM0	ELASAP,SF,MM0,M,RM1	0.0019737
N,SF,MM1,M,RM0	ELASAP,SF,MM1,M,RM0	0.0044476
N,SF,MM1,M,RM0	ELASAP,SF,MM1,M,RM1	0.98489
N,SF,MM1,M,RM0	ELASAP,JF,MM0,M,RM0	7.7162e-08

Continued on next page

Table A.3 – continued from previous page

S_t	S_{t+1}	**P**
N,SF,MM1,M,RM0	ELASAP,JF,MM0,M,RM1	1.7087e-05
N,SF,MM1,M,RM0	ELASAP,JF,MM1,M,RM0	3.8504e-05
N,SF,MM1,M,RM0	ELASAP,JF,MM1,M,RM1	0.0085264
N,SF,MM1,M,RM0	FL	9.989e-05
N,SF,MM1,M,RM1	ELASAP,SF,MM0,M,RM0	9.816e-08
N,SF,MM1,M,RM1	ELASAP,SF,MM0,M,RM1	0.0019631
N,SF,MM1,M,RM1	ELASAP,SF,MM1,M,RM0	4.8982e-05
N,SF,MM1,M,RM1	ELASAP,SF,MM1,M,RM1	0.97959
N,SF,MM1,M,RM1	ELASAP,JF,MM0,M,RM0	8.498e-10
N,SF,MM1,M,RM1	ELASAP,JF,MM0,M,RM1	1.6995e-05
N,SF,MM1,M,RM1	ELASAP,JF,MM1,M,RM0	4.2405e-07
N,SF,MM1,M,RM1	ELASAP,JF,MM1,M,RM1	0.0084806
N,SF,MM1,M,RM1	C	0.0099009
N,SF,MM1,P,RM0	ELASAP,SF,MM0,P,RM0	1.0894e-05
N,SF,MM1,P,RM0	ELASAP,SF,MM0,P,RM1	0.0019717
N,SF,MM1,P,RM0	ELASAP,SF,MM1,P,RM0	0.0054359
N,SF,MM1,P,RM0	ELASAP,SF,MM1,P,RM1	0.9839
N,SF,MM1,P,RM0	ELASAP,JF,MM0,P,RM0	9.4309e-08
N,SF,MM1,P,RM0	ELASAP,JF,MM0,P,RM1	1.707e-05
N,SF,MM1,P,RM0	ELASAP,JF,MM1,P,RM0	4.706e-05
N,SF,MM1,P,RM0	ELASAP,JF,MM1,P,RM1	0.0085179
N,SF,MM1,P,RM0	FL	9.989e-05
N,SF,MM1,P,RM1	ELASAP,SF,MM0,P,RM0	7.8528e-07
N,SF,MM1,P,RM1	ELASAP,SF,MM0,P,RM1	0.0019624

Continued on next page

Table A.3 – continued from previous page

S_t	S_{t+1}	**P**
N,SF,MM1,P,RM1	ELASAP,SF,MM1,P,RM0	0.00039186
N,SF,MM1,P,RM1	ELASAP,SF,MM1,P,RM1	0.97925
N,SF,MM1,P,RM1	ELASAP,JF,MM0,P,RM0	6.7984e-09
N,SF,MM1,P,RM1	ELASAP,JF,MM0,P,RM1	1.6989e-05
N,SF,MM1,P,RM1	ELASAP,JF,MM1,P,RM0	3.3924e-06
N,SF,MM1,P,RM1	ELASAP,JF,MM1,P,RM1	0.0084776
N,SF,MM1,P,RM1	C	0.0099009
N,JF,MM0,G,RM0	ELASAP,JF,MM0,G,RM0	0.0029994
N,JF,MM0,G,RM0	ELASAP,JF,MM0,G,RM1	0.9968
N,JF,MM0,G,RM0	FL	0.00019996
N,JF,MM0,G,RM1	ELASAP,JF,MM0,G,RM0	0.00029718
N,JF,MM0,G,RM1	ELASAP,JF,MM0,G,RM1	0.99029
N,JF,MM0,G,RM1	C	0.0094106
N,JF,MM0,M,RM0	ELASAP,JF,MM0,M,RM0	0.0039992
N,JF,MM0,M,RM0	ELASAP,JF,MM0,M,RM1	0.9958
N,JF,MM0,M,RM0	FL	0.00019996
N,JF,MM0,M,RM1	ELASAP,JF,MM0,M,RM0	0.00039624
N,JF,MM0,M,RM1	ELASAP,JF,MM0,M,RM1	0.99019
N,JF,MM0,M,RM1	C	0.0094106
N,JF,MM0,P,RM0	ELASAP,JF,MM0,P,RM0	0.004999
N,JF,MM0,P,RM0	ELASAP,JF,MM0,P,RM1	0.9948
N,JF,MM0,P,RM0	FL	0.00019996
N,JF,MM0,P,RM1	ELASAP,JF,MM0,P,RM0	0.004931
N,JF,MM0,P,RM1	ELASAP,JF,MM0,P,RM1	0.9857

Continued on next page

Table A.3 – continued from previous page

S_t	S_{t+1}	**P**
N,JF,MM0,P,RM1	C	0.0093688
N,JF,MM1,G,RM0	ELASAP,JF,MM0,G,RM0	0.0034962
N,JF,MM1,G,RM0	ELASAP,JF,MM0,G,RM1	0.9964
N,JF,MM1,G,RM0	FL	9.989e-05
N,JF,MM1,G,RM1	ELASAP,JF,MM0,G,RM0	4.9505e-06
N,JF,MM1,G,RM1	ELASAP,JF,MM0,G,RM1	0.99009
N,JF,MM1,G,RM1	C	0.009901
N,JF,MM1,M,RM0	ELASAP,JF,MM0,M,RM0	0.0044951
N,JF,MM1,M,RM0	ELASAP,JF,MM0,M,RM1	0.99541
N,JF,MM1,M,RM0	FL	9.989e-05
N,JF,MM1,M,RM1	ELASAP,JF,MM0,M,RM0	4.9505e-05
N,JF,MM1,M,RM1	ELASAP,JF,MM0,M,RM1	0.99005
N,JF,MM1,M,RM1	C	0.009901
N,JF,MM1,P,RM0	ELASAP,JF,MM0,P,RM0	0.005494
N,JF,MM1,P,RM0	ELASAP,JF,MM0,P,RM1	0.99441
N,JF,MM1,P,RM0	FL	9.989e-05
N,JF,MM1,P,RM1	ELASAP,JF,MM0,P,RM0	0.00039604
N,JF,MM1,P,RM1	ELASAP,JF,MM0,P,RM1	0.9897
N,JF,MM1,P,RM1	C	0.009901
ELPRACT,NF,MM0,G,RM0	ELASAP,NF,MM1,G,RM0	0.0014999
ELPRACT,NF,MM0,G,RM0	ELASAP,NF,MM1,G,RM1	0.49848
ELPRACT,NF,MM0,G,RM0	ELASAP,SF,MM1,G,RM0	7.125e-08
ELPRACT,NF,MM0,G,RM0	ELASAP,SF,MM1,G,RM1	2.3679e-05
ELPRACT,NF,MM0,G,RM0	FL	0.5

Continued on next page

Table A.3 – continued from previous page

S_t	S_{t+1}	**P**
ELPRACT,NF,MM0,G,RM1	ELASAP,NF,MM1,G,RM0	0.00029691
ELPRACT,NF,MM0,G,RM1	ELASAP,NF,MM1,G,RM1	0.98941
ELPRACT,NF,MM0,G,RM1	ELASAP,SF,MM1,G,RM0	1.4104e-08
ELPRACT,NF,MM0,G,RM1	ELASAP,SF,MM1,G,RM1	4.6999e-05
ELPRACT,NF,MM0,G,RM1	C	0.0094027
ELPRACT,NF,MM0,G,RM1	FL	0.00084129
ELPRACT,NF,MM0,M,RM0	ELASAP,NF,MM1,M,RM0	0.0019999
ELPRACT,NF,MM0,M,RM0	ELASAP,NF,MM1,M,RM1	0.49798
ELPRACT,NF,MM0,M,RM0	ELASAP,SF,MM1,M,RM0	9.5e-08
ELPRACT,NF,MM0,M,RM0	ELASAP,SF,MM1,M,RM1	2.3655e-05
ELPRACT,NF,MM0,M,RM0	FL	0.5
ELPRACT,NF,MM0,M,RM1	ELASAP,NF,MM1,M,RM0	0.00039588
ELPRACT,NF,MM0,M,RM1	ELASAP,NF,MM1,M,RM1	0.98931
ELPRACT,NF,MM0,M,RM1	ELASAP,SF,MM1,M,RM0	1.8805e-08
ELPRACT,NF,MM0,M,RM1	ELASAP,SF,MM1,M,RM1	4.6995e-05
ELPRACT,NF,MM0,M,RM1	C	0.0094027
ELPRACT,NF,MM0,M,RM1	FL	0.00084129
ELPRACT,NF,MM0,P,RM0	ELASAP,NF,MM1,P,RM0	0.0024999
ELPRACT,NF,MM0,P,RM0	ELASAP,NF,MM1,P,RM1	0.49748
ELPRACT,NF,MM0,P,RM0	ELASAP,SF,MM1,P,RM0	1.1875e-07
ELPRACT,NF,MM0,P,RM0	ELASAP,SF,MM1,P,RM1	2.3631e-05
ELPRACT,NF,MM0,P,RM0	FL	0.5
ELPRACT,NF,MM0,P,RM1	ELASAP,NF,MM1,P,RM0	0.0049266
ELPRACT,NF,MM0,P,RM1	ELASAP,NF,MM1,P,RM1	0.98483

Continued on next page

Table A.3 – continued from previous page

S_t	S_{t+1}	**P**
ELPRACT,NF,MM0,P,RM1	ELASAP,SF,MM1,P,RM0	2.3402e-07
ELPRACT,NF,MM0,P,RM1	ELASAP,SF,MM1,P,RM1	4.6782e-05
ELPRACT,NF,MM0,P,RM1	C	0.009361
ELPRACT,NF,MM0,P,RM1	FL	0.00083756
ELPRACT,NF,MM1,G,RM0	ELASAP,NF,MM1,G,RM0	0.001749
ELPRACT,NF,MM1,G,RM0	ELASAP,NF,MM1,G,RM1	0.49848
ELPRACT,NF,MM1,G,RM0	ELASAP,SF,MM1,G,RM0	8.3083e-08
ELPRACT,NF,MM1,G,RM0	ELASAP,SF,MM1,G,RM1	2.3679e-05
ELPRACT,NF,MM1,G,RM0	FL	0.49975
ELPRACT,NF,MM1,G,RM1	ELASAP,NF,MM1,G,RM0	4.9466e-06
ELPRACT,NF,MM1,G,RM1	ELASAP,NF,MM1,G,RM1	0.98931
ELPRACT,NF,MM1,G,RM1	ELASAP,SF,MM1,G,RM0	2.3497e-10
ELPRACT,NF,MM1,G,RM1	ELASAP,SF,MM1,G,RM1	4.6995e-05
ELPRACT,NF,MM1,G,RM1	C	0.0098936
ELPRACT,NF,MM1,G,RM1	FL	0.00074202
ELPRACT,NF,MM1,M,RM0	ELASAP,NF,MM1,M,RM0	0.0022488
ELPRACT,NF,MM1,M,RM0	ELASAP,NF,MM1,M,RM1	0.49798
ELPRACT,NF,MM1,M,RM0	ELASAP,SF,MM1,M,RM0	1.0682e-07
ELPRACT,NF,MM1,M,RM0	ELASAP,SF,MM1,M,RM1	2.3655e-05
ELPRACT,NF,MM1,M,RM0	FL	0.49975
ELPRACT,NF,MM1,M,RM1	ELASAP,NF,MM1,M,RM0	4.9466e-05
ELPRACT,NF,MM1,M,RM1	ELASAP,NF,MM1,M,RM1	0.98927
ELPRACT,NF,MM1,M,RM1	ELASAP,SF,MM1,M,RM0	2.3497e-09
ELPRACT,NF,MM1,M,RM1	ELASAP,SF,MM1,M,RM1	4.6992e-05

Continued on next page

Table A.3 – continued from previous page

S_t	S_{t+1}	**P**
ELPRACT,NF,MM1,M,RM1	C	0.0098936
ELPRACT,NF,MM1,M,RM1	FL	0.00074202
ELPRACT,NF,MM1,P,RM0	ELASAP,NF,MM1,P,RM0	0.0027485
ELPRACT,NF,MM1,P,RM0	ELASAP,NF,MM1,P,RM1	0.49748
ELPRACT,NF,MM1,P,RM0	ELASAP,SF,MM1,P,RM0	1.3056e-07
ELPRACT,NF,MM1,P,RM0	ELASAP,SF,MM1,P,RM1	2.3631e-05
ELPRACT,NF,MM1,P,RM0	FL	0.49975
ELPRACT,NF,MM1,P,RM1	ELASAP,NF,MM1,P,RM0	0.00039573
ELPRACT,NF,MM1,P,RM1	ELASAP,NF,MM1,P,RM1	0.98892
ELPRACT,NF,MM1,P,RM1	ELASAP,SF,MM1,P,RM0	1.8798e-08
ELPRACT,NF,MM1,P,RM1	ELASAP,SF,MM1,P,RM1	4.6976e-05
ELPRACT,NF,MM1,P,RM1	C	0.0098936
ELPRACT,NF,MM1,P,RM1	FL	0.00074202
ELPRACT,SF,MM0,G,RM0	ELASAP,SF,MM0,G,RM0	0.0013384
ELPRACT,SF,MM0,G,RM0	ELASAP,SF,MM0,G,RM1	0.4448
ELPRACT,SF,MM0,G,RM0	ELASAP,SF,MM1,G,RM0	0.00014871
ELPRACT,SF,MM0,G,RM0	ELASAP,SF,MM1,G,RM1	0.049422
ELPRACT,SF,MM0,G,RM0	ELASAP,JF,MM0,G,RM0	1.1587e-05
ELPRACT,SF,MM0,G,RM0	ELASAP,JF,MM0,G,RM1	0.0038508
ELPRACT,SF,MM0,G,RM0	ELASAP,JF,MM1,G,RM0	1.2874e-06
ELPRACT,SF,MM0,G,RM0	ELASAP,JF,MM1,G,RM1	0.00042786
ELPRACT,SF,MM0,G,RM0	FL	0.5
ELPRACT,SF,MM0,G,RM1	ELASAP,SF,MM0,G,RM0	0.00026494
ELPRACT,SF,MM0,G,RM1	ELASAP,SF,MM0,G,RM1	0.88287

Continued on next page

Table A.3 – continued from previous page

S_t	S_{t+1}	**P**
ELPRACT,SF,MM0,G,RM1	ELASAP,SF,MM1,G,RM0	2.9438e-05
ELPRACT,SF,MM0,G,RM1	ELASAP,SF,MM1,G,RM1	0.098097
ELPRACT,SF,MM0,G,RM1	ELASAP,JF,MM0,G,RM0	2.2937e-06
ELPRACT,SF,MM0,G,RM1	ELASAP,JF,MM0,G,RM1	0.0076432
ELPRACT,SF,MM0,G,RM1	ELASAP,JF,MM1,G,RM0	2.5485e-07
ELPRACT,SF,MM0,G,RM1	ELASAP,JF,MM1,G,RM1	0.00084925
ELPRACT,SF,MM0,G,RM1	C	0.0094026
ELPRACT,SF,MM0,G,RM1	FL	0.00084129
ELPRACT,SF,MM0,M,RM0	ELASAP,SF,MM0,M,RM0	0.0017846
ELPRACT,SF,MM0,M,RM0	ELASAP,SF,MM0,M,RM1	0.44435
ELPRACT,SF,MM0,M,RM0	ELASAP,SF,MM1,M,RM0	0.00019828
ELPRACT,SF,MM0,M,RM0	ELASAP,SF,MM1,M,RM1	0.049373
ELPRACT,SF,MM0,M,RM0	ELASAP,JF,MM0,M,RM0	1.5449e-05
ELPRACT,SF,MM0,M,RM0	ELASAP,JF,MM0,M,RM1	0.0038469
ELPRACT,SF,MM0,M,RM0	ELASAP,JF,MM1,M,RM0	1.7166e-06
ELPRACT,SF,MM0,M,RM0	ELASAP,JF,MM1,M,RM1	0.00042743
ELPRACT,SF,MM0,M,RM0	FL	0.5
ELPRACT,SF,MM0,M,RM1	ELASAP,SF,MM0,M,RM0	0.00035325
ELPRACT,SF,MM0,M,RM1	ELASAP,SF,MM0,M,RM1	0.88278
ELPRACT,SF,MM0,M,RM1	ELASAP,SF,MM1,M,RM0	3.925e-05
ELPRACT,SF,MM0,M,RM1	ELASAP,SF,MM1,M,RM1	0.098087
ELPRACT,SF,MM0,M,RM1	ELASAP,JF,MM0,M,RM0	3.0582e-06
ELPRACT,SF,MM0,M,RM1	ELASAP,JF,MM0,M,RM1	0.0076425
ELPRACT,SF,MM0,M,RM1	ELASAP,JF,MM1,M,RM0	3.398e-07

Continued on next page

Table A.3 – continued from previous page

S_t	S_{t+1}	**P**
ELPRACT,SF,MM0,M,RM1	ELASAP,JF,MM1,M,RM1	0.00084916
ELPRACT,SF,MM0,M,RM1	C	0.0094026
ELPRACT,SF,MM0,M,RM1	FL	0.00084129
ELPRACT,SF,MM0,P,RM0	ELASAP,SF,MM0,P,RM0	0.0022307
ELPRACT,SF,MM0,P,RM0	ELASAP,SF,MM0,P,RM1	0.44391
ELPRACT,SF,MM0,P,RM0	ELASAP,SF,MM1,P,RM0	0.00024785
ELPRACT,SF,MM0,P,RM0	ELASAP,SF,MM1,P,RM1	0.049323
ELPRACT,SF,MM0,P,RM0	ELASAP,JF,MM0,P,RM0	1.9312e-05
ELPRACT,SF,MM0,P,RM0	ELASAP,JF,MM0,P,RM1	0.003843
ELPRACT,SF,MM0,P,RM0	ELASAP,JF,MM1,P,RM0	2.1457e-06
ELPRACT,SF,MM0,P,RM0	ELASAP,JF,MM1,P,RM1	0.000427
ELPRACT,SF,MM0,P,RM0	FL	0.5
ELPRACT,SF,MM0,P,RM1	ELASAP,SF,MM0,P,RM0	0.0043961
ELPRACT,SF,MM0,P,RM1	ELASAP,SF,MM0,P,RM1	0.87878
ELPRACT,SF,MM0,P,RM1	ELASAP,SF,MM1,P,RM0	0.00048845
ELPRACT,SF,MM0,P,RM1	ELASAP,SF,MM1,P,RM1	0.097642
ELPRACT,SF,MM0,P,RM1	ELASAP,JF,MM0,P,RM0	3.8058e-05
ELPRACT,SF,MM0,P,RM1	ELASAP,JF,MM0,P,RM1	0.0076078
ELPRACT,SF,MM0,P,RM1	ELASAP,JF,MM1,P,RM0	4.2287e-06
ELPRACT,SF,MM0,P,RM1	ELASAP,JF,MM1,P,RM1	0.00084531
ELPRACT,SF,MM0,P,RM1	C	0.0093609
ELPRACT,SF,MM0,P,RM1	FL	0.00083756
ELPRACT,SF,MM1,G,RM0	ELASAP,SF,MM0,G,RM0	3.4682e-06
ELPRACT,SF,MM1,G,RM0	ELASAP,SF,MM0,G,RM1	0.00098845

Continued on next page

Table A.3 – continued from previous page

S_t	S_{t+1}	**P**
ELPRACT,SF,MM1,G,RM0	ELASAP,SF,MM1,G,RM0	0.0017306
ELPRACT,SF,MM1,G,RM0	ELASAP,SF,MM1,G,RM1	0.49323
ELPRACT,SF,MM1,G,RM0	ELASAP,JF,MM0,G,RM0	3.0025e-08
ELPRACT,SF,MM1,G,RM0	ELASAP,JF,MM0,G,RM1	8.5572e-06
ELPRACT,SF,MM1,G,RM0	ELASAP,JF,MM1,G,RM0	1.4983e-05
ELPRACT,SF,MM1,G,RM0	ELASAP,JF,MM1,G,RM1	0.0042701
ELPRACT,SF,MM1,G,RM0	FL	0.49975
ELPRACT,SF,MM1,G,RM1	ELASAP,SF,MM0,G,RM0	9.8087e-09
ELPRACT,SF,MM1,G,RM1	ELASAP,SF,MM0,G,RM1	0.0019617
ELPRACT,SF,MM1,G,RM1	ELASAP,SF,MM1,G,RM0	4.8946e-06
ELPRACT,SF,MM1,G,RM1	ELASAP,SF,MM1,G,RM1	0.97891
ELPRACT,SF,MM1,G,RM1	ELASAP,JF,MM0,G,RM0	8.4917e-11
ELPRACT,SF,MM1,G,RM1	ELASAP,JF,MM0,G,RM1	1.6983e-05
ELPRACT,SF,MM1,G,RM1	ELASAP,JF,MM1,G,RM0	4.2373e-08
ELPRACT,SF,MM1,G,RM1	ELASAP,JF,MM1,G,RM1	0.0084746
ELPRACT,SF,MM1,G,RM1	C	0.0098936
ELPRACT,SF,MM1,G,RM1	FL	0.00074202
ELPRACT,SF,MM1,M,RM0	ELASAP,SF,MM0,M,RM0	4.4592e-06
ELPRACT,SF,MM1,M,RM0	ELASAP,SF,MM0,M,RM1	0.00098746
ELPRACT,SF,MM1,M,RM0	ELASAP,SF,MM1,M,RM0	0.0022251
ELPRACT,SF,MM1,M,RM0	ELASAP,SF,MM1,M,RM1	0.49274
ELPRACT,SF,MM1,M,RM0	ELASAP,JF,MM0,M,RM0	3.8604e-08
ELPRACT,SF,MM1,M,RM0	ELASAP,JF,MM0,M,RM1	8.5487e-06
ELPRACT,SF,MM1,M,RM0	ELASAP,JF,MM1,M,RM0	1.9263e-05

Continued on next page

Table A.3 – continued from previous page

S_t	S_{t+1}	**P**
ELPRACT,SF,MM1,M,RM0	ELASAP,JF,MM1,M,RM1	0.0042658
ELPRACT,SF,MM1,M,RM0	FL	0.49975
ELPRACT,SF,MM1,M,RM1	ELASAP,SF,MM0,M,RM0	9.8087e-08
ELPRACT,SF,MM1,M,RM1	ELASAP,SF,MM0,M,RM1	0.0019616
ELPRACT,SF,MM1,M,RM1	ELASAP,SF,MM1,M,RM0	4.8946e-05
ELPRACT,SF,MM1,M,RM1	ELASAP,SF,MM1,M,RM1	0.97886
ELPRACT,SF,MM1,M,RM1	ELASAP,JF,MM0,M,RM0	8.4917e-10
ELPRACT,SF,MM1,M,RM1	ELASAP,JF,MM0,M,RM1	1.6982e-05
ELPRACT,SF,MM1,M,RM1	ELASAP,JF,MM1,M,RM0	4.2373e-07
ELPRACT,SF,MM1,M,RM1	ELASAP,JF,MM1,M,RM1	0.0084743
ELPRACT,SF,MM1,M,RM1	C	0.0098936
ELPRACT,SF,MM1,M,RM1	FL	0.00074202
ELPRACT,SF,MM1,P,RM0	ELASAP,SF,MM0,P,RM0	5.4501e-06
ELPRACT,SF,MM1,P,RM0	ELASAP,SF,MM0,P,RM1	0.00098646
ELPRACT,SF,MM1,P,RM0	ELASAP,SF,MM1,P,RM0	0.0027196
ELPRACT,SF,MM1,P,RM0	ELASAP,SF,MM1,P,RM1	0.49225
ELPRACT,SF,MM1,P,RM0	ELASAP,JF,MM0,P,RM0	4.7183e-08
ELPRACT,SF,MM1,P,RM0	ELASAP,JF,MM0,P,RM1	8.5401e-06
ELPRACT,SF,MM1,P,RM0	ELASAP,JF,MM1,P,RM0	2.3544e-05
ELPRACT,SF,MM1,P,RM0	ELASAP,JF,MM1,P,RM1	0.0042615
ELPRACT,SF,MM1,P,RM0	FL	0.49975
ELPRACT,SF,MM1,P,RM1	ELASAP,SF,MM0,P,RM0	7.847e-07
ELPRACT,SF,MM1,P,RM1	ELASAP,SF,MM0,P,RM1	0.001961
ELPRACT,SF,MM1,P,RM1	ELASAP,SF,MM1,P,RM0	0.00039156

Continued on next page

Table A.3 – continued from previous page

S_t	S_{t+1}	**P**
ELPRACT,SF,MM1,P,RM1	ELASAP,SF,MM1,P,RM1	0.97852
ELPRACT,SF,MM1,P,RM1	ELASAP,JF,MM0,P,RM0	6.7933e-09
ELPRACT,SF,MM1,P,RM1	ELASAP,JF,MM0,P,RM1	1.6977e-05
ELPRACT,SF,MM1,P,RM1	ELASAP,JF,MM1,P,RM0	3.3899e-06
ELPRACT,SF,MM1,P,RM1	ELASAP,JF,MM1,P,RM1	0.0084713
ELPRACT,SF,MM1,P,RM1	C	0.0098936
ELPRACT,SF,MM1,P,RM1	FL	0.00074202
ELPRACT,JF,MM0,G,RM0	ELASAP,JF,MM0,G,RM0	0.0015
ELPRACT,JF,MM0,G,RM0	ELASAP,JF,MM0,G,RM1	0.4985
ELPRACT,JF,MM0,G,RM0	FL	0.5
ELPRACT,JF,MM0,G,RM1	ELASAP,JF,MM0,G,RM0	0.00029693
ELPRACT,JF,MM0,G,RM1	ELASAP,JF,MM0,G,RM1	0.98946
ELPRACT,JF,MM0,G,RM1	C	0.0094027
ELPRACT,JF,MM0,G,RM1	FL	0.00084129
ELPRACT,JF,MM0,M,RM0	ELASAP,JF,MM0,M,RM0	0.002
ELPRACT,JF,MM0,M,RM0	ELASAP,JF,MM0,M,RM1	0.498
ELPRACT,JF,MM0,M,RM0	FL	0.5
ELPRACT,JF,MM0,M,RM1	ELASAP,JF,MM0,M,RM0	0.0003959
ELPRACT,JF,MM0,M,RM1	ELASAP,JF,MM0,M,RM1	0.98936
ELPRACT,JF,MM0,M,RM1	C	0.0094027
ELPRACT,JF,MM0,M,RM1	FL	0.00084129
ELPRACT,JF,MM0,P,RM0	ELASAP,JF,MM0,P,RM0	0.0025
ELPRACT,JF,MM0,P,RM0	ELASAP,JF,MM0,P,RM1	0.4975
ELPRACT,JF,MM0,P,RM0	FL	0.5

Continued on next page

Table A.3 – continued from previous page

S_t	S_{t+1}	**P**
ELPRACT,JF,MM0,P,RM1	ELASAP,JF,MM0,P,RM0	0.0049268
ELPRACT,JF,MM0,P,RM1	ELASAP,JF,MM0,P,RM1	0.98487
ELPRACT,JF,MM0,P,RM1	C	0.009361
ELPRACT,JF,MM0,P,RM1	FL	0.00083756
ELPRACT,JF,MM1,G,RM0	ELASAP,JF,MM0,G,RM0	0.0017491
ELPRACT,JF,MM1,G,RM0	ELASAP,JF,MM0,G,RM1	0.4985
ELPRACT,JF,MM1,G,RM0	FL	0.49975
ELPRACT,JF,MM1,G,RM1	ELASAP,JF,MM0,G,RM0	4.9468e-06
ELPRACT,JF,MM1,G,RM1	ELASAP,JF,MM0,G,RM1	0.98936
ELPRACT,JF,MM1,G,RM1	C	0.0098936
ELPRACT,JF,MM1,G,RM1	FL	0.00074202
ELPRACT,JF,MM1,M,RM0	ELASAP,JF,MM0,M,RM0	0.0022489
ELPRACT,JF,MM1,M,RM0	ELASAP,JF,MM0,M,RM1	0.498
ELPRACT,JF,MM1,M,RM0	FL	0.49975
ELPRACT,JF,MM1,M,RM1	ELASAP,JF,MM0,M,RM0	4.9468e-05
ELPRACT,JF,MM1,M,RM1	ELASAP,JF,MM0,M,RM1	0.98931
ELPRACT,JF,MM1,M,RM1	C	0.0098936
ELPRACT,JF,MM1,M,RM1	FL	0.00074202
ELPRACT,JF,MM1,P,RM0	ELASAP,JF,MM0,P,RM0	0.0027486
ELPRACT,JF,MM1,P,RM0	ELASAP,JF,MM0,P,RM1	0.4975
ELPRACT,JF,MM1,P,RM0	FL	0.49975
ELPRACT,JF,MM1,P,RM1	ELASAP,JF,MM0,P,RM0	0.00039575
ELPRACT,JF,MM1,P,RM1	ELASAP,JF,MM0,P,RM1	0.98897
ELPRACT,JF,MM1,P,RM1	C	0.0098936

Continued on next page

Table A.3 – continued from previous page

S_t	S_{t+1}	**P**
ELPRACT,JF,MM1,P,RM1	FL	0.00074202
C	E	1
T	E	1
FL	E	1
E	E	1

Table A.4: State Transition Probabilities for $A_t = LandPract$

S_t	S_{t+1}	**P**
N,NF,MM0,G,RM0	ELPRACT,NF,MM1,G,RM0	0.0024994
N,NF,MM0,G,RM0	ELPRACT,NF,MM1,G,RM1	0.99725
N,NF,MM0,G,RM0	ELPRACT,SF,MM1,G,RM0	1.1873e-07
N,NF,MM0,G,RM0	ELPRACT,SF,MM1,G,RM1	4.7372e-05
N,NF,MM0,G,RM0	FL	0.00019996
N,NF,MM0,G,RM1	ELPRACT,NF,MM1,G,RM0	0.00034686
N,NF,MM0,G,RM1	ELPRACT,NF,MM1,G,RM1	0.99069
N,NF,MM0,G,RM1	ELPRACT,SF,MM1,G,RM0	1.6477e-08
N,NF,MM0,G,RM1	ELPRACT,SF,MM1,G,RM1	4.706e-05
N,NF,MM0,G,RM1	C	0.0089197
N,NF,MM0,M,RM0	ELPRACT,NF,MM1,M,RM0	0.0044989
N,NF,MM0,M,RM0	ELPRACT,NF,MM1,M,RM1	0.99525
N,NF,MM0,M,RM0	ELPRACT,SF,MM1,M,RM0	2.1371e-07
N,NF,MM0,M,RM0	ELPRACT,SF,MM1,M,RM1	4.7277e-05

Continued on next page

Table A.4 – continued from previous page

S_t	S_{t+1}	**P**
N,NF,MM0,M,RM0	FL	0.00019996
N,NF,MM0,M,RM1	ELPRACT,NF,MM1,M,RM0	0.00044596
N,NF,MM0,M,RM1	ELPRACT,NF,MM1,M,RM1	0.99059
N,NF,MM0,M,RM1	ELPRACT,SF,MM1,M,RM0	2.1184e-08
N,NF,MM0,M,RM1	ELPRACT,SF,MM1,M,RM1	4.7055e-05
N,NF,MM0,M,RM1	C	0.0089197
N,NF,MM0,P,RM0	ELPRACT,NF,MM1,P,RM0	0.0054986
N,NF,MM0,P,RM0	ELPRACT,NF,MM1,P,RM1	0.99425
N,NF,MM0,P,RM0	ELPRACT,SF,MM1,P,RM0	2.612e-07
N,NF,MM0,P,RM0	ELPRACT,SF,MM1,P,RM1	4.7229e-05
N,NF,MM0,P,RM0	FL	0.00019996
N,NF,MM0,P,RM1	ELPRACT,NF,MM1,P,RM0	0.0054507
N,NF,MM0,P,RM1	ELPRACT,NF,MM1,P,RM1	0.98558
N,NF,MM0,P,RM1	ELPRACT,SF,MM1,P,RM0	2.5892e-07
N,NF,MM0,P,RM1	ELPRACT,SF,MM1,P,RM1	4.6817e-05
N,NF,MM0,P,RM1	C	0.0089197
N,NF,MM1,G,RM0	ELPRACT,NF,MM1,G,RM0	0.0039986
N,NF,MM1,G,RM0	ELPRACT,NF,MM1,G,RM1	0.99565
N,NF,MM1,G,RM0	ELPRACT,SF,MM1,G,RM0	1.8994e-07
N,NF,MM1,G,RM0	ELPRACT,SF,MM1,G,RM1	4.7296e-05
N,NF,MM1,G,RM0	FL	0.00029991
N,NF,MM1,G,RM1	ELPRACT,NF,MM1,G,RM0	5.4185e-06
N,NF,MM1,G,RM1	ELPRACT,NF,MM1,G,RM1	0.98517
N,NF,MM1,G,RM1	ELPRACT,SF,MM1,G,RM0	2.5739e-10

Continued on next page

Table A.4 – continued from previous page

S_t	S_{t+1}	**P**
N,NF,MM1,G,RM1	ELPRACT,SF,MM1,G,RM1	4.6798e-05
N,NF,MM1,G,RM1	C	0.014778
N,NF,MM1,M,RM0	ELPRACT,NF,MM1,M,RM0	0.0049983
N,NF,MM1,M,RM0	ELPRACT,NF,MM1,M,RM1	0.99465
N,NF,MM1,M,RM0	ELPRACT,SF,MM1,M,RM0	2.3743e-07
N,NF,MM1,M,RM0	ELPRACT,SF,MM1,M,RM1	4.7248e-05
N,NF,MM1,M,RM0	FL	0.00029991
N,NF,MM1,M,RM1	ELPRACT,NF,MM1,M,RM0	5.4185e-05
N,NF,MM1,M,RM1	ELPRACT,NF,MM1,M,RM1	0.98512
N,NF,MM1,M,RM1	ELPRACT,SF,MM1,M,RM0	2.5739e-09
N,NF,MM1,M,RM1	ELPRACT,SF,MM1,M,RM1	4.6795e-05
N,NF,MM1,M,RM1	C	0.014778
N,NF,MM1,P,RM0	ELPRACT,NF,MM1,P,RM0	0.0059979
N,NF,MM1,P,RM0	ELPRACT,NF,MM1,P,RM1	0.99365
N,NF,MM1,P,RM0	ELPRACT,SF,MM1,P,RM0	2.8491e-07
N,NF,MM1,P,RM0	ELPRACT,SF,MM1,P,RM1	4.7201e-05
N,NF,MM1,P,RM0	FL	0.00029991
N,NF,MM1,P,RM1	ELPRACT,NF,MM1,P,RM0	0.00044333
N,NF,MM1,P,RM1	ELPRACT,NF,MM1,P,RM1	0.98473
N,NF,MM1,P,RM1	ELPRACT,SF,MM1,P,RM0	2.1059e-08
N,NF,MM1,P,RM1	ELPRACT,SF,MM1,P,RM1	4.6777e-05
N,NF,MM1,P,RM1	C	0.014778
N,SF,MM0,G,RM0	ELPRACT,SF,MM0,G,RM0	0.0022055
N,SF,MM0,G,RM0	ELPRACT,SF,MM0,G,RM1	0.87998

Continued on next page

Table A.4 – continued from previous page

S_t	S_{t+1}	**P**
N,SF,MM0,G,RM0	ELPRACT,SF,MM1,G,RM0	0.00027259
N,SF,MM0,G,RM0	ELPRACT,SF,MM1,G,RM1	0.10876
N,SF,MM0,G,RM0	ELPRACT,JF,MM0,G,RM0	1.9093e-05
N,SF,MM0,G,RM0	ELPRACT,JF,MM0,G,RM1	0.0076182
N,SF,MM0,G,RM0	ELPRACT,JF,MM1,G,RM0	2.3598e-06
N,SF,MM0,G,RM0	ELPRACT,JF,MM1,G,RM1	0.00094158
N,SF,MM0,G,RM0	FL	0.00019996
N,SF,MM0,G,RM1	ELPRACT,SF,MM0,G,RM0	0.00030607
N,SF,MM0,G,RM1	ELPRACT,SF,MM0,G,RM1	0.87418
N,SF,MM0,G,RM1	ELPRACT,SF,MM1,G,RM0	3.7829e-05
N,SF,MM0,G,RM1	ELPRACT,SF,MM1,G,RM1	0.10805
N,SF,MM0,G,RM1	ELPRACT,JF,MM0,G,RM0	2.6497e-06
N,SF,MM0,G,RM1	ELPRACT,JF,MM0,G,RM1	0.007568
N,SF,MM0,G,RM1	ELPRACT,JF,MM1,G,RM0	3.275e-07
N,SF,MM0,G,RM1	ELPRACT,JF,MM1,G,RM1	0.00093538
N,SF,MM0,G,RM1	C	0.0089197
N,SF,MM0,M,RM0	ELPRACT,SF,MM0,M,RM0	0.0039698
N,SF,MM0,M,RM0	ELPRACT,SF,MM0,M,RM1	0.87821
N,SF,MM0,M,RM0	ELPRACT,SF,MM1,M,RM0	0.00049065
N,SF,MM0,M,RM0	ELPRACT,SF,MM1,M,RM1	0.10854
N,SF,MM0,M,RM0	ELPRACT,JF,MM0,M,RM0	3.4368e-05
N,SF,MM0,M,RM0	ELPRACT,JF,MM0,M,RM1	0.0076029
N,SF,MM0,M,RM0	ELPRACT,JF,MM1,M,RM0	4.2477e-06
N,SF,MM0,M,RM0	ELPRACT,JF,MM1,M,RM1	0.00093969

Continued on next page

Table A.4 – continued from previous page

S_t	S_{t+1}	**P**
N,SF,MM0,M,RM0	FL	0.00019996
N,SF,MM0,M,RM1	ELPRACT,SF,MM0,M,RM0	0.00039352
N,SF,MM0,M,RM1	ELPRACT,SF,MM0,M,RM1	0.8741
N,SF,MM0,M,RM1	ELPRACT,SF,MM1,M,RM0	4.8637e-05
N,SF,MM0,M,RM1	ELPRACT,SF,MM1,M,RM1	0.10803
N,SF,MM0,M,RM1	ELPRACT,JF,MM0,M,RM0	3.4068e-06
N,SF,MM0,M,RM1	ELPRACT,JF,MM0,M,RM1	0.0075673
N,SF,MM0,M,RM1	ELPRACT,JF,MM1,M,RM0	4.2107e-07
N,SF,MM0,M,RM1	ELPRACT,JF,MM1,M,RM1	0.00093528
N,SF,MM0,M,RM1	C	0.0089197
N,SF,MM0,P,RM0	ELPRACT,SF,MM0,P,RM0	0.004852
N,SF,MM0,P,RM0	ELPRACT,SF,MM0,P,RM1	0.87733
N,SF,MM0,P,RM0	ELPRACT,SF,MM1,P,RM0	0.00059969
N,SF,MM0,P,RM0	ELPRACT,SF,MM1,P,RM1	0.10843
N,SF,MM0,P,RM0	ELPRACT,JF,MM0,P,RM0	4.2005e-05
N,SF,MM0,P,RM0	ELPRACT,JF,MM0,P,RM1	0.0075953
N,SF,MM0,P,RM0	ELPRACT,JF,MM1,P,RM0	5.1917e-06
N,SF,MM0,P,RM0	ELPRACT,JF,MM1,P,RM1	0.00093874
N,SF,MM0,P,RM0	FL	0.00019996
N,SF,MM0,P,RM1	ELPRACT,SF,MM0,P,RM0	0.0048097
N,SF,MM0,P,RM1	ELPRACT,SF,MM0,P,RM1	0.86968
N,SF,MM0,P,RM1	ELPRACT,SF,MM1,P,RM0	0.00059446
N,SF,MM0,P,RM1	ELPRACT,SF,MM1,P,RM1	0.10749
N,SF,MM0,P,RM1	ELPRACT,JF,MM0,P,RM0	4.1639e-05

Continued on next page

Table A.4 – continued from previous page

S_t	S_{t+1}	**P**
N,SF,MM0,P,RM1	ELPRACT,JF,MM0,P,RM1	0.0075291
N,SF,MM0,P,RM1	ELPRACT,JF,MM1,P,RM0	5.1464e-06
N,SF,MM0,P,RM1	ELPRACT,JF,MM1,P,RM1	0.00093056
N,SF,MM0,P,RM1	C	0.0089197
N,SF,MM1,G,RM0	ELPRACT,SF,MM0,G,RM0	9.9112e-06
N,SF,MM1,G,RM0	ELPRACT,SF,MM0,G,RM1	0.0024679
N,SF,MM1,G,RM0	ELPRACT,SF,MM1,G,RM0	0.0039546
N,SF,MM1,G,RM0	ELPRACT,SF,MM1,G,RM1	0.98469
N,SF,MM1,G,RM0	ELPRACT,JF,MM0,G,RM0	8.5804e-08
N,SF,MM1,G,RM0	ELPRACT,JF,MM0,G,RM1	2.1365e-05
N,SF,MM1,G,RM0	ELPRACT,JF,MM1,G,RM0	3.4236e-05
N,SF,MM1,G,RM0	ELPRACT,JF,MM1,G,RM1	0.0085247
N,SF,MM1,G,RM0	FL	0.00029991
N,SF,MM1,G,RM1	ELPRACT,SF,MM0,G,RM0	1.3431e-08
N,SF,MM1,G,RM1	ELPRACT,SF,MM0,G,RM1	0.0024419
N,SF,MM1,G,RM1	ELPRACT,SF,MM1,G,RM0	5.3588e-06
N,SF,MM1,G,RM1	ELPRACT,SF,MM1,G,RM1	0.97432
N,SF,MM1,G,RM1	ELPRACT,JF,MM0,G,RM0	1.1627e-10
N,SF,MM1,G,RM1	ELPRACT,JF,MM0,G,RM1	2.114e-05
N,SF,MM1,G,RM1	ELPRACT,JF,MM1,G,RM0	4.6392e-08
N,SF,MM1,G,RM1	ELPRACT,JF,MM1,G,RM1	0.0084349
N,SF,MM1,G,RM1	C	0.014778
N,SF,MM1,M,RM0	ELPRACT,SF,MM0,M,RM0	1.2389e-05
N,SF,MM1,M,RM0	ELPRACT,SF,MM0,M,RM1	0.0024654

Continued on next page

Table A.4 – continued from previous page

S_t	S_{t+1}	**P**
N,SF,MM1,M,RM0	ELPRACT,SF,MM1,M,RM0	0.0049432
N,SF,MM1,M,RM0	ELPRACT,SF,MM1,M,RM1	0.9837
N,SF,MM1,M,RM0	ELPRACT,JF,MM0,M,RM0	1.0725e-07
N,SF,MM1,M,RM0	ELPRACT,JF,MM0,M,RM1	2.1344e-05
N,SF,MM1,M,RM0	ELPRACT,JF,MM1,M,RM0	4.2795e-05
N,SF,MM1,M,RM0	ELPRACT,JF,MM1,M,RM1	0.0085161
N,SF,MM1,M,RM0	FL	0.00029991
N,SF,MM1,M,RM1	ELPRACT,SF,MM0,M,RM0	1.3431e-07
N,SF,MM1,M,RM1	ELPRACT,SF,MM0,M,RM1	0.0024418
N,SF,MM1,M,RM1	ELPRACT,SF,MM1,M,RM0	5.3588e-05
N,SF,MM1,M,RM1	ELPRACT,SF,MM1,M,RM1	0.97427
N,SF,MM1,M,RM1	ELPRACT,JF,MM0,M,RM0	1.1627e-09
N,SF,MM1,M,RM1	ELPRACT,JF,MM0,M,RM1	2.1139e-05
N,SF,MM1,M,RM1	ELPRACT,JF,MM1,M,RM0	4.6392e-07
N,SF,MM1,M,RM1	ELPRACT,JF,MM1,M,RM1	0.0084345
N,SF,MM1,M,RM1	C	0.014778
N,SF,MM1,P,RM0	ELPRACT,SF,MM0,P,RM0	1.4867e-05
N,SF,MM1,P,RM0	ELPRACT,SF,MM0,P,RM1	0.0024629
N,SF,MM1,P,RM0	ELPRACT,SF,MM1,P,RM0	0.0059319
N,SF,MM1,P,RM0	ELPRACT,SF,MM1,P,RM1	0.98271
N,SF,MM1,P,RM0	ELPRACT,JF,MM0,P,RM0	1.2871e-07
N,SF,MM1,P,RM0	ELPRACT,JF,MM0,P,RM1	2.1322e-05
N,SF,MM1,P,RM0	ELPRACT,JF,MM1,P,RM0	5.1354e-05
N,SF,MM1,P,RM0	ELPRACT,JF,MM1,P,RM1	0.0085076

Continued on next page

Table A.4 – continued from previous page

S_t	S_{t+1}	**P**
N,SF,MM1,P,RM0	FL	0.00029991
N,SF,MM1,P,RM1	ELPRACT,SF,MM0,P,RM0	1.0989e-06
N,SF,MM1,P,RM1	ELPRACT,SF,MM0,P,RM1	0.0024408
N,SF,MM1,P,RM1	ELPRACT,SF,MM1,P,RM0	0.00043845
N,SF,MM1,P,RM1	ELPRACT,SF,MM1,P,RM1	0.97389
N,SF,MM1,P,RM1	ELPRACT,JF,MM0,P,RM0	9.5131e-09
N,SF,MM1,P,RM1	ELPRACT,JF,MM0,P,RM1	2.1131e-05
N,SF,MM1,P,RM1	ELPRACT,JF,MM1,P,RM0	3.7957e-06
N,SF,MM1,P,RM1	ELPRACT,JF,MM1,P,RM1	0.0084312
N,SF,MM1,P,RM1	C	0.014778
N,JF,MM0,G,RM0	ELPRACT,JF,MM0,G,RM0	0.0024995
N,JF,MM0,G,RM0	ELPRACT,JF,MM0,G,RM1	0.9973
N,JF,MM0,G,RM0	FL	0.00019996
N,JF,MM0,G,RM1	ELPRACT,JF,MM0,G,RM0	0.00034688
N,JF,MM0,G,RM1	ELPRACT,JF,MM0,G,RM1	0.99073
N,JF,MM0,G,RM1	C	0.0089197
N,JF,MM0,M,RM0	ELPRACT,JF,MM0,M,RM0	0.0044991
N,JF,MM0,M,RM0	ELPRACT,JF,MM0,M,RM1	0.9953
N,JF,MM0,M,RM0	FL	0.00019996
N,JF,MM0,M,RM1	ELPRACT,JF,MM0,M,RM0	0.00044599
N,JF,MM0,M,RM1	ELPRACT,JF,MM0,M,RM1	0.99063
N,JF,MM0,M,RM1	C	0.0089197
N,JF,MM0,P,RM0	ELPRACT,JF,MM0,P,RM0	0.0054989
N,JF,MM0,P,RM0	ELPRACT,JF,MM0,P,RM1	0.9943

Continued on next page

Table A.4 – continued from previous page

S_t	S_{t+1}	**P**
N,JF,MM0,P,RM0	FL	0.00019996
N,JF,MM0,P,RM1	ELPRACT,JF,MM0,P,RM0	0.0054509
N,JF,MM0,P,RM1	ELPRACT,JF,MM0,P,RM1	0.98563
N,JF,MM0,P,RM1	C	0.0089197
N,JF,MM1,G,RM0	ELPRACT,JF,MM0,G,RM0	0.0039988
N,JF,MM1,G,RM0	ELPRACT,JF,MM0,G,RM1	0.9957
N,JF,MM1,G,RM0	FL	0.00029991
N,JF,MM1,G,RM1	ELPRACT,JF,MM0,G,RM0	5.4187e-06
N,JF,MM1,G,RM1	ELPRACT,JF,MM0,G,RM1	0.98522
N,JF,MM1,G,RM1	C	0.014778
N,JF,MM1,M,RM0	ELPRACT,JF,MM0,M,RM0	0.0049985
N,JF,MM1,M,RM0	ELPRACT,JF,MM0,M,RM1	0.9947
N,JF,MM1,M,RM0	FL	0.00029991
N,JF,MM1,M,RM1	ELPRACT,JF,MM0,M,RM0	5.4187e-05
N,JF,MM1,M,RM1	ELPRACT,JF,MM0,M,RM1	0.98517
N,JF,MM1,M,RM1	C	0.014778
N,JF,MM1,P,RM0	ELPRACT,JF,MM0,P,RM0	0.0059982
N,JF,MM1,P,RM0	ELPRACT,JF,MM0,P,RM1	0.9937
N,JF,MM1,P,RM0	FL	0.00029991
N,JF,MM1,P,RM1	ELPRACT,JF,MM0,P,RM0	0.00044335
N,JF,MM1,P,RM1	ELPRACT,JF,MM0,P,RM1	0.98478
N,JF,MM1,P,RM1	C	0.014778
C	E	1
T	E	1

Continued on next page

Table A.4 – continued from previous page

S_t	S_{t+1}	**P**
FL	E	1
E	E	1

BIBLIOGRAPHY

BIBLIOGRAPHY

[1] *Carbon Fiber 6040 Propeller*, (accessed 2017).

[2] *20A range Current Sensor ACS712 Module*, (accessed 2019).

[3] *BeagleBone Blue*, accessed 2019.

[4] C. Ampatis and E. Papadopoulos. Parametric design and optimization of multirotor aerial vehicles. In *2014 IEEE International Conference on Robotics and Automation (ICRA)*, pages 6266–6271, Hong Kong, China, May 2014.

[5] Gavin K. Ananda, Michael S. Selig, and Robert W. Deters. Experiments of propeller-induced flow effects on a low-reynolds-number wing. *AIAA Journal*, 56(8):3279–3294, 2018.

[6] Saurabh Arora and Prashant Doshi. A survey of inverse reinforcement learning: Challenges, methods and progress. *Artificial Intelligence*, 297:103500, 2021.

[7] ASTM-F3005-14a. Standard specification for batteries for use in small unmanned aircraft systems (suas). *ASTM International,West Conshohocken, PA, 2014*, 2014.

[8] Ella M Atkins, Igor Alonso Portillo, and Matthew J Strube. Emergency flight planning applied to total loss of thrust. *Journal of Aircraft*, 43(4):1205–1216, 2006.

[9] E. Balaban, S.Narasimhan, M.Daigle, I.Roychoudhury, A.Sweet, C.Bond, and G.Gorospe. Development of a mobile robot test platform and methods for validation of prognostics-enabled decision making algorithms. *International Journal of Prognostics and Health Management*, 4(1):87, 2013.

[10] Moses Bangura, Marco Melega, Roberto Naldi, and Robert Mahony. Aerodynamics of rotor blades for quadrotors. *arXiv preprint arXiv:1601.00733*, 2016.

[11] R. Beard and T.McLain. *Small Unmanned Aircraft: Theory and Practice*, chapter 4. Princeton University Press, 2012.

[12] Dmitry Bershadsky, Steve Haviland, and Eric N. Johnson. Electric multirotor uav propulsion system sizing for performance prediction and design optimization. In *AIAA SciTech Forum*, San Diego, CA, Jan 2016. AIAA.

[13] Brett Bethke, Luca Bertuccelli, and Jonathan How. *Experimental Demonstration of Adaptive MDP-Based Planning with Model Uncertainty*. 2012.

[14] Sungjin Choi and Jon Ahn. A computational study on the aerodynamic influence of a pusher propeller on a mav. In *54th AIAA Aerospace Sciences Meeting, AIAA SciTech Forum*, San Deigo, CA, Jun 2010. AIAA.

[15] S. Ci, N. Lin, and D. Wu. Reconfigurable battery techniques and systems: A survey. *IEEE Access*, 4:1175–1189, 2016.

[16] Reece A Clothier and Rodney A Walker. *Handbook of Unmanned Aerial Vehicles*, chapter Safety Risk Management of Unmanned Aircraft Systems, pages 2229–2275. Springer Dordrecht, 2015.

[17] Yao Da, Xiaodong Shi, and Mahesh Krishnamurthy. Health monitoring, fault diagnosis and failure prognosis techniques for brushless permanent magnet machines. In *IEEE Vehicle Power and Propulsion Conference*, pages 1–7, 2011.

[18] Matthew Daigle and Shankar Sankararaman. Advanced methods for determining prediction uncertainty in model-based prognostics with application to planetary rovers. In *Annual Conference of the PHM Society*, volume 5, 2013.

[19] Patrick Darmstadt, Ralph Catanese, Allan Beiderman, Fernando Dones, Ephraim Chen, Mihir Mistry, Brian Babie, Mary Beckman, and Robin Preator. Hazards analysis and failure modes and effects criticality analysis (fmeca) of four conceptvehicle propulsion systems. *NASA/CR—2019-220217*, 2019.

[20] Timothy Darrah, Marcos Quiñones-Grueiro, Gautam Biswas, and Chetan S. Kulkarni. *Prognostics Based Decision Making for Safe and Optimal UAV Operations*. 2021.

[21] Robert W. Deters, Stefan Kleinke, and Michael S. Selig. Static testing of propulsion elements for small multirotor unmanned aerial vehicles. In *AIAA AVIATION Forum*, Denver, CO, Jun 2017. AIAA.

[22] Pedro FA Di Donato and Ella M Atkins. Optimizing steady turns for gliding trajectories. *Journal of Guidance, Control, and Dynamics*, 39(12):2627–2637, 2016.

[23] G. J. J. Ducard and M.-D. Hua. Discussion and practical aspects on control allocation for a multi-rotor helicopter. *ISPRS - International Archives of the Photogrammetry, Remote Sensing and Spatial Information Sciences*, XXXVIII-1/C22:95–100, 2011.

[24] E.Balaban and J.J.Alonso. A modeling framework for prognostic decision making and its application to uav mission planning. In *Annual Conference of The Prognostics and Health Management Society*, pages 1–12, 2013.

[25] E.F.Hogge, B.M. Bole, S.L. Vazquez, C.S Kulkarni, T.H.Strom, B.L.Hill, K.M.Smalling, and C.C.Quach. Verification of prognostic algorithms to predict remaining flying time for electric unmanned vehicles. *International Journal of Prognostics and Health Management*, 2018.

[26] John V. Foster and David Hartman. High-fidelity multi-rotor unmanned aircraft system (UAS) simulation development for trajectory prediction under off-nominal flight dynamics. In *17th AIAA Aviation Technology, Integration, and Operations Conference*. American Institute of Aeronautics and Astronautics, jun 2017.

[27] Kai Goebel and Bhaskar Saha. *Prognostics Applied to Electric Propulsion UAV*, pages 1053–1070. Springer Netherlands, 2015.

[28] X. Gong, R. Xiong, and C. C. Mi. Study of the characteristics of battery packs in electric vehicles with parallel-connected lithium-ion battery cells. *IEEE Applied Power Electronics Conference and Exposition*, pages 3218–3224, 2014.

[29] Javier Gonzalez-Rocha, Prashin Sharma, Ella Atkins, and Craig Woolsey. A study of the wind sensing performance of pusher and puller hexacopter small unmanned aircraft. *Journal of Aircraft*, 2021.

[30] Patrick Y. Haas, Christophe Balistreri, Piero Pontelandolfo, Gilles Triscone, Hasret Pekoz, and Antonio Pignatiello. Development of an unmanned aerial vehicle uav for air quality measurement in urban areas. In *AIAA AVIATION Forum*, Atlanta, GA, Jun 2014. AIAA.

[31] Gabriel Hoffmann, Haomiao Huang, Steven Waslander, and Claire Tomlin. Quadrotor helicopter flight dynamics and control: Theory and experiment. In *Guidance, Navigation, and Control and Co-located Conferences*, Hilton Head, SC, Aug 2007. AIAA.

[32] E.B Iversen, J.M.Morales, and H.Madsen. Optimal charging of an electric vehicle using a markov decision process. *Applied Energy*, 123:1–12, 2014.

[33] K. P. Jain and M. W. Mueller. Flying batteries: In-flight battery switching to increase multirotor flight time. In *IEEE International Conference on Robotics and Automation (ICRA)*, pages 3510–3516, 2020.

[34] I. Jennions. *Integrated Vehicle Health Management: The Technology*. SAE International Warrendale, PA, 2013.

[35] Joseph Kim and Ella Atkins. Airspace geofencing and flight planning for low-altitude, urban, small unmanned aircraft systems. *Applied Sciences*, 12(2):576, 2022.

[36] Joseph Kim, Prashin Sharma, Ella Atkins, Natasha Neogi, Evan Dill, and Steven Young. Assured contingency landing management for advanced air mobility. In

IEEE/AIAA 40th Digital Avionics Systems Conference (DASC), pages 1–12, 2021.

[37] D. Kotarski, P. Piljek, H. Brezak, and J. Kasać. Design of a fully actuated passively tilted multirotor uav with decoupling control system. In *8th International Conference on Mechanical and Aerospace Engineering (ICMAE)*, pages 385–390, Prague, Czech Republic, July 2017.

[38] C.S. Kulkarni and M.Corbetta. Health management and prognostics for electric aircraft powertrain. *AIAA Propulsion and Energy Forum*, 2019.

[39] Simon Lindblom. *Modelling and control of a hexarotor UAV*. PhD dissertation, Linkoping University,Sweden, 2015.

[40] M.J. Logan, J.Gundlach, and T. Vranas. Design considerations for safer small uas. *AIAA Information Systems- AIAA Infotech @ Aerospace*, 2018.

[41] R. Mahony, V. Kumar, and P. Corke. Multirotor aerial vehicles: Modeling, estimation, and control of quadrotor. *IEEE Robotics Automation Magazine*, 19(3):20–32, Sep. 2012.

[42] M. Vidyasagar Mark W Spong, Seth Hutchison. In *Robot Modelling And Control*, chapter 5, pages 163–201. John Willey And Sons Inc., New Jersey, 2006.

[43] Daniel Mellinger, Nathan Michael, and Vijay Kumar. Trajectory generation and control for precise aggressive maneuvers with quadrotors. *The International Journal of Robotics Research*, 31(5):664–674, 2012.

[44] C. Mikolajczak, M.Kahn, K.White, and R.T.Long. Lithium-ion batteries hazard and use assessment. *Fire Protection Research Foundation Report*, 2011.

[45] M.L.Putterman. *Markov Decision Processes: Discrete Stochastic Dynamic Programming*. John Wiley & Sons, 2005.

[46] D Subbaram Naidu. *Optimal control systems*. CRC press, 2002.

[47] N.Eleftheroglou, S.S. Mansouri, T.Loutas, P.Karvelis, G.Georgoulas, G.Nikolakopoulos, and D. Zarouchas. Intelligent data-driven prognostic methodologies for the real-time remaining useful life until the end-of-discharge estimation of the lithium-polymer batteries of unmanned aerial vehicles with uncertainty quantification. *Applied Energy*, 254, 2019.

[48] Cosme A Ochoa and Ella M Atkins. Urban metric maps for small unmanned aircraft systems motion planning. *Journal of Aerospace Information Systems*, 19(1):37–52, 2022.

[49] Isaac Olson and Ella Atkins. Qualitative failure analysis for a small quadrotor unmanned aircraft system. *AIAA Guidance, Navigation, and Control Conference*, 2013.

[50] M. Osborne, J. Lantair, Z. Shafiq, X. Zhao, V. Robu, D. Flynn, and J. Perry. UAS Operators Safety and Reliability Survey: Emerging Technologies towards the Certification of Autonomous UAS. *4th International Conference on System Reliability and Safety (ICSRS)*, pages 203–212, 2019.

[51] G.L. Plett. *Battery Management Systems, Volume I: Battery modeling*, volume 1. Artech House, 2015.

[52] G.L. Plett. *Battery Management Systems, Volume II: Equivalent Circuit Methods*, volume 1, chapter 1. Artech House, 2015.

[53] T. Potteiger, W. Strayhorn, K. R. Pence, and G. Karsai. A dependable, prognostics-incorporated, n-s modular battery reconfiguration scheme with an application to electric aircraft. *IEEE/AIAA 36th Digital Avionics Systems Conference*, pages 1–9, 2017.

[54] P.Sharma and E.M.Atkins. Experimental investigation of tractor and pusher hexacopter performance. *Journal of Aircraft*, 56(5):1920–1934, 2019.

[55] P.Sharma and E.M.Atkins. Prognostics-based decision making for safe autonomous flight. *Doctoral Symposium, Annual Conference of the PHM Society 2020*, 2020.

[56] Chidong Qiu, Xinbo Wu, Changqing Xu, Xiang Qiu, and Zhengyu Xue. An approximate estimation approach of fault size for spalled ball bearing in induction motor by tracking multiple vibration frequencies in current. *Sensors*, 20(6), 2020.

[57] Quan Quan. In *Introduction to Multicopter Design and Control*, chapter 4, pages 73–95. Springer Singapore, 2017.

[58] R.Schacht-Rodríguez, J-C.Ponsart, CD.García-Beltrán, and CM.Astorga-Zaragoza. Prognosis and health management for the prediction of uav flight endurance. *10th IFAC Symposium on Fault Detection, Supervision and Safety for Technical Processes SAFEPROCESS*, 51(24):983–990, 2018.

[59] Carl R Russell, Jaewoo Jung, Gina Willink, and Brett Glasner. Wind tunnel and hover performance test results for multicopter uas vehicles. In *72nd American Helicopter Society International Annual Forum and Technology Display*, West Palm Beach, FL, May 2016.

[60] Bhaskar Saha, Kai Goebel, Scott Poll, and Jon Christophersen. Prognostics methods for battery health monitoring using a bayesian framework. *IEEE Transactions on Instrumentation and Measurement*, 58(2):291–296, 2009.

[61] Kanika Saini, S. S. Dhami, and Vanraj. Predictive monitoring of incipient faults in rotating machinery: A systematic review from data acquisition to artificial intelligence. *Archives of Computational Methods in Engineering*, 2022.

[62] S. Saxena, Y. Xing, and M.G Pecht. PHM of li-ion batteries. *Prognostics and Health Management of Electronics*, pages 349–375, 2018.

[63] R. Schacht-Rodríguez, J. C. Ponsart, C. D. García-Beltrán, C. M. Astorga-Zaragoza, and D. Theilliol. Mission planning strategy for multirotor uav based on flight endurance estimation*. In *International Conference on Unmanned Aircraft Systems (ICUAS)*, pages 778–786, June 2019.

[64] Johann Schumann, Nagabhushan Mahadevan, Adam Sweet, Anupa R. Bajwa, Michael Lowry, and Gabor Karsai. *Model-based System Health Management and Contingency Planning for Autonomous UAS*. 2019.

[65] Prashin Sharma, Benjamin Kraske, Joseph Kim, Zakariya Laouar, Ella Atkins, and Zachary Sunberg. Investigation of risk-aware mdp and pomdp contingency management autonomy for uas. *In Preparation*, 2022.

[66] S.Thein and Y.S.Chang. Decision making model for lifecycle assessment of lithium-ion battery for electric vehicle - a case study for smart electric bus project in korea. *Journal of Power Sources*, 249:142–147, 2014.

[67] James Strawson. *RC Pilot*, accessed 2019.

[68] Yu Sui and Shiming Song. A multi-agent reinforcement learning framework for lithium-ion battery scheduling problems. *Energies*, 13(8), 2020.

[69] Richard S Sutton and Andrew G Barto. *Reinforcement learning: An introduction*. MIT press, 2018.

[70] L. Tang, G. J. Kacprzynski, K. Goebel, A. Saxena, B. Saha, and G. Vachtsevanos. Prognostics-enhanced automated contingency management for advanced autonomous systems. In *International Conference on Prognostics and Health Management*, pages 1–9, 2008.

[71] L. Tang, G. J. Kacprzynski, K. Goebel, and G. Vachtsevanos. Case studies for prognostics-enhanced automated contingency management for aircraft systems. In *IEEE Aerospace Conference*, pages 1–11, March 2010.

[72] B. Theys, G. Dimitriadis, P. Hendrick, and J. De Schutter. Influence of propeller configuration on propulsion system efficiency of multi-rotor unmanned aerial vehicles. In *International Conference on Unmanned Aircraft Systems (ICUAS)*, pages 195–201, Arlington, VA, June 2016. IEEE.

[73] P. Weicker. *A Systems Approach to Lithium-Ion Battery Management*, chapter 1. Artech House, 2013.

[74] M. Wohlfahrt-Mehrens, C. Vogler, and J. Garche. Aging mechanisms of lithium cathode materials. *Journal of Power Sources*, 127(1):58–64, 2004.

[75] Seokkwan Yoon, Patricia Ventura Diaz, D Douglas Boyd Jr, William M Chan, and Colin R Theodore. Computational aerodynamic modeling of small quadcopter vehicles. In *American Helicopter Society (AHS) 73rd Annual Forum Fort Worth, Texas*, 2017. AHS Paper 73-2017-0015.

[76] Steven Yoon, Henry C. Lee, and Thomas H. Pulliam. Computational analysis of multi-rotor flows. In *AIAA SciTech Forum*, San Deigo, CA, Jan 2016. AIAA.

[77] Larry A. Young. *Conceptual Design Aspects of Three General Sub-Classes of Multi-Rotor Configurations: Distributed, Modular, and Heterogeneous*. American Helicopter Society, Moffett Field, CA 94035, Jan 2015.

[78] Omid Zandi and Javad Poshtan. Fault diagnosis of brushless dc motors using built-in hall sensors. *IEEE Sensors Journal*, 19(18):8183–8190, 2019.

[79] B. Zhang, L.Tang, J.Decastro, M.Roemer, and K. Goebel. Autonomous vehicle battery state-of-charge prognostics enhanced mission planning. *International Journal of Prognostics and Health Management*, 5(8), 2014.

[80] Bin Zhang, Chris Sconyers, Romano Patrick, and George Vachtsevanos. A multi-fault modeling approach for fault diagnosis and failure prognosis of engineering systems. *Annual Conference of the Prognostics and Health Management Society*, (1465), 2009.

[81] Shen Zhang, Shibo Zhang, Bingnan Wang, and Thomas G. Habetler. Deep learning algorithms for bearing fault diagnostics - a review. In *2019 IEEE 12th International Symposium on Diagnostics for Electrical Machines, Power Electronics and Drives (SDEMPED)*, pages 257–263, 2019.